1992

Solid state chemistry of some polar intermetallic tetrelides of the rare-earth and alkaline-earth metals

Arnold Mejia Guloy
Iowa State University

Order Number 9220970

Solid state chemistry of some polar intermetallic tetrelides of the rare-earth and alkaline-earth metals

Guloy, Arnold Mejia, Ph.D.

Iowa State University, 1992

U·M·I
300 N. Zeeb Rd.
Ann Arbor, MI 48106

Solid state chemistry of some polar intermetallic tetrelides of the rare-earth and alkaline-earth metals

by

Arnold Mejia Guloy

A Dissertation Submitted to the
Graduate Faculty in Partial Fulfillment of the
Requirements for the Degree of
DOCTOR OF PHILOSOPHY

Department: **Chemistry**
Major: **Inorganic Chemistry**

Approved:

Signature was redacted for privacy.

In Charge of Major Work

Signature was redacted for privacy.

For the Major Department

Signature was redacted for privacy.

For the Graduate College

Iowa State University
Ames, Iowa

1992

TABLE OF CONTENTS

INTRODUCTION

Solid state chemistry, particularly the exploratory syntheses of inorganic materials, has experienced a renaissance over the past few years. This was brought about by the discovery of interesting and unprecedented properties such as high temperature superconductivity,[1] charge density waves,[2] heavy fermions[3] and other unusual electronic and magnetic properties in novel solid state materials. More importantly, the potential of exploratory synthesis has been emphasized by expectations that future new discoveries await an "explorer." Its importance in solid state chemistry cannot be overemphasized, for what new properties could be measured and discovered without the syntheses of the solid state materials? In many instances the initial synthesis of a material preceded the discovery of its novel physical property by many years;[4] the synthesis of alkaline-earth-metal-substituted La_2CuO_4 and the discovery of its high temperature superconductivity is an example.[5,6]

In understanding solid state materials and their syntheses, one has to be keenly aware of structure-bonding-property relationships. These interrelationships have had an important role in understanding chemical systems. On the other hand, unlike organic chemistry, solid state chemistry suffers from the inability of current basic chemical principles and concepts to completely understand and predict composition, structure, and reaction mechanisms of solid state materials. Hence the synthesis of novel solids is as much an art as a science, and much of its direction has been guided by empirical rules developed from past serendipitous and intuitive discoveries. However, this lack of

predictive power offers not only an opportunity and a source of challenge but also of wonder and surprise.

Once a new compound is synthesized, it is probable that some of its properties can be reasonably predicted. However, the cases in which the ability to predict properties fail are not unusual. Therefore, physical properties of a new material must be measured to see if novel behavior is present. This also contributes to building a larger body of knowledge that will add insight into the syntheses of other new solid materials.

The syntheses of intermetallic compounds offers a fertile ground for exploratory work. Not only does it offer a wide area for adventure in the many elements that are available, but it also provides a testing ground for any new intuitive and innovative concepts of chemical bonding. Developing a rational approach in the syntheses of new intermetallic phases is a challenge since their bonding involves many interrelated and often complex factors. One such challenge is in combinations between transition and non-transition metals, where present ideas about their bonding are not yet well established.

As chemists, we continually look for bonds in materials, and the Zintl concept[7] provides an effective and useful way to describe chemical bonding in a large range of crystal structures. In this simple scheme, electropositive metals act merely as electron donors, donating electrons to their more electronegative bonding partners. The latter elements then form bonds to satisfy the octet rule, yielding anionic clusters, chains, layers and networks. The Zintl concept has been widely used by many "explorers" in directing and rationalizing the syntheses of non-transition intermetallics. In our attempts to

REVIEW OF LITERATURE

Intermetallic Compounds

When two metals A and B are melted together and the liquid mixture is then slowly cooled, different equilibrium phases appear as a function of composition and temperature. These equilibrium phases are described by a condensed-phase diagram. The solid region of a binary phase diagram usually contains one or more intermediate phases, in addition to terminal solid solutions. In solid solutions, the solute atoms may occupy random substitutional positions in the host-metal lattice, preserving the crystal structure of the host. Interstitial solid solutions also exist wherein the small atoms occupy interstitial sites in the larger host-metal lattice. Solid solutions normally have wide compositional ranges. On the other hand, an intermediate phase has a narrow compositional range and a crystal structure different from those of the the component metals. These "narrow" intermediate phases are commonly known as "intermetallic compounds" or "intermetallics".[8,9,10]

An intermetallic compound, CuZn, was first reported by Karl Karsten in 1839 after observing that CuZn reacted with acids differently from other Cu-Zn solutions of different proportions.[11] Many systematic studies on intermetallic compounds ensued. The important constitutional studies by Tamman[12,13,14,15] in applying the phase rule and the physico-chemical studies of Kurnakov[16,17] led Desch[18,19] to direct the attention of many scientists to the study of intermetallics. During the early stages, unaware of the atomic ordering which occurred in intermetallics, researchers were deeply puzzled by many physical property anomalies of these phases.

The introduction and use of X-ray diffraction in structural studies proved to be the most valuable development in the study of these solid state materials. It led to a recognition of long-range ordering in intermetallics and enabled direct structural studies of solid state compounds. Structure-bonding relationships was also a natural result.

In 1926 Hume-Rothery[20] and Westgren and Phragmen[21] made important contributions in understanding intermetallic compounds by proposing an electron counting scheme for compounds of the noble metals with s-p elements. Hume-Rothery correlated the crystal structures of compounds, which are now known as Hume-Rothery phases, with the average number of valence electrons per atom. This led to electron concentrations of 1.38, 1.48, 1.62 and 1.75 per atom for the fcc α-phase,bcc β-phase, γ-phase and hcp ε-phase respectively. This concept was theoretically justified by the works of Mott and Jones[22] and improved by the pseudo-potential calculations of Heine.[23] However, recent critiques by Pettifor[24] and a review by Massalski and Mizutani[25] contend that an accurate explanation of the Hume-Rothery rules has not yet been achieved due to the neglect of overlapping d-orbitals and the inability to correctly include ionic and electron correlation effects. Hume-Rothery and co-workers also generalized their rules on the formation of primary solid solutions based on (1) size rule, (2) the electrochemical factor and (3) the relative valence effect.[26,27] Furthermore, Darken and Gurry[28,29] made an important step in predicting solid solubility by combining the first two rules into correlations between size and electronegativity in what are now called Darken-Gurry maps. A nice discussion on the theoretical validity of these rules is given by Alonso and March.[30]

Another important concept in the formation and stability of intermetallic compounds is based on the sizes of the constituent metal atoms. This was first introduced by Biltz and Laves[31,32,33,34] and formalized by Frank and Kasper.[35,36] It states that complex structures found in intermetallic compounds can be explained in terms of the geometrical requirements of sphere close-packing which are associated with the atomic radius ratio of the component atoms. It can also be restated that the coordination polyhedra in intermetallics have the following features: (1) triangular faces because of effective tetrahedral close-packing, (2) convex polyhedron and (3) five or six edges meet at each corner.[28] Laves[37] also added that the geometrical factor is guided by three principles, namely: (1) space filling: the tendency to fill space as well as possible, i.e., high coordination number; (2) symmetry: the tendency to form arrangements of the highest possible symmetry; and (3) connection: the tendency to form the closest connections between like atoms. These concepts were best illustrated in the MgX_2 type compounds and extended to other related binary MX_2 and ternary derivative compounds now collectively known as Laves phases.[38]

The correlation between structural preferences of MgX_2 compounds with the ratio of the atomic radii of the components was surprisingly accurate, and research to explain the stability of the Laves phases has been active.[39,40,41,42,43] Theoretical studies on Laves phases using pseudo-potential theory have shown that although geometrical factors in these phases are dominant, electrostatic effects alone lead to unfavorable energies and that distorted structures are favored. These results have been supported by the experimental work on $MgZn_2$ and $MgCu_2$ by Ohba et.al.[44] It can then be said that only through the balanced interplay of electrostatic and electronic effects can the structure of

to simple valence rules, partly due to the lack of structural information.[59,60,61,62,63,64] Since then efforts to structurally characterize the compounds were pursued.[65,66] Finally, Corbett and co-workers[67] presented a general method for isolating and crystallizing many "naked" cluster polyanions, now known as Zintl anions.[68,69] This represented a clear link between intermetallic solid state compounds and the isolated metal-clusters of molecular chemists.

Attempts to classify intermetallics based on structure and bonding were made and have led to popular generalizations. Hume-Rothery[70] developed a set of general rules in the formation of intermetallics wherein (1) electronegativity differences between the constituent atoms, (2) the tendency of s-p metals and transition metals to fill their s-p and d shells, (3) size-factor effects, (4) electron concentration, and (5) "orbital restrictions"; related to the symmetry conditions for orbital hybridization, are postulated to control the stability of all intermetallic structures.

Pearson[51] also classified intermetallics into groups based on the most important factor which governs their crystal structure. **Electron** compounds are governed by the number of electrons per atom, and an important class in this group are the Hume-Rothery phases. Laves phases and the so called Frank-Kasper phases[37] form another group which rely on **geometric** requirements in their structural preference. The third class of intermetallics are called **valence** compounds. This group includes the normal valence compounds such as Mg_2Sn and compounds which also obey the Zintl concept like NaPb. However, Parthe[71] and recently, Girgis[72] showed that these three groups do not have clear boundaries and that in most intermetallic compounds all three principles, size, valence and electron concentration, are simultaneously involved.

Recently, the creative use of structure maps in predicting the structures of binary and pseudo-binary intermetallics was introduced.[73,74] This semi-empirical approach involves "threading onto a string" all the elements in the periodic table according to their respective "Mendeleev numbers". The structure map is made by plotting Mendeleev numbers of the two constituent elements along two perpendicular axes. Compounds with similar "coordinate Mendeleev numbers" have similar crystal structures. Another successful map approach based on size, electrons per atom, and electronegativity was also introduced by Villars and co-workers.[75] The use of structure maps have the advantage of simplicity but, as in any empirical theory, they suffer from the inability to offer a physical argument to explain the successes and failures their approach. Furthermore, structure maps do not foresee the discovery of new structures and compounds. It must then be understood that any classification of intermetallics should only be treated as an illustration of trends.

Present theories on the formation of intermetallics would not be complete without the mention of the Brewer-Engel and the Miedema theories. These two apparently conflicting theories illustrate the thermodynamic aspects of the formation of intermetallics. They deal mainly with compound formation between transition metals. The Brewer-Engel theory[76,77,78] relies heavily on the maximum hybridization of the metal orbitals such that a "back-bonding" type of charge transfer occurs. The theory suggests that the stability of a metallic structure depends on the interplay of the promotion energy and the number of bonding electrons. The theory has been successful in predicting thermodynamic values of transition metal compounds especially between early and late transition elements.

The phenomenological Miedema theory[79] presents a different view. It assumes that no "back-bonding" occurs and that minimal charge transfer, i.e., minimal volume change, occurs in transition metal intermetallics. The theory also relies on the electronegativity differences of the component atoms, and charges flow at the atom boundaries to stabilize the "contact potential" between neighboring metal Wigner-Seitz cells, in the direction opposite to the Engel-Brewer model. An empirical equation was developed to relate parameters representing electronegativity and electron density at the boundary of the Wigner-Seitz[80] atomic cell with the heats of formation. The theory has been widely used to predict the signs and magnitudes of heats of formation of intermetallics. Quantum mechanical justifications of the theory have been presented[81] but has not been generally accepted.[82]

Although both Brewer-Engel and Miedema theories were successful in predicting heats of formation of many binary transition metal intermetallics, their success in dealing with formation of Zintl phases and Zintl-like phases has been very limited. This has been attributed to large volume contractions and homonuclear "clustering" found in Zintl phases.[75]

The Zintl-Klemm Concept

The Zintl-Klemm concept evolved from the seminal ideas of E.Zintl[26,83,84,85,86] which explained the structural behavior of binary intermetallic phases in which one component is an electropositive element, alkali or an alkaline-earth metal and the other, an s-p metal. Zintl's systematic investigations led to intermetallic compounds which seemed to contradict the Hume-Rothery rules. Zintl explained the structural peculiarities

by assuming the presence of both ionic and covalent parts in their bonding picture. Instead of applying Hume-Rothery's idea of a valence electron concentration, he proposed an electron transfer from the electropositive to the electronegative atoms (ionic part) and related the anionic substructure to known isoelectronic elemental structures (covalent part), e.g. Tl^- in NaTl is isoelectronic to C,Si and Ge, and consequently, a diamond substructure is formed. Zintl also hypothesized that the structures of these intermetallics would be salt-like.[33,57,87]

Klemm and Busmann[88,89,90] formalized Zintl's ideas and applied them to other binary and ternary intermetallics. Klemm[88] further developed a general description of Zintl phases and associated structure and bonding features to their physical properties.

Klemm's description of Zintl phases as following the Zintl picture of charge transfer is manifested by a volume contraction and a large negative enthalpy of formation.[88,91] Furthermore, the covalent pseudo-element or anion framework formed exhibited a structure closely related to that of an isoelectronic element and this component was typically salt-like. Zintl phases are generally brittle, semiconducting and do not show temperature-independent paramagnetism.[92] These conclusions were derived from the many studies made by Klemm and were rationalized by electron counting rules related to the filled-octet or 8-N rule. The same concept was independently developed by Mooser and Pearson[93,94,95] in explaining the chemical bonding of semiconductors. Pearson[96] proposed an electron counting rule for semiconductors and Zintl phases containing anions to the right of Zintl border. This rule is expressed by the relation

$$(n_e+b_a-b_c)/n_a = 8$$

where n_e = total number of valence electrons; n_a = number of anions; b_a = the number of electrons involved in forming anion-anion bonds; b_c = number of electrons involved in forming cation-cation bonds and any unshared valence electrons on the cations. In spite of the general success of the Zintl-Klemm concept, some anomalies existed. Physical property measurements (magnetic, electrical and thermal)[97,98,99,100] on some compounds that satisfy the structural characteristics of a Zintl phase showed them to be metallic or to exhibit temperature-independent paramagnetism. Most of these phases contained metalloids near or left of the Zintl boundary. Another anomalous characteristic of some Zintl phases was the presence of a homogeneity range, e.g. in NaTl[101] and LiCd.[102] This was contrary to the original ideas of Zintl and have led others to propose different bonding schemes,[103,104] but none has had the creative success in directing synthesis as the Zintl model. Other cases that presented problems were the unusual stoichiometries exhibited by $Na_{15}Pb_4$ and similar compounds.[105] Hence it is inaccurate to impose and define a sharp boundary between Zintl and metallic phases, and it is in these overlapping regimes where much chemistry still lies to be discovered and understood.

Successful use of the Zintl-Klemm concept in the syntheses of new binary and ternary Zintl phases is represented by the works of Schäfer and co-workers at Darmstadt.[106,107,108] Other workers[109,110,111,112,113,114] have been encouraged and inspired to apply and extend the Zintl-Klemm concept in the exploratory syntheses of other ternary and even transition-metal Zintl phases. Other theoretical researchers have even used the Zintl model, in the framework of a rigid band approach, to explain the chemical bonding of solids containing main-group and transition metals.[115]

The extensive investigations at Stuttgart of von Schnering and his co-workers[116,117,118,119,120] on lithium Zintl phases and on phosphorus compounds have led to an evolution of the original Zintl-Klemm ideas. Nesper and von Schnering[121,122,123] have extended the Zintl-Klemm ideas to include Zintl phases with "wrong physical properties". Furthermore, they have proposed that the electronic structures of unusual lithium silicides and germanides can be understood with the introduction of one-electron cage orbitals[118] -- a cation-centered electronic state delocalized over the metal atoms which envelop or isolate certain polyanionic fragments or clusters.

In addition, an electron counting scheme has been developed[123] to take into account Zintl phases which exhibit non-stoichiometry. For a compound $A_aX_xV_d$ (A=cation, X=anion, V=defect) this electron counting scheme is expressed by the equation:

$$E = (8 - N)(a + x) + N^*(d)$$

where E = the total number of valence electrons per formula unit, and N^* is the mean number of broken two-center two-electron bonds per defect. This relationship can also be derived from the set of rules developed by Parthé for tetrahedral structures.[124,125]

An extended counting scheme that incorporates the magic numbers for cluster compounds was also derived[112] and is expressed by the relation

$$E = (8 - N)(a + x) + N^*(d) + E_c$$

where E_c is the cluster 'magic' electron count. The above description extended the Zintl-Klemm concept to include and rationalize multi-center bonding found in electron deficient compounds having polyanionic clusters and in "electron-rich" metal-atom cluster systems.

Theoretical and physical studies on the validity of the Zintl picture of intermetallic phases have also been numerous.[119,126,127,128] Modern band structure calculations were done on binary and ternary Zintl phases with the NaTl structure.[129,130,131] Their results confirmed the conclusions drawn from a bonding scheme that these are simultaneously ionic and covalent. Altogether quantum mechanical studies on Zintl-like phases supported the original "polar-covalent" assumptions made by Zintl and Brauer[83] and presented by Hückel,[132] they underscore the brilliance and simplicity of the Zintl-Klemm concept.

The effective charge transfer[133] between atoms and the bonding character in intermetallics depend largely on the difference in electronegativities of the component elements. Consequently, one of the criticisms on the Zintl concept is the unreasonable assignment of "ionic charges".[134] The description of Na^+Tl^- and Li^+In^- based on the Zintl-Klemm concept was not contrary to the accurate theoretical and experimental picture if the assignment of "charges" was only in a **formal oxidation state** sense.[135] Therefore what is actually represented by the Zintl formalism is the number of occupied Wannier-like electronic states.[136,137] In Zintl phases these states are mostly bonding or non-bonding, and they are largely derived from the metalloid atomic states, whereas the antibonding states, which are unoccupied in normal Zintl phases and valence compounds, are mainly of the electropositive atom. It may then be assumed that if we could extend the electronic scheme to other intermetallic phases regardless of the "class", we have the basis to probe into their chemical bonding. Nesper[119] nicely illustrates this concept by describing electrons of intermetallics as being in "core potential valleys of two or more atoms, in two-center two-electron bonds or multi-center bonds unaware that their core

potential valleys may be covered by a sea of electrons high in energy... Zintl phases and valence compounds correspond to the structured continents on earth, while in (inter)metallic phases the similarly well structured sub-ocean formations are shielded from direct view by the sea level (Fermi level)". Hence, he suggests that for a certain metallic structure there exists a "Zintl prototype" with unfilled conduction bands.

Although the model neglects one very important factor, the stability of competing phases, one can carefully choose to probe a system and structure that exists with a relatively wide range of electron counts and less stringent geometrical requirements. One such structure is the Mn_5Si_3-type,[138] assumed by ~170 reported binary compounds having a 5:3 ratio between electropositive and electronegative atoms. One can accordingly exploit the electron count on a given Mn_5Si_3-type compound and tune its electronic properties.

Phases that are rich in the transition-metal component, such as M_5T_3 (Mn_5Si_3-type) phases, will likely also exhibit significant M-M bonding. Valence electrons that remain after the predominantly main group element (T) valence states are filled will occur in a conduction band with major contributions from electropositive metal (M). Just how far to the left in the periodic table the main-group element can lie and still have no overlap between filled, main-group derived valence bands and the metal-derived conduction bands remains to be determined. However, we can anticipate that the more electropositive metals and many of the main-group metals or metalloids will form what we term "polar intermetallics", compounds in which strong heteroatomic bonding and the above valence generalities apply.[139]

Mn_5Si_3-type Intermetallics

Our interest in compounds with the Mn_5Si_3 structure was inspired by previous work done in this laboratory. Earlier work on Zr_5Sb_3Z (Z = interstitial atom)[140] and their zirconium tin and lead analogs[141] have indicated that by using high temperature techniques, a rich variety of interstitial compounds can be obtained. Not only have small main group elements been successfully incorporated into the $Zr_5(Sb,Sn,Pb)_3$ binaries but first row transition metals and heavier main group elements as well. These observations led us to infer that physical properties of the host binaries could be tuned by the nature and amount of interstitial atoms that could be introduced into a Mn_5Si_3-type structure.

The compounds in Mn_5Si_3 structure have long been known or suspected to take up interstitials, carbon and oxygen most often, or even to require the same for stability.[142,143,144,145] Very few quantitative studies of structure or composition have appeared in support of these ideas, however. The breadth of the binary M_5B_3 phases that form with this structure and appear to be candidates is remarkable as well, some 155 by one count,[138] in phases that encompass transition metals (M) from groups 2 through 6 together with main-group elements (B) involving all members of the boron, carbon and nitrogen families.

The hexagonal Mn_5Si_3 structure ($D8_8$-type) in the space group $P6_3/mcm$ and its interstitially filled variants can be described as having two types of seemingly independent metal(Mn) chains which extend along the c-axis (see Figure 1). One type of manganese atoms form linear chains, each atom surrounded by a slightly twisted trigonal prism of silicon atoms. These linear metal chains are similar to transition metal chains

found in the so-called A15 compounds,[146] but differ in that they extend in only one direction. The second structural feature is formed by manganese confacial octahedra or trigonal antiprisms also surrounded by confacial antiprisms of silicon. The interstitial site is located at the center of each metal octahedron. The local silicon coordination of each manganese atom in the antiprism chains is the same as those found in the well known linear Chevrel phases.[147,148] Other interesting descriptions of the structure have been presented based on its similarity to NiAs and the mineral apatite.[149]

The octahedral interstitial sites at the center of these confacial chains have been the subject of many studies, especially on the stabilization of pseudo-binary and ternary compounds with the Mn_5Si_3 structure. Many single crystal studies have now settled the questions of the amounts of interstitials incorporated and where they go. This confirms what had been estimated earlier in other systems, largely on the basis of powder diffraction and lattice constants. Pioneering in this work were Novotny and Parthé.[150,151] They were the first group to recognize the stabilization of certain phases having the Mn_5Si_3 structure by a third element like carbon, boron and oxygen in the system Mo-Si-C. Hence interstitial-stabilized ternary Mn_5Si_3-type phases were called Novotny phases.[152] Although Parthé[153] generalized a description of these phases, it was Aronsson[154] who first correctly proposed that the stabilizing third element occupied the octahedral interstitial site in the Mn_5Si_3. Later work by Brewer and Krikorian[155] led to similar results.

According to Parthé, Novotny phases are described as follows:[156] (1) they have a $D8_8$ structure which is stabilized by small amounts of B, C, N, or O; (2) they exhibit a homogeneity range; the amount of interstitial necessary to stabilize the phase increases

with period within each group, and also increases within each period with the group number of the metal component; (3) they show a wider homogeneity range than other silicide or germanide systems. These generalizations were in many cases proven to be untrue, particularly with the subsequent determination of both true binary and interstitially stabilized ternaries having the Mn_5Si_3 structure. Furthermore, the homogeneity range of these phases are not totally inclusive; there are many exceptions wherein narrow stoichiometric ranges of the interstitial elements are found suggesting the importance of electronic factors. The successful introduction of some transition metal as interstitials also belies the suggestion that size effects dominate the interstitial chemistry of the host compound.

Previous work in this laboratory by Hurng on the polar intermetallic Ca_5Sb_3Z, Z=halogen, analogs[157] have led to the relatively successful use of the Zintl-Klemm concept in rationalizing the structural preference of compounds in the alkaline-earth and main group elements. The 5-3 compounds of zirconium with main-group elements, on the other hand, cannot be so understood mainly because of the relatively large number of "excess" electrons residing on the conduction bands.

Using ideas derived from the extended Zintl-Klemm concept on metal-rich systems like the Zr_5Sb_3 and Zr_5Sn_3, we can infer that the excess electrons reside on the early transition-metal-derived bands. It is therefore a natural step to decrease the extra electrons by going into the rare-earth-metal tetrelide systems e.g. La_5Ge_3 and La_5Pb_3. This would allow us to probe the conduction bands in the Mn_5Si_3-type compounds. This also allows for the possible tuning of the electron counts on the metal-derived conduction bands by introducing interstitial atoms in the Mn_5Si_3 structure type. Introducing

electronegative elements into the interstitial site may "soak up" the electrons from the conduction band and localize them in the interstitial-based orbitals. The successful incorporation of transition metal interstitials in Zr_5Sb_3 and Zr_5Sn_3 have also broadened the possibilities in tuning the electronic properties of these and similar host compounds.

In probing the validity and limits of the extended Zintl-Klemm concept in polar intermetallic systems, we must choose a system with a structure known to be electronically robust, i.e., it exists over a wide range of electron counts. A test system must also be on or near the interface between Zintl and metallic phases. One such collection of systems are the M_5X_3 rare-earth metal tetrelides with the Mn_5Si_3 structure type.

SYNTHESES AND CHARACTERIZATION

General Approach

The syntheses of inorganic solids is often associated with considerable problems for the chemist.[158] Many of these are based on the high temperatures required to induce significant reaction rates and a sensitivity towards moisture, oxygen, or other adventitious impurities that complicates their handling. Furthermore, solid state syntheses suffer from the lack of purification methods. Incidental processes such as evaporation, reactivity of containers, and adventitious impurities affect the stoichiometry of the reactions in many unforeseeable ways. Another important facet which requires attention is the limited number of characterization techniques available. Nearly all effective characterization methods usually require an adequate degree of crystallinity, hence, effective means of crystal growth are often incorporated in any solid state preparation.

Among the oldest methods of solid state synthesis is the reaction of a mixture of components at elevated temperatures, a technique that is widely used in the syntheses of intermetallic compounds. The completeness of the reaction sought -- reaching a state of equilibrium -- demands high temperatures because of small diffusion coefficients and large diffusion distances and as a rule the products are what one expects from thermodynamic considerations.[159] Since the kinetics of solid state reactions are mostly unknown and almost impossible to determine,[160] other important aspects of chemistry on the mechanistic level and at lower temperatures are lost.

The general procedure in the exploratory synthesis that was embarked on in this work is summarized in a flowchart illustrated in Figure 2. The crucial points in the process are:

a) The use of high purity materials.

b) Identification and structural characterization of the products.

c) Obtaining and growing single crystals of unknown phases.

d) Syntheses of single phase products.

e) The measurement of physical properties.

Materials

The lack of purification during and after synthesis and the often perverse effects of impurities on high temperature solid state synthesis were avoided to some extent by the use of high purity starting materials. Impurities were also minimized in the handling of reaction materials, and the "history" of the initial reagents were noted if applicable.

Due to the sensitivity to oxygen and moisture, all reagents and products were stored and handled in a glove box and manipulated on a vacuum line equipped with a mercury diffusion pump. The glove boxes used were continuously purged with dry helium or nitrogen, and the atmosphere cleaned by molecular sieves and oxygen scavengers. The moisture content of the dry box atmosphere was monitored and maintained at <1 ppm. The oxygen content was not quantitatively determined but 60 watt "light bulb tests" of 12 hours or more indicated a low value of less than 3 ppm.

In this work, all high purity active metals (Ca, La, Nd, Pr) were obtained from Ames Laboratory. Calcium metal chunks had been triply distilled, and their surfaces

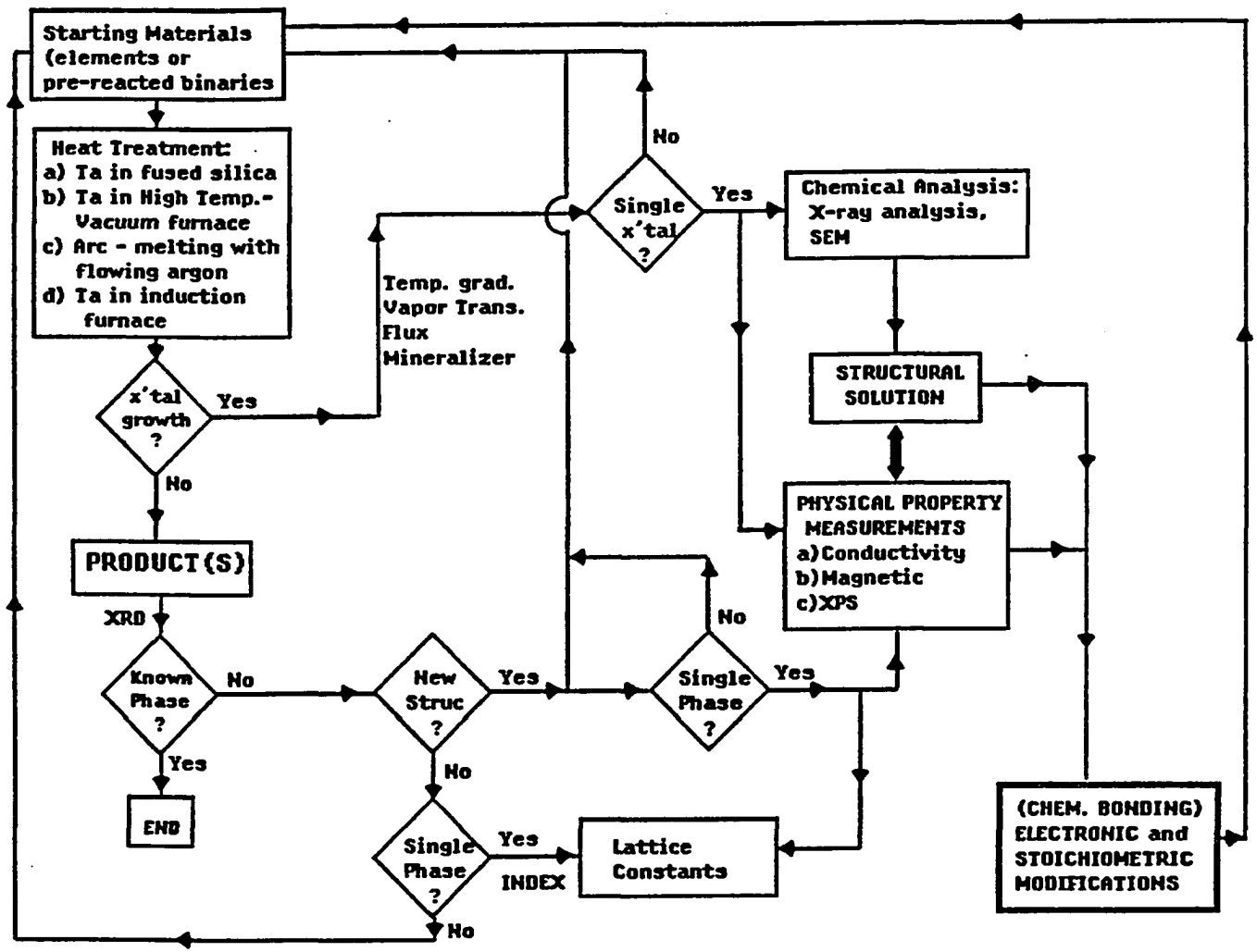

Figure 2. A flowchart of the general experimental approach

Table 1. Ternary components used in the syntheses

material	source	purity	form
B	Aesar	99.5%	crystalline
C	Union Carbide	spectro. grade	powder
Al	United Mineral and Chem.	high purity	wire
Mg	Fisher Scientific	99.999%	turnings
P, red	Aldrich 99.999%	lumps	
S	Alfa Products	99.999%	powder
Ti	Ames Lab		chips
Cr	A.D. Mackay	99.95%	chips
Mn	A.D. Mackay	99.9%	chips
Fe	Plastic Metals	99.9%	chips
Co	Aesar	99.9+%	chips
Ni	Matheson Coleman & Bell		sheets
Cu	J.T. Baker Chem	99.99%	turnings
Zn	Fisher Scientific	99.99%	granules
Ga	Johnson Matthey	99.999%	granules
As	Aldrich 99.9999%	lumps	
Se	American Smelting & Ref.	99.999%	granules
Ag	G.Frededrick Smith	Reagent	small granules
Cd	Cominco Products	99.999%	strips
In	Aesar	99.9999%	shots
Sb	Allied Chemical & Dye		lump
Te	United Mineral & Chem.	99.999%	lumps
Ru	Engelhard	99.95%	powder
Bi	Oak Ridge National Lab.	reactor grade	metal bar
V	Fisher Scientific	99.99%	powder
La_2O_3	Ames Lab	99.999%(dry)	powder
$LaCl_3$	in-Lab preparation	sublimed	powder
LaN	in-Lab preparation		powder

scraped clean before use. Lanthanum, neodymium and praseodymium metal rods were scraped of the dark surface before they were cut and weighed. No electropolishing was done on the rare earth metals to reduce adventitious carbon.

The tetrelides (Si, Ge, Sn and Pb) were obtained from commercial sources. Electronic grade silicon rods and germanium chunks were used as received. Tin (Baker's analyzed; 99.99%) had shiny surface upon fusion and was also used as received. Lead was obtained as an electrolytic bar (99.9999%), cold-rolled to sheet (3 mm thick), and the dark oxidized surface was scraped off before use.

The sources and forms of other reagents are presented in Table 1. Most of them were used as received. Whenever appropriate, the surface of the various solid reactants were scraped clean before use.

Containers

The high temperature reactions in our preparation of rare-earth and alkaline-earth tetrelides can be viewed as multi-component reactions that also involved the containers. Hence the choice of an inert container was crucial in the syntheses. The known reactivity of active metals such as alkaline-earth metals and rare-earth metals with popular ceramic containers required that refractory metal containers be used.[161] Characteristics of inertness, strength, ease of fabrication and availability limited the choices to tantalum, niobium, tungsten and molybdenum. The difficulty in welding molybdenum and tungsten containers and the lower melting point and lower strength of niobium made tantalum the metal of choice. Likewise, tantalum has been used in many metallurgical applications because it is inert to a wide variety of metals.

programmable temperature controller with ramp and soak capabilities. The surfaces of the samples remained completely clean to the eye in this process.

Regular tubular resistance and Marshall furnaces with small temperature gradients were also used for annealing and sintering reactions at temperatures less than 1050°C. These furnaces were placed at an angle or set vertically. Tantalum reaction containers were sealed in silica jackets to prevent atmospheric attack. Temperatures were measured using adequate thermocouples and temperature controllers. Quenching reactions were done by taking the silica jacket containing the reaction containers from the furnace and dipping it into cold running water.

Quenching reactions from higher temperatures (>1100°C) could not be done with the high-temperature high-vacuum furnace because of its well insulated setup. An alternative method was the use of an induction furnace, where temperatures are limited only by the melting point of the container. The red radiation of the Ta containers disappears in less than 4 minutes after the power is turned off, which is normally an effective quenching rate. However, for faster quenching, the evacuated chamber is back-filled with cold nitrogen gas by dipping the end of the inlet hose into liquid nitrogen.

Synthetic Methods

Melting

Direct fusion of the elements is the simplest method of synthesis and therefore the one usually employed in the absence of complicating problems. There were two ways the reactions were done -- use of a high-temperature high-vacuum furnace and arc-melting.

There are many advantages of melting the elements. Melting usually ensures reaching equilibrium (homogeneity) and coupled with slow cooling usually provides good single crystals of congruently melting compounds. Annealing after fusion is usually needed for preparing peritectic compounds.

Arc-melting offers a fast, simple and easy way to prepare intermetallics. It is a very effective method to test the possibility of unknown reactions. The high temperatures involved tend to overcome any kinetic barriers inherent in solid state reactions and lead to complete reactions in a short time. The stirring effect of the electric arc also allows the use of coarse materials and cold pressed pellets. However, the high temperatures usually results in loss of material, especially for volatile ones. This deters the use of the technique in preparing lead compounds and other interstitial compounds with volatile components. Another aspect of arc melting is the possible occurrence of inhomogeneities in the as-cast button. Inhomogeneities are due to various reasons: wide differences in the melting points of the components and the large temperature gradients in the charge. In such cases, it was best to arc melt prereacted binaries instead of elements, turning and re-melting the arc melted buttons several times and/or annealing the as-cast buttons at lower temperatures. Moreover, arc-melting reactions under flowing gas are susceptible to contamination. This has been observed in previous work in this laboratory.[164]

Arc-melting reactions were carried out in a Centorr 55A single arc furnace. Pieces of the elements or powders of prereacted binaries were carefully weighed in the glove box and then quickly transported and transferred into the arc furnace chamber through well capped vials protected in a dessicator. The reaction charge was melted on a water-cooled copper hearth. The reactions proceeded after the argon flow gas had been gettered

by previously melting zirconium. A pressure slightly greater than atmospheric was maintained inside the melting chamber to reduce the possibility of contamination from the outside air. The water-cooled hearth prevents the reaction between the sample and container but may result in sharp temperature gradients leading to compositional inhomogeneities. This problem was minimized by turning the sample several times as well as by annealing the sample. Annealing was done to enhance homogenization and to obtain incongruently melting compounds that are not accessible through direct melting techniques. This was accomplished by placing the sample buttons into Ta tubes that were welded, sealed in silica jackets, then heated in resistance furnaces.

Sintering technique

Another synthetic method employed in this work was powder sintering. Well mixed, pressed pellets of the appropriate elements and prereacted binary powders were placed in Ta containers. They were welded shut and heated in the high temperature high vacuum furnace at a temperature lower than the melting point of the eutectics. This method has the advantage of good control over the composition of the final product and can provide reliable results for lattice parameter-composition relationships. However, the possible need for regrinding and pressing and re-firing of a second pellet as well as its inability to produce single crystals made this method a secondary technique in this work.

Chemical vapor transport

In cases wherein melting and sintering reactions did not provide single crystals, chemical transport techniques were applied. The method can be used if at least one of the reacting solids is chemically transportable via the gas phase, under an appropriate temperature gradient (50-100°C), by means of a heterogeneous equilibrium. In addition,

if the reaction product is transportable, solid diffusion is no longer important. The product is carried away within the temperature gradient. Hence, this technique also acts as a "purification" route. Another advantage of the method are the relatively low reaction temperatures which allow some access to low temperature "metastable" phases. The crucial experimental factors in any chemical transport reaction is the choice of a transporting agent and the determination of an effective temperature gradient.[165,166] These factors are governed to a large extent by the thermodynamics of the equilibrium of the gaseous species. In a successful transport reaction, single crystals suitable for X-ray analysis are virtually assured.

Since there are no established thermodynamic data on the chemical species associated with the intermetallic systems of interest, most conditions were obtained by trial and error. Halides of the interstitial elements were in most cases used as transporting agents. Temperature gradients were set between 50 to 100°C. In most cases the iodides produced better results. Transport reactions also required longer Ta tube containers and placement in a Lindberg zone furnace at temperatures ranging between 700-900°C to allow for the necessary thermal gradients. The reactants were prereacted compounds in their powder form or stoichiometric mixtures of the elements and binaries. In most attempts, transport was successful in producing single crystals, but powder patterns of the products indicated a mixture of compounds was present.

Metal flux reactions

Another method employed to obtain suitable crystals for x-ray analysis was the use of a metal solvent. This method takes advantage of the natural ability of precipitation from solution to produce good sized single crystals. Analogous to the dissolution of salt-

like compounds in fused salt media, intermetallic compounds can be dissolved by molten metals. Crystallization may be achieved by supersaturation of the solution through slow cooling or by evaporation of the solvent metal. Ideally, good control of nucleation will provide suitable single crystals for physical property measurements. However, most metal flux reactions that were attempted resulted in the formation of compounds that were contaminated by the solvent.

Metal flux reactions with Zn, Cd, In, and Pb as possible solvents were attempted. Open tantalum or molybdenum crucibles were used in all of the metal flux reaction experiments. The basic problem that arose from these reactions was how to separate the products from the solvent. Boiling off the solvent as well as physically separating the product crystals from the solvent matrix were attempted but the crystals obtained were mostly compounds contaminated by the solvent. In certain instances, e.g., with indium as "solvent", the reactions resulted in new compounds. With a suitably inert solvent and better controlled conditions, the potential of growing large single crystals may yet be realized. However, from a synthetic point of view, the method offered another way of obtaining novel compounds.

Characterization Techniques

Powder x-ray diffraction

Since most of the products from our synthetic attempts were in the form of, or could be reduced to, crystalline powders, Guinier powder diffraction was used as the primary method of structural characterization. The powder patterns were obtained for powdered samples fixed on a 1/4" x 1" rectangular metal frame by cellophane tape with

was done.[169,170] These allowed for the unambigous determination of unit cell parameters, Laue symmetries and systematic absences. Film work with exposures of 24-48 hours was also important in determining the presence or absence of any superstructure. Initial film methods are important in any subsequent automatic data collection-refinement work because their results are unambigous. Therefore, any complete single crystal work must include Wiessenberg and/or precession film data.

After the necessary film work was done, data collection on the crystal of interest was undertaken on a single crystal diffractometer. Three four-circle diffractometers were available during the course of this work, an Ames Lab instrument (DATEX), an Enraf-Nonius-Delft CAD-4 diffractometer, and a rotating-anode-equipped AFC6R-Rigaku diffractometer. All three used Mo Kα radiation and checked standard reflections every 100-150 reflections to determine instrumental instability and crystal decay. In all the single crystal work, decay was found to be negligible or absent and no corrections for decay were necessary. Data were collected using θ-ω scans unless some problems made it necessary to use another scan type. Orientation matrices for data collection on DATEX were obtained from the different angle settings of 15 reflections found from a Polaroid rotation photograph. On the other hand, the CAD-4 and Rigaku instruments relied on 25 reflections found from a random search. The unit cell parameters and symmetries obtained from the diffractometers were inspected for their standard deviations and compared with the results obtained from film work, if any, before proceeding to data collection. At least 4 psi-scans for empirical absorption corrections were measured after data collection. In all single crystal analysis undertaken, the treatment of absorption effects was very important in arriving at satisfactory crystallographic solution.

There were three structure refinement packages available for use, CHES,[171] TEXSAN[172] and SDP.[173] CHES is capable of handling data from all three diffractometers and has the advantage of correctly treating psi-scan measurements with respect to their 2θ dependence. It has the disadvantage of being less user friendly and initially presented problems in transcribing data collected from CAD-4 and Rigaku. SDP was used exclusively for data collected from CAD-4. It has the advantage of universal acceptance and popularity. TEXSAN is a relatively new crystallographic package, and it is being improved continuously. It is also the most user friendly of the three but can only handle data from Rigaku and CAD-4. Unlike CHES, TEXSAN and SDP incorrectly process psi-scan data in that they do not include 2θ dependence and only average the measurements. However, the two software packages include a powerful numerical absorption correction program, DIFABS,[174] which applies 2θ dependence and other absorption correction factors properly.

Reflection data collected were generally treated in the same manner by the different crystallographic softwares. They were processed with Lorentz-polarization corrections and psi-scan based empirical absorption corrections.[175] Observed reflections with $I/\sigma_I > 3$ were averaged in the proper Laue symmetry.

Initial structural models were derived from direct method calculations using SHELXS-76[176] or from the positional parameters of an isostructural compound. Full matrix least squares refinements were employed using scattering factors of neutral atoms, and anomalous dispersion was applied for heavy atoms (Z>10). Refinements of scale factor, positional and isotropic thermal parameters and, if needed, a secondary extinction coefficient were pursued until convergence was achieved at (shift/esd) < 0.02. Once

isotropic refinements converged, DIFABS was applied, and final anisotropic refinements carried to convergence. Final refinements that included occupancy parameters were usually done to check the correctness of the model. Any significant deviation from ideal occupancy meant that the intermetallic was non-stoichiometric or that the non-ideal position was occupied by different atoms. Only careful chemical analyses and phase equilibration reactions distinguished one hypothesis from the other. Final Fourier electron density and difference Fourier maps were also calculated and analyzed to confirm the correctness of the structural model. Final lattice parameters were obtained from careful indexing and comparisons of the experimental and calculated Guinier powder patterns. These parameters had smaller standard deviations and higher accuracy and were subsequently used for atomic distance and angle calculations using the program ORFFE.[177] All crystallographic calculations were done on a DEC2000 workstation and a Microvax II computer.

Chemical Analyses

Electron microscopic analysis

A JEOL JSM-840 scanning electron microscope equipped with a KEVEX EDX system was used for elemental analyses. Qualitative analysis was a routine test on interesting samples obtained from our synthetic work. Although the results were not accurate, they complemented the results from single crystal x-ray analysis. Samples were prepared within a nitrogen atmosphere drybox and transported in a sealed glass tube. Exposure to air cannot be avoided in transferring the samples into the test chamber, but careful efforts were made to minimize it.

Samples for accurate quantitative analysis required a flat, microscopically smooth surface to maintain the validity of the path length calculation and to assure that the surface to be analyzed was homogeneous. The samples were prepared by choosing well faced crystals and fixing them in a half-inch long copper tube with epoxy. The crystals were oriented in such a way that a flat face was exposed. The sample surface was polished by sandpaper and fine leather. Silver paint was applied over the areas between the crystals and the rim of the copper tube to provide good electrical contact.

Samples were inspected in the back scattering and topological modes to determine the sites for elemental analysis. Whenever possible, the bulk compositions were used as standards to reduce any matrix effects in the analyses. Otherwise, well-defined stoichiometric binaries and the pure elements were used as standards.

Atomic absorption spectroscopy

For very air sensitive samples, e.g. $Ca_{5.67}Pb_3$, chemical analysis was done by employing atomic absorption spectroscopy. Samples were quantitatively analyzed for alkaline-earth metal with the aid of a Perkin-Elmer spectrometer. Several single crystals were selected in the glove box with the aid of a microscope and brought out in a previously weighed vial. These were dissolved in ~1.5 M HNO_3 at 40°C and volumetrically diluted. Comparable standard solutions were prepared from the nitrates.

Physical Characterization

Magnetic susceptibility

Magnetic susceptibility measurements were made with the assistance of Professor Douglas Finnemore and Jerome Ostenson of the Physics Department on a Superconducting Quantum Interference Device (SQUID) equipped with magnetic property measurement system (MPMS) from Quantum Design.

Fused silica containers for normal use were made by evenly collapsing a 20 cm, 3 mm i.d. silica tube at a point 8.5 cm away from one end. Care was taken such that the density of the silica tubes were uniform along the length. The longer end was attached to a silica ball joint. Samples were powdered, weighed, and carefully placed in the silica containers. The containers were then sealed at a point 8.5 cm away from the sample with the aid of a torch while under a low pressure of helium on a vacuum line. This setup led to erratic signals from the magnetometer for ferromagnetic and weakly paramagnetic samples that was attributed to the inherent anisotropy of the melted area of the sample container. Also, the uneven distribution of the powdered sample around the sealed sample chamber resulted in uneven gradients along the length of the tube.

A better container was designed by the author and J. Ostensen for ferromagnetic and weakly paramagnetic samples. This was made by sliding and fitting a 8.5-cm long, 3-mm diameter silica rod into a 21-cm long, 3-mm i.d. fused silica tube. The rod was fixed into the tube by fusing their common ends. The sample pieces were weighed (~20 mg) and placed into the open end of the silica container within a helium atmosphere glove box. Another 3 mm silica rod, ~12 cm long was slid and fitted into the open end of the silica container such that the sample was pressed between two silica rods. The sample

container was inserted into a short and narrow rubber tube to temporarily make an air-tight fit around the unsealed end. The container was taken out of the dry box and sealed under He at a point 8.5 cm from the sample. A standard sample container filled with helium was made to account for the diamagnetic correction of the sample holder.

All magnetic measurements were done automatically by programming it into the MPMS software. Measurements were made usually at 5° intervals between 6-300°K during the warming cycle. Field dependent measurements (1,3,5 Tesla) were also made on all samples at 100°K and room temperature.

Data analysis was done using the program DATAPLOT[178] on a VAX workstation. Diamagnetic corrections for core electrons were applied to all data (see Appendix B).

Electrical conductivity

Whenever applicable the electrical conductivity of representative compounds were qualitatively and, in a few cases, quantitatively determined. The conductivities were measured using three methods, simple two-probe method, 4-probe method and the Q-factor method. Simple two- probe methods were used initially to determine the room temperature conductivity of the obtained single phase products. The measurements were done on pressed pellets or large crystalline chunks using a commercial multi-meter (Hewlett-Packard E2373A) inside a helium atmosphere glove box. More accurate measurements were done using a 4-probe device designed by L. Wolfe.[179] Four-probe measurements on pressed pellets were done only on $La_{15}Ge_9Fe$ and La_5Ge_3 due to limited tenure of the device. Another accurate method that was used in this work was the "Q" method.[180]

Samples for resistivity measurements via the Q-method were prepared by grinding the sample. The desired sample particles were separated by sizes using standard testing sieves (nos. 40, 60 and 100). The optimum size was found to be particles between 150-250 micrometers. The sample was then transferred into ~2.0 cm diameter pyrex tubes. An insulating matrix (silica powder) was intimately mixed with the sample, and then the container was sealed under vacuum. Measurements were made during the warming cycle from liquid nitrogen temperature to room temperature in intervals of 10 degrees. Data were analyzed using the DATAPLOT program.

X-ray photoelectron spectroscopy

XPS experiments were conducted with the help of James Anderegg on an AEI-200B spectrometer using Al Kα (1486.6 eV). Samples were ground in an agate mortar and pestle under helium atmosphere within a glove box that was attached directly to the spectrometer, and then mounted on an indium substrate. The binding energy of peaks was determined by using adventitious carbon as an internal standard (285.0 eV).

The spectra were obtained by multiple scans and signal averaging using a Nicolet 1180 computer system. In some cases where the signals were weak due to surface effects, the sample surface was etched for 5 minutes by argon beam. This method was only used sparingly in severe cases because etching often led to surface reorganization and unforeseen chemical changes that do not reflect the properties of the bulk.

Extended-Hückel calculations

In order to obtain a theoretical understanding of structure-bonding-property relationships in terms of orbital interactions, it was necessary to calculate approximate electronic band structures of representative compounds. One of the more popular semi-

empirical theories on solid state band structures is the extended-Hückel theory based on the tight-binding (LCAO) method. This allows the orbital symmetry interactions in the compounds to be analyzed. Orbital interactions[181] have been very useful to chemists in order to understand the chemical bonding involved in molecules. The extended-Hückel band formalism applies it to solid state materials.

The program JDCBAND used in the band structure calculations was a modified version of the programs used in Cornell (NEW5) and University of Chicago (BIG5).[182,183] The modifications dealt with the array size capacity and the addition of symmetry elements in the algorithms.[184] Atomic parameters, H_{ii} and Slater exponents, were obtained from literature. Whenever possible, H_{ii} values were obtained from self-consistent, charge iteration calculations on chemically similar systems. Double zeta expansions of the Slater exponents of d-orbitals were used in all calculations. In cases where Slater exponents were unknown, values were obtained by interpolation of the values of the elements within a period. Relevant atomic orbital parameters are listed in Appendix A.

LANTHANUM GERMANIDES AND THEIR 5:3 TERNARY DERIVATIVES

Introduction

Research on rare-earth metal carbides and silicides have been extensive mainly because of their importance in high-technology applications. Although the germanides offer a wider variety of electronic and optical properties of importance to modern engineering, the data on germanides have been comparatively sparse and very little research have been done on the rare-earth metal germanides.[185,186,187] Similarly, research concerning structure and bonding relationships in heavier rare-earth-metal tetrelides such as stannides and plumbides have also been exiguous.

Our research on the La-Ge binary system was prompted by our interest on the potential interstitial chemistry of La_5Ge_3. This interest was based on the idea of "tuning" the electronic structure of the host La_5Ge_3 by introducing different interstitial atoms into the empty octahedral sites of its Mn_5Si_3-type structure. Previous work in this laboratory on Zr_5Sb_3, Zr_5Sn_3 and Ca_5Sb_3 and their ternary interstitial derivatives lend support to this concept.

The latest La-Ge binary phase diagram[188] indicates that there are 5 known binary compounds, namely LaGe, $LaGe_{2-x}$, La_4Ge_3, La_5Ge_4 and La_5Ge_3. The intermediate phases La_5Ge_3 and $LaGe_{2-x}$ which were reported to be nearly stoichiometric and congruently melting at 1475° and 1500°C, respectively, are the most studied phases in the La-Ge binary system. The phase diagram is also characterized by other compounds, peritectic La_3Ge and LaGe, and two peritectoid phases, La_5Ge_4 and La_4Ge_3. However, a

review of the sources of the assessed diagram[189] reveal that the alloys were obtained by arc melting in an argon atmosphere. Furthermore, inspection of the quality of the starting materials reveal 99.79% and 99.99% purity for La and Ge, respectively, with oxygen as their major impurity. This was deemed unsatisfactory because, based on past experience, the effect of impurity oxygen and/or carbon is crucial to the phase stability of many metal-rich systems. Similarly, other independent researches on La_5Ge_3 neglected the effects of oxygen and carbon impurities in their investigations.[190]

More interestingly, earlier published reports[191,192,193] on the germaniothermal reactions of Nd_2O_3 have indicated that their results can be extended to the germaniothermal synthesis of the binary phases, La_5Ge_3 and $LaGe_2$ from lanthanum oxide and germanium. They are represented by the supposed reactions

$$La_2O_3 + 7Ge \text{ ---> } 3GeO_{(g)} + 2LaGe_2$$

$$5La_2O_3 + 21Ge \text{ ---> } 15GeO_{(g)} + 2La_5Ge_3.$$

These high temperature reactions are not well understood and details about their stoichiometry have not yet been completely determined. Lynchak et al.[9-10] described the conditions in obtaining the digermanide and R_5Ge_3 compounds from these reactions. They reported that only congruently melting compounds can be prepared via the germaniothermal reactions. Moreover temperatures greater than 1300°C (the 5:3 compound required higher temperatures than its corresponding digermanide) and high-vacuum conditions were necessary to initiate and sustain these reactions. Surprisingly, the few reports about germaniothermal reactions discounted the significance of stabilization of the products by oxygen and other impurities. This is particularly applicable when the quality of their starting materials was unsatisfactory.

It was also observed from past work by Parthé and co-workers[194,195] as well as in this laboratory that many of the reported lattice parameters of 5:3 phases, with the Mn_5Si_3 structure, between early transition metals combined with tetrelides and heavier pnictides correspond to impurity-stabilized phases. A review of the prior works by Parthé and his co-workers[196,197,198] and Gladyshevskii and his associates[199,200,201] on many rare-earth-metal tetrelides as well as the studies of Mayer and Shidlovsky[202] on rare-earth metal germanides presented many inconsistencies in the reported lattice parameters and observed chemical properties, particularly that of La_5Ge_3. From the reported syntheses and characterization by Gladyshevskii and co-workers as well as by Parthé's group, one gets the impression that La_5Ge_3 is adequately air-stable. Mayer and Shidlovsky did not describe the sensitivity of La_5Ge_3 to the atmosphere. Our work however finds that La_5Ge_3 is considerably moisture and air sensitive. The conflicting observations could be attributed to various factors in the synthesis procedures and conditions of the starting materials. More importantly, many other previous studies neglected interstitial stabilization by oxygen and carbon.

This chapter will report the results of our attempts to characterize La_5T_3 tetrelides and synthesize their ternary interstitial compounds. The variety of interstitials that can be incorporated into the host binary apparently allowed us to modulate the chemical bonding and physical properties of the host compound without greatly altering or breaking up the host structure. A summary of the successful reactions of interstitials is listed in Table 2. Unsuccessful reactions were also fruitful in that new compounds with novel structures were discovered.

Table 2. Summary of La_5T_3Z compounds

lanthanum tetrelide	Z atoms	structure type (space group)
La_5Ge_3:		$Mn_5Si_3(P6_3/mcm)$
	B, C, O, P, S, Cl, Cr, Mn, Fe, Co, Ni, Cu, Zn As, Se, Ru, Cd and Sb	filled-Mn_5Si_3 ($P6_3/mcm$)
	Si	Zr_5Si_4 ($P4_12_12$)
	Si, Sn, and Pb	Sm_5Ge_4 (Pnma)
	Ga and In	Gd_5Si_4 (Pnma)
La_5Pb_3:		$Mn_5Si_3(P6_3/mcm)$
	B, C, P, S, Cl, Cr, Mn, Fe, Co, Ni, Cu, Zn, As, Se, Ru, Ag, Cu, and Sb	filled-Mn_5Si_3 ($P6_3/mcm$)
	O and N	Cr_5B_3 (I4/mcm)
	Si, Ge, and Sn	Sm_5Ge_4 (Pnma)
La_5Sn_3:		W_5Si_3 (I4/mcm)
	C and O	filled-Mn_5Si_3 ($P6_3/mcm$)

A review of the binary La-Ge system was also undertaken to clarify its many uncertainties, particularly on $LaGe_{2-x}$, La_4Ge_3, and La_5Ge_4. Special attention is made on La_4Ge_3 and La_5Ge_4 because of their interesting structural reltionships with many of the newly synthesized ternary derivatives. Other binary compounds LaGe and La_3Ge are also described.

A new class of compounds, $La_{15}Ge_9Z$; Z=interstitial atom, with a hexagonal $\sqrt{3}$ x $\sqrt{3}$ superstructure of the Mn_5Si_3 structure type will also be presented and discussed. This superstructure is brought about by the novel ordering of the interstitial atoms, Z, accompanied by a Peierls-like distortion of the chains of confacial octahedra containing the interstitial atoms.

The reaction of La_5Ge_3 with other tetrelides and group 13 elements resulted in structures that contained dimers. The number of dimers in the structure varied. This was attributed to size and electronic effects. The interrelationships between the different 5-4 structures, namely, Zr_5Si_4, Gd_5Si_4, Sm_5Ge_4 and Eu_5As_4 types, were investigated and clarified.

Other new compounds, La_5RuGe_2 and Nd_5RuGe_2, represented structures related to the Yb_5Sb_3 and Rh_5Ge_3 structure types. The chemical bonding in these compounds as well as their relationships with the several known 5:3 structures will also be discussed.

Likewise, a parallel study was also done on La_5Pb_3 and its interstitial compounds. An interesting group of interstitial compounds La_5Pb_3Z (Z = O or N), having a structure similar to the Cr_5B_3-type were synthesized. The small interstitial atoms were found to occupy tetrahedral interstitial sites in contrast to the interstitial-stabilized Mn_5Si_3-type phases.

Investigations on the reported dimorphic nature of binary La_5Sn_3 was also undertaken. The results indicate that the true binary La_5Sn_3 exists in the W_5Si_3 structure type. The reported binary La_5Sn_3 having the Mn_5Si_3 structure was found to be interstitially stabilized by oxygen and/or carbon. The unaccounted effects of carbon and oxygen contributed to the inaccurate reports about the dimorphic nature of La_5Sn_3.

Experimental Section

All rare-earth metal tetrelides and their ternary derivatives were synthesized by fusing the elements and/or prereacted binaries in tantalum tubes. Stoichiometric amounts of the elements (crushed La turnings, crushed germanium ingots, Pb chips and interstitial elements) were cold pressed and loaded into tantalum tubes. The tantalum tubes containing the reagents were sealed and put into a tantalum canister inside an alumina muffle tube of the high temperature furnace (HTF). The furnace is described in the previous Chapter. The HTF was slowly heated to 1100°C in 8 hours and allowed to equilibrate for another 12 hours. It was then heated to 1300°C in 3 hours and annealed at that temperature for 12-24 hours more depending on the reactivity of the charge. Then the temperature was lowered to 1100°C and annealed for 2-3 days; afterwards the sample was slowly cooled to room temperature in 24 to 36 hours.

The samples are then taken out of the furnace and opened inside a nitrogen atmosphere glove box. The products are ground and pressed into pellets, reloaded and reheated in the HTF. This cycle is repeated (2-3 times) depending on the homogeneity of the sample. A sample is prepared for powder x-ray work to calculate lattice parameters and to help determine the product compositions.

Arc melting was also used to synthesize some interstitial compounds of La_5Ge_3. This was done by weighing stoichiometric amounts of the elements in the glove box and keeping the reactants in a clean and air tight glass vials. The vials were then transferred to a dessicator and taken to the arc furnace room.

The reactants are quickly placed on the copper hearth and inserted into the furnace chamber. In the transfer process, the starting materials are exposed to the atmosphere for about 3-5 seconds. The arc furnace chamber is sealed and flushed several times with argon with care to prevent the gas from scattering the reactants. An argon gas flow in then allowed to pass through the sample chamber, keeping the chamber pressure slightly greater than atmospheric. A two-gram zirconium button is then melted as a getter. Next, the reaction charge was arc melted for several seconds, turned over, and then melted again. The process of arc melting the getter and the charge and turning over the button was repeated several times to ensure the homogeneity of the products.

After arc melting, the products were quickly transferred from the copper hearth into a clean glass vial, flushed with argon gas and then tightly covered. The glass vials were replaced into the dessicator, where argon gas was continuously flushed through. The products are finally stored in the dry box to await characterization by Guinier powder diffraction experiments. For some quenching reactions at temperatures lower than the arc melting temperatures, the reaction buttons are placed in sealed tantalum containers and annealed in the induction furnace for 12 hours at about 1300°C and quenched to room temperature.

Single crystals of La_4Ge_3, La_5Ge_3, La_5Ge_3Cr, $La_5Ge_3Z_{0.33}$ (Z = Mn, Fe, Co, Ni, C, and P), Nd_5RuGe_2, La_5Ge_3Si, La_5Ge_3Ga and La_5Pb_3O obtained from melting and

Table 3. Structure types and cell constants for lanthanum - germanium phases

reaction stoichiometry	product(s)	structure type (space group)	cell constants (A)
$La_{0.8}Ge_{0.2}$	La + La_3Ge	Ti_3P ($P4_2/n$)	a = 12.740(3); c = 6.303(2)
*$La_{0.75}Ge_{0.25}$	La_3Ge	Ti_3P ($P4_2/n$)	a = 12.741(2); c = 6.298(1)
$La_{0.65}Ge_{0.35}$	La_3Ge + La_5Ge_3	Ti_3P + (MS)	
$La_{0.625}Ge_{0.375}$	La_5Ge_3	Mn_5Si_3($P6_3$/mcm)(MS)	a = 8.941(1); c = 6.878(1)
$La_{0.6}Ge_{.4}$	La_5Ge_3 + La_5Ge_4	(MS) + (SG)	
[a]$La_{0.57}Ge_{0.43}$	La_4Ge_3	anti-Th_3P_4(I-43d)	a = 9.3548(3)
$La_{0.55}Ge_{0.45}$	La_5Ge_4	Sm_5Ge_4(Pnma)(SG)	a = 8.065(1); b = 15.474(2) c = 8.172(1)
$La_{0.5}Ge_{0.5}$	LaGe	FeB (Pnma)	a = 8.488(1); b = 4.128(1) c = 6.122(1)
$La_{0.4}Ge_{0.6}$	LaGe + $LaGe_{1.6}$	FeB + $GdSi_2$(Imma)	
$La_{0.375}Ge_{0.625}$	$LaGe_{1.67}$	$GdSi_2$(Imma)[b]	a = 4.312(1); b = 4.408(1) c = 14.188(1)
$La_{0.35}Ge_{0.65}$	$LaGe_{1.67}$ + Ge	$GdSi_2$(Imma)[b]	a = 4.313(1); b = 4.406(1) c = 14.188(1)

* peritectic; needs prolonged annealing at T < 850°C

[a] peritectic; needs prolonged annealing at T < 1200°C

[b] structure at room temperature

LaGe

The 1:1 compound LaGe was successfully indexed to the FeB structure,[205] based on careful inspection of its Guinier powder diffraction pattern with the aid of the GUIN and POWD programs. It confirmed previous reports of Parthé[206] and Tharp[207] that indicated LaGe was isotypic with FeB. However three very weak lines were observed which could not be indexed with any other binary La-Ge compounds nor to elemental La or Ge structures. These extra lines were also observed to disappear with the other weak lines of LaGe upon inspection of the products from off-stoichiometric reactions. This suggested that the extra lines were innate to the LaGe structure. This also implies that the actual LaGe structure might exist in a lower symmetry relative to the FeB-type.

The orthorhombic FeB structure in space group Pnma can be described as rows of boron-centered iron trigonal prisms stacked side to side (see Figure 3). The boron centers form zigzag chains along the trigonal prism rows. The individual trigonal prisms of FeB-type structures can have different relative dimensions which lead to 2 types of classes./ One group of FeB-type compounds have prisms that are elongated perpendicular to the zigzag chain direction. The other group of compounds have their prisms shortened. Based on its axial ratios, binary LaGe can be classified as belonging to the latter group.

The FeB structure is also closely related to the CrB and MoB structure types. They all have the same building unit -- trigonal prisms of metal atoms centered by nonmetal atoms that form zigzag chains. Their differences lie in the relative orientation of the trigonal prism units as shown in Figure 3.

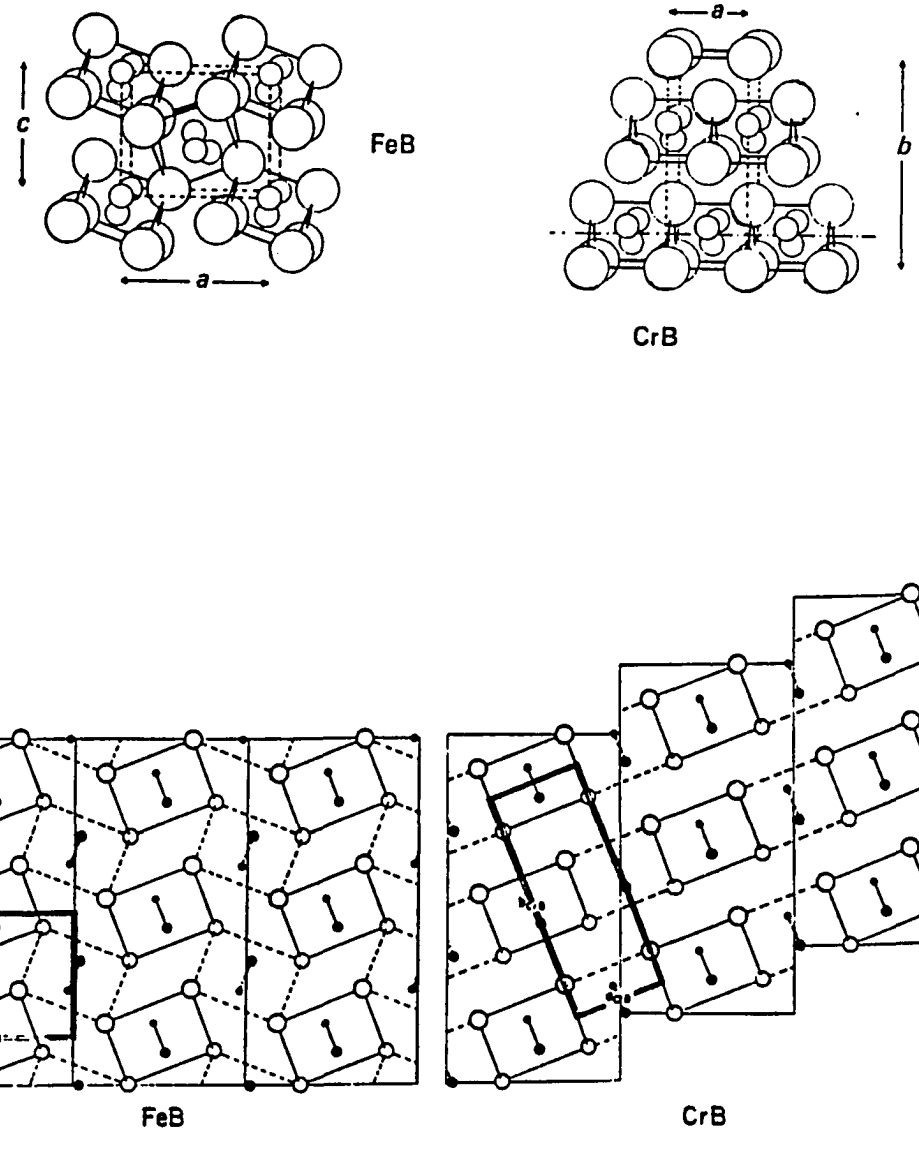

Figure 3. Top: The orthorhombic (Pnma) FeB structure and the closely related CrB structure. Large circles, metal atom; small circles, non-metal atoms. Bottom: The geometrical relationship between FeB and CrB structure types

It has been reported that rare-earth metal monosilicides and monogermanides crystallize in either FeB or CrB-types.[206] Some (DySi, HoSi, ErSi, and PrGe) were even reported dimorphic, having both FeB and CrB structures. In the case of LaGe, electrical conductivity studies report that it exhibits a "polymorphic transformation" similar to $LaGe_{2-x}$, wherein a metal to semiconductor transition occurs at 440°C.[208] Furthermore, the binary phase diagram of La-Ge also reported an undetermined nonstoichiometry range exists in the region about LaGe. A significant nonstoichiometry supports a character similar in nature to $LaGe_{2-x}$.

The appearance of weak extra lines in the LaGe room temperature powder pattern may indicate that a symmetry breaking transformation that is related to the reported "polymorphic transformation" possibly exists in LaGe. This is interesting especially when the number of electrons is taken into account. If indeed the Ge atoms form chains then the compound has one electron more than its prototypical Zintl phase

$$[La^{3+} + (2b)Ge^{2-} + 1e^{-}].$$

This means that the undistorted compound is metallic with the electron residing in conduction bands which are antibonding with respect to Ge-Ge chain bonds. However, this situation is unstable with respect to distortions on the chain leading to some localization of the electron and possible formation of dimers or oligomers. However, the reported transformation reveals that the semiconducting phase exists at higher temperatures (>440°C) and that the lower temperature phase is metallic. Attempts to grow single crystals of LaGe adequate for single crystal x-ray investigations were unsuccessful. Thus, further structural and physical studies are necessary to completely understand the character of LaGe.

La_5Ge_4

La_5Ge_4 was one of the first binaries studied other than La_5Ge_3. It was described as having the Sm_5Ge_4 structure.[209] Equilibration experiments aided by Guinier powder diffraction analysis confirmed the reported structure and stoichiometry of La_5Ge_4. The results also indicate the absence of any significant phase width in La_5Ge_3 and La_5Ge_4 in contrast to the high temperature (T > 1000°C) behavior observed in Zr_5Sn_3 which exhibits self-interstitial behavior resulting in Zr_5Sn_4 which is isostructural with Ti_5Ga_4.[210]

The orthorhombic structure of La_5Ge_4 and Sm_5Ge_4 can be conveniently described in terms of 3 types of networks that occur along the a-c plane (see Figure 4). Layer G contains a 4^4 net of isolated Ge atoms. Layer S is composed of a $3^2{\cdot}4{\cdot}3{\cdot}4$ net of La atoms. There are twice as many La atoms per layer in S as there are germaniums in G. Layers G and S are similar to those found in the tetragonal $CuAl_2$ structure type.[211] The S-type net is a frequent structural pattern in intermetallic compounds.[212] Layer C is a merging of layers G and S in to one layer, but with the Ge atoms forming the $3^2{\cdot}4{\cdot}3{\cdot}4$ net and La making up the 4^4 net. The lanthanum atoms occupy the centers of the squares formed by the Ge network. The Ge network in layer C form short Ge-Ge distances (~2.6A) which may be considered dimers. Layer C and S are also found in the U_3Si_2 structure type.[213] The stacking sequence for $0<y<1/2$ is GSCSG with layer C at y = 1/4 lying on the mirror plane in the space group Pnma. A two-fold screw axis passing through the origin operates on these nets to produce the stacking sequence for $1/2<y<1$. Hence the structure of La_5Ge_4 can be described as a hybrid of the $CuAl_2$ and U_3Si_2 networks with the appropriate number of layers to give the desired composition. As will be described in a

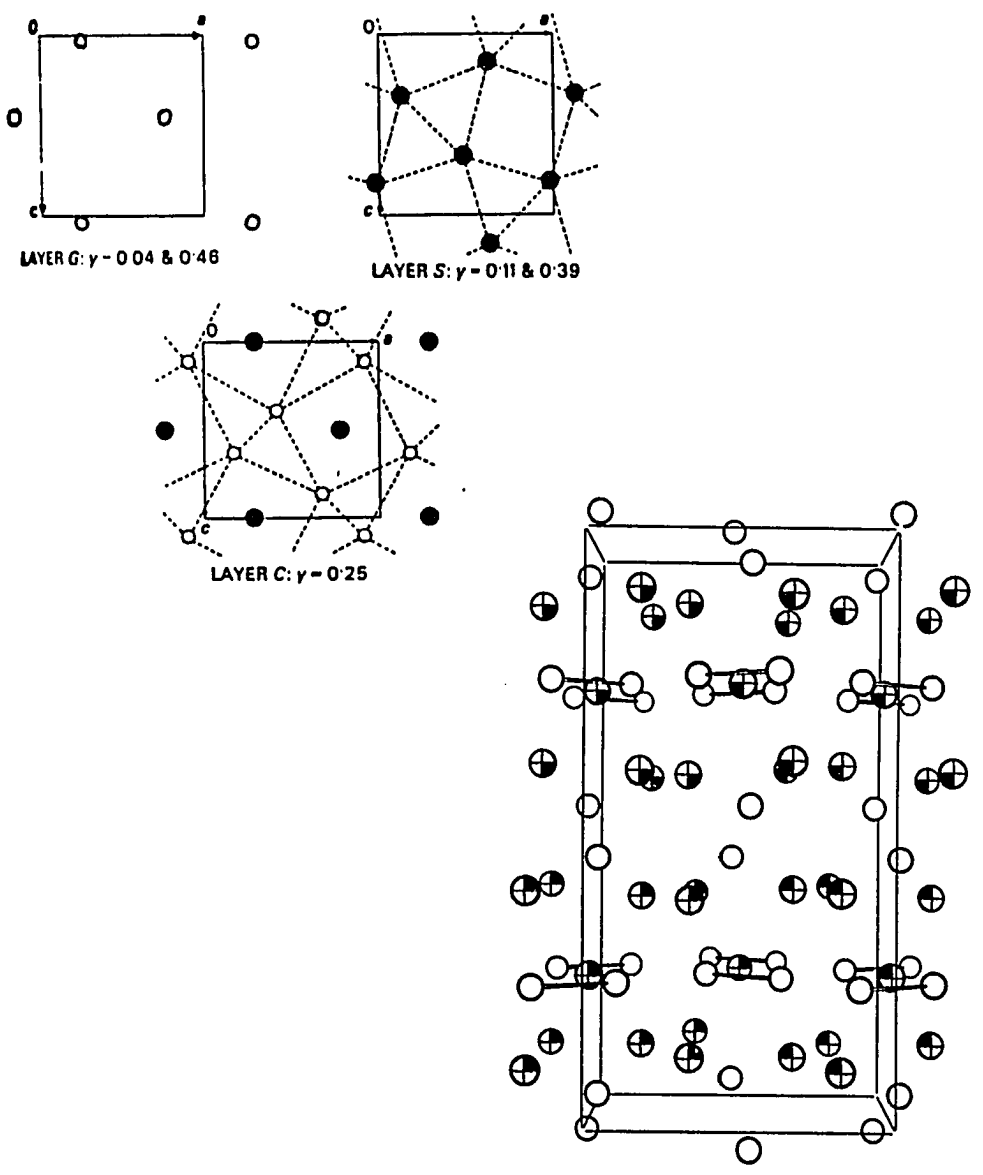

Figure 4. a) The three types of layers are shown and their elevation along the b axis. Open circles: La; shaded circles: Ge: open circles. b) The orthorhombic structure of La_5Ge_4 (Pnma) as formed from the stacking of the above layers (GSCSG), La: shaded circles, Ge: open circles

later section, it was discovered that these networks and layer arrangements in Sm_5Ge_4 are also present in related structures of Gd_5Si_4,[214] Zr_5Si_4,[215] and Eu_5As_4.[216] Their differences lie in the distances between layers and in the distortions on the layers which determine the presence and absence of dimers. These features and relationships will be important in understanding the structural behavior of the different La_5Ge_3Z (Z = tetrelides, Ga and In) compounds which do not have the Mn_5Si_3-type structure.

Simple electron counting, represented by

$$10La^{3+} - [4Ge^{4-}(\text{G layers}) + 2Ge_2^{6-}(\text{C layer})]$$

$$= 30e^- - (16+12)e^- = 2 \text{ electrons} = 1 \text{ electron/formula unit},$$

results in La_5Ge_4 as having one electron more than what a Zintl phase would have. We can also infer that the extra electrons reside on conduction bands that are antibonding with respect to the Ge dimers. This implies a metallic character for La_5Ge_4 and that the bond order of the Ge dimers is 1/2.

La_4Ge_3

An important compound in the La-Ge binary system is La_4Ge_3. This compound was extensively used as a starting material in many reactions that required binaries as starting materials. It is also worth noting that based on its known structural characteristics and electron counts, La_4Ge_3 is formally considered a Zintl phase. Based on published binary phase diagrams of La-Ge, La_4Ge_3 melts incongruently, hence the synthesis of the compound involved fast melting of the elements in tantalum containers in a high temperature furnace at 1200°C. This is followed by annealing at 1050°C for two weeks. The synthesis of new compounds having related structures led us to investigate the single crystal structure of La_4Ge_3.

Structure determination The single crystal used for structure determination was obtained as described above. A cubic crystal with dimensions 0.08 x 0.08 x 0.08 mm was selected by preliminary oscillation photos. It was indexed on a CAD4 diffractometer to have a body centered cubic cell. This confirmed results from powder diffraction and precession investigations. Axial photos about the three principal axes revealed the Laue symmetry Im-3m, and a photograph along the [111] direction also verified the body centering. As no decay corrections were necessary, the data processing included empirical absorption corrections based on three ψ-scans and data averaging in the Laue class Im3m. The structure refinements were proceeded with the SDP software package. An initial model based on the Th_3P_4 structure parameters was used. Full-matrix least squares refinement in the space group I-43d proceeded to final residuals of R = 2.3%; R_w = 2.4%. The structural solution was characterized by well-behaved thermal parameters and reasonable esd's. Careful inspection of a final difference Fourier map indicated the absence of unusual or spurious residual peaks. The lattice parameters were recalculated by least squares fit of the Guinier powder data using NBS silicon as an internal reference. A summary of the data collection parameters, atomic parameters, and important interatomic distances and angles are given in Tables 4-6, respectively.

Structure description An attempt to undertake a single crystal study on La_4Ge_3 was done to confirm its reported anti-Th_3P_4 structure.[217] This was also done to better understand this complicated structure that is assumed by many ternary and binary intermetallics. In particular, a number of new ternary compounds synthesized in our exploratory work were found to be isostructural with or closely related to La_4Ge_3.

Table 4. Data collection and refinement parameters for La_4Ge_3

space group	I-43d
Z	4
crystal dimension	0.8 x 0.8 x 0.8 mm
diffractometer	Enraf-Nonius CAD4
2θ max	65°
indices collected	(±h, k, ±l)
reflections:	
measured	1629
observed (>$3\sigma_I$)	1249
independent	112
R_{ave}	3.2% (observed data)
no. of parameters refined	9
R (refinement)	2.4%
R_w (refinement)	2.9%
G.O.F. 1.10	
largest parameter shift	0.01
absorption coefficient	460.9 (cm^{-1}, Mo Kα)
secondary extinction coeff.	$7.2(1) \times 10^{-7}$
transmission range	24.38% - 99.56%
largest residual peaks	1.55 e^-/A^3 (<1.0A from La)
cell parameter (Guinier):	
a = 9.3548(3)A	
Volume = 818.66(3)A^3	

Table 6. Important interatomic distances and angles in La_4Ge_3

atom	atom	distance	atom	atom	distance
La	Ge	3.4208(2) (4x)	La	La	3.6577(4) (4x)
La	Ge	3.0685(1) (4x)	La	La	3.6576(2) (4x)

Distances are in Angstroms. Estimated standard deviations in the least significant figure are given in parentheses.

Interatomic angles,(°)

atom	atom	atom	angle(°)	atom	atom	atom	angle(°)
La	Ge	La	132.30(6)	La	Ge	La	85.42(2)
La	Ge	La	64.64(3)	La	Ge	La	68.37(2)
La	Ge	La	135.577(8)	La	Ge	La	77.02(1)
La	Ge	La	91.859(4)	La	Ge	La	159.25(8)
Ge	La	Ge	84.58(3)	Ge	La	Ge	107.23(3)
Ge	La	Ge	79.49(1)	Ge	La	Ge	161.32(2)
Ge	La	Ge	90.93(3)				

Angles are in degrees. Estimated standard deviations in the least significant figure are given in parentheses

The difficult and complicated Th_3P_4 structure[218] has been described in terms of coordination polyhedra by Kripyakevich.[219] The coordination sphere surrounding the Th(Ge) can be described as an octavertigon of 8P(La) atoms and each P(La) atom is surrounded by octahedra of 6Th(Ge) atoms. Furthermore, Bärnighausen[220] explained that each metal atom is connected to three other metal atoms, forming two distinct enantiomorphic sets of three-connected ten-membered rings in which the distances are comparable to that of the metal. Inspection of the interatomic distances do not reveal short contacts between Ge atoms and the distances between La atoms (~3.70A) are longer than the Pauling single bond distance of 3.40A but shorter than those found in the metal. The observed La-Ge distances in a La_8Ge octavertigon are 3.07A (4x) and 3.42A (4x). They can be compared to the La-Ge Pauling single bond of 3.0A and to observed La-Ge distances in La_5Ge_3 and La_5Ge_4 of 3.22A and 3.03A respectively.

A more useful description was made by Hyde and Andersson[221] in terms of space-filling array of bisdisphenoids and tetrahedra of La(P) atoms, as shown in Figure 5. A bisdisphenoid can be described as two interpenetrating tetrahedra. Its exact shape is variable and the distances from its center to the 8 vertices fall into two groups of four, each group corresponding to distances to a tetrahedron. The distances to the vertices of one tetrahedron are all equal but are different from those to the vertices of the other. Thus the coordination number is best expressed as 4 + 4 rather than 8. In La_4Ge_3 and Th_3P_4, the Ge(Th) atoms occupy all the centers of the bisdisphenoids leaving the tetrahedral sites empty. The distances between the vertices and the central atom are almost identical in Th_3P_4. However, as is observed in La_4Ge_3 the two type of distances are considerably different resulting in essentially 4-coordinate Ge atoms.

Although Hyde and Andersson cited the presence of bisdisphenoids in the the La_5Ge_3 structure, their description of how they are arranged in the structure was not clear. Inspection of the network of bisdisphenoidal "clusters" reveal that they are arranged linearly along an axis. The in-line arrangement of these units result in the orthogonal arrangement of two adjacent edges from two neighboring bisdisphenoids. These edges consequently make up two edges of a tetrahedron, as shown in Figure 6. The other four edges are derived from other in-line arrangements of bisdisphenoids. Hence the tetrahedral arrangement of the bisdisphenoids result in empty tetrahedral interstitial sites. A view of the complex structure of La_4Ge_3 is illustrated in Figure 7.

Based on the bisdisphenoidal and tetrahedral arrangement of the La(P) atoms in La_4Ge_3 (anti-Th_3P_4), it is interesting to note that other analogous structures exist. UCo[222] in the space group $I2_13$ differs from La_4Ge_3 in that all bisdisphenoidal and tetrahedral interstices are empty. The SiF_4 structure[223] in space group I-43m presents the tetrahedral analog of La_4Ge_3. In this structure the tetrahedral sites are occupied by Si and bisdisphenoidal sites are empty. Another interesting analogs are Pu_2C_3,[224] Rb_2O_3 and Cs_2O_3[225] in the space group I-43d. These represent a rather large group of compounds, are also closely related to the La_4Ge_3 structure. The Pu atoms occupy the La positions and C_2 or O_2 groups take the Ge positions. Consequently, the resulting stoichiometries are $Pu_4(C_2)_3 = Pu_2C_3$, and $(Rb)Cs_4(O_2)_3 = (Rb)Cs_2O_3$.

A literature search also revealed the more interesting $Y_3Au_3Sb_4$ structure,[226] the filled analog of La_4Ge_3. The Sb_4Y_3 part is analogous to La_4Ge_3, with Au occupying all tetrahedral interstitial sites. There are 19 known compounds with this structure but its anti-type, filled-M_4G_3 (M = rare-earth or transition metal; G = main group element), has

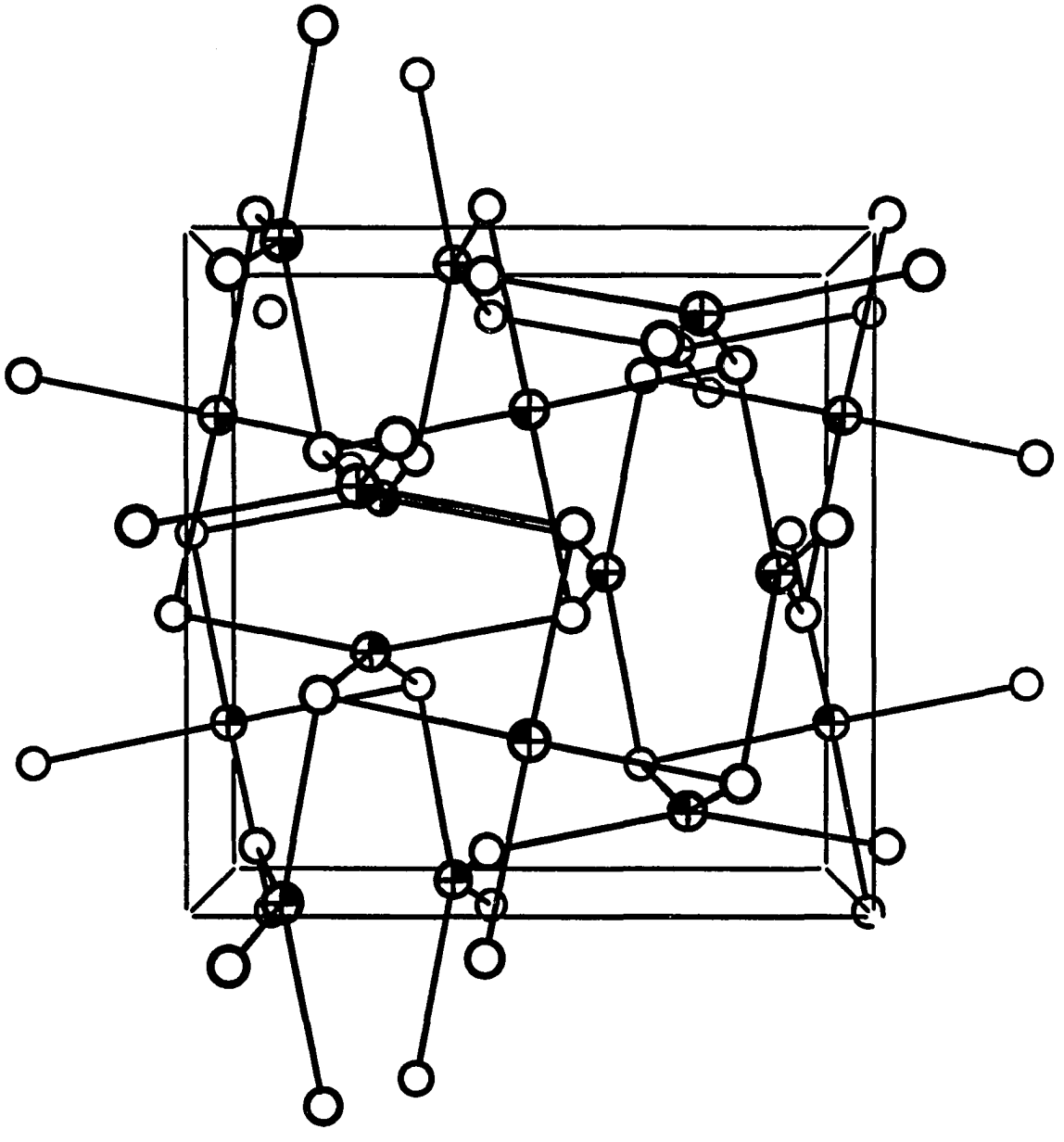

Figure 7. ORTEP drawing along [010] of the cubic La_4Ge_3 structure. The short La-Ge distances are outlined. La: open spheres, Ge: octant shaded spheres

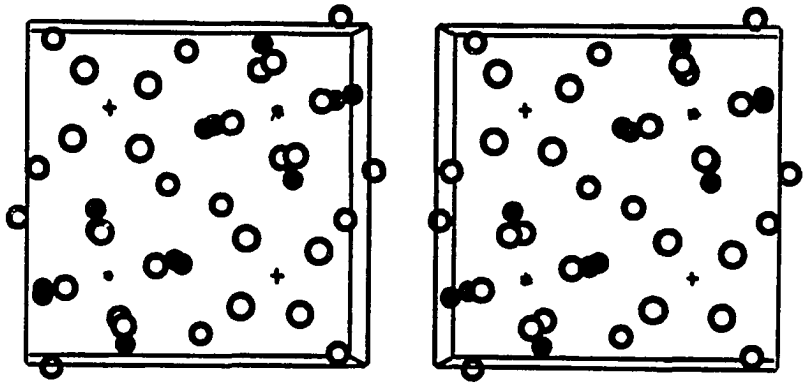

Figure 8. Stereoscopic [001] view of the tetragonal La_3Ge structure -- Ti_3P-type ($P4_2/n$). La: open circles, Ge: crossed-hatched circles, octahedral sites: *, tetrahedral sites: +

the remaining germanium atoms. This structural description implies that potential interstitial hosts may exist in many Ti_3P-type compounds.

La_5Ge_3

In our study of the interstitial chemistry of La_5Ge_3, it was deemed necessary to fully characterize and establish the true nature of the compound. Single crystal x-ray diffraction and equilibration studies were done to determine if La_5Ge_3 was a Novotny phase. The equilibration experiments on La_5Ge_3 are summarized in Table 7. The equilibration studies indicate that a negligible homogeneity range exists for La_5Ge_3. This is illustrated by the presence of La_5Ge_4 and La_3Ge in the Ge-rich and La-rich off-stoichiometric products. This was also confirmed by comparing the observed lattice parameters of the La_5Ge_3 products in the various equilibration experiments as shown in Figure 9.

The plot of lattice parameters with respect to stoichiometry show minimal dependence and confirms that La_5Ge_3 is a line compound with a negligible (or absent) homogeneity range. Although the equilibration experiments provide an implicit proof of the compound's stability as a true binary, the possibility of self-interstitial stabilization cannot be discounted without a single crystal structure determination. Single crystal studies answered questions about the interstitial stabilization of the binary compound.

Structure determination The single crystal used in for X-ray analysis was selected by visual inspection and preliminary oscillation photos. A gem-like crystal was mounted and data collected using the DATEX diffractometer. One set of redundant data was collected up to $2\theta_{max} = 55°$. The data were corrected for absorption using four ψ-scans and averaged for space group $P6_3/mcm$ which was selected based on information

Table 7. Summary of $La_5Ge_{3\pm x}$ reactions

composition	conditions [temp(°C)]	products	lattice parameters of Mn_5Si_3-type phase (A)
$La_5Ge_{2.5}$	M (1250°)	La_5Ge_3(MS) + La	a = 8.937(2); c = 6.874(1)
$La_5Ge_{2.5}$	AN (800°)	La_5Ge_3(MS) + La_3Ge	a = 8.938(1); c = 6.874(1)
$La_5Ge_{2.75}$	M (1250°)	La_5Ge_3(MS) + La_3Ge	a = 8.938(1); c = 6.876(1)
La_5Ge_3	M (1250°)	La_5Ge_3(MS)	a = 8.9409(5); c = 6.8784(6)
La_5Ge_3	Q (1400°)	La_5Ge_3(MS)	a = 8.941(1); c = 6.877(1)
La_5Ge_3	AM	La_5Ge_3(MS)	a = 8.942(1); c = 6.872(1)
$La_5Ge_{3.10}$	M (1250°)	La_5Ge_3(MS) + trace La_5Ge_4	a = 8.940(1); c = 6.880(1)
$La_5Ge_{3.25}$	M (1250°)	La_5Ge_3(MS) + La_5Ge_4	a = 8.941(2); c = 6.879(1)
La_5Ge_3	AM	La_5Ge_3 (ref. 49 and 50)	a = 8.96(1); c = 6.74(1)
La_5Ge_3	G'thermal	La_5Ge_3 (ref. 52)	a = 8.97(1); c = 6.76(1)
La_5Ge_3	M (1500°)	La_5Ge_3 (ref. 51)	a = 8.95(1); c = 6.90(1)

M: melting in Ta containers, then slow cooling.; AN: annealing after melting.;
Q: quenching in an induction furnace; AM: arc-melting; G'thermal: germaniothermal reaction

from axial photos and diffraction conditions. Absorption effects were corrected only by empirical absorption corrections that were based on 4 psi-scans. However, 2-theta dependence was applied in the calculation of the correction coefficients. An initial structural model was obtained using atomic parameters of the Mn_5Si_3 structure. Isotropic and anisotropic refinement (CHESCAT) of all parameters including that which accounts for secondary extinction, and occupancies resulted in final residuals of R = 3.4%; R_w = 3.8%. The final structural solution resulted in well-behaved thermal and positional parameters with adequate standard deviations. Refinement of occupancies did not result in any significant deviation (<1%) from the ideal stoichiometry of La_5Ge_3. This was supported by chemical analysis using quantitative SEM, where the calculated stoichiometry was $La_5Ge_{3.04(1)}$. A summary of the structural solution with important parameters including interatomic distances and angle is given in Tables 8-10.

Structure description The single crystal investigation confirmed that La_5Ge_3 was isostructural with Mn_5Si_3. There were no unusual features in the La_5Ge_3 crystal structure and the interstitial sites were not marked by significant residual electron densities. A careful analysis of the difference Fourier map revealed that the octahedral interstices were essentially unoccupied, although a small residual peak of 1.6 e^-/A^3 is noted. Only the presence of hydrogen cannot be discounted but it is highly improbable. The high temperatures (>1200°C) and high vacuum that were used in the synthesis would have driven off any residual hydrogen from the reaction. Furthermore, the relatively large size of the interstitial cavity precludes strong bonding interactions of hydrogen with the lanthanum atoms comprising the octahedral hole. Hence, the studies on La_5Ge_3 confirm the compound is a true binary and not interstitially stabilized.

Table 8. Data collection and refinement parameters for La_5Ge_3

space group	$P6_3/mcm$
Z	2
crystal dimension	0.15 x 0.08 x 0.08 mm
diffractometer	DATEX
2θ max	55°
collected indices	±h, k, l
reflections:	
measured	1218
observed ($>3\sigma_I$)	903
independent	270
R_{ave}	2.6% (observed data)
no. of parameters refined	15
R (refinement)	3.4%
R_w (refinement)	3.8%
largest parameter shift	0.01
absorption coefficient	312 (cm^{-1}, Mo Kα)
secondary extinction coeff.	$2.3(2) \times 10^{-8}$
largest residual peaks	1.6 e^-/A^3 at (0,0,0)
cell parameters (Guinier):	
a = 8.9409(5) A	
c = 6.8784(6) A	
volume = 476.19(9) A^3	

Table 9. Refined parameters for La_5Ge_3

atom	x	y	z	Occupancy
La(1)	1/3	2/3	0	1
La(2)	0.2399(1)	0	1/4	0.990(8)
Ge	0.6007(2)	0	1/4	0.980(8)

B values

Atom	B11	B22	B33	B12	B13	B23
La(1)	2.12(2)	B11	1.71(2)	1/2 B11	0	0
La(2)	1.87(2)	1.73(1)	2.23(2)	1/2 B22	0	0
Ge	1.80(4))	1.69(3)	2.85(3)	1/2 B22	0	0

Table 10. Important interatomic distances and angles in La_5Ge_3

atom	atom	distance	atom	atom	distance
La(1)	Ge	3.2894(4) (6x)	La(2)	La(2)	3.715(1) (2x)
La(2)	Ge	3.226(1) (1x)	La(2)	La(2)	4.053(1) (4x)
La(2)	Ge	3.7228(9) (2x)	La(1)	La(1)	3.4392(4) (2x)
La(2)	Ge	3.113(1) (2x)	La(1)	La(2)	3.876(1) (6x)

Distances are in Angstroms. Estimated standard deviations in the least significant figure are given in parentheses

Interatomic angles,

atom	atom	atom	angle(°)	atom	atom	atom	angle(°)
La(1)	La(1)	La(1)	180	La(1)	Ge	La(2)	73.81(2)
La(2)	Ge	La(2)	72.11(3)	Ge	La(1)	Ge	161.80(4)
La(2)	La(2)	La(2)	54.55(4)	La(2)	La(2)	La(2)	149.31(2)
La(1)	Ge	La(1)	64.35(1)	La(1)	Ge	La(1)	147.62(4)

Angles are in degrees. Estimated standard deviations in the least significant figure are given in parentheses

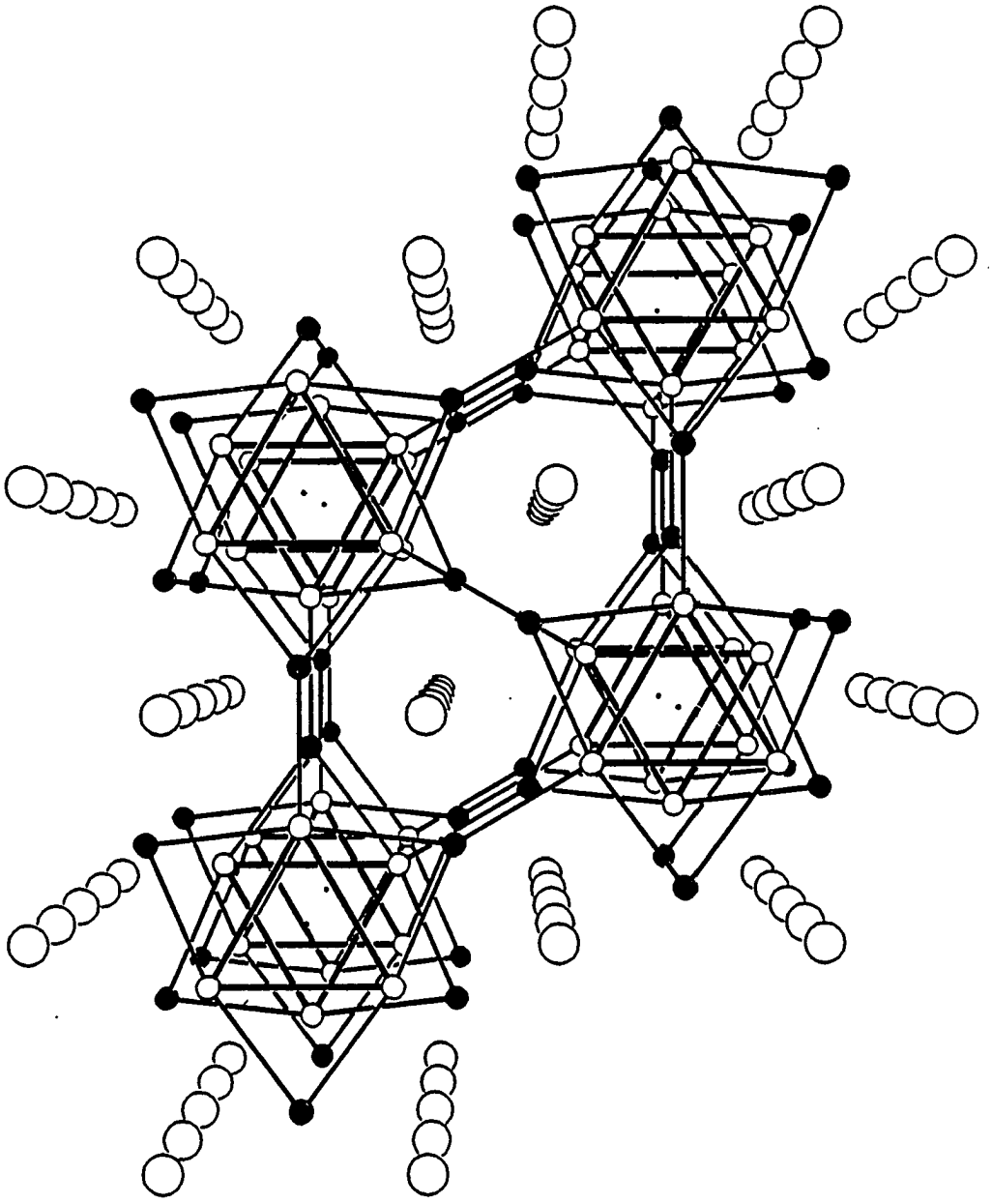

Figure 10. ORTEP drawing of the hexagonal structure, Mn_5Si_3-type ($P6_3/mcm$), of La_5Ge_3 along the c-axis. Open circles: La, shaded circles: Ge. The interstitial sites are marked by dots. Thermal ellipsoids are drawn at 90% probability

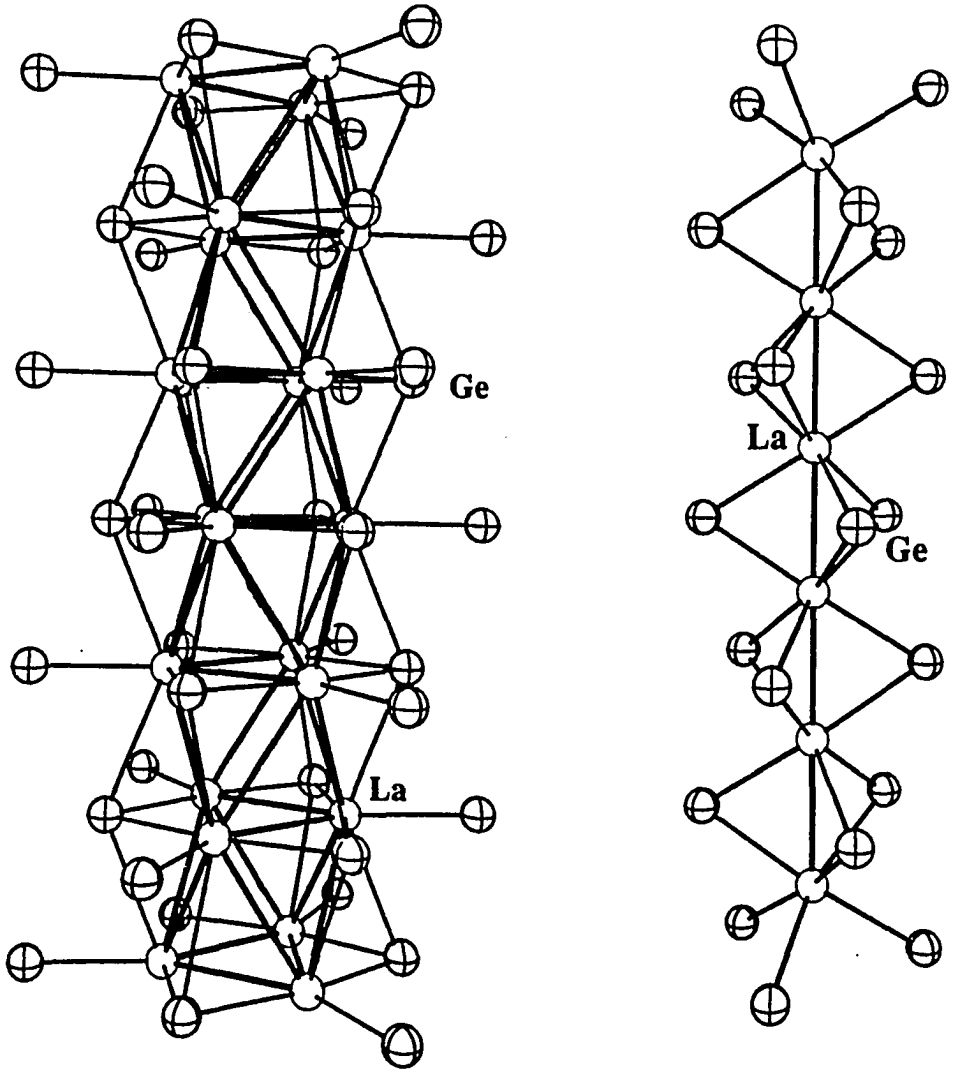

Figure 11. ORTEP drawing of La_5Ge_3 partial structures perpendicular to the c-axis: a) A trigonal antiprism column of La(2) and Ge; b) A nominal linear chain of La(1) in a Ge environment. Thermal ellipsoids are drawn at 90% probability

Arbuckle,[231] Gladyshevskii,[232] and Mayer and Shidlovsky[233] particularly those obtained from arc-melting and germaniothermal reactions. Our results conform best with those reported by Mayer and Shidlovsky. Those reported by Parthé and Arbuckle and that from Gladyshevskii were significantly smaller than those obtained in our experiments. A possible rationale for this puzzle is that the compounds previously reported by Parthé and Gladyshevskii actually corresponded to ternary interstitial phases.

Germaniothermal and arc-melting reactions by Lyutaya and Goncharuk[234] also reported parameters close to Parthé's values. They also noted that La_5Ge_3 obtained from their reactions were virtually air stable, contrary to our results. However, inspection of their synthetic procedures revealed that the reported purity of the La metal used was 99.2%. The very pervasive oxygen would be sufficient to account for most conflicting observations as glove box protection for the lanthanum reagent was not provided.

The above inconsistencies led us to investigate the interstitial stabilization of La_5Ge_3. Particularly the possible effects of oxygen, carbon and other elements on the Mn_5Si_3-type La_5Ge_3 structure. The study of the effects of oxygen might shed light on the stability of La_5Ge_3 products from germaniothermal reactions.

Mn_5Si_3-type Ternary Derivatives of La_5Ge_3

La_5Ge_3O

The germaniothermal reaction synthesis of La_5Ge_3 was mimicked by reacting amounts of La_2O_3, Ge and La that corresponded to the nominal stoichiometry of La_5Ge_3O. Single phase products were obtained from reactions heated in the usual manner by using the high temperature furnace. Results of powder diffraction

experiments are shown in Table 11. They indicate that the calculated lattice parameters of La_5Ge_3O are almost identical (within 3σ) to the cell parameters reported by Arbuckle and Parthé for products obtained from arc-melting and to those obtained from the germaniothermal reactions of Lyutaya. Arc-melting experiments also provided a way to synthesize single phase products of La_5Ge_3O and confirmed that the previously reported arc-melted products were indeed the oxide La_5Ge_3O. Equilibration experiments also show that at lower oxygen content, $La_5Ge_3O_x$ ($0.33<x<1.0$), extra lines corresponding to a $\sqrt{3}$ x $\sqrt{3}$ superstructure were observed. The relative intensities of the superstructure lines increased as x approached 0.33. Moreover, broadening of the three most intense lines were also observed at oxygen contents in the range $0.33 < x < 1.0$. This suggested that the products may have been a mixture of the fully-stoichiometric La_5Ge_3O, having the Mn_5Si_3 structure, and the substoichiometric $La_5Ge_3O_{0.33}$ with the $La_{15}Ge_9Z$ structure type. This means that there are only two phases which exist over the range $0.33 < x < 1.0$ and are possibly responsible for the variation in the lattice parameters of previously reported compounds derived from arc-melting and germaniothermal reactions. However, even at $x = 0.25$ the weak $\sqrt{3}$ x $\sqrt{3}$ superstructure lines were observed and the most intense peaks were also broadened. Thus, one cannot completely establish whether the $La_5Ge_3O_{0.33}$ structure has a homogeneity range over the range $0.0<x<0.33$ or that two phases exist at this range, namely, La_5Ge_3 and $La_5Ge_3O_{0.33}$.

A striking observation of the results from the equilibration experiments is that the c parameter of $La_{15}Ge_9O$ is almost identical to the c parameter reported by Gladyshevskii for La_5Ge_3 that was obtained from fusion of the elements. Comparing the cell constants of the calculated subcell of $La_{15}Ge_9O$ with those reported by Gladyshevskii, which were

Table 11. Summary of La_5Ge_3O reactions

composition	conditions	products	lattice parameters(A)	Ref
La_5Ge_3	S	La_5Ge_3(MS)	a = 8.941(1)	this work
			c = 6.878(1)	
La_5Ge_3O	S	La_5Ge_3(MS)	a = 8.957(1)	this work
			c = 6.759(1)	
La_5Ge_3O	AM	La_5Ge_3(MS)	a = 8.962(2)	this work
			c = 6.766(1)	
$La_5Ge_3O_{0.75}$	S	La_5Ge_3O(MS) + $La_{15}Ge_9O$	a = 8.956(2)	this work
			c = 6.762(2)	
$La_5Ge_3O_{0.5}$	S	La_5Ge_3O(MS) + $La_{15}Ge_9O$	a = 15.537(1)	this work
			c = 6.760(2)	
$La_5Ge_3O_{0.33}$	S	$La_{15}Ge_9O$	a = 15.535(1)	this work
			c = 6.758(1)	
La_5Ge_3	G'thermal	La_5Ge_3 + GeO	a = 8.97(1)	52
			c = 6.76(1)	
La_5Ge_3	AM	La_5Ge_3(MS)	a = 8.96(1)	49
			c = 6.74(1)	
La_5Ge_3	S'	La_5Ge_3(MS)	a = 8.95(1); c = 6.90(1)	51
La_5Ge_3	F	La_5Ge_3(MS)	a = 8.96(1); c = 6.74(1)	50

S: sintering at 1250°C; AM: arc-melting reactions; G'thermal: germaniothermal reaction
S': induction heating at 1500°C; F: fusion of elements at 1300°C

obtained from a Debye-Scherrer camera with CrK radiation, reveal a perfect match. The extra lines corresponding to the $\sqrt{3} \times \sqrt{3}$ supercell would not be likely seen by Debye-Scherrer methods, which are less precise in general use.

Oxygen occupies all the interstitial sites in the host La_5Ge_3 and leads to a contraction of La octahedral "cluster" as evidenced by the decrease in the c-parameter of La_5Ge_3O compared to La_5Ge_3. This relative contraction has also been observed in Zr_5Sb_3 and Zr_5Sb_3O,[235] and it has been rationalized in terms of the relatively smaller atomic size of oxygen with respect to the interstitial hole. This can also be used to explain the contraction of the lattice parameters in La_5Ge_3O since La is larger than Zr resulting in a larger interstitial hole for oxygen atoms. In $La_5Ge_3O_{0.33}$, the oxygen atoms partially occupy the interstitial sites in an ordered manner. The $La_5Ge_3O_{0.33}$ structure will be described in a later section.

The results of our experiments on La_5Ge_3O cast doubts on the binary nature of the germaniothermal reaction products. The nature of the reaction and the innate affinity of La_5Ge_3 for oxygen leads us to conclude that the products of germaniothermal reactions are really oxygen impurity stabilized. This is supported by visual inspection of the apparent air-stability of the oxygen stabilized compounds as compared to the binary La_5Ge_3. Extensive studies on the nature of $LaGe_{2-x}$ also showed that the tetragonal $LaGe_2$ phase that was observed from germaniothermal reactions is actually oxygen stabilized,[236] leading to a reformulation of the germaniothermal reactions into

$$5La_2O_3 + 19Ge \text{ ---> } 2La_5Ge_3O + 13GeO$$

$$La_2O_3 + (7\text{-}2x)Ge \text{ ---> } 2LaGe_2(O)_x + (3\text{-}2x)GeO.$$

La_5Ge_3C

Another common interstitial which could have possibly complicated the studies on La_5Ge_3 is carbon. In most studies on Novotny phases, stabilization by carbon has been found to be the most frequent.[237] This is also true with many of the previously published work on rare-earth metal silicides wherein carbon has been successfully incorporated into many RE_5Si_3 host structures.[238,239,240,241] These studies also reported superstructures, including a $\sqrt{3} \times \sqrt{3}$ superstructure, for $R_5Si_3C_x$ compounds that were substoichiometric in carbon but no details of the superstructure were described.

Studies on rare-earth silicides including Y_5Si_3 by Parthé[242] yielded Mn_5Si_3-type compounds which had relatively larger c/a than other isostructural transition metal silicides. Parthé suggested that charge transfer (bonding) between the two types of metal atoms could explain this effect. However, inspection of the $Y_5Si_3C_x$ cell parameters obtained by Button and McColm[55] revealed that the Y_5Si_3 compound reported by Parthé had even smaller lattice parameters and probably corresponded to the oxide interstitial compound. The increase in the c/a ratio was then attributed by Button and McColm to the effects of interstitials.

The similarity of the rare-earth silicides to the germanides made it necessary to study the behavior of $La_5Ge_3C_x$. Initial investigations on carbon interstitial stabilization of R_5Ge_3 was reported by Mayer.[18,243] Our work confirms that La_5Ge_3C is isotypic with a filled-Mn_5Si_3-type, also known as the Ti_5Ga_4 structure type. The lattice parameters obtained from equilibration experiments involving $La_5Ge_3C_x$ are summarized in Table 12. A plot of the lattice parameter with x, as illustrated in Figure 13, shows a slight linear

Table 12. Summary of $La_5Ge_3C_x$ reactions

composition	conditions [temp(°C)]	products	lattice parameters of Mn_5Si_3-type phase (A)
La_5Ge_3C	S (1250°)	La_5Ge_3(MS) + LaC_2	a = 8.956(1); c = 6.910(1)
La_5Ge_3C	AM	La_5Ge_3(MS)	a = 8.958(2); c = 6.895(2)
$La_5Ge_3C_{0.85}$	S (1250°)	La_5Ge_3(MS)	a = 8.955(1); c = 6.903(1)
$La_5Ge_3C_{0.75}$	S (1250°)	La_5Ge_3(MS)	a = 8.950(1); c = 6.896(1)
$La_5Ge_3C_{0.50}$	S (1250°)	La_5Ge_3(MS) + $La_{15}Ge_9C$	a = 8.948(1); c = 6.889(2)
$La_5Ge_3C_{0.33}$	S (1250°)	$La_{15}Ge_9C$	a = 15.4674(6); c = 6.8795(5)
$La_5Ge_3C_{0.25}$	S (1250°)	$La_{15}Ge_9C$	a = 15.468(1); c = 6.880(1)
$La_5Ge_3C_{1.25}$	S (1250°)	La_5Ge_3(MS) + extra lines	a = 8.955(1); c = 6.906(2)
$La_5Ge_3C_{1.5}$	S (1250°)	two phases (no MS-phase)	a = 9.311(2)[a]
$La_5Ge_3C_{1.75}$	S (1250°)	two phases (no MS-phase)	
$La_5Ge_3C_{2.0}$	S (1250°)	$La_5Ge_2C_2$ + other phases	a = 8.267(1); b = 12.381(2)[b] c = 4.463(2) (Pbam)

[a] refined lattice parameter for the "cubic phase"

[b] refined lattice parameter for orthorhombic $La_5Ge_2C_2$

S: Sintering reactions at indicated temperatures over a total of 10 days.

AM: arc-melting reaction

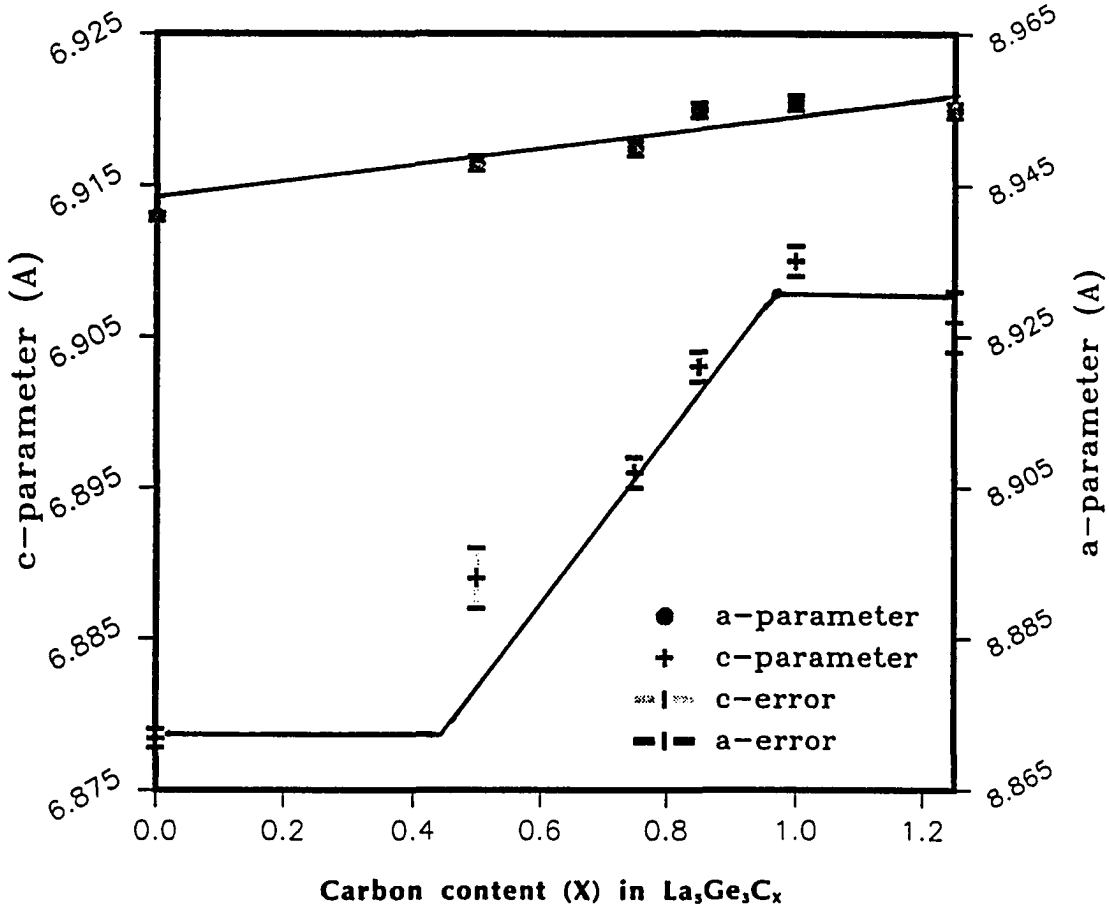

Figure 13. Variation of $La_5Ge_3C_x$ a and c unit cell parameters (A) with carbon content (x)

width in $La_5Ge_3C_{1-x}$, and the synthesis of $La_{15}Ge_9C$ suggest that more elaborate electronic structure characterizes the structural behavior of the ternary Mn_5Si_3-type host compound. Similar to that observed in La_5Ge_3O, the phase relationships, based on equilibration experiments, at x values less than 0.33 cannot be conclusively determined. However, single crystal work on $La_{15}Ge_9C$ show that the compound is indeed stoichiometric.

Reactions involving carbon contents greater than one resulted in multiphase reactions that included an orthorhombic Sm_5Ge_4-type phase, an unknown cubic phase and $La_5Ge_2C_2$. The first two phases were identified by analyzing the powder diffraction by the use of TREOR. They were obtained from reactions with nominal carbon contents with 1.5 and 1.75. Since TREOR is limited by indexing lines that may not belong to the same phase it is possible that the "cubic" phase is composite pattern of more than one phase. However, the good fit of the few (10) lines remaining after reflections of the Sm_5Ge_4-type phase had been assigned convinced us that the "cubic" phase was real. The other compound that was obtained from the excess carbon reactions was $La_5Ge_2C_2$.[45] Its structure is closely related to the Rh_5Ge_3 structure and contains C_2 dimer units.

$La_5Ge_3B_x$

The reactions of La_5Ge_3 with B also yielded an interstitial compound La_5Ge_3B. Its lattice parameters were comparable to those of La_5Ge_3C and indicated a relative expansion of the cell relative to the empty host La_5Ge_3. However, equilibration reactions reveal a significant phase width in $La_5Ge_3B_x$. A plot of lattice parameters with x (see Figure 14) shows that the cell parameters linearly increase with increasing boron content in the range $0.3 < x \leq 0.9$. The cell parameters do not show a significant change outside

this range. Moreover, careful analyses of the powder patterns indicated the absence of $La_{15}Ge_9B$. This behavior is in contrast to that of La_5Ge_3O which does not show any significant homogeneity range and where the appearance of variations in lattice parameters can be attributed to the presence of a $\sqrt{3} \times \sqrt{3}$ superstructure phase. The results can be rationalized in terms of the Zintl rule, wherein electron counting rules suggest that the phase $La_5Ge_3B_{0.6}$, contained in the homogeneity range, should be a Zintl phase. Yet, the presence of a substantial homogeneity range typical of metallic phases is contrary to the Zintl concept.

La_5Ge_3Z; Z = Pnictogen

Following the results of the carbon and boron interstitial experiments, attempts were made to synthesize the Zintl phase analog of an interstitially-stabilized La_5Ge_3 phase. Based on our electron counting scheme, pnictide interstitials would provide the proper electron count for a Zintl phase family of La_5Ge_3Z. Single phase products corresponding to the compounds La_5Ge_3P, La_5Ge_3As and La_5Ge_3Sb were successfully synthesized from high temperature powder sintering reactions of La_4Ge_3 and LaZ (Z= P, As, Sb) (see Table 13)

$$La_4Ge_3 + LaZ \text{ ---> } La_5Ge_3Z$$

The synthesis of single phase products from the elements was difficult because of the inherent reactivity of P and As with the tantalum container. The binaries, LaP and LaAs, were conveniently synthesized from the elements in a sealed silica tube at 300 - 600°C. However, La_5Ge_3Sb could be made by the usual method of melting the elements at 1200°-1300°C in tantalum containers. Attempts to synthesize the bismuth analog proved to be unsuccessful regardless of the synthetic method. The reactions involving bismuth

Table 13. Summary of La_5Ge_3Z with Mn_5Si_3-type structure Z = main group elements

composition	conditions [temp(°C)]	lattice parameters of Mn_5Si_3-type phase (A)	cell volume (A^3)	c/a ratio
La_5Ge_3	S	a = 8.941(1); c = 6.878(1)	476.2(1)	0.769
La_5Ge_3B	S	a = 8.970(1); c = 6.915(1)	481.8(1)	0.770
La_5Ge_3C	S	a = 8.956(1); c = 6.910(1)	480.1(1)	0.771
La_5Ge_3O	S	a = 8.962(1); c = 6.766(1)	470.2(1)	0.752
La_5Ge_3P	B	a = 8.980(1); c = 6.982(1)	487.6(1)	0.778
La_5Ge_3As	B	a = 9.104(1); c = 7.121(1)	511.0(1)	0.782
La_5Ge_3Sb	S	a = 9.156(1); c = 7.231(1)	525.0(1)	0.790
La_5Ge_3S	B	a = 8.992(1); c = 7.031(1)	492.3(1)	0.782
La_5Ge_3Se	B	a = 9.112(1); c = 7.161(1)	515.0(1)	0.786
La_5Ge_3Cl	B	a = 8.955(1); c = 6.897(2)	495.3(1)	0.781

S: Sintering reactions at 1250-1300 C over a total of 10-14 days

B: Prereacted binaries are slowly heated to 1200 C and annealed at 1000 C over 10 days

resulted in multi-phasic products and attempts to completely characterize them were not pursued. The failure to synthesize the bismuth compound could be ascribed to size tolerance effects of the host structure. The possible destabilization of a Mn_5Si_3-type structure with respect to other metal-metal bonded structures is a restatement of the observed behavior. This destabilization could result from a considerable overlap of the Bi valence bands and the metal-derived conduction bands. There were no attempts to synthesize the nitrogen analog La_5Ge_3N.

Careful analysis of the powder patterns established that the compounds, La_5Ge_3Z; (Z = P, As, Sb), were isotypic with the filled-Mn_5Si_3 (Ti_5Ga_4-type) structure. No extra lines corresponding to a superstructure were observed in any powder diffraction pattern. Semi-quantitative chemical analysis of individual crystals using SEM yielded $La_5Ge_{2.97(5)}P_{1.1(3)}$, $La_5Ge_{3.0(1)}As_{0.9(1)}$, and $La_5Ge_{3.0(2)}Sb_{.95(5)}$ close to the loaded stoichiometries of La_5Ge_3Z. The $\sqrt{3} \times \sqrt{3}$ superstructure lines were observed in the powder patterns of substoichiometric $La_5Ge_3P_x$ $0.33<x\leq0.9$. This indicated the presence of the compound $La_{15}Ge_9P$. The $La_{15}Ge_9Z$ analogs of the heavier As and Sb interstitial compounds were not observed.

Large expansion of the lattice parameters of the pnictide interstitial compounds compared with the values of empty binary host distinguished the compounds from La_5Ge_3. Moreover, the dull appearance of the interstitial compounds, based on visual inspection, in contrast to the metallic luster of La_5Ge_3 implied a semiconducting character. Furthermore, the interstitial compounds were also observed to be relatively less air-sensitive than the binary host.

Physical properties Magnetic susceptibility measurements on the representative compound La_5Ge_3P indicated the compound was diamagnetic after corrections have been applied (χ_M = -8.3(4) x 10^{-7} emu/mol). This implied that the compound could be semiconducting or semimetallic. Simple two-probe room temperature measurements on La_5Ge_3P inside a glove box registered a resistivity of 0.2 Ω. The more accurate Q-factor measurements revealed a temperature-dependence characteristic of a semiconductor (-0.98%) with a calculated band gap of ~0.11 eV. The measurements gave room temperature resistivity values close to 580 μΩ-cm. It could be argued that the band gap of the heavier As and Sb compounds will be smaller due to the more metallic character of the heavier interstitial pnictides, i.e., have higher H_{ii} values. Thus, we could hypothesize that the valence and conduction bands could slightly overlap in La_5Ge_3Sb leading to semimetallic properties. This could provide us the opportunity to manipulate band gaps in isostructural interstitial compounds.

The results of the structural and physical studies on the La_5Ge_3Z pnictide interstitial compounds fully agree with the Zintl-Klemm concept. These compounds are considered valence compounds and further support the concept of "exposing the bonding continents" by soaking-up the "sea of conduction electrons" in the La_5Ge_3 host. Therefore, we can expect new compounds with different properties by further exploiting the interstitial chemistry of La_5Ge_3.

Later in this chapter, results of extended Hückel calculations on La_5Ge_3P will be discussed in relation to other Mn_5Si_3-type compounds and 5-3 structures.

La_5Ge_3Z; Z = Chalcogen

Synthesis of the chalcogenide analogs La_5Ge_3S and La_5Ge_3Se as well as the halide La_5Ge_3Cl provided more evidence of the extensive interstitial chemistry of La_5Ge_3. The chalcogenides were best synthesized at high temperatures in Ta containers using pre-reacted binaries as starting materials

$$LaZ + La_4Ge_3 \text{ --> } La_5Ge_3Z \text{ ; } Z = S, Se.$$

Similarly, the chloride was synthesized from the reaction

$$1/3\ LaCl_3 + 2/3La + La_4Ge_3 \text{ ---> } La_5Ge_3Cl$$

in Ta containers. The Guinier powder patterns of the single phase products in La_5Ge_3S, La_5Ge_3Se and La_5Ge_3Cl indicated that the compounds were isostructural with the filled-Mn_5Si_3 structure (see Table 13). There were three weak extra lines associated with LaOCl in the La_5Ge_3Cl experiments but the large expansion of the La_5Ge_3 cell parameters provided evidence for the successful incorporation of the halide. Likewise, the chalcogenide compounds showed large increases in their cell parameters relative to the host's, and all lines were indexed with the filled-Mn_5Si_3 structure. Further experiments to determine the phase width of the compound were not pursued.

Attempts to synthesize the heavier analogs with Te and I were not successful, perhaps owing to the size of the interstitial atoms. These reactions resulted in many unknown phases which could not be indexed to the known phases in the La-Ge-Te and La-Ge-I binary and ternary systems. There were no attempts to further characterize their products.

La_5Ge_3Z; Z = Transition Metals

Initial successes of Garcia and Kwon to introduce transition metal interstitials into Zr_5Sb_3 and Zr_5Sn_3 have led us to synthesize a similar class of transition metal interstitial compounds -- La_5Ge_3Z. The chemistry of transition metal interstitials successfully incorporated into La_5Ge_3 was amazingly extensive. They included Cr, Mn, Fe, Co, Ni, Cu, Zn, Cd, and Ru. These compounds were synthesized by a variety of methods, namely, melting in Ta tubes, arc-melting, and powder sintering. High-temperatures (La_5Ge_3 m.p. = 1475°C) were necessary to bring the reactions to completion. Generally, melting the reactants and slowly cooling the melt was necessary to ensure that equilibrium was reached. This technique also allowed us to obtain well-faceted single crystals for structural analyses. The syntheses of the La_5Ge_3Z transition metal interstitial derivatives are summarized in Table 14.

Careful inspection and analysis of the powder diffraction patterns, and quantitative chemical analysis by SEM on some crystals were used to help determine and characterize the products.

La_5Ge_3Cr

Structure determination Single crystal structure investigations on La_5Ge_3Cr confirm powder diffraction studies which indicate that it is isostructural with Mn_5Si_3. A single crystal was obtained from sintering reactions of the elements in welded tantalum containers. Structure determination was done with the aid of a DATEX diffractometer and CHES program. Axial polaroid photos and Weissenberg photographs of the single crystal of La_5Ge_3Cr confirmed the Laue class P6/mmm and lattice parameters obtained from the single crystal and Guinier powder diffaction studies.

The structure refinement proceeded with the necessary corrections for Lorentz polarization effects, and absorption (based on 4 ψ-scans). Data reduction and averaging resulted in $R_{ave} = 2.8\%$. Least squares refinements started with La_5Ge_3 model parameters previously determined. The interstitial atom was found by the difference Fourier calculations and refined well with Cr parameters. Anisotropic refinement with ideal occupancies resulted in satisfactory residuals of $R = 2.4\%$; $R_w = 2.9\%$. Final refinements included varying the occupancies of the Ge and Cr sites. Careful inspection of the difference Fourier maps did not show any spurious peaks and the thermal parameters are well behaved. The refined stoichiometry was found to be $La_{4.99(1)}Ge_{3.02(1)}Cr_{.97(2)}$ in agreement with the ideal stoichiometry. Other pertinent data, refined atomic parameters, and interatomic distances and angles in the single crystal investigations on La_5Ge_3Cr are summarized in Tables 15-17.

Structure description The crystal structure of La_5Ge_3Cr, isostructural with La_5Ge_3, does not show unusual characteristics pertaining to interatomic distances. The structure is characterized by the Cr-centered trigonal antiprisms and nominal La linear chains enveloped with the proper germanium atoms. The observed La-Ge distances are comparable to those found in other La-Ge compounds such as La_4Ge_3 and La_5Ge_3. The shortest La-La distances, 3.5524(4)A, found in the linear chains are longer than those found in the binary La_5Ge_3 as evidenced by the c-parameter expansion. However the observed La-Cr distances, 2.801(1)A, are comparatively shorter than the sum of Pauling single bond radii of La and Cr, 2.95A, implying strong La-interstitial bonding interactions. There are no known La-Cr binary compounds in which we could compare the observed La-Cr distances. However, the relative contractions are in the same order as

Table 15. Data collection and refinement parameters for La_5Ge_3Cr

space group	$P6_3/mcm$
Z	2
crystal dimension	0.10 x 0.08 x 0.08 mm
diffractometer	DATEX
2θ max	55°
collected indices	±h, k, l
reflections:	
measured	1246
observed ($>3\sigma_I$)	922
independent	278
R_{ave}	2.8% (observed data)
no. of parameters refined	15
R (refinement)	2.4%
R_w (refinement)	2.9%
largest parameter shift	0.01
absorption coefficient	342 (cm^{-1}, Mo Kα)
secondary extinction coeff.	$2.8(2) \times 10^{-8}$
largest residual peaks	1.01 e^-/A^3 (<1.0) from La(1)
cell parameters (Guinier):	
a = 9.0043(7)A	
c = 7.1048(8)A	
volume = 498.86(6)A^3	

Table 17. Important interatomic distances and angles in La_5Ge_3Cr

atom	atom	distance	atom	atom	distance
La(1)	Ge	3.2866(4) (6x)	La(2)	La(2)	4.160(1) (4x)
La(2)	Ge	3.280(1)	La(2)	Ge	3.106(2) (2x)
La(2)	La(2)	3.751(1) (2x)	Cr	Cr	3.5524(4) (2x)
La(1)	La(1)	3.5524(4) (2x)	La(1)	La(2)	3.921(1) (6x)
La(2)	Cr	2.801(1) (6x)			

Distances are in Angstroms. Estimated standard deviations in the least significant figure are given in parentheses

Interatomic angles,

atom	atom	atom	angle(°)	atom	atom	atom	angle(°)
La(1)	La(1)	La(1)	180.00	La(1)	Ge	La(2)	73.32(2)
La(2)	Ge	La(2)	73.08(3)	Ge	La(1)	Ge	75.46(2)
Ge	La(1)	Ge	161.80(4)	La(2)	La(1)	La(2)	101.08(1)
La(1)	La(2)	La(1)	83.05(2)	La(1)	La(2)	La(1)	53.88(2)
La(2)	La(2)	La(2)	60.00	La(2)	La(2)	La(2)	149.83(2)
La(2)	La(2)	Ge	150.00	La(2)	La(2)	Ge	52.96(4)
La(1)	Ge	La(1)	65.43(1)	La(1)	Ge	La(1)	146.63(4)
La(2)	Cr	La(2)	84.07(4)	La(2)	Cr	La(2)	95.93(4)

Angles are in degrees. Estimated standard deviations in the least significant figure are given in parentheses

those found in the transition-metal-centered rare-earth-metal halides when compared to their corresponding La-Z single bond distances.

The synthesis of the chromium analog, La_5Ge_3Cr, marks the first time Cr has been successfully incorporated into a Mn_5Si_3-type structure. The compound as well as its Mn, Co, Ni, Cu, Zn, Cd, and Ru analogs were synthesized in the usual manner, by melting then annealing the starting materials in sealed Ta tubes at high temperatures (1250°C). Nevertheless, our many attempts to synthesize vanadium, titanium and other early transition-metal analogs of La_5Ge_3Z were unsuccessful. Garcia and Kwon were also unsuccessful in their attempts to incorporate Cr and other early transition metals into Zr_5Sb_3 and Zr_5Sn_3.

La_5Ge_3Fe

In the case of La_5Ge_3Fe, quenching from temperatures greater than 1350°C was necessary for its preparation. La_5Ge_3Fe was best prepared via arc-melting or by induction heating at 1400°C and quenching using tantalum containers lined with molybdenum. Otherwise, La_5Ge_3Fe decomposes into two phases, namely, $La_{15}Ge_9Fe$ having the $\sqrt{3} \times \sqrt{3}$ Mn_5Si_3-superstructure and another unknown phase. The existence of La_5Ge_3Fe was inferred from the expansion of the cell dimensions compared with those of La_5Ge_3 and the ferromagnetic character of the compound. However, the possibility of disorder of Fe and Ge in the Ge(1) and interstitial sites cannot be ruled out.

The unknown phase observed in the decomposition of La_5Ge_3Fe can be indexed with the body-centered cubic structure of La_4Ge_3 (anti-Th_3P_4) in the space group I-43d with lattice parameter a = 9.414(4)A. SEM chemical analysis on samples containing the cubic phase revealed that its composition was close to $La_4Ge_{2.3}Fe_1$. Investigation on the

apparent iron substoichiometry of the overall products led us to examine the Ta containers for iron. The results of qualitative SEM experiments also revealed a some amount of iron incorporated in the Ta containers. The Ta-Fe binary phase diagram[244] show iron and tantalum form a solid solution at the T-rich range, even at a temperature of only 800°C. This allows for the excess Fe from the decomposition reaction of La_5Ge_3Fe to enter the Ta container. This has also been observed in the studies on Zr-Sb-Fe and Zr-Sn-Fe systems.[245]

Equilibration reactions also indicated a stochiometric range exists in the compound, in the range $La_4Ge_{2.8}Fe_{0.6}$ to $La_4Ge_{2.0}Fe_{1.3}$. This implies that Fe is incorporated into the Ge sites in the La_4Ge_3 structure. Substitutional defect structures of the anti-Th_3P_4 structure have been previously reported in rare-earth metal bismuthides.[246,247] However, the total Ge and Fe content in $La_4Ge_{2.0+x}Fe_{1.3-y}$ is seen to be more than the allowed stoichiometric value if the Ge and Fe occupy one site in the La_4Ge_3 structure. This could be explained by assuming the excess iron or germanium atoms are in the tetrahedral interstitial sites of a Th_3P_4-type structure as in $Y_3Au_3Sb_4$.[248] It is worth noting that despite our many attempts, a compound with the stoichiometry $La_4Ge_3Fe_x$ that is stoichiometric in Ge was not successfully synthesized. Single crystal investigations and chemical analysis on the Ru analog $La_4Ge_{2.25}Ru_{1.1}$ showed that the tetrahedral sites were partially occupied by ruthenium.[249]

The above results led to a formulation of the decomposition reaction of La_5Ge_3Fe as

$$2La_5Ge_3Fe \text{ ---> } 1/3\ La_{15}Ge_9Fe + 5/4\ La_4Ge_{2.4}Fe_{0.6+x} + [(11/12)-x]Fe_{(Ta)}.$$

Physical property measurements Magnetic property measurements on La_5Ge_3Fe samples revealed a distinct evidence of long range magnetic ordering that is ferromagnetic in nature. The field dependence and hysteresis experiments, see Figure 15 and 16, revealed that the compound is a very soft ferromagnet with an observed saturation magnetic moment of $1.93\mu_B$ per Fe atom comparable to those of metal Fe ($2.2\mu_B$). The value for μ_{eff} corresponds to two unpaired spins per formula unit. In view of the characteristic behavior of La_5Ge_3Fe, it is natural to associate this ferromagnetism with the iron sublattice.

The observed magnetic interaction between Fe atoms could be attributed to the close Fe-Fe distances, c/2 = 3.6A, between neighboring interstitial sites in an antiprism column that is coupled by conduction electrons. Furthermore, one would expect a high degree of magnetic anisotropy for a ferromagnetic state based on the crystal structure of La_5Ge_3Fe.

Although a quantitative description of the ferromagnetic coupling between iron atoms is not possible with only data for powder samples, the fact that the compound is still ferromagnetic at room temperature implies strong magnetic coupling between Fe in three dimensions. Because of the large iron-iron distances between chains, the coupling along the a-b plane depends on an exchange interaction between iron and the six La neighbors to give an electron spin polarization at the latter sites. Coupling between columns of iron-centered trigonal antiprisms may take place via a second linear chain of La atoms. The strength of the exchange interactions would then determine the degree of three dimensional magnetic interactions. Subsequent extended-Hückel band structure calculations on La_5Ge_3Fe show that the overlap population between the La(1) in the

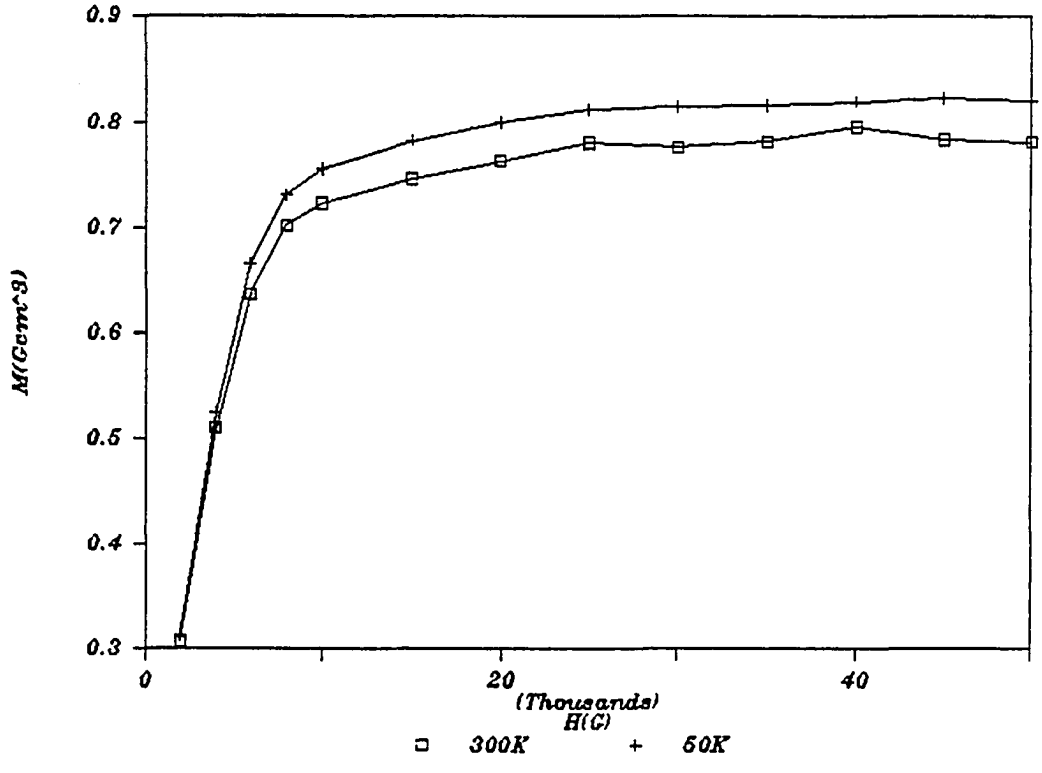

Figure 15. A plot of the field (H) dependence of the magnetization (M) of La_5Ge_3Fe at different temperatures, 300 and 50 K

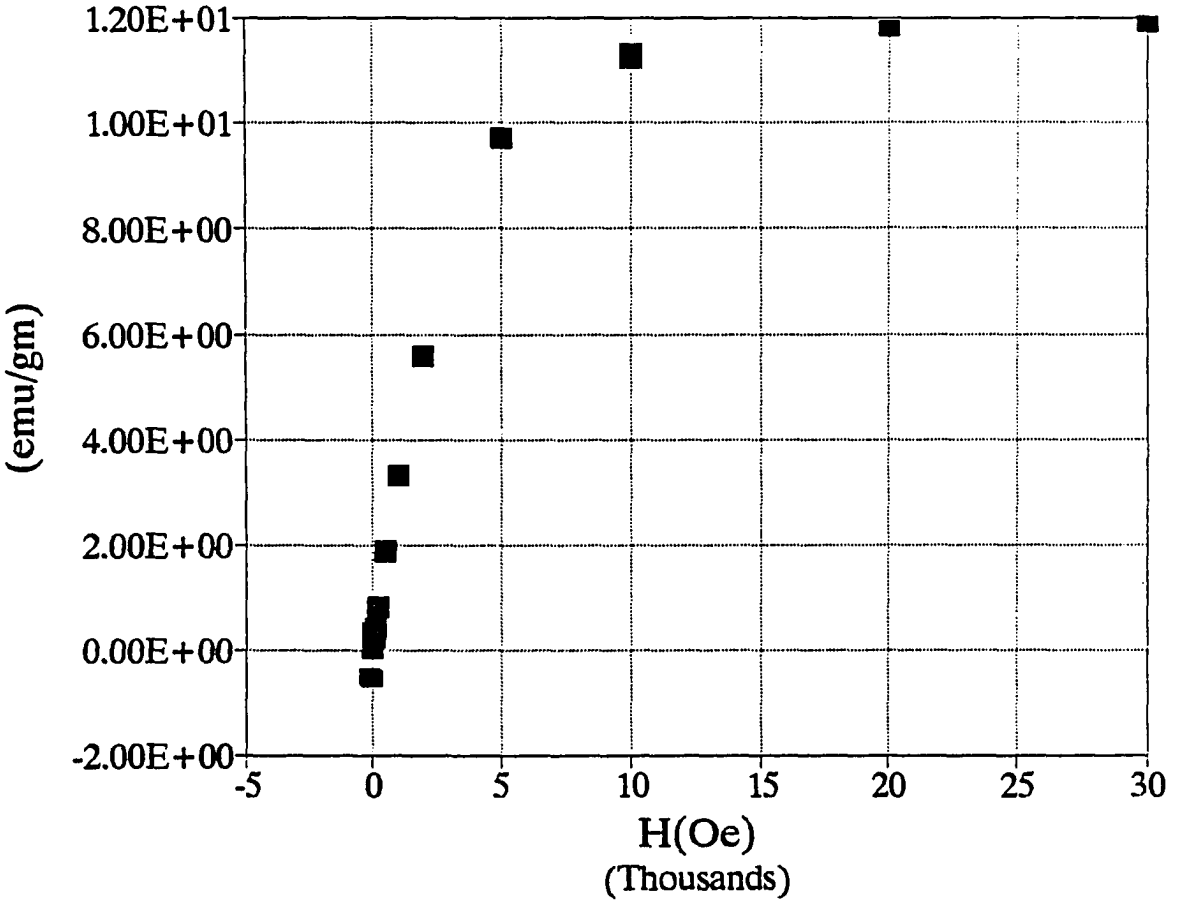

Figure 16. Magnetic hysteresis curve of La_5Ge_3Fe at K. Note there is no reverse magnetic field needed to quench the magnetization

linear chains and the La(2) in the antiprisms was around 0.104, a fairly significant bonding interaction.

Long range coupling between iron atoms within the confacial antiprism chains would also be possible through the mediation of conduction electrons -- itinerant electrons. The itinerant model uses the mobility of d-electrons, through the mechanism of "indirect exchange", an exchange force acting via antiparallel spins. If an outer electron of atom A is spin up, then a nearby conduction electron will have spin down; the spin on this conduction electron will then force an adjacent electron on atom B to have spin up. Thus, the spins on adjacent atoms A and B are forced into parallel spins by the influence of conduction electrons. This has been used to explain many metallic ferromagnets and reviewed by Herring.[250] Subsequent electrical conductivity experiments on powder samples, by means of Q-method, reveal that La_5Ge_3Fe is indeed metallic with a resistivity of ~80$\mu\Omega$-cm at room temperature and a resistivity dependence of +0.53% deg^{-1}.

Photoelectron spectroscopic data PES data were secured with the aid of an AEI-200B spectrometer and Al Kα radiation. An indium substrate was used to mount the sample on and core levels were referenced to adventitious carbon. For comparison, measurements were also made on La_5Ge_3.

Valence band measurements did not provide much information except for the obvious Fermi edges of La_5Ge_3 and La_5Ge_3Fe. The observed Fermi edges confirmed their metallic behavior as revealed by electrical conductivity measurements and extended-Hückel calculations.

Core-binding shifts presented more contrast. Although the two types of lanthanum were not resolved in both La_5Ge_3 and La_5Ge_3Fe, the composite $3d_{5/2}$ binding energies 837.2 (La_5Ge_3), and 838.5 (La_5Ge_3Fe) eV, were in accord with 834 eV of the metal. The higher binding energies indicates an overall oxidation of La with respect to the metal. The germanium $3d_{5/2}$ core levels found at 26.2 eV in both La_5Ge_3 and La_5Ge_3Fe were lower than the corresponding metal peak at 28.0 eV, qualitatively in agreement with the reduced state of Ge in the compounds. Finally, the iron $2p_{3/2}$ and $2p_{1/2}$ binding energies were found at 705.8 and 719.0 eV.[251] These values are lower than those of the metal at 706.75 and 719.95 eV, respectively. The lower bonding energies of iron suggest a more reduced state than the metal. This observation is in agreement with the results of the extended-Hückel calculations on both La_5Ge_3 and La_5Ge_3Fe wherein the calculated Fe charge was negative.

La_5Ge_3Z (Z = Mn, Co, Ni)

The syntheses of the compounds did not present difficulties as those described in the iron analog. The preparation of the ternary phases from the elements was done following the usual high temperature reactions (1250°C) in welded tantalum containers. The powder diffraction patterns of slow cooled products yielded clear and sharp lines that could be completely indexed with a filled-Mn_5Si_3 structure. However, reactions with lower interstitial content (but greater than 1/3) resulted in mixed phases corresponding to a filled-Mn_5Si_3 phase and a superstructure phase with a $\sqrt{3} \times \sqrt{3}$ related expansion of the La_5Ge_3 subcell. The refined cell parameters of the Mn_5Si_3-type phases were nearly identical with the values for the fully stoichiometric interstitial phases. This was observed for the three elements Mn, Co, and Ni.

Syntheses using arc-melting techniques were also successful in providing single phase La_5Ge_3Z compounds. However, the powder pattern lines of the arc-melted samples were usually diffuse and their refined cell parameters were consistently larger (>0.02A).

La_5Ge_3Z (Z = Cu, Zn, Cd)

The sintering of binary reagents with a corresponding La-Ge binary was found to be the most efficient way to synthesize the La_5Ge_3 interstitial compounds of copper, zinc, and cadmium. These synthetic approach did not need temperatures in excess of 1200°C. Instead reactions could be satisfactorily completed at temperatures below 1000° C. Hence this allowed the use of ordinary resistance furnaces with the reactions contained in welded Ta tubes jacketed in silica glass tubes. Reactions with lower interstitial contents resulted in a $La_{15}Ge_9Z$ phase in the copper system. Both zinc and cadmium did not yield any $La_{15}Ge_9Z$ despite attempts at higher temperatures (>1200°C).

Crystal Chemistry of La_5Ge_3Z

The compounds with the formula La_5Ge_3Z, Z = transition metals, and some group 15-17 main group elements, are isostructural with Ti_5Ga_4, a filled-Mn_5Si_3 structure (see Figure 17). As in many compounds with a filled-Mn_5Si_3 structure, their structures are characterized by antiprism columns and linear chains of the metal atoms (La). The centers of the face-sharing La octahedra which make up the antiprism columns are occupied by the transition metal interstitial atoms, Z. The local arrangements of the interstitial atoms also form nominal chains along the c-axis. The shortest interatomic distances between the interstitial atoms are found along the chain axis and correspond to half of the c-parameter. These distances are quite large for significant localized bonding

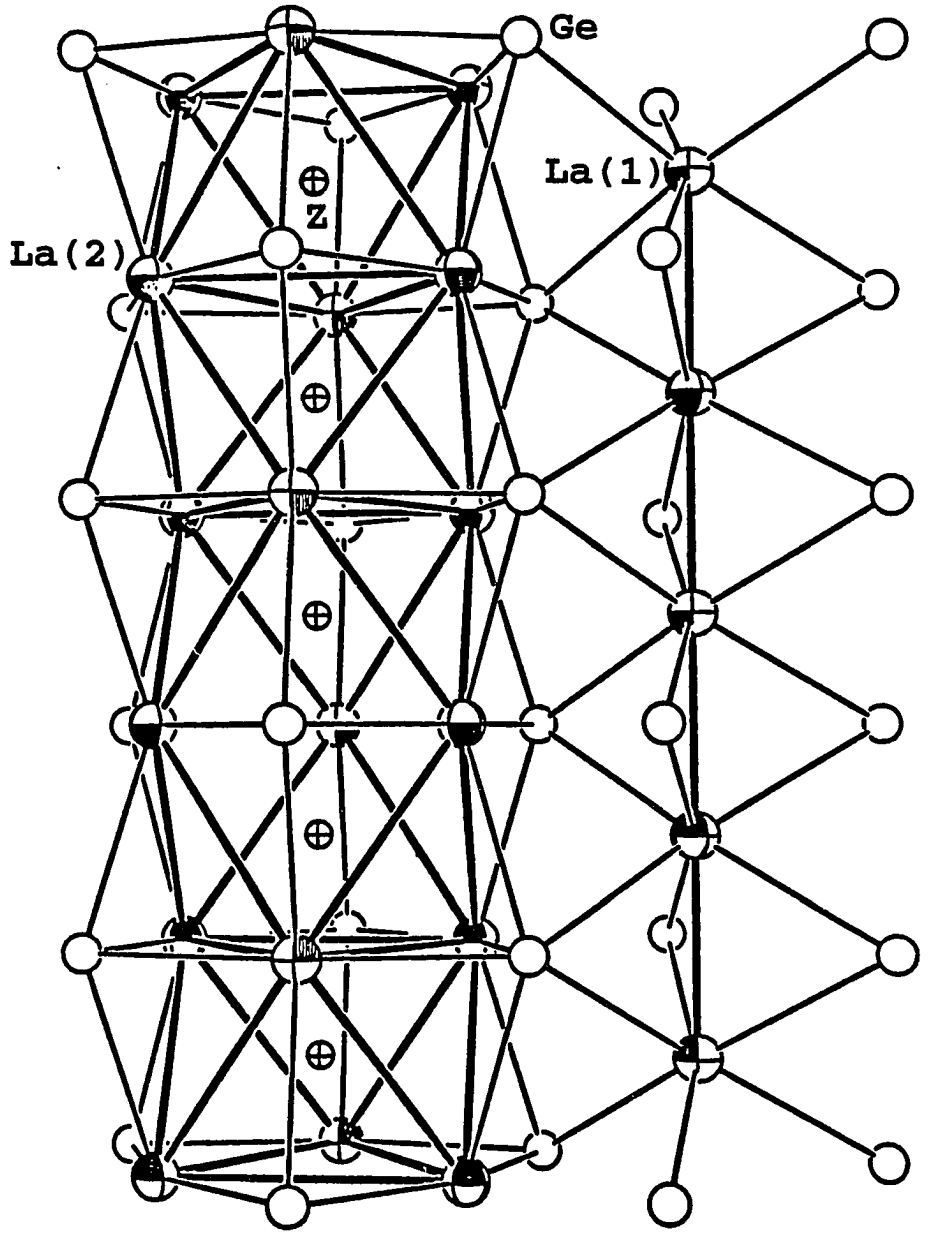

Figure 17. The confacial trigonal antiprismatic column (left) and the linear (right) La chains viewed perpendicular to the c-axis of the filled-La_5Ge_3 (Ti_5Ga_4-type) structure. Large circles, lanthanum; medium circles, germanium; small circles, interstitial Z

interactions between interstitial atoms, yet close enough for some magnetic interactions to occur as in La_5Ge_3Fe. Like previous researches on Mn_5Si_3-like transition metal interstitial compounds, the compounds of Cu, Zn and Cd showed the largest expansions compared to interstitial compounds within the same period. Similarly, the heavier main group elements yielded the largest lattice expansions in La_5Ge_3 among the non-metal interstitials. Thus, a plot of the unit cell volume of the various La_5Ge_3Z interstitial compounds with the atomic number show a linear dependence that could be correlated with the atomic sizes of the interstitial atoms. This is illustrated in Figure 18. Another interesting observation are the increases in the c/a ratios (see Tables 13 and 14) with all elements, except O. This could be attributed to coulombic repulsions between neighboring interstitial atoms within a column of face sharing octahedra. The exception of oxygen is probably due to its small atomic size.

Chemical bonding in La_5Ge_3Z

The success in being able to incorporate metals to the right of Cr could be generally restated in terms of thermodynamics of the ternary system - the stability of alternate phases. This is particularly applicable to unsuccessful reactions which result in multi-phasic products involving binary and other ternary compounds.

However, an electronic reason, based on the character and increasing occupancy of the d-bands as one moves to the right of the 3d period, is likewise pertinent, particularly for unsuccessful reactions of La_5Ge_3 and a metal (e.g. V and Ti). The trend of the character of the d-bands is illustrated by the diagram in Figure 19 as presented by Varma and Wilson[252] and justified by Andersen.[253,254] The increased nuclear charge is more incompletely screened and electrons more tightly bound as one moves across the period.

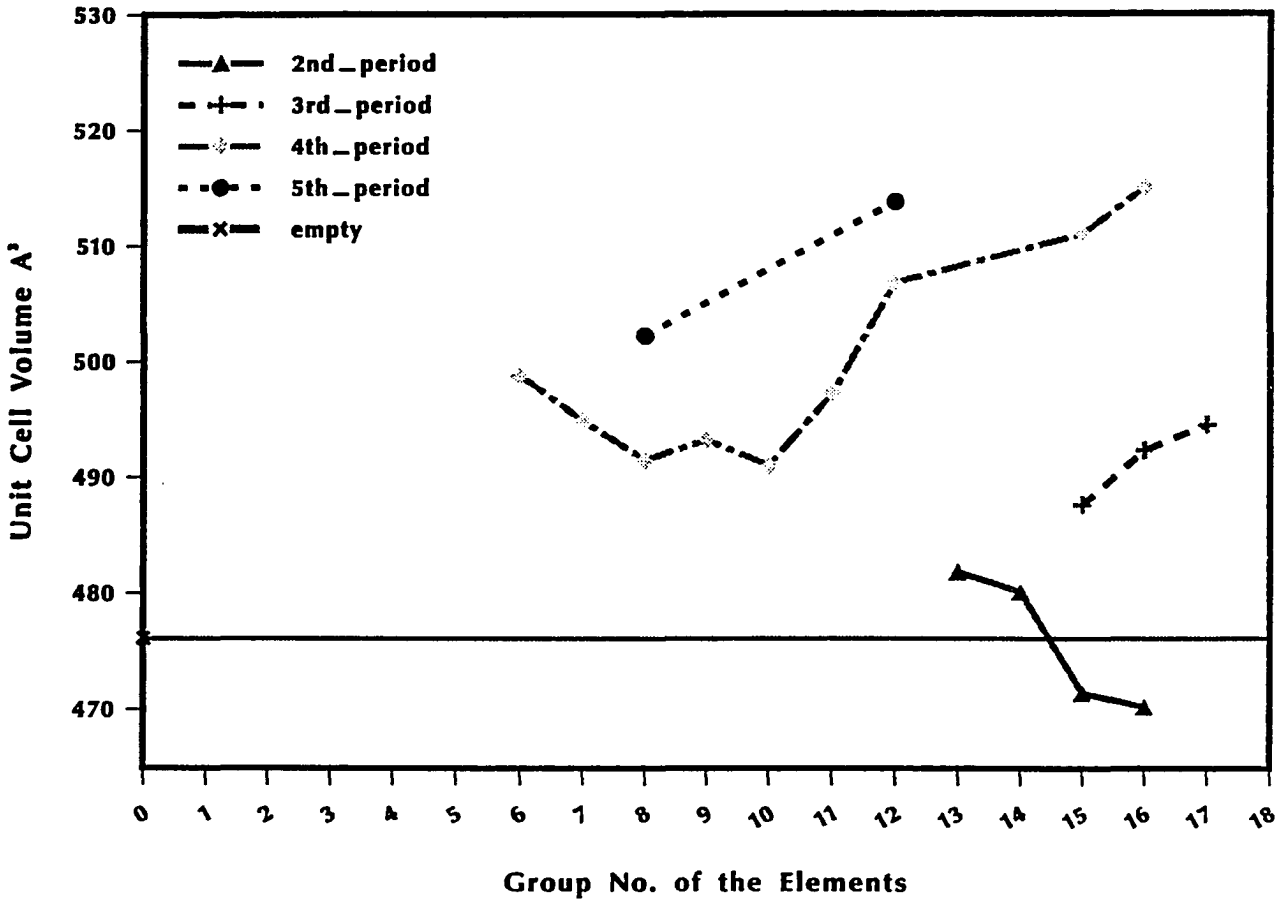

Figure 18. Unit cell volumes (A^3) of La_5Ge_3Z as a function of period and group of Z. The solid line parallel with the x-axis marks the reference volume of the host La_5Ge_3 host

As a result, the d-bands decrease in energy and become narrower. At the right side of Cr in the diagram, the Fermi level falls as one moves to the right and the work function of the metal increases. To the left of Cr the d-bands are more dispersed and less occupied.

Now, we imagine superimposed on this variable-energy sea of d electrons are the schematic La-Ge bonding and antibonding bands of La_5Ge_3 as shown in Figure 19. The La-Ge antibonding bands are also bonding with respect to some La-La interactions. As we turn on the possible interactions between the interstitial d-bands with the host's conduction and valence bands, one would expect the d-bands to the right of Cr to more strongly interact with the La-derived conduction bands. This leads to a partial "electron transfer" from the La-derived bands to the transition metal bands resulting in strong La-Z bonds. The partial "electron transfer" from the La bands to the interstitial atoms is supported by XPS measurements on La_5Ge_3Fe.

Photoelectron measurements result in core shifts that indicate a negative character of the interstitial atoms. For the more dispersed and less occupied d-bands to the left of Cr, their effect would also be to accept the electrons from the conduction bands. However, as we also move to the left of Cr the Fermi levels of the d-bands are observed to decrease and may fall below the highest occupied states of the La-Ge bonding levels. This implies the transfer of electrons from the conduction and valence bands of the host to the interstitial bands. This could result in the destabilization of the bonding framework in the La_5Ge_3 host structure.

The observed behaviors of Zr_5Sb_3 and Zr_5Sn_3 in their inability to incorporate Cr can be explained by the more metallic property of the main group partners. The bonding

levels of Zr-Sb and Zr-Sn extend to higher energy than the La-Ge bonding bands and possibly cross the Cr d-band limits.

Extended-Hückel calculations

Extended Hückel calculations were done on La_5Ge_3, La_5Ge_3P and La_5Ge_3Fe to gain additional understanding into their bonding and to relate the results to the qualitative electronic picture implied by structural descriptions, physical properties and XPS measurements.

The extended-Hückel calculations, as described in the previous chapter, were done using a modified BIG5 program, JDCBAND. Atomic parameters for La, Ge, and P were obtained from the literature and, whenever necessary, from charge-iteration calculations on actual and hypothetical models. Atomic parameters of iron were obtained from charge-iterated calculations on hypothetical LaFe model with identical La-Fe distances as those found in the actual structures. The atomic parameters are presented in Appendix A. A summary of the results of these calculations are presented in Table 18.

The notation used in identifying the atoms will follow the label used in the structure determination of La_5Ge_3 and La_5Ge_3Cr. Intraplanar interactions refer to the interactions along the a-b plane particularly between La(2) atoms making up one shared trigonal face. Interplanar interactions refer to interactions along the c axis, an example of which is between La(2) atoms that form opposite shared trigonal faces.

Electronic structure of La_5Ge_3 The calculated band structure of La_5Ge_3 is represented by the density of states shown in Figure 20. The atomic and orbital projections of the DOS reveal substantial mixing between the La and Ge orbitals as illustrated by the large dispersion of the bands derived from their respective atomic

Table 18. Summary of Extended-Hückel Calculations on La_5Ge_3 and La_5Ge_3Z

compounds	La_5Ge_3	"La_5Pn_3"	La_5Ge_3P	La_5Ge_3Fe
Fermi Energy(E_f),eV	-9.19	-8.78	-9.376	-9.313
Overlap Populations:				
La(1) - Ge	0.2634	0.2725	0.3013	0.3032
La(2) - Ge(ave)	0.2955	0.2942	0.2628	0.2580
La(1) - La(1)	0.0998	0.1273	0.0883	0.0596
La(1) - La(2)	0.1007	0.1213	0.0417	0.0360
La(2) - La(2)(xy)	0.1902	0.2255	0.0407	0.0312
La(2) - La(2)(z)	0.1748	0.2007	0.1543	0.1201
La(2) - Z			0.1910	0.1874
Z - Z			-0.019	0.0053
Average Net Charges:				
La(1)	+0.34		+0.40	+0.37
La(2)	+0.26		+0.63	+0.24
Ge	-0.487		-0.52	-0.47
Z (interstitial)			-1.115	-0.12
Total Energy, eV	-674.05	-727.96	-868.60	-804.46

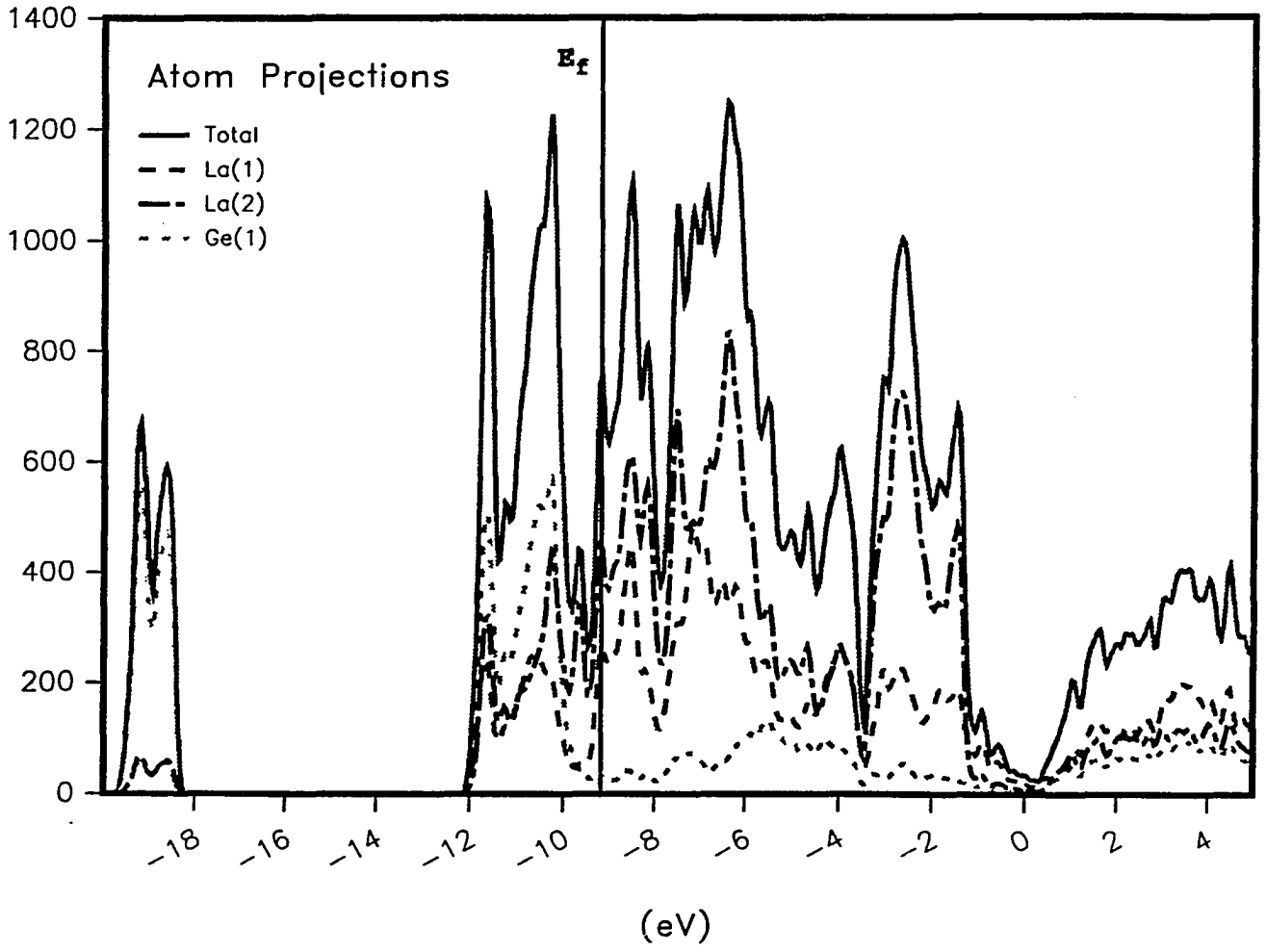

Figure 20. Density of states (DOS) diagram of the valence and conduction band regions in La_5Ge_3 with the corresponding atomic projections. La(2) occurs in the confacial chain

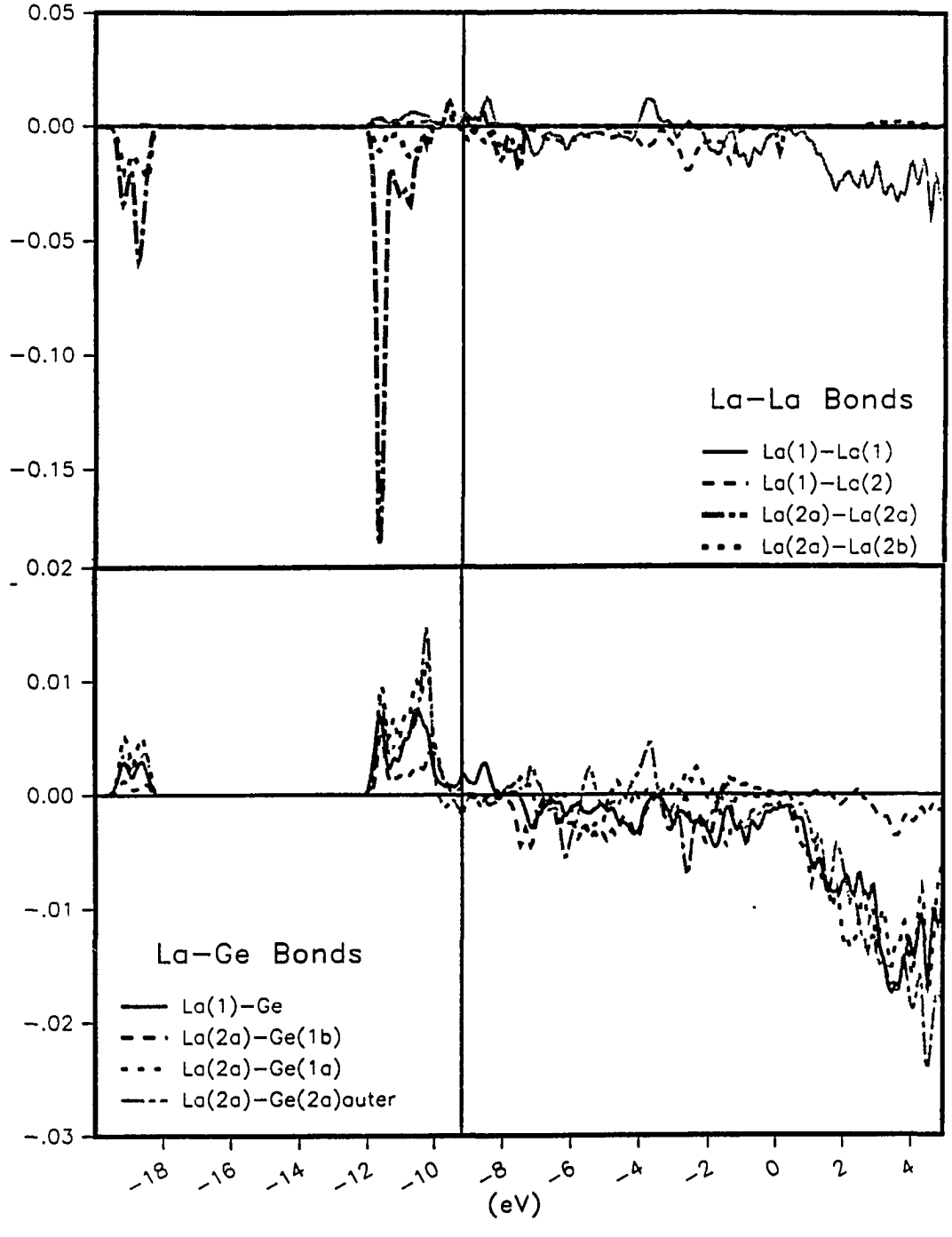

Figure 21. COOP curves for La_5Ge_3. The positive values on the curves represent bonding interactions while negative values denote an antibonding character

the existence of RE_5Pn_3 phases in the Mn_5Si_3-type and have more electrons in the RE-derived conduction bands.

Electronic structure of La_5Ge_3P As expected, La_5Ge_3P was found to exhibit a low density of states at E_f attributed to an "opening" of an energy gap (~0.08 eV) between the Ge-derived valence bands and the metal-derived conduction bands. This is illustrated in the compound's total DOS and atomic projections as shown in Figure 22. The bands below E_f can be assigned as follows: Ge s-bands around -17.0 eV; P-bands from -15.0 to about -12.0 eV; and the Ge p-bands from -12.0 to E_f (-9.403 eV). The broad metal-derived conduction bands make up the structures above E_f. Nevertheless, the significant mixing between La and Ge is still present and indicated by the atomic projections of DOS.

The COOP curves, shown in Figure 23, show similar features that were observed in the La_5Ge_3 band structure. The results of COOP calculations also show the very weak interaction between La(1) chain atoms and the strong bonding overlap between La(2) and phosphorus.

Furthermore, the average La-Ge interactions show that maximum bonding is achieved at the electron count of La_5Ge_3P. Some residual La-Ge bonding states still remain above E_f and may explain the existence of electron richer phases La_5Ge_3S and La_5Ge_3Cl. The accompanying rise in E_f, -9.066 eV for "La_5Ge_3S" and -8.911 eV for "La_5Ge_3Cl" based on a rigid band approach, do not show major antibonding interactions except those between La(2) atoms. These interactions are antibonding particularly along the z-axis. This is borne out by the calculations on La_5Ge_3 which show a dominant La(2) character of the bands near E_f. Since La(2)-Ge interaction is strongest along the

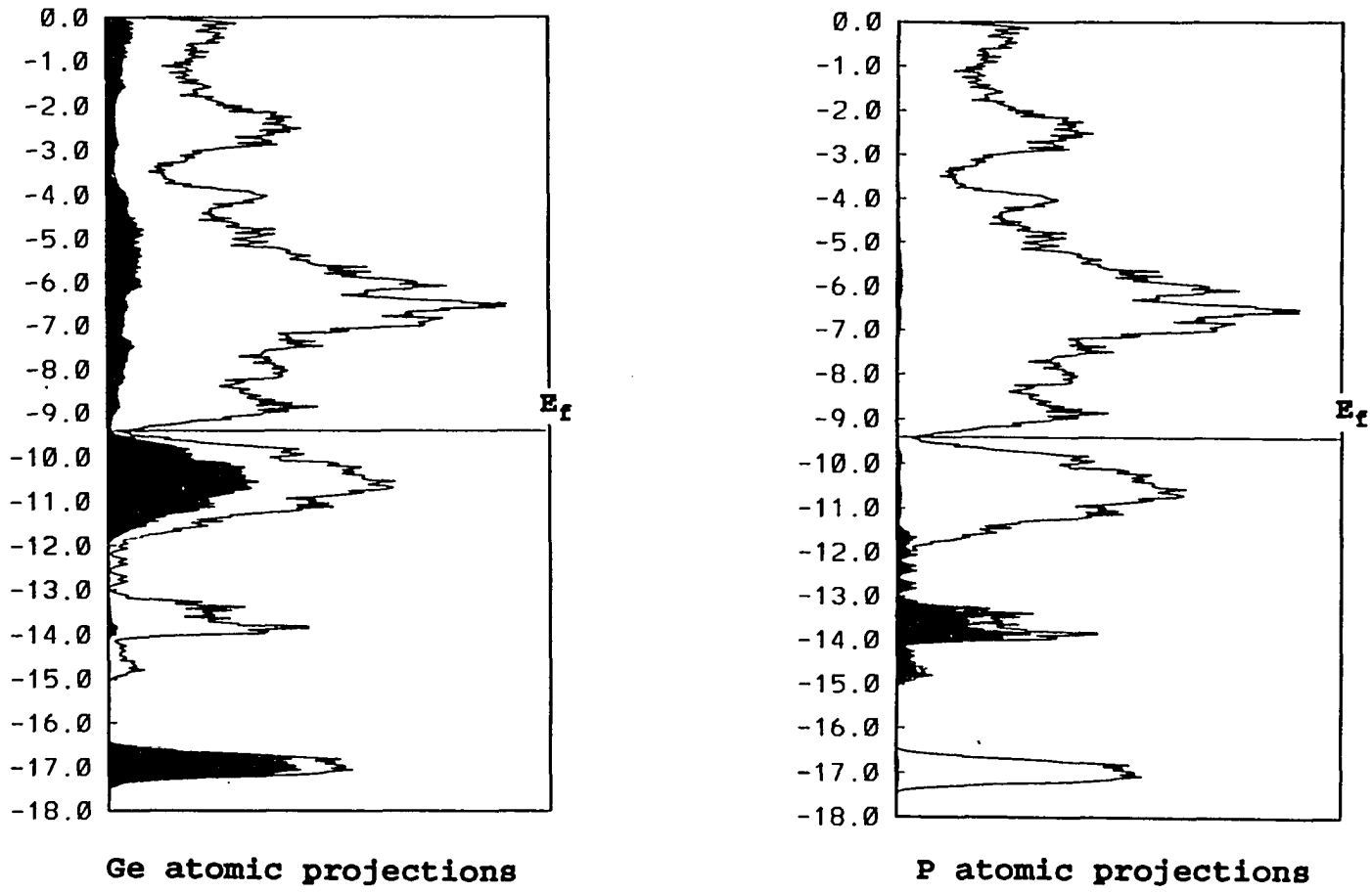

Figure 22. DOS curve for La_5Ge_3P. The shaded regions represent the atomic orbital projections as indicated by the labels. The Fermi energy E_f is indicated by a solid line

x-y plane, the La(2) d-bands with the corresponding components are slightly higher in energy than those with z-component. Thus the nature of the La(2) bands immediately above E_f have mainly z-components and are antibonding. This also provides a reason for the observed rise in c/a ratios found for most La_5Ge_3Z interstitial compounds.

An interesting question is how and why does an energy gap, which is absent in the host La_5Ge_3 band structure, form in La_5Ge_3P? We trace the interaction of phosphorus with the host bands and naturally find the large interaction of La(2) and P. Phosphorus only interacts, to a significant extent, with La(2). This perturbation leads to a bonding (stabilization) of the P bands and further antibonding destabilization of the La(2) bands. Thus the La(2) bands which make-up most of the La bands near E_f effectively rise in energy with respect to the other host-derived bands and an energy gap is formed. This small energy gap 0.08 eV agrees surprisingly well with the observed band gap (0.11 eV) obtained from the Q-method.

Electronic structure of La_5Ge_3Fe The DOS of the band structure of La_5Ge_3Fe is shown Figure 24. The total electron count of La_5Ge_3Fe results in a Fermi energy, E_f = -9.313 eV, that cuts across the Fe d-bands showing a high density of states at E_f. The Ge derived s-bands are located about -19.0 eV, while the Ge p-bands are broadened from -12.0 to ~-10.0 eV due to large mixing of the Ge and La orbitals. The Fe interstitial bands characterize the nature of the Fermi level. These together with the metal-derived bands form a broad structure that ranges from ~-10 eV to energies above E_f. The DOS atomic projections also show the some overlap between the s (~-9.5 to -8.0 eV) and d bands(~-10.0 to -9.0 eV) of Fe.

The orbital interactions in La_5Ge_3Fe can be appreciated by the use of the COOP plots as illustrated in Figure 25. The La-Ge interactions show their interactions are mainly bonding. Furthermore, the bonding states are nearly filled and maximized at E_f. Increasing or decreasing the electron counts, to a certain extent, do not significantly perturb the La-Ge interactions. The added or subtracted electrons involve mainly the interstitial d and s states.

The COOP of La-Fe interactions reveal strong bonding overlap attributed to mixing of the Fe sd-states with the La d-orbitals. However, the La-Fe interaction does not result in significant "splitting" the d-bands of iron into groups imposed by the symmetry of the Fe-La_6 geometry. This could be attributed to the contracted nature of Fe d-orbitals. Thus, the electrons residing at the Fe d-orbitals are practically localized on the d-bands and the delocalized electrons reside at the broadened Fe s-bands that extend below E_f. This feature could explain the ferromagnetic ordering observed in La_5Ge_3Fe. The long-ranged magnetic ordering is represented by the interaction between localized d-electrons of iron mediated by conduction electrons on the broad s-bands. Furthermore, the COOP plots reveal that interactions between interstitial Fe atoms are very weakly bonding (overlap population = 0.005) along the formal chain of interstitial atoms. Hence the Fe-Fe interaction is "through-space" and is consistent with ferromagnetic interactions. The calculated electron distribution of Fe is 8.12 e^-/Fe indicating a slight negative character in agreement with the measured XPS core-shifts.

The La-La interactions had similar features as those in the La_5Ge_3 host. Weak La(1)-La(1) interactions were also observed in the COOP curves. Similar to the effects of phosphorus interstitials, the overlap between the germanium- and lanthanum-based bands

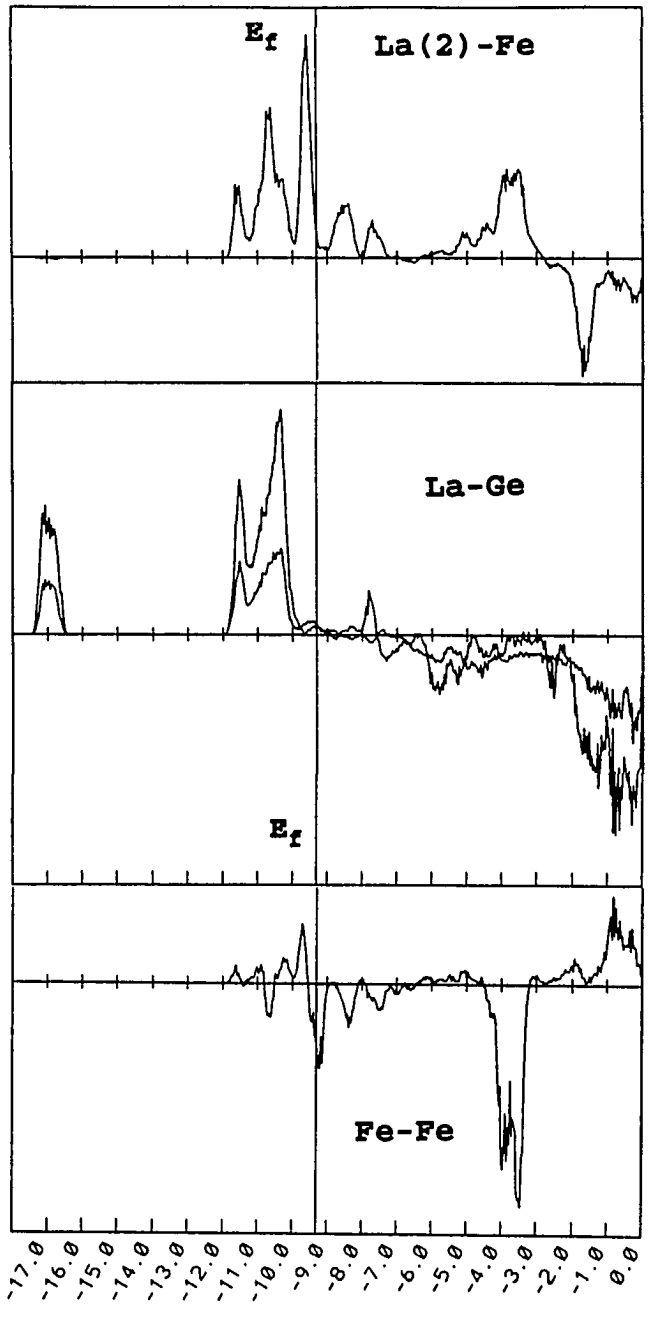

Figure 25. COOP curves for La_5Ge_3Fe. The positive values on the curves represent bonding interactions while negative values denote an antibonding character for atom pairs as indicated

Table 19. Summary of $La_{15}Ge_9Z$-type phases

composition	conditions [temp(°C)]	lattice parameters of Mn_5Si_3-type phase (A)	volume (A^3)	c/a ratio
$La_{15}Ge_9Mn$	S	a = 15.4964(3); c = 6.884(1)	1431.6(3)	0.4442
$La_{15}Ge_9Fe$	C	a = 15.4810(2); c = 6.8768(3)	1427.1(1)	0.4442
$La_{15}Ge_9Co$	S	a = 15.4950(2); c = 6.8686(4)	1428.2(1)	0.4433
$La_{15}Ge_9Ni$	S	a = 15.5001(2); c = 6.873(1)	1430.0(1)	0.4434
$La_{15}Ge_9Cu$	S	a = 15.5164(3); c = 6.9005(5)	1438.7(1)	0.4447
$La_{15}Ge_9Ru$	S	a = 15.5180(3); c = 6.9014(5)	1439.3(1)	0.4447
$La_{15}Ge_9C$	S	a = 15.4674(6); c = 6.8795(5)	1425.4(2)	0.4448
$La_{15}Ge_9O$	S	a = 15.535(1); c = 6.758(1)	1412.4(2)	0.4350
$La_{15}Ge_9P$	C	a = 15.4946(3); c = 6.8649(5)	1435.7(2)	0.4430
$La_{15}Ge_9$(ideal)		a = 15.486(1); c = 6.878(1)	1428.5(4)	0.4441

S: Sintering reactions of binaries and elements at 1250-1350°C over a total of 10-15 days

C: Prereacted binaries and elements slowly heated to 1200°C and annealed at 1000C over 10 days

Table 20. SEM chemical analyses of some $La_{15}Ge_9Z$ compounds

sample	La (at%)	Ge (at%) (by difference)	Z (at%)
$La_{15}Ge_9Mn$	59.8(2)	34.6(3)	5.6(3)
$La_{15}Ge_9Fe$	60.6(2)	35.0(3)	4.4(3)
$La_{15}Ge_9Co$	58.7(2)	35.4(3)	5.9(4)
$La_{15}Ge_9Ni$	60.2(2)	36.7(3)	3.1(3)
$La_{15}Ge_9Cu$	60.1(2)	36.1(2)	3.8(3)
ideal values	60.0	36.0	4.0

taken and mirror planes were observed perpendicular to the axes as well as a six-fold symmetry. To confirm the Laue symmetry, 6/mmm, precession photos at zero and higher levels, and axial photos were taken. Four-fold redundant data sets (h,k,l) and (-h,k,-l) were collected up to $2\theta_{max} = 55°$, and three ψ-scans were measured. The data preparation included an empirical absorption correction based on the ψ-scan measurements and Lorentz and polarization corrections. Other important parameters of the data collection and structure refinement are summarized in Table 21.

Inspection of the reflection data and precession photographs indicated reflection conditions corresponding to the possible space groups $P6_3/mmc$, P62c and $P6_3mc$. The last acentric space group proved to be correct during the structure refinement. Accurate cell parameters were later obtained by careful inspection and least squares fit of the experimental powder data with the calculated data of the refined structure solution, using NBS silicon as reference.

Starting parameters for the full-matrix least squares refinement were taken from direct methods (SHELXS-86) and included all the La and Ge positions. The interstitial atomic peaks were revealed by a difference Fourier map. Isotropic refinements resulted in $R = 5.5\%$, $R_w = 7.3\%$. Owing to the inadequacy of psi-scan based empirical absorption corrections, a numerical correction DIFABS was applied. This resulted in a final anisotropic refinement, $R = 2.6\%$; $R_w = 3.4\%$, with well behaved thermal parameters and reasonable esd's. Refinement of the La and Ge occupancies did not reveal any significant deviations from ideal values. However, the interstitial Fe showed an occupancy of only 92.7(1)%. Final difference Fourier calculations indicated the largest positive peak of $1.13e^-/A^3$ close to Fe at (0,0,0.625) and a negative peak of

Table 21. Data collection and refinement parameters for $La_{15}Ge_9Fe$

space group	$P6_3mc$
Z	2
crystal dimension	0.15 x 0.08 x 0.08 mm
diffractometer	Enraf-Nonius CAD4
2θ max	55°
collected indices	h, k, ±l
reflections:	
measured	2219
observed ($>3\sigma_I$)	2102
independent	688
R_{ave}	2.8% (observed data)
no. of parameters refined	48
R (refinement)	2.6%
R_w (refinement)	3.4%
largest parameter shift	0.01
absorption coefficient	436.9 (cm^{-1}, Mo Kα)
secondary extinction coeff.	$2.3(2) \times 10^{-8}$
largest residual peaks	1.13 e^-/A^3 at (0,0,0.625)
cell parameters (Guinier):	
a = 15.4810(2) A	
c = 6.8768(3) A	
volume = 1427.3(1) A^3	

Table 22. Refined parameters for $La_{15}Ge_9Fe$

atom	x	y	z	Occupancy	B_{equi}
La(1)	0.01768(5)	0.34207(5)	0	1	0.78(1)
La(2)	0.25333(4)	2x	0.2771(1)	1	0.70(2)
La(3)	0.08020(4)	2x	0.7245(1)	1	0.71(1)
La(4)	0.41368(4)	2x	0.7401(1)	1	0.71(2)
Ge(1)	0.19995(8)	2x	0.7115(2)	1	0.64(4)
Ge(2)	0.13280(8)	2x	0.2721(2)	1	0.78(4)
Ge(3)	0.46610(9)	2x	0.2613(2)	1	0.84(4)
Fe	1/3	2/3	0.5160(3)	1	1.89(4)

B values

Atom	B11	B22	B33	B12	B13	B23
La(1)	0.76(2)	1.19	0.83(2)	0.37(1)	-0.12(3)	-0.07(2)
La(2)	0.64(2)	0.67(3)	1.05(4)	1/2 B22	0.07(2)	B13
La(3)	0.52(2)	0.69(3)	0.98(4)	1/2 B22	0.03(2)	B13
La(4)	0.50(3)	0.65(3)	1.07(4)	1/2 B22	0.04(2)	B13
Ge(1)	0.44(4)	0.71(5)	0.86(5)	1/2 B22	0.16(3)	B13
Ge(2)	0.43(4)	0.64(5)	1.3(1)	1/2 B22	0.07(3)	B13
Ge(3)	0.52(4)	0.56(5)	1.5(1)	1/2 B22	0.03(3)	B13
Fe	1.85(4)	B11	1.90(7)	1/2 B22	0	0

Table 23. Important interatomic distances and angles in $La_{15}Ge_9Fe$

atom	atom	distance	atom	atom	distance
La(1)	La(1)	3.4709(2)(2x)	La(3)	La(3)	3.7247 (2x)
La(1)	La(2)	3.760(2)	La(3)	La(3)	4.0555(1) (4x)
La(1)	La(2)	4.009(1)	La(3)	Ge(1)	3.2122(1)
La(1)	Ge(1)	3.190(2)	La(3)	Ge(2)	3.123(1) (2x)
La(1)	Ge(1)	3.301(2)	La(4)	Ge(1)	3.089(1)
La(1)	Ge(2)	3.192(2)	La(4)	La(4)	3.7315 (2x)
La(1)	Ge(2)	3.291(2)	La(4)	Ge(1)	3.125(1) (2x)
La(1)	Ge(3)	3.267(2)	La(4)	Ge(3)	3.227(1)
La(1)	Ge(3)	3.217(2)	La(2)	La(2)	3.7156 (2x)
La(2)	La(4)	3.843(1) (2x)	La(2)	La(4)	3.840(1)
La(2)	La(4)	4.273(1) (2x)	La(2)	Ge(2)	3.2321(1)
La(2)	Ge(3)	3.1065(5)(2x)	La(2)	Fe	2.702(3) (3x)
La(4)	Fe	2.701(3) (3x)			

Distances are in Angstroms. Estimated standard deviations in the least significant figure are given in parentheses

Interatomic angles,

atom	atom	atom	angle(°)	atom	atom	atom	angle(°)
La(1)	La(1)	La(1)	164.30(3)	Ge(1)	La(1)	Ge(1)	157.83(5)
La(2)	Ge(1)	La(3)	117.2(1)	La(2)	Ge(1)	La(2)	134.20(1)
La(2)	Fe	La(4)	178.1(1)	La(2)	Fe	La(2)	86.87(7)
La(2)	Ge(1)	La(4)	73.21(3)				

Angles are in degrees. Estimated standard deviations in the least significant figure are given in parentheses

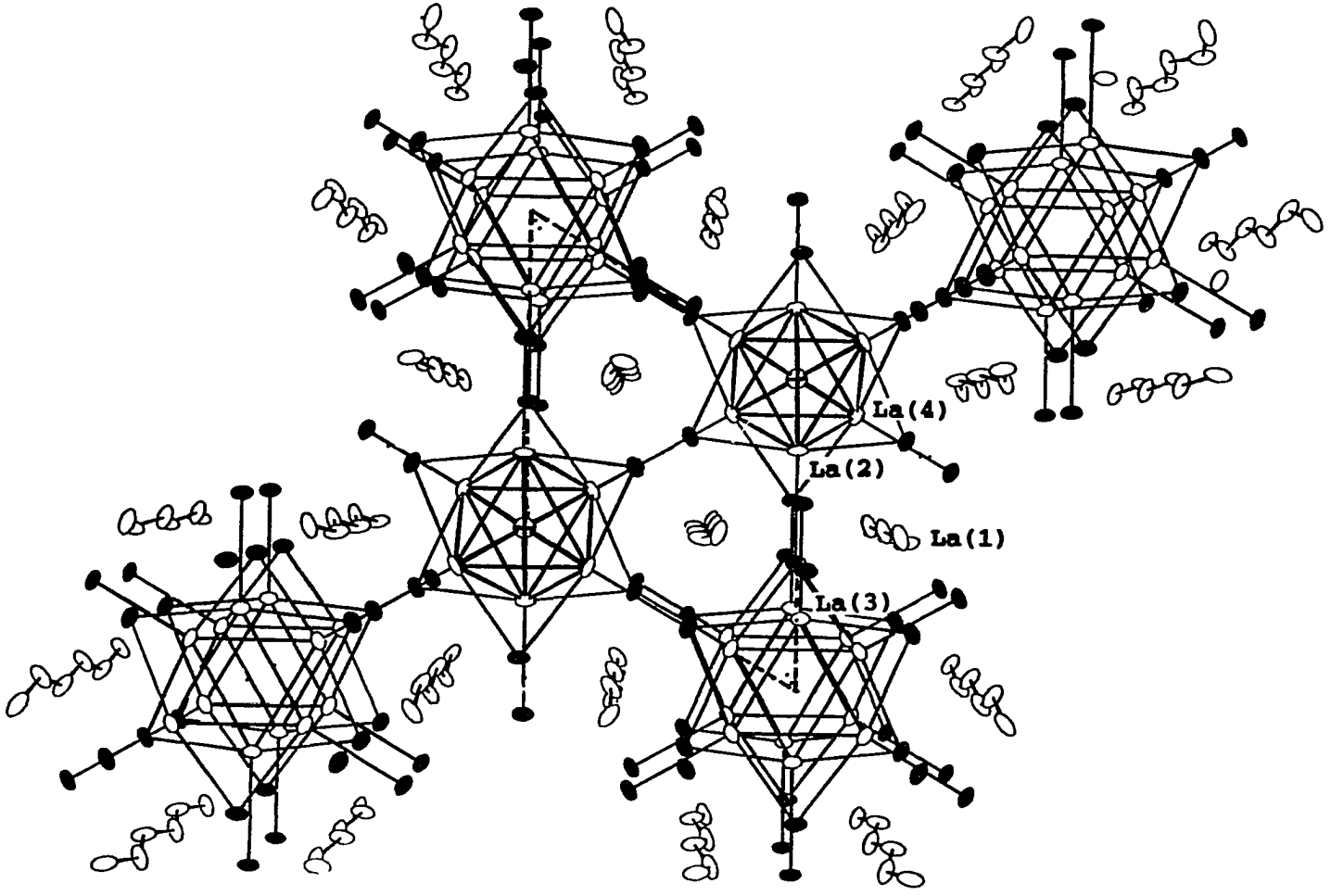

Figure 26. An ORTEP drawing along [001] of the unit cell of $La_{15}Ge_9Fe$. The dashed lines indicate the Mn_5Si_3-type subcell. Thermal ellipsoids are drawn at 90% probability. Open circles: La, shaded circles: Ge, crossed-hatched circles: Fe

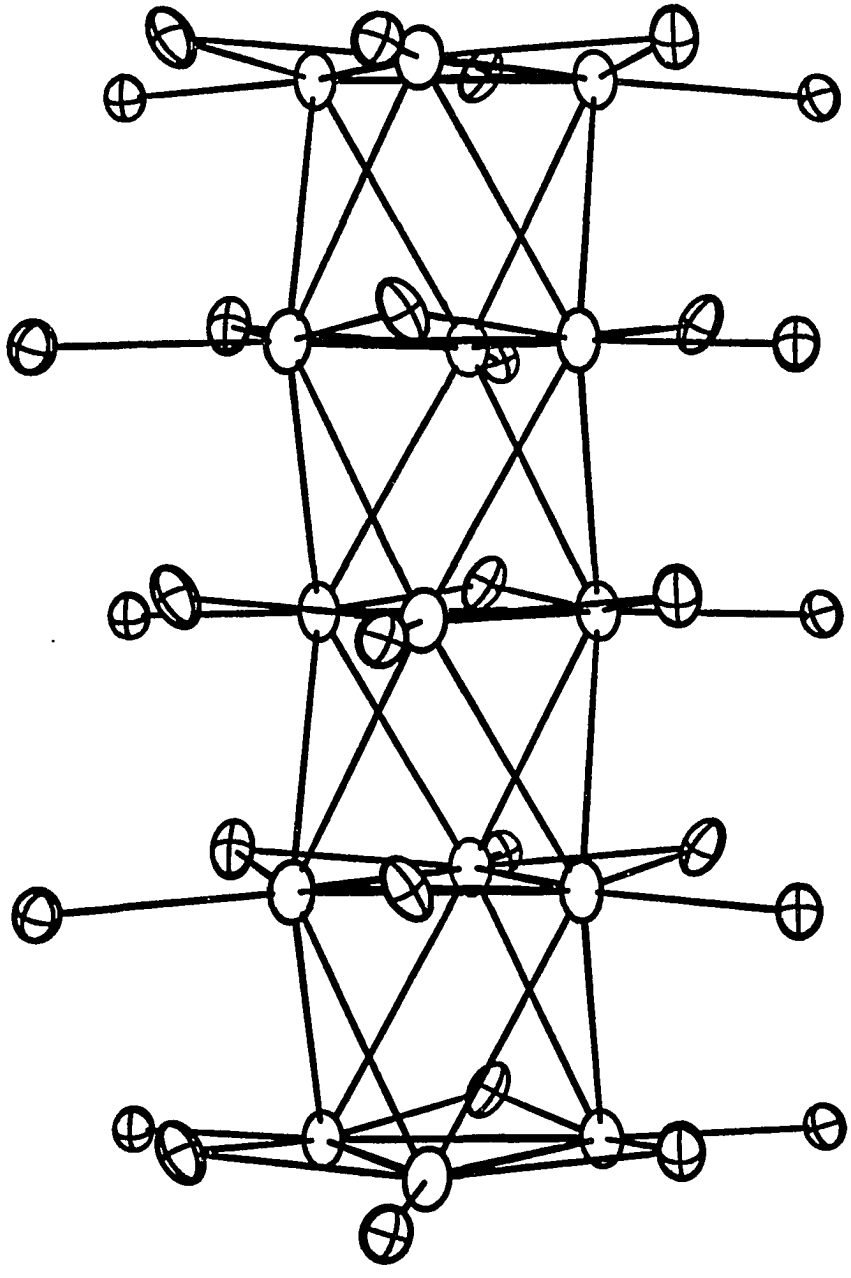

Figure 28. An ORTEP drawing along [110] of an empty trigonal antiprism column in $La_{15}Ge_9Fe$. Thermal ellipsoids are drawn at 90% probability. Open circles: La, crossed-hatched circles: Ge

The ordering of the interstitial Fe atoms induce interesting structural effects relative to the host La_5Ge_3 structure. The alternate occupation of the interstitial holes in the half-filled confacial trigonal antiprisms results a "clustering" of the La atoms around the interstitial Fe and short La-Fe distances (2.702(3)A), as compared to the sum of the Pauling single bond radii of La and Fe (2.86A). The "clustering" of La_6Fe units also results in an alternate short-long Peierls-like La-La distortion along the c-axis of the half-filled trigonal antiprism columns. Furthermore, the interstitial atoms in the two half-filled columns, along (1/3,2/3,z) and (2/3,1/3,z), are displaced with respect to each other by half the c-parameter. This means that the iron atoms in the two kinds of half-filled columns are not coplanar (see Figure 29).

The empty columns show a relative contraction along the chain axis of the trigonal antiprism units compared to its corresponding La_5Ge_3 unit as evidenced by the smaller c-parameter of $La_{15}Ge_9Fe$. However, the La(3) atoms are displaced outward from the center of a shared trigonal face relative to their ideal positions in the host structure. Hence, the empty columns in $La_{15}Ge_9Fe$ are topologically identical with the empty columns found in the host structure but with slightly larger La-La distances (3.725 and 4.056 A in $La_{15}Ge_9Fe$; 3.715 and 4.053A in La_5Ge_3). Moreover, the distances between the metal trigonal faces in the empty column are close to the average of the distances between the trigonal faces in the half-filled counterpart.

Other interesting features of the $La_{15}Ge_9Fe$ structure are the nominal La linear chains (La(1)) that run parallel with the columns. In the binary La_5Ge_3 structure, these chains are linear and uniformly surrounded by a "twisted-trigonal prism" arrangement of Ge atoms intermediate between that of a trigonal prism and an antiprism. In $La_{15}Ge_9Fe$,

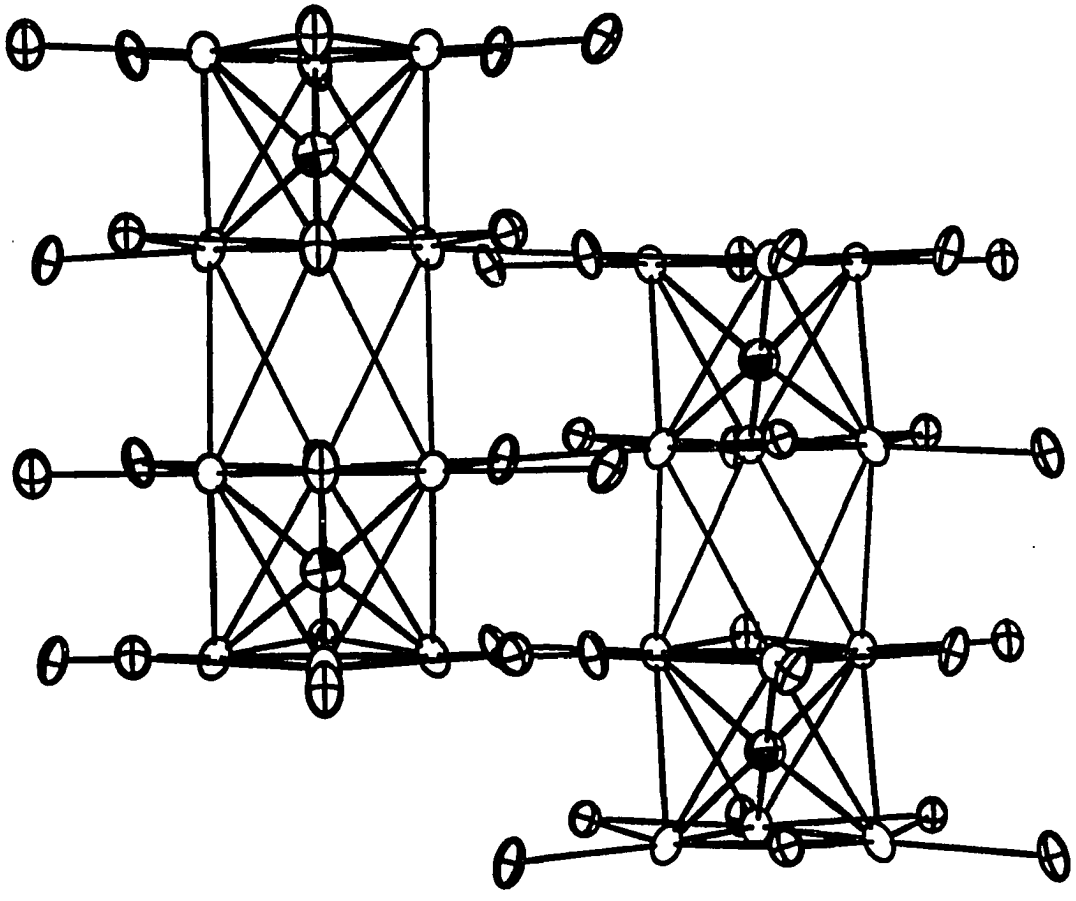

Figure 29. Orientation of two neighboring half-filled columns in $La_{15}Ge_9Fe$. The view is along [110]. Open circles: La, crossed-hatched circles: Ge, shaded circles: Fe

the uniformity is broken and the La linear chains are buckled from linearity to an angle of 164.30(3)° (see Figure 30). As will be observed in other isostructural compounds, the buckling angle depends on the type of interstitial atom. Despite the relative contraction of the c-parameter, the La(1)-La(1) distances in $La_{15}Ge_9Fe$ are longer (3.4709(2)A) than those observed in the empty La_5Ge_3 host (3.4392(4)A). This can be attributed to the buckling distortion on the La(1) chains where the La(1) atoms are effectively displaced within the a-b plane.

Even though the space group $P6_3mc$ allows for the displacement of germanium from being coplanar with the lanthanum trigonal planes, the observed germanium positions are close to the ideal values and are essentially coplanar with the corresponding La atoms (see Figure 31). The many distortions in the structure also result in different La-Ge distances many of which are shorter than those observed in La_5Ge_3. However, these observed distances are comparable to those found in other binary La-Ge compounds. The La-La distances show a contrasting behavior and are generally larger than those found in the La_5Ge_3 host. These observations suggest stronger La-Ge bonding and weaker La-La interactions in $La_{15}Ge_9Fe$ relative to the corresponding interactions in the host. This hypothesis agrees with the effects predicted from the idea that the excess electrons in La_5Ge_3 are soaked-up by the interstitial atoms. Based on the simple scheme, the "excess" electrons reside in electronic states that are slightly antibonding with respect to La-Ge interactions but slightly bonding with respect to La-La interactions. Hence, transfer of these electrons into interstitial-derived states results in the observed trends.

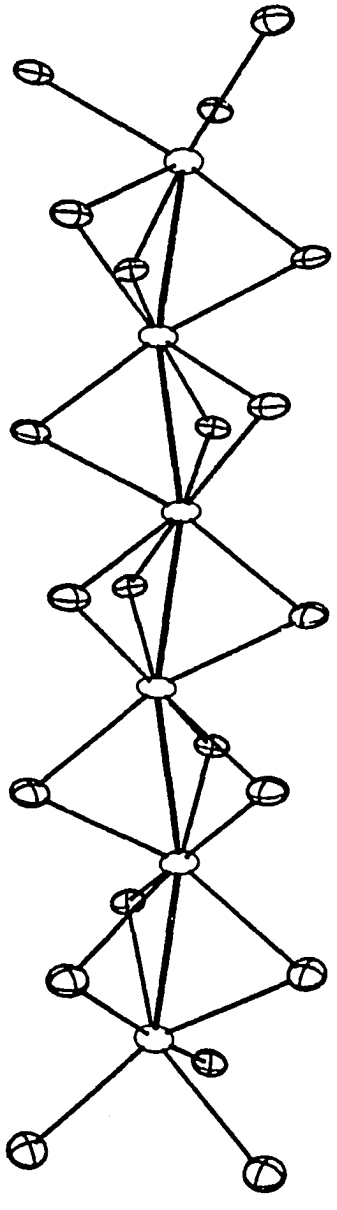

Figure 30. An ORTEP drawing along [110] of the nominal La(1) buckled chains in $La_{15}Ge_9Fe$. Open circles: La, crossed-hatched circles: Ge

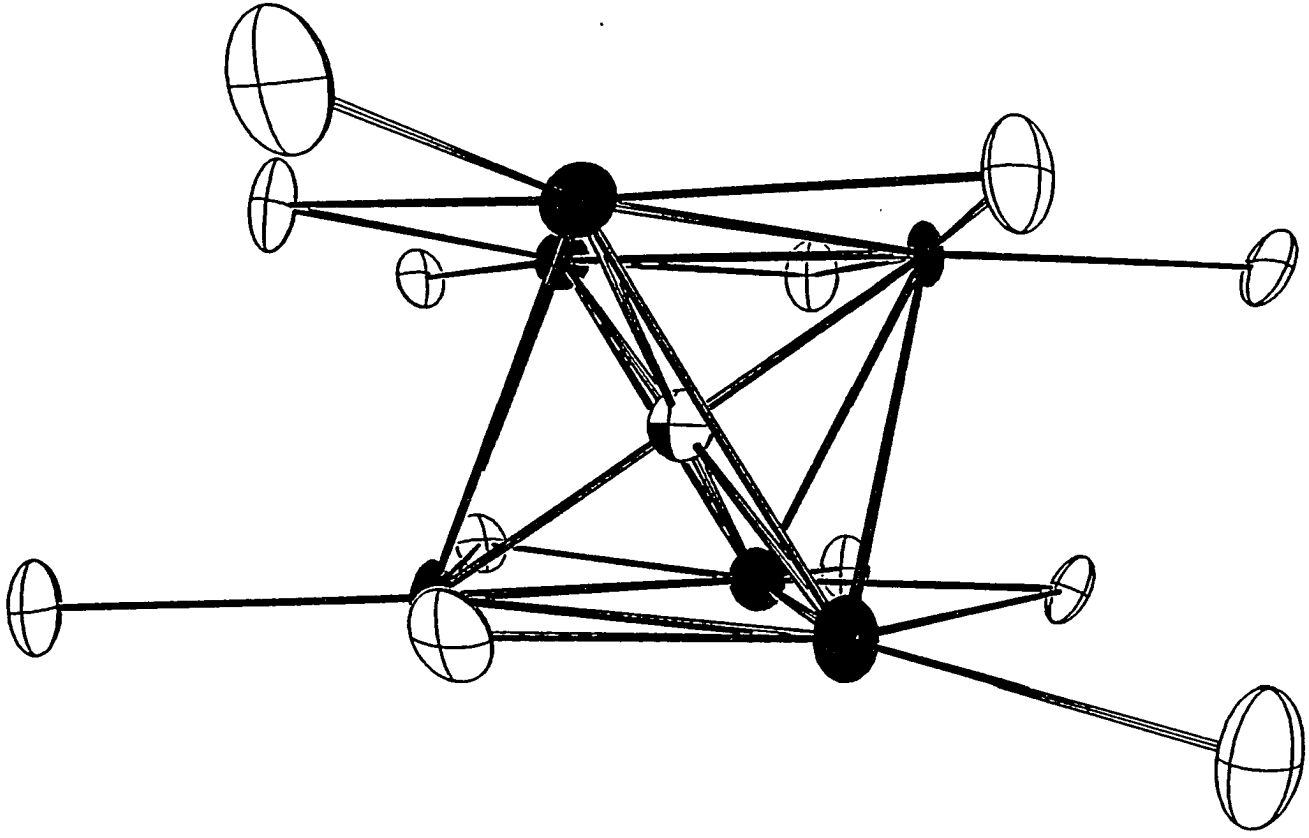

Figure 31. An ORTEP drawing of an La_6FeGe_{12} "cluster". Note the nearly in-plane arrangement of the Ge atoms with the La atoms along the a-b plane. Shaded atoms: La, crossed hatched atoms: Ge, octant-shaded atom: Fe

Inspection of the La-Fe distances imply strong La-Fe bonding, although La-Fe binary phase diagram reports indicate the absence of any La-Fe binary compound.[255,256] The La-Fe distance of 2.70A is comparable to an extrapolated value based on Y-Fe and Sc-Co distances in transition metal centered rare-earth-metal iodide clusters.[257] As in La_5Ge_3Z transition metal interstitial compounds, the short interstitial-La distances can be attributed to the partial charge transfer from La to Fe thereby contracting the effective intermetallic distance.

$La_{15}Ge_9Co$

The compound was synthesized in the same manner as $La_{15}Ge_9Fe$. Its preparation required high temperatures, >1200°C, in Ta containers. This was done with the aid of the high temperature furnace equipped with programmable ramp and soak capabilities. However, best results were obtained when a cobalt germanide $CoGe_2$ was reacted with La and Ge at 1000°C for seven days then slow cooled to room temperature. Crystals obtained from this reaction as well as from high-temperature reactions of the elements proved to be single based on preliminary oscillation photos.

Structure determination A hexagonal block-like single crystal of $La_{15}Ge_9Co$, from a stoichiometric reaction was selected after preliminary oscillation photographs. A redundant set of data was collected using an Enraf-Nonius CAD4 diffractometer after the cell was indexed from 25 reflections selected by SEARCH. Axial photos taken along the three axes revealed the same Laue symmetry, P6/mmm, as in $La_{15}Ge_9Fe$. Following the usual data preparation with SDP software, the structure refinement proceeded in the same manner as in $La_{15}Ge_9Fe$ resulting in final residuals of $R = 1.8\%$; $R_w = 3.2\%$. Absorption corrections included empirical corrections based on

four ψ-scans, and the application of DIFABS before anisotropic refinement. The crystal structure solution included well behaved atomic and thermal parameters and satisfactory esd's. Inspection of the final difference Fourier map indicated a residual peak of 0.86 e^-/A^3 close to the lanthanum atoms (La(1)) forming the linear chain. The atomic parameters, and important bond distances and angles are summarized in Tables 24-26.

Structure description Results of the x-ray analyses revealed that the $La_{15}Ge_9Co$ was isostructural with $La_{15}Ge_9Fe$ and possessed the same novel structural features. These features were derived from the novel ordering of the Co interstitial atoms in the host La_5Ge_3 structure. The interesting features included the contraction of the trigonal La faces toward the interstitial atom resulting in a Peierls-like distortion of two-thirds of the La antiprism columns, as well as the buckling of the nominal La(1) linear chains. The differences between the iron and cobalt analogs arise in the degree of the distortions induced on the La_5Ge_3 host. Comparing the buckling angle and the difference in the interplanar distances between shared faces of the trigonal antiprisms reveal the cobalt analog presents a more distorted structure. However, the same general effects observed in $La_{15}Ge_9Fe$ are also present in $La_{15}Ge_9Co$. These involve the shortening of the average La-Ge distances and lengthening of average La-La distances compared to those observed in the empty host. Similarly, the observed La-Co distances (2.665(2)A) are shorter than the sum of the Pauling single bond radii of La and Co (2.75A). The overall effect of these distortions may be related to electronic reasons. Hence, comparing the structures of the different isostructural compounds was necessary.

Table 24. Data collection and refinement parameters for $La_{15}Ge_9Co$

space group	$P6_3mc$
Z	2
crystal dimension	0.10 x 0.05 x 0.05 mm
diffractometer	Enraf-Nonius CAD4
2θ max	55°
collected indices	±h, k, l
reflections:	
measured	2398
observed (>$3\sigma_I$)	2040
independent	688
R_{ave}	3.1% (observed data)
no. of parameters refined	48
R (refinement)	1.8%
R_w (refinement)	3.2%
largest parameter shift	0.01
absorption coefficient	439.4 (cm^{-1}, Mo Kα)
secondary extinction coeff.	$3.1(2) \times 10^{-8}$
largest residual peaks	0.86 e^-/A^3
cell parameters (Guinier):	
a = 15.4950(2) A	
c = 6.8686(4) A	
volume = 1428.2(1)A^3	

Table 25. Refined parameters for $La_{15}Ge_9Co$

atom	x	y	z	Occupancy
La(1)	0.34209(7)	0.01771(6)	0	1.0
La(2)	0.41282(6)	-x	0.7583(1)	1.0
La(3)	0.25413(6)	-x	0.2179(1)	1.0
La(4)	0.07895(6)	-x	0.7709(1)	1.0
Ge(1)	0.1331(1)	-x	0.2248(1)	1.0
Ge(2)	0.4664(1)	-x	0.2361(1)	1.0
Ge(3)	0.1992(1)	-x	0.7853(1)	1.0
Co	1/3	2/3	-0.0162(2)	1.0

B values

Atom	B11	B22	B33	B12	B13	B23
La(1)	1.43(2)	1.09(2)	0.58(2)	0.52(2)	0.00(2)	-0.04(4)
La(2)	0.83(2)	B11	1.26(3)	0.33(2)	-0.02(1)	-B13
La(3)	0.87(2)	B11	0.97(3)	0.43(2)	0.03(1)	-B13
La(4)	0.80(2)	B11	1.76(3)	0.30(2)	-0.05(1)	-B13
Ge(1)	0.85(4)	B11	1.17(5)	0.42(4)	-0.10(4)	-B13
Ge(2)	0.89(4)	B11	1.54(5)	0.39(4)	-0.04(4)	-B13
Ge(3)	0.85(4)	B11	1.90(5)	0.38(4)	-0.11(4)	-B13
Co	2.20(5)	B11	2.4(1)	1/2 B11	0	0

Table 26. Important interatomic distances and angles in $La_{15}Ge_9Co$

atom	atom	distance	atom	atom	distance
La(1)	La(1)	3.4709(2)(2x)	La(4)	La(4)	3.670(1) (2x)
La(1)	La(2)	3.774(1)	La(4)	La(4)	4.0353(6) (4x)
La(1)	La(2)	4.009(1)	La(4)	Ge(1)	3.229(1)
La(1)	Ge(1)	3.281(2)	La(4)	Ge(2)	3.128(1) (2x)
La(1)	Ge(1)	3.202(2)	La(3)	Ge(1)	3.248(1)
La(1)	Ge(2)	3.257(2)	La(3)	La(3)	3.682(1) (2x)
La(1)	Ge(2)	3.226(2)	La(3)	Ge(1)	3.114(1) (2x)
La(1)	Ge(3)	3.306(1)	La(3)	Ge(3)	3.317(1)
La(1)	Ge(3)	3.171(2)	La(2)	La(2)	3.695(1) (2x)
La(2)	La(3)	3.808(1) (2x)	La(2)	Ge(2)	3.583(1)
La(2)	La(3)	4.279(1) (2x)	La(2)	Ge(2)	3.245(1)
La(2)	Ge(3)	3.1408(5)(2x)	La(2)	Co	2.664(2) (3x)
La(3)	Co	2.665(2) (3x)			

Distances are in Angstroms. Estimated standard deviations in the least significant figure are given in parentheses

Interatomic angles,

atom	atom	atom	angle(°)	atom	atom	atom	angle(°)
La(1)	La(1)	La(1)	164.24(1)	Ge(3)	La(1)	Ge(3)	157.60(6)
La(3)	Ge(3)	La(4)	118.14(5)	La(3)	Ge(3)	La(3)	132.89(7)
La(2)	Co	La(4)	178.9(1)	La(2)	Co	La(2)	88.9(1)
La(2)	Ge(3)	La(4)	72.21(4)				

Angles are in degrees. Estimated standard deviations in the least significant figure are given in parentheses

$La_{15}Ge_9Ni$ and $La_{15}Ge_9Mn$

Structure determination The Ni and Mn compounds were also synthesized from the usual high-temperature reactions (T>1250°C) of the elements in tantalum containers. Reactions of La, Ge and lower melting germanides (NiGe and Mn_3Ge_2) at 1000°C were also successful in producing the desired products. Aside from the lower temperature requirements, reactions involving binaries as starting materials also provided a better stoichiometric control in the syntheses of the interstitial compounds. However, single crystals were more easily obtained from high temperature reactions of the elements at temperatures greater than 1250°C.

Single crystals isolated from these reactions were analyzed using the Rigaku AFC6R diffractometer supported by the Texsan crystallographic software after preliminary oscillation photos. Collection of x-ray data proceeded after the cell parameters were indexed from 25 reflections obtained by program SEARCH. The indexed cell corresponded with those obtained from a careful inspection of their Guinier powder diffraction patterns that were indexed with the $La_{15}Ge_9Fe$ refined crystal structure with the aid of GUIN and POWD programs. The structural refinement of the above compounds proceeded smoothly. As the structure type was known, the structure determination process was trivial. Nevertheless, precautions were taken to ensure the correct selection of the space group since symmetry changes from distortions are possible. Anisotropic refinement after application of DIFABS resulted in residuals of R = 2.8%; R_w = 2.8% for $La_{15}Ge_9Mn$ and R = 2.5%; R_w = 2.2%, for $La_{15}Ge_9Ni$. A summary of the crystal structure solutions are presented in Table 27. Refined parameters, important interatomic distances and angles in $La_{15}Ge_9Mn$ and $La_{15}Ge_9Ni$ are listed in

Table 28. Refined parameters for $La_{15}Ge_9Mn$

atom	x	y	z	Occupancy
La(1)	0.341657(7)	0.016592(6)	0	1.0
La(2)	0.412307(6)	2x	0.26117(1)	1.0
La(3)	0.254768(6)	2x	0.72473(1)	1.0
La(4)	0.078590(6)	2x	0.27357(1)	1.0
Ge(1)	0.13351(1)	2x	0.73222(3)	1.0
Ge(2)	0.46685(1)	2x	0.74373(3)	1.0
Ge(3)	0.19964(1)	2x	0.28835(3)	1.0
Mn	1/3	2/3	0.48144(3)	1.0

U values

Atom	U11	U22	U33	U12	U13	U23
La(1)	0.01351(2)	0.01680(2)	0.00603(2)	0.007(2)	0.006(2)	0.003(4)
La(2)	0.00972(2)	0.01014(2)	0.01587(3)	1/2 U22	0.002(1)	2U13
La(3)	0.00910(2)	0.01013(2)	0.01394(3)	1/2 U22	-0.001(1)	2U13
La(4)	0.00943(2)	0.01124(2)	0.01990(3)	1/2 U22	0.001(1)	2U13
Ge(1)	0.01072(4)	0.01249(4)	0.01891(5)	1/2 U22	-0.003(2)	2U13
Ge(2)	0.00964(4)	0.00864(4)	0.02037(6)	1/2 U22	-0.003(2)	2U13
Ge(3)	0.00989(4)	0.01104(4)	0.01309(5)	1/2 U22	0.0004(5)	2U13
Mn	0.03727(5)	U11	0.03788(1)	1/2 U11	0	0

Table 29. Important interatomic distances and angles in $La_{15}Ge_9Mn$

atom	atom	distance	atom	atom	distance
La(1)	La(1)	3.4707(5)(2x)	La(4)	La(4)	3.6536(1)(2x)
La(1)	La(2)	3.800(1)	La(4)	La(4)	4.0369(4)(4x)
La(1)	La(2)	4.001(1)	La(4)	Ge(1)	3.484(1)
La(1)	Ge(1)	3.180(2)	La(4)	Ge(3)	3.2506(2)(2x)
La(1)	Ge(1)	3.297(2)	La(4)	Ge(1)	3.133(1) (2x)
La(1)	Ge(2)	3.274(2)	La(3)	Ge(1)	3.2551(1)
La(1)	Ge(2)	3.198(2)	La(3)	La(3)	3.6524(1)(2x)
La(1)	Ge(3)	3.202(1)	La(3)	Ge(2)	3.122(1) (2x)
La(1)	Ge(3)	3.289(2)	La(3)	Ge(3)	3.349(1)
La(2)	La(2)	3.6714(1)(2x)	La(2)	La(3)	3.828(1) (2x)
La(2)	La(3)	4.255(1) (2x)	La(2)	Ge(2)	3.2458(2)
La(2)	Ge(3)	3.130(1) (2x)	La(2)	Mn	2.692(2) (3x)
La(3)	Mn	2.694(2) (3x)			

Distances are in Angstroms. Estimated standard deviations in the least significant figure are given in parentheses

Interatomic angles,

atom	atom	atom	angle(°)	atom	atom	atom	angle(°)
La(1)	La(1)	La(1)	165.26(1)	Ge(3)	La(1)	Ge(3)	157.71(6)
La(3)	Ge(3)	La(4)	118.07(5)	La(3)	Ge(3)	La(3)	132.90(7)
La(2)	Mn	La(3)	177.1(1)	La(2)	Mn	La(2)	89.5(1)
La(2)	Ge(3)	La(3)	72.34(4)				

Angles are in degrees. Estimated standard deviations in the least significant figure are given in parentheses

Table 30. Refined parameters for $La_{15}Ge_9Ni$

atom	x	y	z	Occupancy
La(1)	0.01773(4)	0.34220(5)	0	1.0
La(2)	0.41335(5)	2x	0.26077(7)	1.0
La(3)	0.25372(6)	2x	0.72270(7)	1.0
La(4)	0.08015(6)	2x	0.27551(8)	1.0
Ge(1)	0.1334(1)	2x	0.7284(1)	1.0
Ge(2)	0.4666(1)	2x	0.7400(1)	1.0
Ge(3)	0.2004(1)	2x	0.2890(1)	1.0
Ni	2/3	1/3	-0.0149(1)	1.0

B values

Atom	U11	U22	U33	U12	U13	U23
La(1)	0.01305(2)	0.01655(2)	0.00667(3)	0.00579(2)	0.0035(1)	0.0019(1)
La(2)	0.00962(4)	0.01166(4)	0.01672(6)	1/2 U22	-0.00010(6)	2U13
La(3)	0.00836(5)	0.01021(6)	0.01402(8)	1/2 U22	-0.0005(1)	2U13
La(4)	0.00992(5)	0.01181(6)	0.01883(8)	1/2 U22	-0.0008(1)	2U13
Ge(1)	0.01079(9)	0.0114(1)	0.0208(1)	1/2 U22	-0.0033(1)	2U13
Ge(2)	0.00821(9)	0.0068(1)	0.0133(1)	1/2 U22	-0.0025(1)	2U13
Ge(3)	0.01009(9)	0.0133(1)	0.0119(1)	1/2 U22	-0.0010(1)	2U13
Ni	0.03015(9)	U11	0.0510(1)	1/2 U11	0	0

Tables 28-29 and 30-31, respectively.

Structure description The structure investigations on $La_{15}Ge_9Mn$ and $La_{15}Ge_9Ni$ reveal that both compounds are isostructural with $La_{15}Ge_9Fe$. The use of the Rigaku AFC6R diffractometer generally resulted in better esd's of the refined parameters compared to the results using CAD4. This can be attributed to the higher intensities of the x-rays in the latter.

Being isostructural with $La_{15}Ge_9Fe$, both structures were characterized by the distortions associated with the ordering of the Mn and Ni atoms in the La_5Ge_3 host. These include the Peierls'-like distortions of two-thirds of the confacial antiprism chains as well as the buckled linear chains of La(1). The differences between the different $La_{15}Ge_9Z$ compounds are subtle and lie mainly in the degree of the distortions on the host structure.

$La_{15}Ge_9Z$ (Z = Cu and Ru)

Like the previously desdribed $La_{15}Ge_9Z$ analogs, $La_{15}Ge_9Cu$ and $La_{15}Ge_9Ru$ were also synthesized from high temperature (>1250°C) reactions of the elements inside welded Ta containers. The copper analog was also made from the reaction of binary $LaCu_2$ with La and Ge at 1000°C. The ruthenium compounds was made by the reaction of the elements at 1350°C. However, the Cu and Ru compounds were identified only from careful inspection of their powder diffraction patterns that clearly showed the $\sqrt{3}$ x $\sqrt{3}$ superstructure lines. The calculated powder patterns of a Mn_5Si_3-type and the $La_{15}Ge_9Fe$-type structures are illustrated in Figure 32. The patterns show the three weak reflections associated with the $\sqrt{3}$ x $\sqrt{3}$ superstructure that were used to verify the

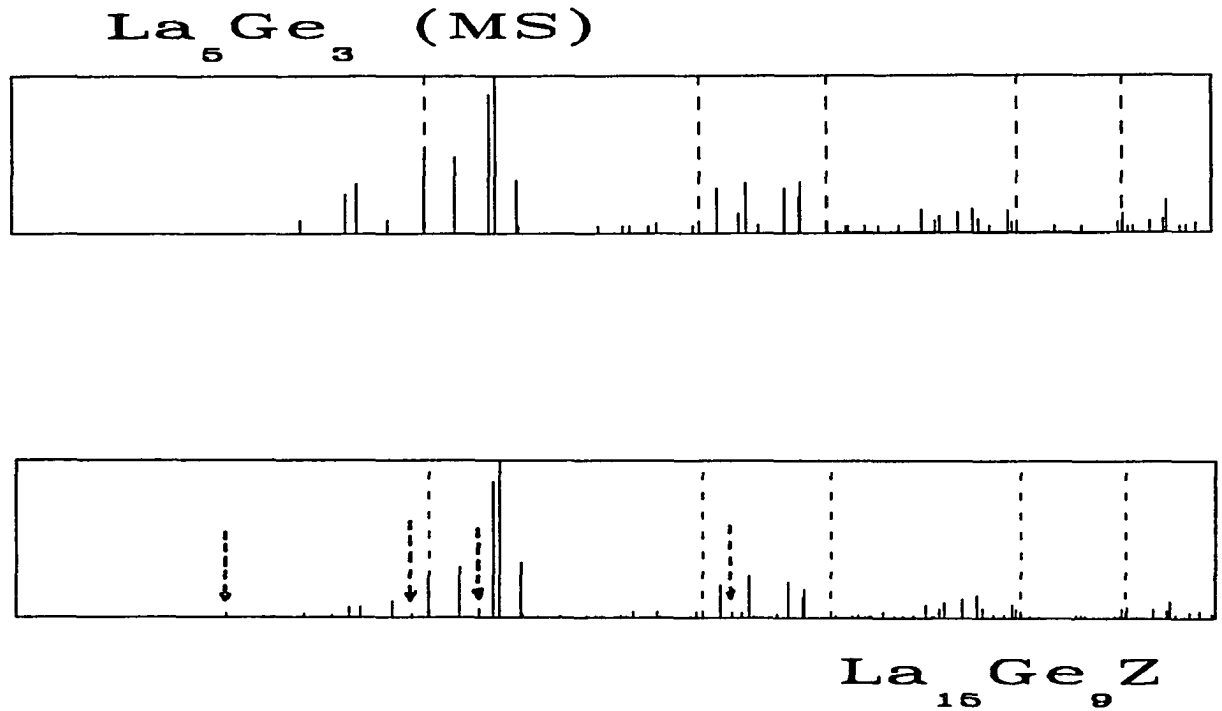

Figure 32. Calculated powder diffraction patterns of a) La_5Ge_3 having the Mn_5Si_3-type structure, and b) $La_{15}Ge_9Fe$-type structure with idealized lattice parameters. Arrows mark the "signature" reflections of the $La_{15}Ge_9Fe$-type cell

$La_{15}Ge_9Z$ structure. The observed cell parameters of $La_{15}Ge_9Cu$ and $La_{15}Ge_9Ru$ were larger than those observed in the previously described analogs of $La_{15}Ge_9Z$.

Attempts to synthesize other transition metal analogs of $La_{15}Ge_9Z$ with Cr, V, and Ti were unsuccessful. In reactions involving chromium the $\sqrt{3}$ x $\sqrt{3}$ lines were absent in the powder diffraction patterns of the product. A Mn_5Si_3-type phase with larger lattice parameters than the empty host La_5Ge_3 was observed. However, the observed lattice parameters of the products were less than those of La_5Ge_3Cr. This suggests that La_5Ge_3Cr, with the filled-Mn_5Si_3 structure, exhibits a homogeneity range. It is also possible, but less likely, that some substitution of Cr for Ge may have occurred. The limits of the homogeneity range of La_5Ge_3Cr were not determined. The absence of a $\sqrt{3}$ x $\sqrt{3}$ cell but the presence of a Mn_5Si_3-type $La_5Ge_3Cr_x$ phase suggests that subtle effects in electronic and geometric requirements may govern the relative stability of $La_{15}Ge_9Z$ with respect to Mn_5Si_3-type phases.

In the V and Ti reactions, the powder patterns of the products revealed only Mn_5Si_3-type phases. Their refined cell parameters did not show any appreciable difference from the cell parameters of La_5Ge_3. This indicated negative results identical with attempts to synthesize their fully-filled analogs. Furthermore, SEM analysis of the tantalum containers found titanium incorporated in the container walls.

$La_{15}Ge_9Z$ (Z = Main group elements)

Attempts to rationalize the cell parameter variations previously reported in the oxide and carbide La_5Ge_3Z compounds led us to investigate the $La_{15}Ge_9Z$ analogs found in the oxygen and carbon systems. Similarly, equilibration experiments on La_5Ge_3P led us to discover the phosphorus analog $La_{15}Ge_9P$.

Structure determination Single crystals of $La_{15}Ge_9C$ and $La_{15}Ge_9P$ obtained from high-temperature reactions were investigated using the Rigaku-AFC6R diffractometer and Texsan crystallographic software. The crystals were chosen after preliminary oscillation photos and visual inspections. Redundant data sets were collected to $2\theta_{max} = 70°$(carbon) and 65°(phosphorus) after the cells were indexed from 25 reflections by the programs SEARCH and INDEX. After the usual data preparation, refinement began by using the $La_{15}Ge_9Fe$ model minus the interstitial. The interstitial atoms were located by subsequent difference Fourier calculations. Further least-squares refinement of the single crystal data proceeded without any unusual difficulty. Following isotropic refinement and DIFABS corrections, anisotropic refinements led to final residuals of R = 2.4%;R_w = 3.2% for $La_{15}Ge_9C$, and R = 2.6%; R_w = 3.4% for $La_{15}Ge_9P$. The structure solutions were marked by well-behaved thermal parameters and sufficiently low esd's. The final difference Fourier resulted in insignificant residual peaks with electron densities close to 1.5 e^-/A^3, close (<1.3 A) to La(1) atoms that make up the linear chains. The accurate cell parameters were later obtained by careful inspection of the experimental Guinier powder diffraction patterns and indexing them to the calculated powder patterns of their refined structures. A summary of the single crystal x-ray studies on $La_{15}Ge_9C$ and $La_{15}Ge_9P$ are presented in Table 31. Refined parameters, important interatomic distances and angles are listed in Tables 32-35.

Structure description The structures of $La_{15}Ge_9C$ and $La_{15}Ge_9P$ are isotypic with $La_{15}Ge_9Fe$. The same structural features such as the Peierls-like distortion of the antiprism columns, the buckled La "linear" chains and the ordered interstitial atoms were observed. The degree of distortions observed in the carbide were close to those observed

Table 31. Data collection and refinement parameters for $La_{15}Ge_9Z$

compound	$La_{15}Ge_9C$	$La_{15}Ge_9P$
space group	$P6_3mc$	$P6_3mc$
Z	2	2
crystal dimension(mm)	0.12 x 0.06 x 0.06	0.10 x 0.05 x 0.05
diffractometer	Rigaku-AFC6R	Rigaku-AFC6R
2θ max	70°	65°
collected indices	h, ±k, l	h, ±k, l
reflections:		
measured	6918	5029
observed ($>3\sigma_I$)	4387	3171
independent	933	736
R_{ave} (all data)	9.2%	8.2%
no. of parameters refined	48	50
R (refinement)	2.4%	2.6%
R_w (refinement)	3.2%	3.4%
largest shift/err	0.01	0.01
absorption coefficient	312.3 (cm^{-1}, Mo Kα)	313.4 (cm^{-1}, Mo Kα)
secondary extinction coeff.	$9.4(3) \times 10^{-8}$	$4.6(3) \times 10^{-8}$
largest residual peaks	1.16 e^-/A^3	1.62 e^-/A^3
cell parameters (Guinier):		
a	15.4674(4) A	15.4946(3)A
c	6.8795(5) A	6.8649(5)
volume	1431.6(3)A^3	1435.7(3)

Table 32. Refined parameters for $La_{15}Ge_9C$

atom	x	y	z	Occupancy
La(1)	0.01760(3)	0.34197(3)	0	1.0
La(2)	0.41357(3)	-x	0.74102(4)	1.0
La(3)	0.25338(3)	-x	0.27905(4)	1.0
La(4)	0.07996(3)	-x	0.72599(4)	1.0
Ge(1)	0.13302(5)	-x	0.27201(6)	1.0
Ge(2)	0.46616(5)	-x	0.26139(6)	1.0
Ge(3)	0.19987(5)	-x	0.71169(6)	1.0
C	1/3	2/3	0.51449(8)	1.0

U values

Atom	U11	U22	U33	U12	U13	U23
La(1)	0.01429(4)	0.01847(4)	0.00825(6)	0.0067(2)	-0.0005(4)	-0.0003(2)
La(2)	0.01040(4)	U11	0.01787(6)	0.0042(2)	0.0009(2)	-U13
La(3)	0.00961(5)	U11	0.01547(7)	0.0036(3)	0.0000(2)	-U13
La(4)	0.01133(5)	U11	0.01857(7)	0.0044(3)	0.0009(2)	-U13
Ge(1)	0.01115(5)	U11	0.02000(8)	0.0051(4)	0.0008(4)	-U13
Ge(2)	0.01042(5)	U11	0.02461(8)	0.0041(4)	0.0006(4)	-U13
Ge(3)	0.01045(5)	U11	0.01289(8)	0.003694)	0.0020(4)	-U13
C	B = 1.234					

Table 33. Important interatomic distances and angles in $La_{15}Ge_9C$

atom	atom	distance	atom	atom	distance
La(1)	La(1)	3.4719(1) (2x)	La(4)	La(4)	3.7104(9) (2x)
La(1)	La(2)	3.763(1)	La(4)	La(4)	4.0523(3) (4x)
La(1)	La(2)	3.990(1)	La(4)	Ge(1)	3.432(1)
La(1)	Ge(1)	3.188(2)	La(4)	Ge(3)	3.214(1) (2x)
La(1)	Ge(1)	3.287(2)	La(4)	Ge(1)	3.1233(8) (2x)
La(1)	Ge(2)	3.265(2)	La(3)	Ge(1)	3.225(1)
La(1)	Ge(2)	3.216(2)	La(3)	La(3)	3.710(1) (2x)
La(1)	Ge(3)	3.188(2)	La(3)	Ge(2)	3.105(1) (2x)
La(1)	Ge(3)	3.300(2)	La(3)	Ge(3)	3.303(2)
La(2)	La(2)	3.7233(9) (2x)	La(2)	La(3)	3.835(1) (2x)
La(2)	La(3)	4.278(1) (2x)	La(2)	Ge(2)	3.225(1)
La(2)	Ge(3)	3.1241(7) (2x)	La(2)	C	2.670(3) (3x)
La(3)	C	2.668(3) (3x)			

Distances are in Angstroms. Estimated standard deviations in the least significant figure are given in parentheses

Interatomic angles,

atom	atom	atom	angle(°)	atom	atom	atom	angle(°)
La(1)	La(1)	La(1)	164.39(2)	Ge(3)	La(1)	Ge(3)	157.83(6)
La(3)	Ge(3)	La(4)	117.47(5)	La(3)	Ge(3)	La(3)	134.11(3)
La(2)	C	La(3)	178.8(1)	La(2)	C	La(2)	89.0(1)
La(2)	Ge(3)	La(3)	70.33(7)				

Angles are in degrees. Estimated standard deviations in the least significant figure are given in parentheses

Table 34. Refined parameters for $La_{15}Ge_9P$

atom	x	y	z	Occupancy
La(1)	0.01732(5)	0.34193(6)	0	1.0
La(2)	0.41298(5)	-x	0.744061(7)	1.0
La(3)	0.25388(5)	-x	0.282311(7)	1.0
La(4)	0.07960(5)	-x	0.730467(7)	1.0
Ge(1)	0.13365(7)	-x	0.27327(8)	1.0
Ge(2)	0.46675(7)	-x	0.26101(8)	1.0
Ge(3)	0.20038(7)	-x	0.71572(8)	1.0
P	2/3	1/3	0.5052(1)	1.0

B values

Atom	U11	U22	U33	U12	U13	U23
La(1)	0.01375(4)	0.01739(4)	0.00679(5)	0.00679(3)	0.0020(1)	0.0008(1)
La(2)	0.01174(4)	U11	0.01653(6)	0.00630(5)	0.0003(1)	-U13
La(3)	0.00906(4)	U11	0.01314(8)	0.00359(5)	0.0000(1)	-U13
La(4)	0.01020(4)	U11	0.02038(8)	0.00326(5)	0.0010(1)	-U13
Ge(1)	0.01319(7)	U11	0.0274(1)	0.00455(7)	0.0045(1)	-U13
Ge(2)	0.00976(8)	U11	0.0187(1)	0.00569(7)	0.0032(1)	-U13
Ge(3)	0.01048(7)	U11	0.0105(1)	0.00452(7)	0.0001(1)	-U13
P	0.0223(1)	U11	0.0329(1)	1/2 U11	0	0

in $La_{15}Ge_9Co$. The nearly identical La-Co and La-C distances could possibly represent the closest possible approach between La atoms in the $La_{15}Ge_9Z$ compounds. The phosphorus compound exhibits a smaller c-axis compared to the transition metal interstitial compounds. It also shows significantly larger La-Z distances than those found in $La_{15}Ge_9C$ and $La_{15}Ge_9Co$. However, the observed La-Z distances in $La_{15}Ge_9C$ (2.669(3)A) and $La_{15}Ge_9P$ (2.692(3)A) could be compared with the sums of the Pauling single bond radii of 2.49 A and 2.79 A for La-C and La-P, respectively.

The synthesis of $La_{15}Ge_9O$ was not unexpected. Results of Guinier powder diffraction, observation of $\sqrt{3} \times \sqrt{3}$ superstructure lines, equilibration experiments, and virtually single-phase products obtained from stoichiometric reactions provided satisfactory proof of its existence. The refined **a** parameter of $La_{15}Ge_9O$ matched well with the lattice parameters of La_5Ge_3 obtained from germaniothermal reactions and fusion experiments of Gladyshevskii if the **a**-parameter is ideally reduced to the Mn_5Si_3-type subcell value. Similar to the effects of oxygen in other Mn_5Si_3-type phases, the **c**-parameter of $La_{15}Ge_9O$ is less than that of the binary La_5Ge_3 host. This could be attributed to size effects of oxygen and the large interstitial cavity in La_5Ge_3.

Attempts to synthesize other main group element analogs of $La_{15}Ge_9Z$, Z = B, As, Sb, S, and Cl, were unsuccessful. These attempts were made only through high temperature (~1300°C) reactions in tantalum containers followed by slow cooling to room temperature. Other synthetic routes were not attempted. The negative results were inferred from the absence of the $\sqrt{3} \times \sqrt{3}$ superstructure lines in the Guinier powder diffraction patterns of products. Instead only lines of the Mn_5Si_3-type subcell were observed.

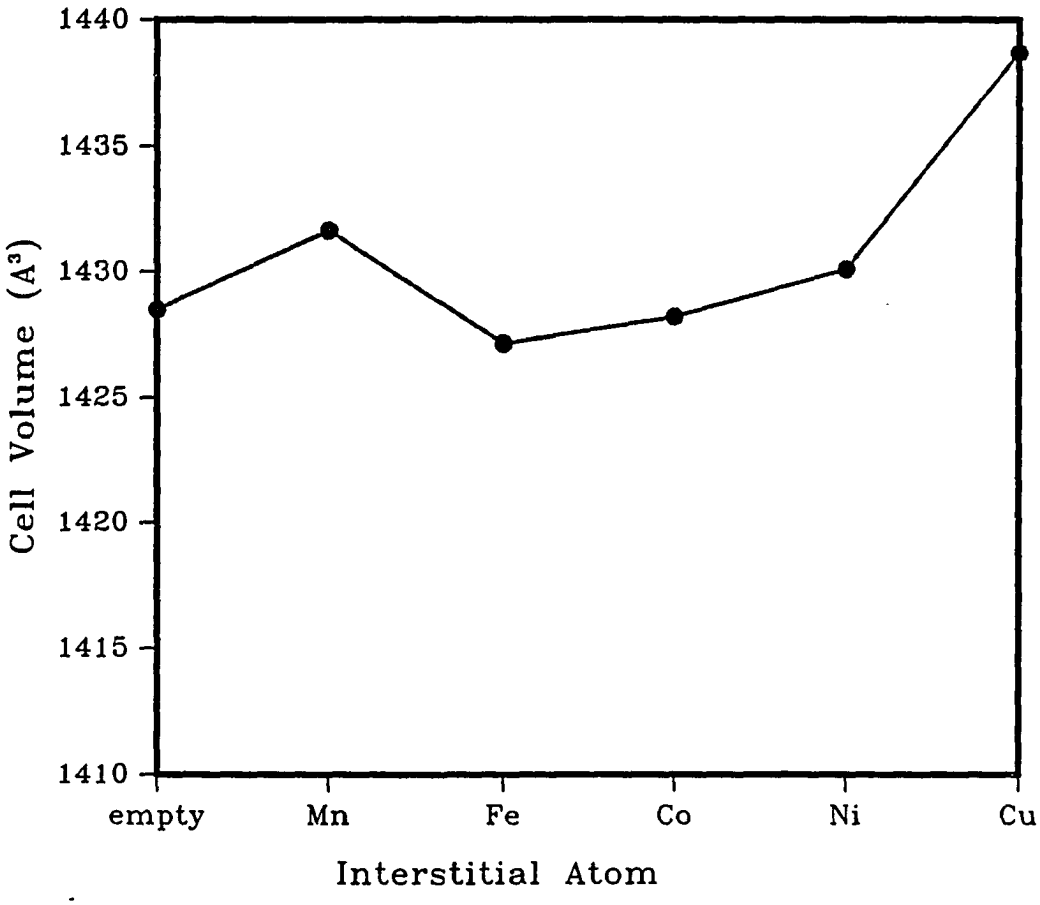

Figure 33. Variation of the cell volumes of $La_{15}Ge_9Z$; Z = 3d-metals. The volume of an ideal $La_{15}Ge_9$ cell derived from La_5Ge_3 is marked "empty"

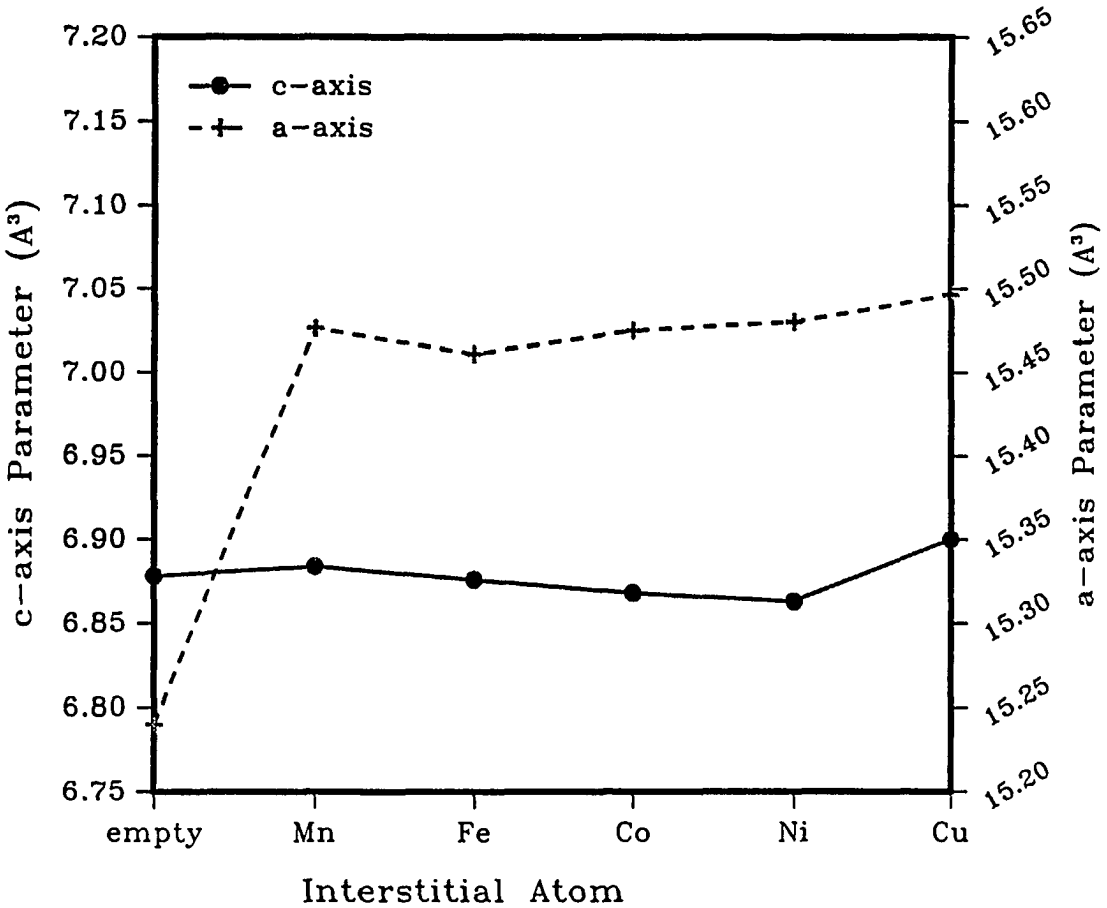

Figure 34. Variation of lattice parameters of $La_{15}Ge_9Z$; Z = 3d-metals. The cell parameters of an ideal $La_{15}Ge_9$ cell derived from La_5Ge_3 values are marked "empty"

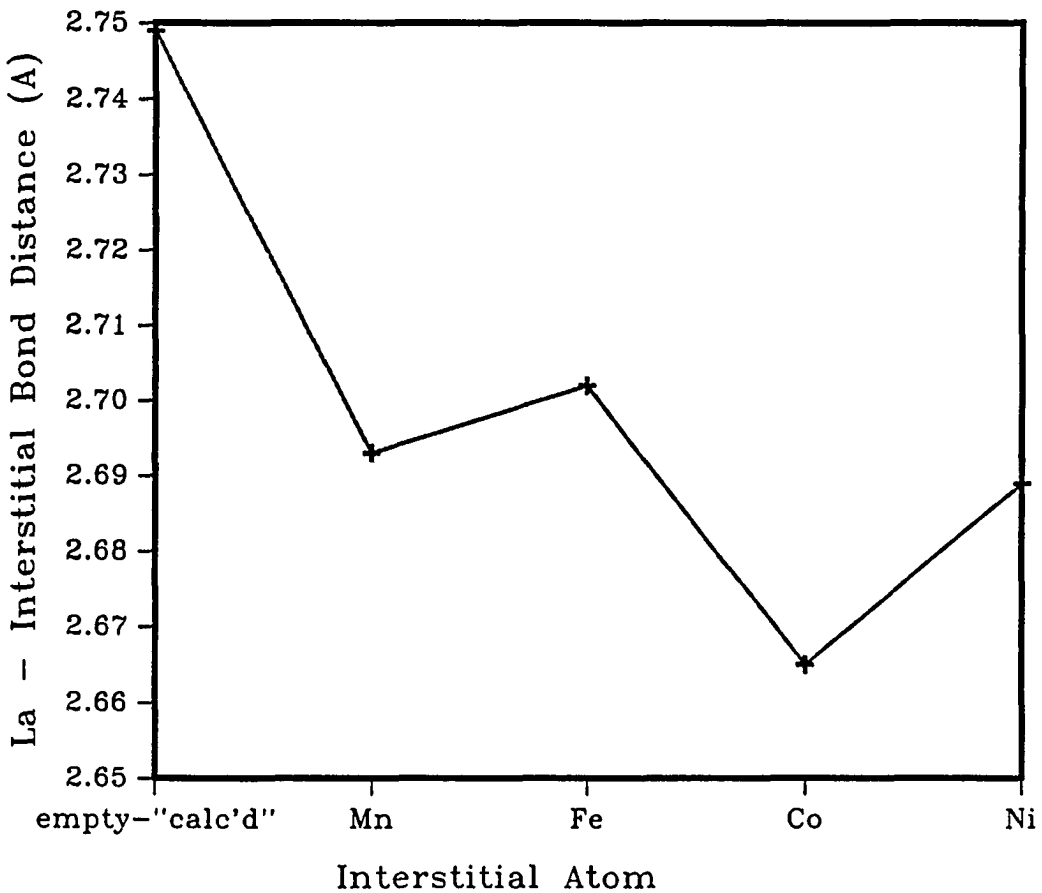

Figure 35. Variation of La-Z(interstitial) distances in $La_{15}Ge_9Z$; Z = Mn, Fe, Co, and Ni. The La-(interstital site) distance in La_5Ge_3 is marked "empty-calc'd"

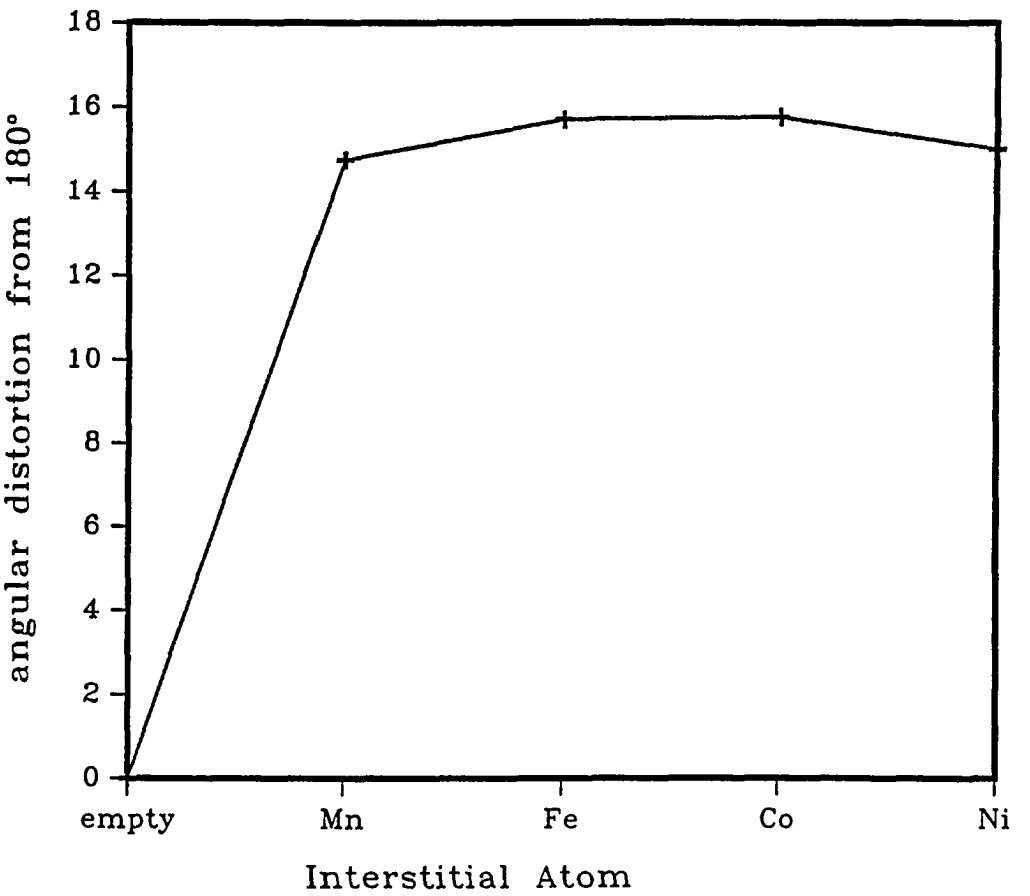

Figure 37. Variation of the angular distortion of the nominal La(1) linear chains from 180° in $La_{15}Ge_9Z$; Z = Mn, Fe, Co, and Ni. The value for La_5Ge_3 is marked "empty"

electron counts, i.e., subtitution by Fe, Ni and Mn results in smaller distortions. Although $La_{15}Ge_9Co$ and $La_{15}Ge_9Fe$ exhibit the largest distortion angles of the nominal La(1) linear chains, the degree of angular distortions could be considered as fairly constant. This suggests that the buckling of the La(1) chains can be largely attributed to matrix effects. Hence, the major structural factors lie in the Peierls-like distortions induced by the interstitial atoms on the confacial trigonal antiprism chains.

The observed maxima in $La_{15}Ge_9Co$ tempts us to formulate a general scheme. A simple electron counting applied on $La_{15}Ge_9Co$ results in a formal electron count of 18,

$$[\ (15 \times 3) - (9 \times 4) + 9 = 18\ ],$$

on an "La_6Co cluster". Likewise, electron counts of 16, 17, 18, 19 and 20 result for the Mn, Fe, Co , Ni, and Cu analogs, respectively.

The successful syntheses of main group interstitial analogs of $La_{15}Ge_9Z$ suggests that a similar electronic rule also applies. Appying the simple electron counting rule based on the electronegativity of the metals and non-metals

$$[(15 \times 3) - (9 \times 4) + Y\ (e^- \text{ from } Z)]$$

lead to electron counts of 13, 14, and 15 on the La_6Z clusters in $La_{15}Ge_9C$, $La_{15}Ge_9P$ and $La_{15}Ge_9O$, respectively. This electron counting scheme has been successful in explaining the structural behavior of zirconium and rare-earth-metal halide clusters.

The less polar nature of the $La_{15}Ge_9Z$ compounds poses a problem in successfully justifying the simple electronic scheme. It implies that the cluster electrons are to a certain degree localized on the Z-centered "clusters" contrary to the metallic lustre of the compounds. However, the less polar nature of the compounds may explain the wide range of electron counts this class of interstitial compounds apparently take. Further

physical and theoretical studies are necessary to fully understand the electronic behavior of these class of compounds.

Magnetic data of $La_{15}Ge_9Z$ (Z = transition metals)

Magnetic susceptibility measurements on powdered samples of the Fe, Co, and Ni analogs of $La_{15}Ge_9Z$ were undertaken. The magnetic susceptibility curves are illustrated in Figures 38 and 39. The results indicate all of the $La_{15}Ge_9Z$ compounds measured were paramagnetic. The measured paramagnetic moments were larger than the weak temperature-independent moment exhibited by the Pauli paramagnet, La_5Ge_3. The calculated moments (after diamagnetic core corrections) of the Fe ($1.83\mu_B$), Co ($1.40\mu_B$), and Ni ($1.04\mu_B$) analogs revealed that $La_{15}Ge_9Ni$ had the weakest paramagnetic moment per interstitial atom. The observed moments can be compared with the elemental saturation moments of 2.2, 1.72, and 0.6 μ_B for Fe, Co, and Ni metals, respectively. This indicates that the behavior of the 3d bands dominates the magnetic character of the compounds. The larger distances between the interstitial atoms in $La_{15}Ge_9Z$ deters the effects of exchange forces in the spin alignments between neighboring interstitial atoms. This suggest that the spins of the interstitial atoms are "diluted" in the host matrix. These results coupled with the structural features generally imply a trend in the observed structural and magnetic characteristics that relies on the number of electrons introduced by the (3-d) transition metal interstitials.

XPS data of $La_{15}Ge_9Z$ (Z = transition metals)

Photoelectron spectra of the iron, and nickel compounds were also briefly examined. Photoelectron spectroscopic data were obtained with the aid of an AEI-200B spectrometer and Al Kα radiation, as described earlier. Samples were mounted on

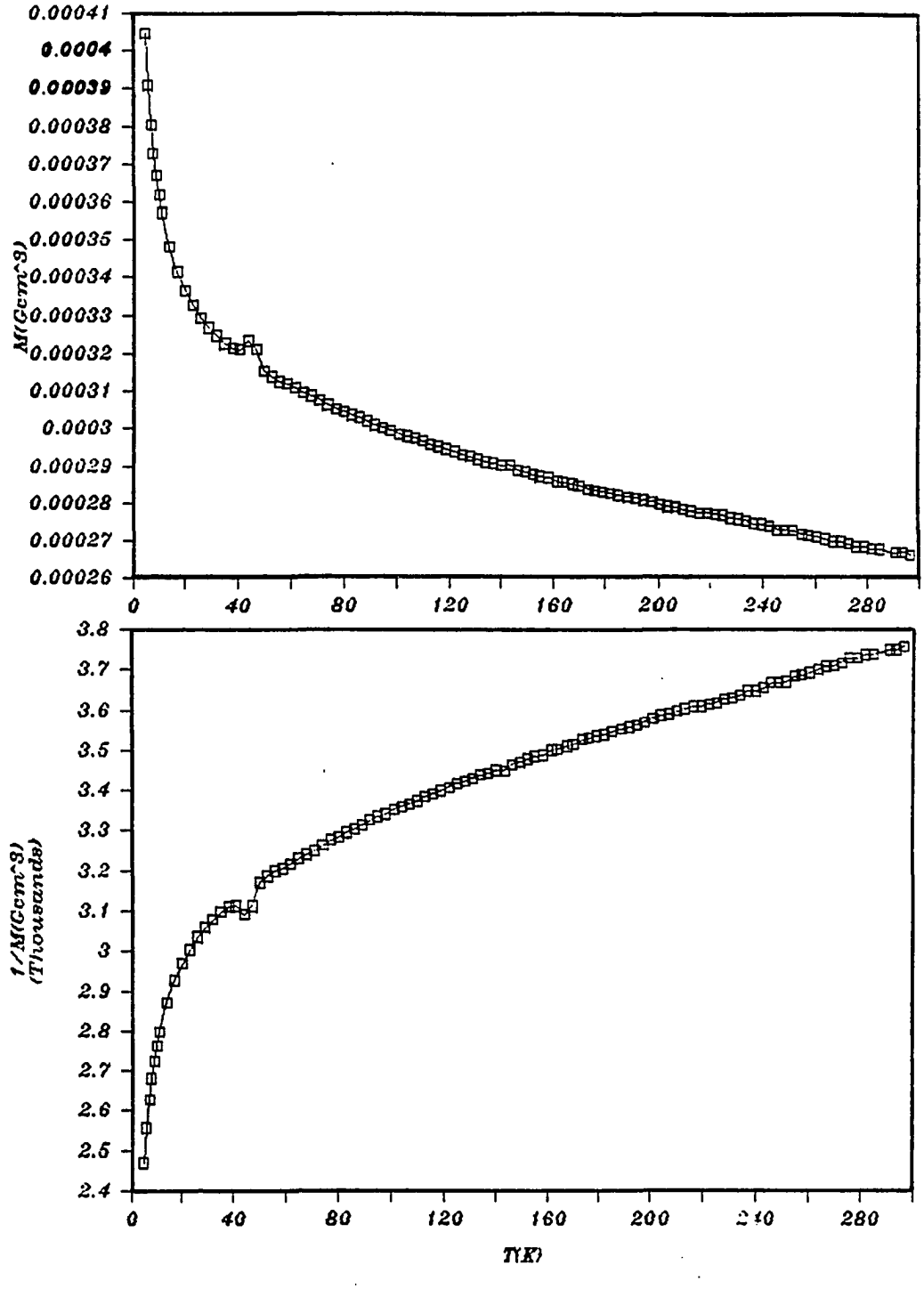

Figure 38. Plot of magnetic susceptibility χ (top) and χ^{-1} (bottom) vs (T) temperature measurements of $La_{15}Ge_9Fe$ at 5KG

an indium substrate. The observed binding energies were referenced to adventitious carbon at 285.0 eV.

The use of XPS did not resolve much of the valence bands although the clear Fermi edges were visible for both compounds. However, it was also evident that $La_{15}Ge_9Fe$ had a higher density of states at or near the Fermi edge than the Ni analog. Core level shifts examined by XPS (Al Kα) are listed in Table 36. The different types of lanthanum atoms were not resolved but their composite $3d_{5/2}$ and $3d_{3/2}$ binding energies are reasonable in comparison with 834.0 and 851.0 eV for the metal.[258] The 3d energy in elemental germanium, 28.95 eV,[258] is correspondingly reduced to 26.0 eV in $La_{15}Ge_9Fe$ and 26.8 eV in $La_{15}Ge_9Ni$. The iron photoelectron lines $2p_{3/2}$ and $2p_{1/2}$ at 705.3 and 718.9 eV, respectively, were shifted to lower in binding energies than from 706.75 and 719.95 eV in the metal. The shift to lower binding energies indicated that the iron atoms in $La_{15}Ge_9Fe$ were more reduced than the metal. This is particularly evident when compared to the core shifts of Fe_2O_3 (710.7 and 724.3 eV). The core shifts of the iron in $La_{15}Ge_9Fe$ were larger compared to those of La_5Ge_3Fe (705.8 and 719.0 eV). This is in accord with the idea that the "excess" electrons in the host-derive bands were transferred to the interstitial-derived bands as predicted by the electron counting scheme. Since there are fewer interstitials in $La_{15}Ge_9Fe$, there will be more electrons transferred per interstitial atom. Hence a more "anionic" Fe atom exists in $La_{15}Ge_9Fe$. The measurements on $La_{15}Ge_9Ni$ were not so useful because the Ni photoelectron lines, $2p_{3/2}$ and $2p_{1/2}$ located at about 850-860 eV, were masked by the La peaks.

Table 36. XPS core shifts in $La_{15}Ge_9Fe$ and $La_{15}Ge_9Ni$

compound	La_5Ge_3	La_5Ge_3Fe	$La_{15}Ge_9Fe$	$La_{15}Ge_9Ni$	Ca_5Pb_3Fe
core shifts:					
La levels:					
$3d_{5/2}$	837.2	838.5	838.2	836.2	
$3d_{3/2}$	854.0	854.2	853.8	852.9	
Ge levels:					
3d	26.2	26.2	26.0	26.6	
(28.0 in metal)					
Fe levels:[a]					
$2p_{3/2}$		705.8	705.3		707.2
$2p_{1/2}$		719.0	718.9		720.8

[a] Literature values are: 706.8, 720.0 eV in metal; 710.7, 724.3 eV in Fe_2O_3

THE "ELECTRON-POORER" La_5Ge_3Z PHASES

The investigations on the filled-Mn_5Si_3-type phases, La_5Ge_3Z showed the apparent success of the Zintl concept in explaining structure-bonding-property relationships. In spite of the successful incorporation of boron and carbon into La_5Ge_3, attempts to synthesize fully-filled analogs of heavier group 14 and 13 elements were unsuccessful. This was not surprising because our simple electron counting scheme indicated that these compounds, La_5Ge_3Z (Z = group 13 and 14), do not have enough electrons to fully fill the non-metal-derived valence states. Instead they form structures closely related to known M_5X_4 structures namely Zr_5Si_4,[215] Gd_5Si_4,[214] Sm_5Ge_4,[209] and Eu_5As_4[216] structure types. These structure types have a common structural feature; X_2 dimers. They differ largely on the number of dimers per formula unit, and in how these dimers are arranged. The Zr_5Si_4 and Gd_5Si_4 structures have 2 dimers per formula unit, on the other hand, the Sm_5Ge_4 and Eu_5As_4 have only one. This section will discuss the syntheses and structural relationships of the different La_5Ge_3Z (Z = group 13 and 14) phases. The synthesis of the substoichiometric phase $La_5Ge_3Si_{0.75}$ having the filled-Mn_5Si_3 structure will be noted.

La_5Ge_3Z (Z = Group 14)

$La_5Ge_3Si_x$

Parallel to the syntheses experiments involving La_5Ge_3C and La_5Ge_4, the syntheses of other La_5Ge_3Z compounds with Z = Si, Sn and Pb were pursued. Results from these experiments are summarized in Table 37. Our interest was to understand the

Table 37. Summary of La_5Ge_3Z (Z = Ge, Si, Sn, Pb) phases

composition	conditions [temp(°C)]	lattice parameters (A) (spacegroup)	volume (A^3)	structure type
La_5Ge_4	S	a = 8.065(1); b = 15.474(2) c = 8.172(1); (Pnma)	1019.8(4)	Sm_5Ge_4
$La_5Ge_3Si_{0.75}$	A	a = 8.937(1); c = 6.944(2) ($P6_3/mcm$)	480.2(2)	Mn_5Si_3
α-La_5Ge_3Si	S	a = 8.059(1) b = 15.454(1) c = 8.165(1); (Pnma)	1016.9(4)	Sm_5Ge_4
β-La_5Ge_3Si	A	a = 8.148(1); c = 15.294(2) ($P4_12_12$)	1015.4(4)	Zr_5Si_4
La_5Si_4	S	a = 8.046(1); c = 15.432(1) ($P4_12_12$)	999.0(4)	Zr_5Si_4
La_5Ge_3Sn	S	a = 8.156(1); b = 15.630(2) c = 8.292(1); (Pnma)	1057.0(4)	Sm_5Ge_4
La_5Ge_3Pb	S	a = 8.176(1); b = 15.625(2) c = 8.288(1); (Pnma)	1058.8(4)	Sm_5Ge_4
La_5Sn_4	S	a = 8.435(1); b = 16.194(2) c = 8.630(1); (Pnma)	1178.8(5)	Sm_5Ge_4
La_5Pb_4	S	a = 8.536(1); b = 16.314(2) c = 8.675(1); (Pnma)	1208.1(4)	Sm_5Ge_4

S: Sintering reactions of binaries and elements at 1100-1300°C over a total of 10-15 days,
A: Arc-melting binaries and/or elements

Sm_5Ge_4 structure which is assumed by many 5:4 rare-earth metal tetrelides and to rationalize its structure and bonding using the Zintl-Klemm concept. The syntheses of three structurally different compounds in the stoichiometry range $La_5Ge_3Si_x$; $0.75 \leq x \leq 1.0$, provided interesting structure-bonding problems.

Syntheses Initial attempts to synthesize the Zintl phase $La_5Ge_3Si_{0.75}$ was done using high temperature reactions at 1200°C. The elements were used as starting reagents in sealed tantalum containers. These attempts resulted in multi-phase products which included Mn_5Si_3-type and Sm_5Ge_4-type phases. However, a different approach, arc-melting of the elements for the reaction

$$La_5Ge_3 + 3/4\ Si \text{ ---> } La_5Ge_3Si_{0.75}$$

was successful in yielding a single-phase Mn_5Si_3-type product. This high-temperature phase represented the Zintl phase in the system $La_5Ge_3Si_x$.

Annealing the as-cast buttons of $La_5Ge_3Si_{0.75}$ resulted in a disproportionation reaction of the compound into $La_5(Ge,Si)_3$ and $La_5(Ge,Si)_4$ as observed from powder diffraction patterns of the resulting products. The ternary 5-4 compound could be assigned to the Sm_5Ge_4 structure type but with smaller cell parameters than La_5Ge_4. Indexing of diffraction lines corresponding to the Mn_5Si_3-type product yielded lattice parameters close to that of binary La_5Ge_3. However, the error in the cell parameters was not enough to allow us to conclude that the Mn_5Si_3-type product was indeed La_5Ge_3 and not mixed $La_5Ge_{3-x}Si_x$. Hence, we could not not determine the exact ratios of Ge and Si in the annealed reactions. However, we could infer that the disproportionation reaction could be represented by the reaction

$$La_5Ge_3Si_{0.75} \text{ ---> } 1/4\ La_5Ge_3 + 3/4\ La_5Ge_3Si.$$

The structure of β-La_5Ge_3Si

Structure determination The single crystal structure investigation of the high temperature (β)-phase of La_5Ge_3Si proceeded in the usual manner. Redundant data sets and three ψ-scans were collected after a tetragonal cell was indexed by 25 reflections using the program SEARCH. Data preparation included absorption corrections based on three ψ-scans, Lorentz and polarization corrections, and averaging in the Laue symmetry P4/mmm. Precession and Laue cone photographs were also taken and confirmed the tetragonal cell (a = 8.148(1) A, c = 15.294(2)A from Guinier powder patterns) with Laue symmetry of 4/mmm. Careful inspection of the reflection data and higher level precession photos indicated systematic reflection conditions 00l; l = 4n and 0k0; k = 2n. These corresponded to the possible space groups $P4_12_12$, and $P4_32_12$. The latter one proved to be correct during refinement (R_{ave} = 3.8%).

The structure was refined in the space group $P4_12_12$ using an initial model obtained from direct methods (SHELXS). This model could not distinguish between Si and Ge sites, hence these peaks were all initially assigned to germanium. The weighting scheme was according to the counting statistics, and the secondary extinction parameter was refined (1.93(2) x 10^{-7}). Isotropic refinement resulted in large thermal parameters for the germanium sites. Refinement of the germanium sites led to occupancies of ~86.5% Ge. Anisotropic refinement after application of DIFABS resulted in final residuals of R = 2.4%; R_w = 3.0%. The final refined occupancies in the tetrelide sites were 86.5(2)% and 86.9(2)% for Ge(1) and Ge(2), respectively. These occupancies corresponded to mixed occupancies of 76.0% Ge and 24.0% Si for Ge(1), and 76.7% Ge and 23.3% Si for Ge(2), resulting in a refined stoichiometry of $La_5Ge_{3.05(2)}Si_{0.95(2)}$, close to the loaded

stoichiometry of La_5Ge_3Si. The final difference Fourier maps did not exhibit any unusual residual peaks. The largest was 1.3 e^-/A^3 which was 2.1 A from Ge(1). A summary of the single crystal structure solution is presented in Tables 38-40.

Structure description The structure of β-La_5Ge_3Si was found to be isotypic with the tetragonal Zr_5Si_4 structure type.[259] Although the structure has not been satisfactorily described,[260] the structure can still be generally pictured as having tetrelide dimers (dumbbells). In β-La_5Ge_3Si, the tetrelide dimers have interatomic distances of 2.675(1)A, which can be compared to the Si-Si dimeric bond distance of 2.30 in U_3Si_2 and 2.658 A in the Ge-Ge dimer bonds in Sm_5Ge_4. The Pauling single bond distances[261] for Si_2 and Ge_2 are 2.34 and 2.50 A, respectively. In the isolated tetrelide dimers, each tetrelide atom is nominally surrounded by 8 lanthanum atoms forming a bicapped trigonal prism or a face-sharing square antiprism. Two bicapped prisms share a square face to form a unit of $La_{12}T_2$ (T = tetrelide) as shown in Figure 40, with the tetrelide atoms moving from the center toward the common square face. However, in β-La_5Ge_3Si these $La_{12}T_2$ units are distorted, with the loss of one metal coordination, to form $La_{11}T_2$ fragments as shown in Figure 41. These units are close-packed with the lanthanum atoms used as common vertices, $[Ge_2(La_{4/4} + La_{4/4} + La_{3/6})]$, that results in a nominal stoichiometry La_5T_4. The observed La-La distances in β-La_5Ge_3Si (3.6015(5) - 3.7595(6)A) typify usual metal-metal distances in lanthanum intermetallics but are relatively shorter than their corresponding distances in La_5Ge_4 (3.631(1) - 3.986(1)Å) and La_5Ge_3Ga (3.684(1) - 3.962(1)Å).

The β-La_5Ge_3Si structure, a Zr_5Si_4-type, can also be considered as another distorted variant of U_3Si_2 caused by the decrease in the number of lanthanum positions.

Table 38. Data collection and refinement parameters for β-La_5Ge_3Si

space group	$P4_12_12$
Z	4
crystal dimension	0.06 x 0.06 x 0.10 mm
diffractometer	Enraf-Nonius CAD4
2θ max	65°
collected indices	h, $\pm$k, $\pm$l
reflections:	
measured	7783
observed (>3σ_I)	6690
independent	885
R_{ave}	3.1% (observed data)
no. of parameters refined	46
R (refinement)	2.4%
R_w (refinement)	3.0%
largest parameter shift	0.01
absorption coefficient	322.4 (cm^{-1}, Mo Kα)
secondary extinction coeff.	$1.93(6) \times 10^{-7}$
largest residual peaks	1.3 e^-/A^3
cell parameters (Guinier):	
a = 8.148(1) A	
c = 15.294(2) A	
volume = 1051.4(4)A^3	

Table 39. Refined parameters for β-La_5Ge_3Si

atom	x	y	z	Occupancy
La(1)	0.01450(5)	0.13562(5)	0.62484(4)	1.0
La(2)	0.18565(6)	x	0.0	1.0
La(3)	0.99086(5)	0.36801(6)	0.20482(3)	1.0
Ge(1)	0.0655(1)	0.2932(1)	0.81119(7)	0.865(2)
Ge(2)	0.3007(1)	0.3409(1)	0.69191(6)	0.869(2)

B values

Atom	B11	B22	B33	B12	B13	B23
La(1)	0.63(1)	0.65(1)	0.59(1)	0.02(1)	-0.07(1)	-0.12(1)
La(2)	0.84(1)	B11	0.77(2)	-0.02(2)	-0.09(1)	-B13
La(3)	0.73(1)	0.67(1)	0.76(1)	0.05(1)	-0.11(1)	-0.16(1)
Ge(1)	0.85(3)	0.89(3)	0.68(3)	-0.09(3)	-0.05(3)	0.04(3)
Ge(2)	0.60(3)	0.76(3)	1.04(3)	-0.20(3)	0.14(4)	-0.16(3)

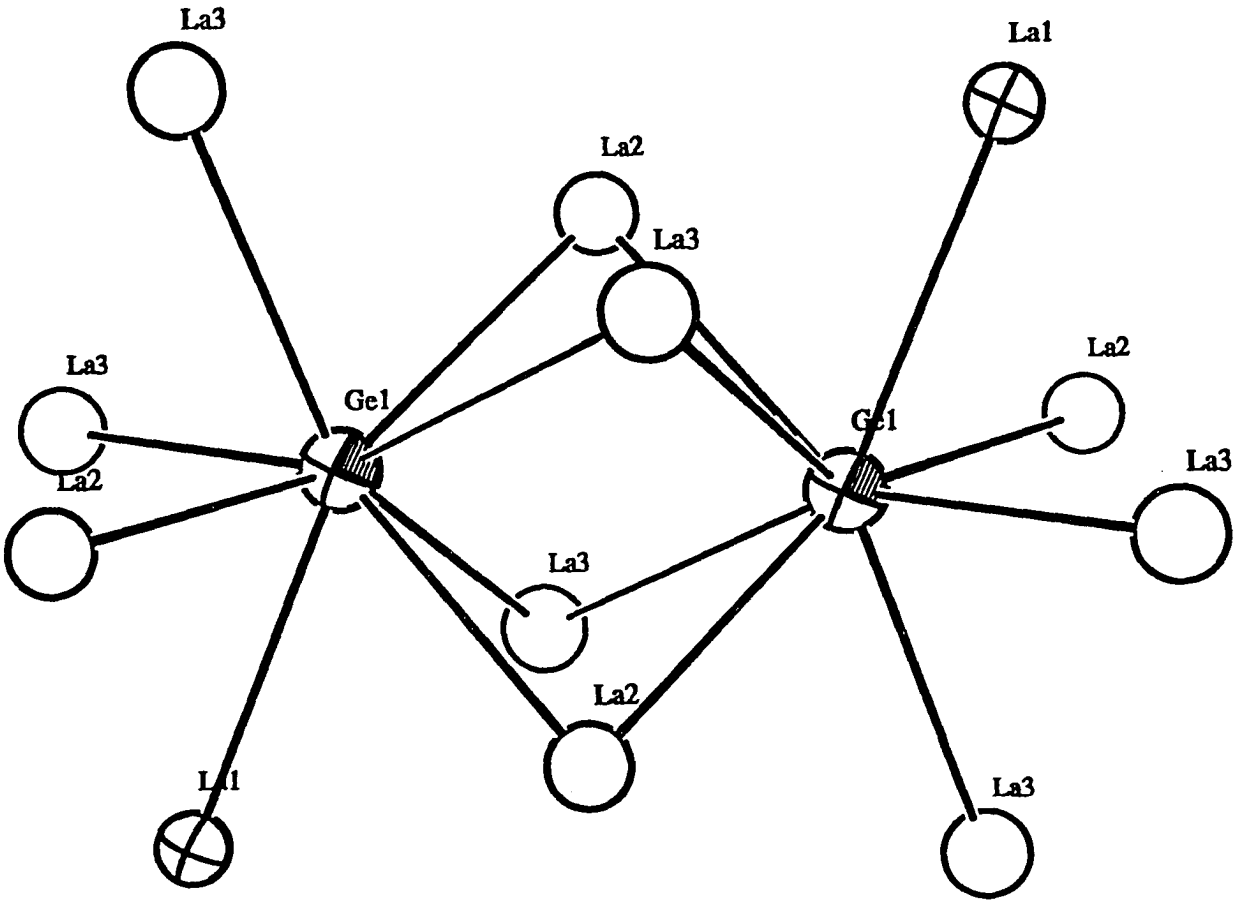

Figure 40. A tetrelide $(Ge)_2$ dimer and its La coordination: bicapped trigonal prisms that share a common square face. Open and cross-hatched circles: La, octant shaded circles: Ge

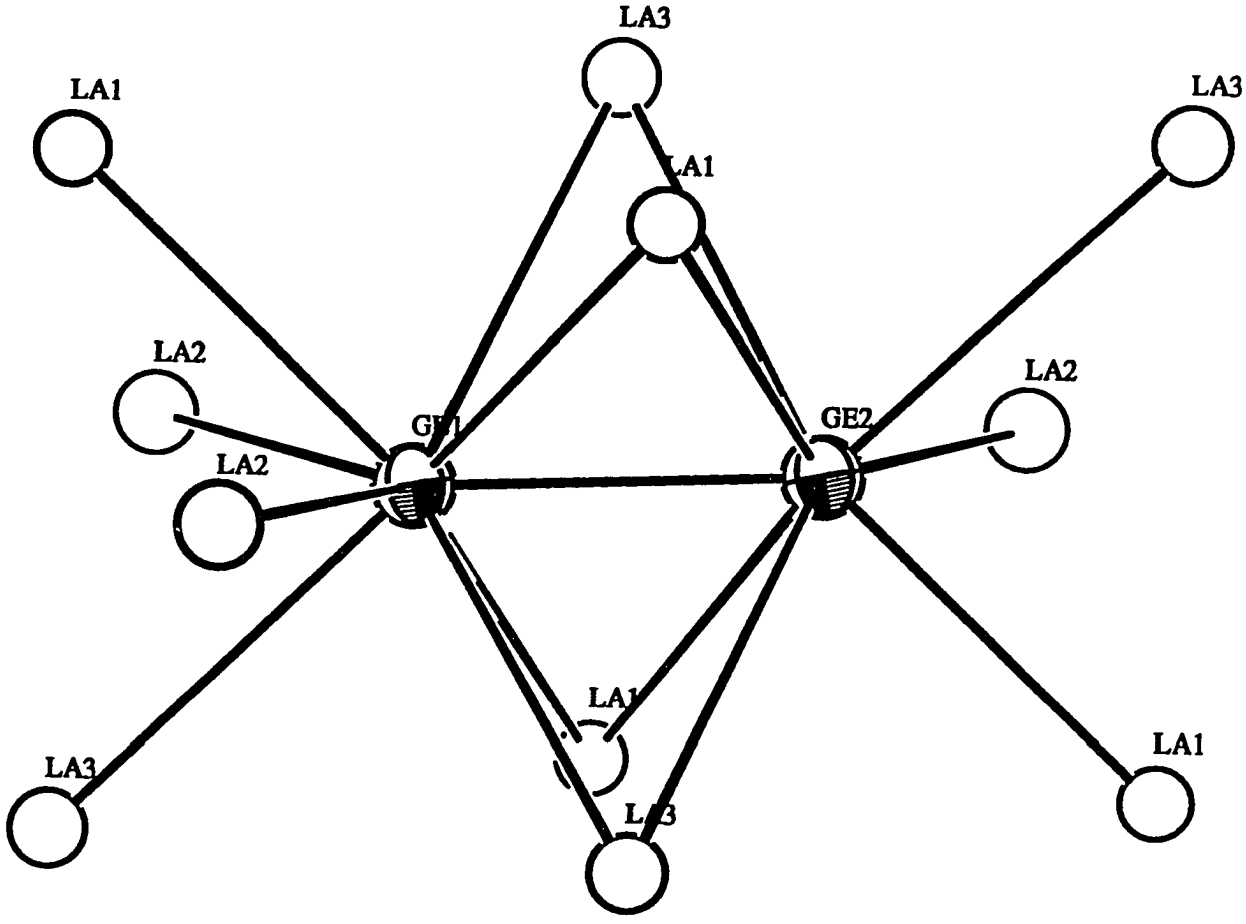

Figure 41. The $La_{11}(Ge,Si)_2$ unit in β-La_5Ge_3Si. Note the missing La atom bonded to Ge(2). Open circles: La, octant shaded circles: Ge

The U_3Si_2 structure also contains dumbbells of Si_2^{-6} with a $U_{12}Si_2$ building unit formed from two Si-centered square antiprisms fused through the square faces. This was alluded to by Karpinskii and Evseev.[262] Since other 5-4 tetrelide structures have often been described as derived from the U_3Si_2 structures, structural relationships between the different structures must be made clear to understand the observed structural preferences, particularly between Zr_5Si_4, Sm_5Ge_4, Gd_5Si_4, Eu_5As_4, and other related structures.

We begin with the relationship between the α (Sm_5Ge_4-type) and β (Zr_5Si_4-type) phases of La_5Ge_3Si. The structural differences between α-La_5Ge_3Si and β-La_5Ge_3Si begin with the number of dimers in the structure. The α-La_5Ge_3Si has one dimer per formula unit and β-La_5Ge_3Si has two dimers. The space groups (Pnma and $P4_12_12$, respectively) of the two phases do not represent a group-subgroup relationship. However, inspection of the lattice parameters of the α-phase indicates a pseudo-tetragonal cell with b as the pseudo-tetragonal axis and both structures are closely related to the U_3Si_2 structure type. Detailed inspection of the structures do not immediately reveal any close structural relationships. The dimers in the α-phase lie perpendicular to the pseudo-tetragonal axis, whereas, the dimers in the β-phase were tilted along the tetragonal axis. How then do we relate the two seemingly different structures? (see Figure 42.)

To better understand the differences, we start with a common structural unit -- an La(2)-centered La_8 (La(1) and La(3)) cube that is capped on the faces with Ge(Si) -- $La(La)_8Si_6$. This can also be better described as an octahedral coordination of Ge(Si) around La(2), face-capped by 8 lanthanum atoms. The coordination around La(2) is shown in Figure 43. This structural unit, also called a bicapped cuboctahedron, is also present, but slightly distorted, in all Sm_5Ge_4-type structures as shown in Figure 44. The

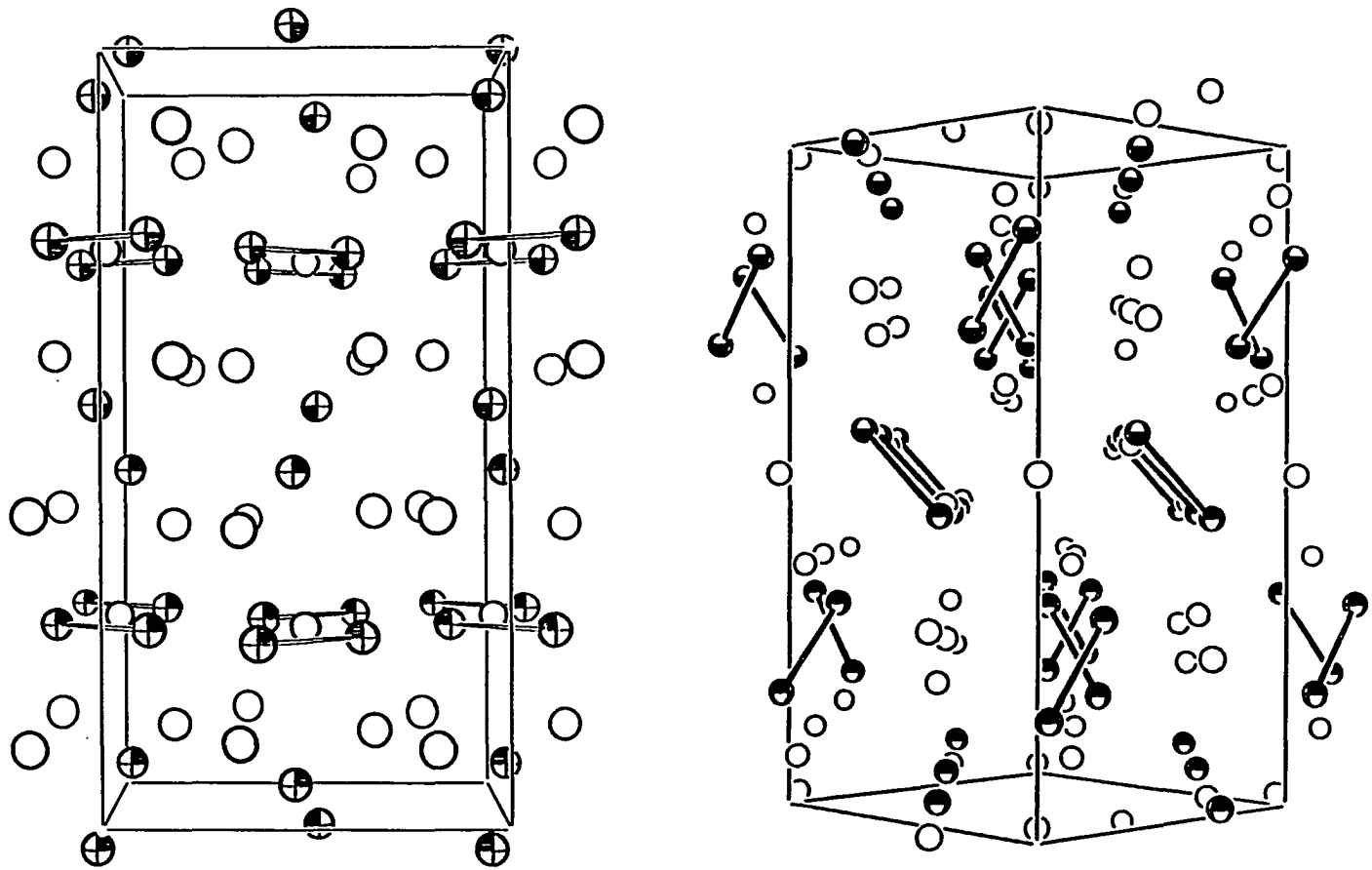

Figure 42. ORTEP drawing of the unit cells of (left) La_5Ge_4: Sm_5Ge_4-type and (right) β-La_5Ge_3Si: Zr_5Si_4-type. Open circles: La, octant shaded circles: Ge(Si)

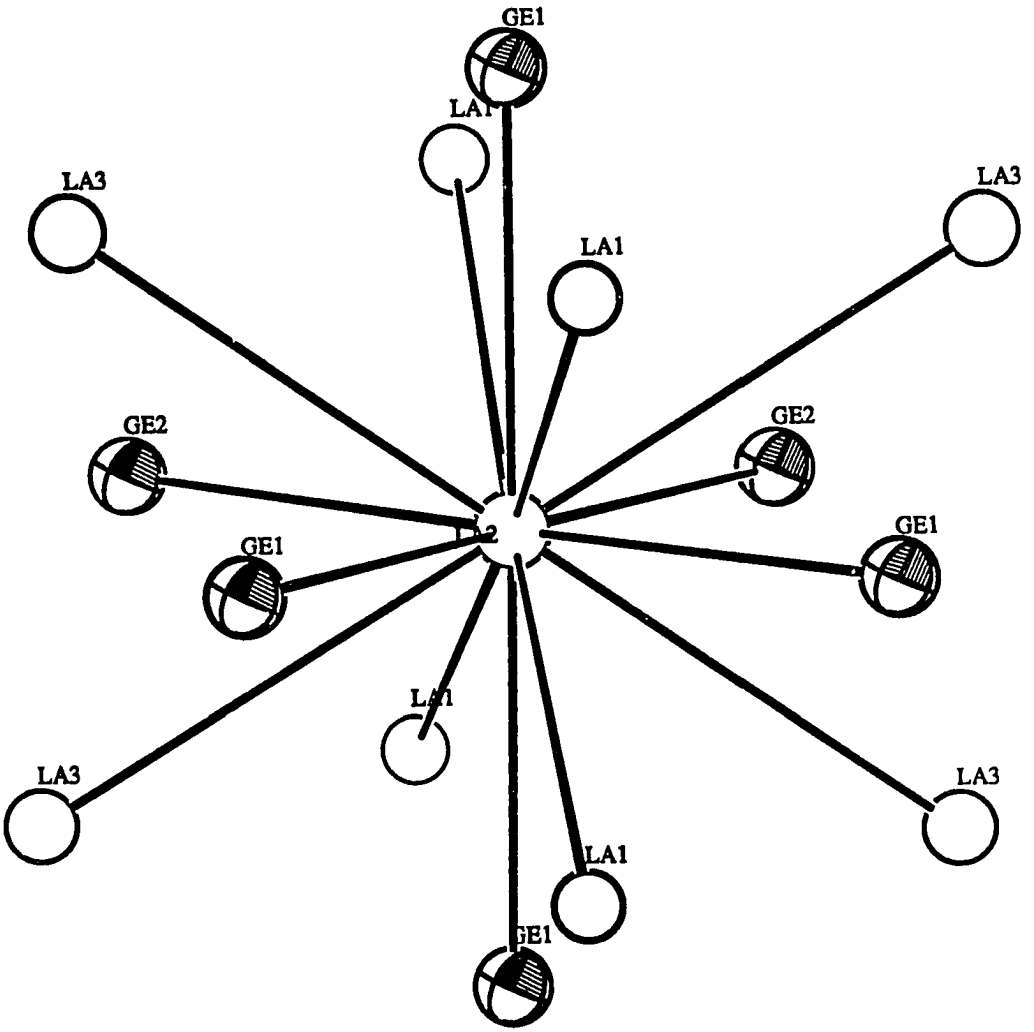

Figure 43. An $La(La)_8(Ge,Si)_2$ unit in β-La_5Ge_3Si. Open circles: La, octant shaded circles: Ge(Si)

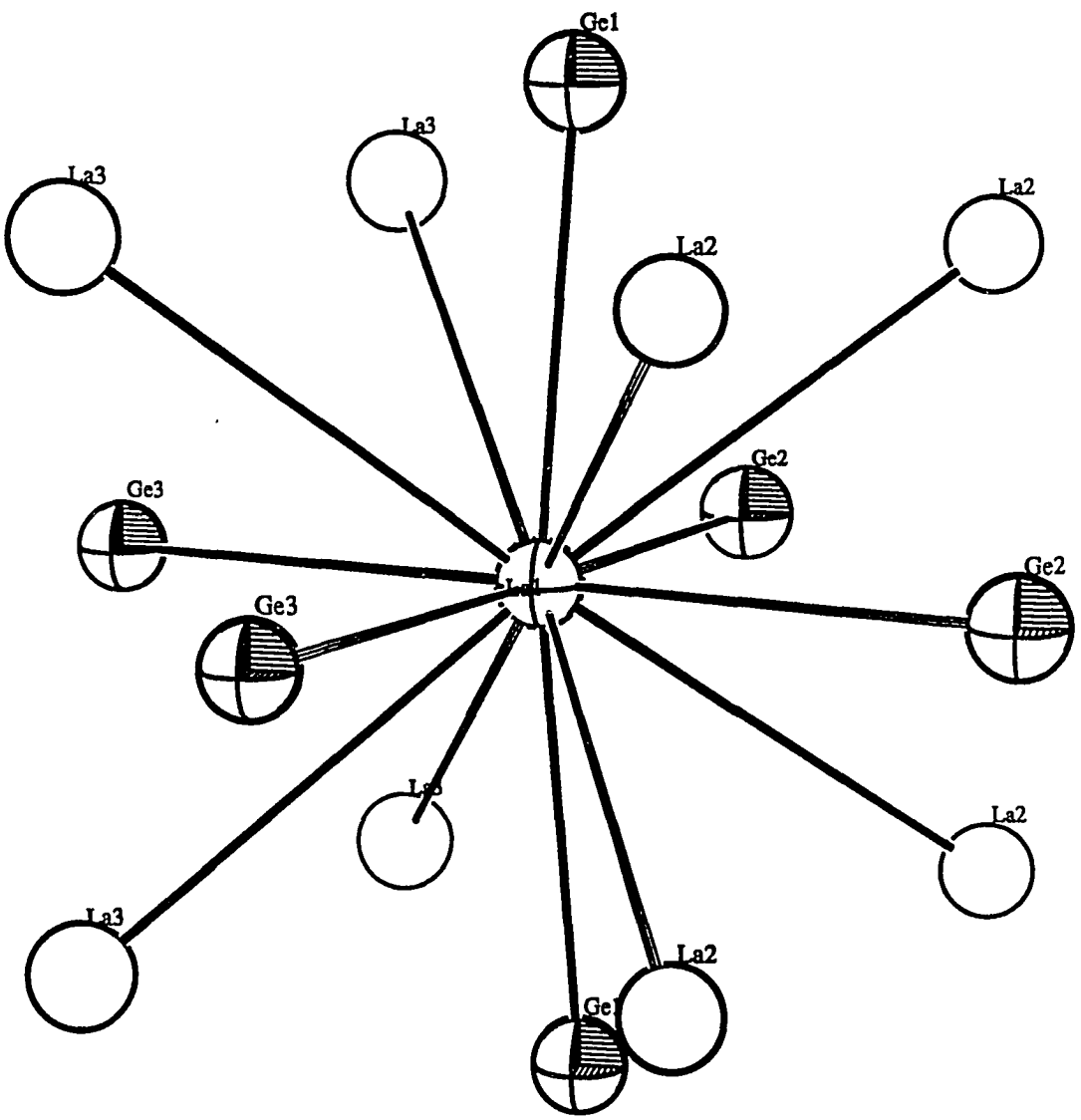

Figure 44. A distorted $La(La)_8(Ge)_4$ unit in La_5Ge_4, Sm_5Ge_4-type structure. Open and crossed hatched circles: La, octant shaded circles: Ge

connectivity between the La_9Si_6 units in β-La_5Ge_3Si is shown in Figure 45. Two units are twisted with respect to their octahedral axis and fused to share 3 common atoms: La(3), La(1), and Ge(1). In addition, adjacent germanium atoms Ge(2) in one unit and Ge(1) in the other make a close approach resulting in a Ge(1)-Ge(2) dimer. This connectivity between La_9Si_6 units is reprised in a tetrahedrally close-packed manner forming a three-dimensional network of La_9Si_6 units, as shown in Figure 46. Tetrahedral packing of structural units is often used to rationalize and differentiate many intermetallic structures and it conforms with the Frank-Kasper rules.

The resulting Ge_2 dimer coordination in Figure 41 shows that Ge(1) is shared by 2 La_9Ge_6 units through its connectivity to two La(2) atoms. On the other hand, Ge(2) shows only one connectivity to a La_9Ge_6 unit represented by La(2). There are four Ge(1) and two Ge(2) atoms that make up the Ge_6 coordination around each La(2). This observation and note that every La atom in the cubic environment of La(2) is shared by another La_9Ge_6 unit results in the observed stoichiometry, $La(La_{8/2}Ge_{4/2}Ge_2) = La_5Ge_4$.

The α-La_5Ge_3Si (Sm_5Ge_4-type) structure can also be explained in terms of the different packing of La_9Ge_6 units. The La_9Ge_6 unit, with La(1) being the center, in a Sm_5Ge_4-type structure is illustrated in Figure 44. A "tilting" displacement of the Ge(1) atoms (Ge(1)-La(1)-Ge(1) = 171.2°) from the c-axis perpendicular to the pseudo-tetragonal axis, b is observed. The displacement distortion effectively lowers the symmetry on the central La(1) atom, thus, the overall symmetry is orthorhombic. In the α-structure, La_9Ge_6 units are interconnected to form layers that extend along the a-c plane, in contrast to the three dimensional packing of La_9Ge_6 units in β-La_5Ge_3Si. In the layer-like formations, each La_9Ge_6 "cluster" is connected to four other units. The

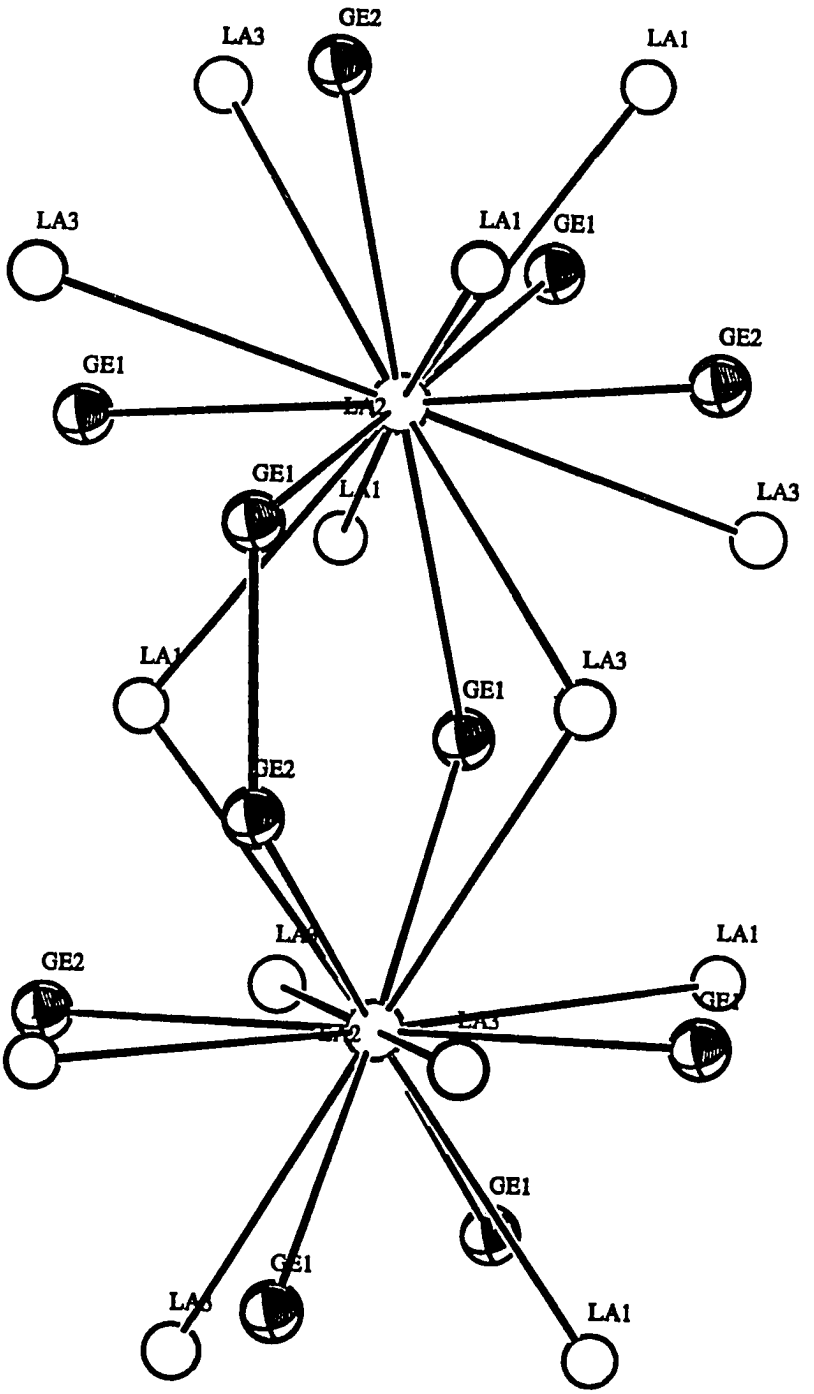

Figure 45. Connectivity of two $La(La)_8(Ge,Si)_2$ in β-La_5Ge_3Si. Open circles: La, octant shaded circles: Ge(Si)

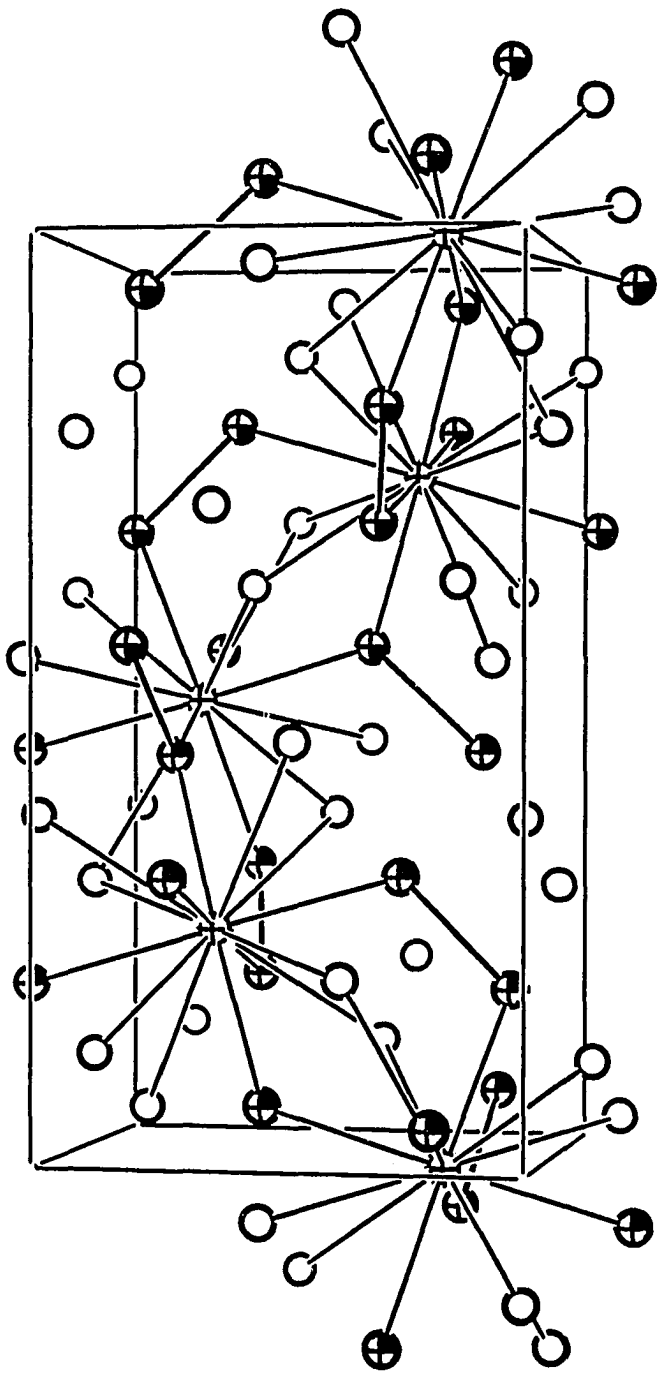

Figure 46. Tetrahedral interconnectivity of $La_9(Ge,Si)_2$ units in β-La_5Ge_3Si forming a tetragonal unit cell. Open circles: La, octant shaded circles: Ge(Si)

connectivity between units, as shown in Figures 47-49, is represented by the sharing of two lanthanums and one germanium atom vertices. The other linkage between two La_9Ge_6 units is made up of Ge(2)-Ge(3) dimers. This is very similar to the connectivity found in β-La_5Ge_3Si. However, twisting of the La_9Ge_6 units is not required for the formation of a layer-like structure, as shown in Figure 50. Thus, the twisting of La_9Ge_6 units observed in β-La_5Ge_3Si is made to accommodate the efficient tetrahedral close packing of the La_9Ge_6 structural units. Furthermore, all four germanium atoms (2 Ge(2) and 2 Ge(3)) in the α-structure that lie on the plane of connectivity are actually shared by two La_9Ge_6 units, leaving Ge(1) unshared. This is contrary to that observed in β-La_5Ge_3Si, where all Ge(Si) atoms are shared. The connectivity of La_9Ge_6 units in α-La_5Ge_3Si results in a regular 12 coordination, fused bicapped trigonal prismatic environment around the Ge_2 dimers as shown in Figure 51. The layer arrangement of the La_9Ge_6 units also result in the presence of "dangling" or unshared axial germaniums Ge(1) on the "surface" of the layer-like formation. These germanium atoms are not common vertices of neighboring La_9Ge_6 units. The coordination around two nearest neighboring Ge(1) atoms, as shown in Figure 52, could be described as a slightly distorted bicapped trigonal prisms sharing a common square face. The distances between the nearest "dangling" germanium atoms in α-La_5Ge_3Si are greater than 3.7A and do not constitute bonding interactions. In La_5Ge_4, the distances between Ge(1) atoms are even larger at 3.89A. The observed "tilting" of the Ge(1) atoms from the pseudo-tetragonal axis of the La_9Ge_6 unit toward another Ge(1) atom may represent matrix effects or a tendency to "dimer formation". Nonetheless, the large interatomic distance and the

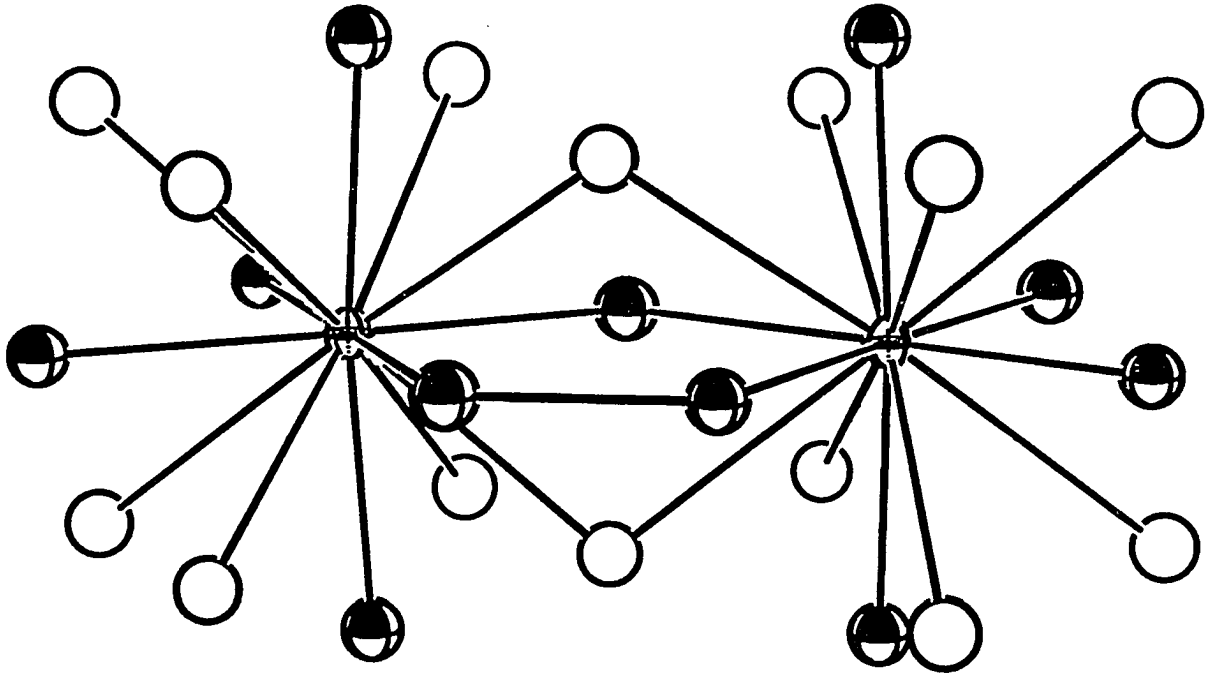

Figure 47. Connectivity of two La_9Ge_6 units in a Sm_5Ge_4-type structure. Open and crossed-hatched circles: La, octant shaded circles: Ge(Si)

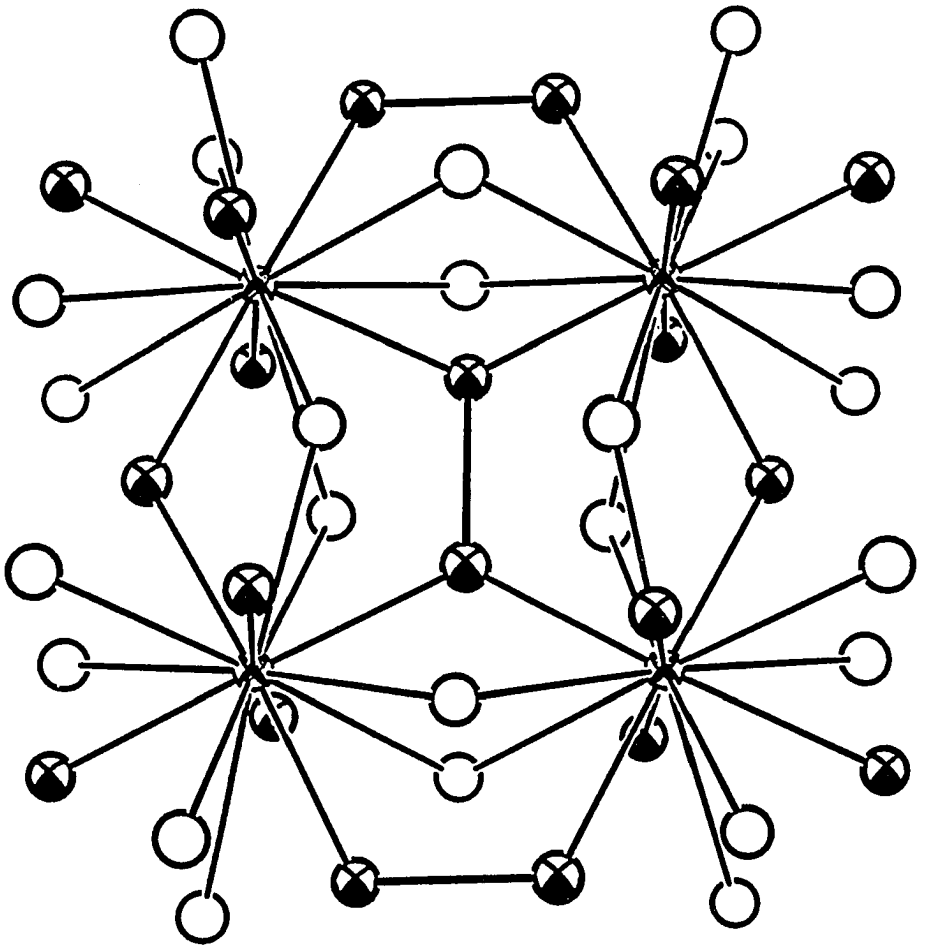

Figure 48. Interconnectivity of the La_9Ge_6 units in a Sm_5Ge_4-type structure forming a layer along the a-c plane. Open and crossed-hatched circles: La, octant shaded circles: Ge

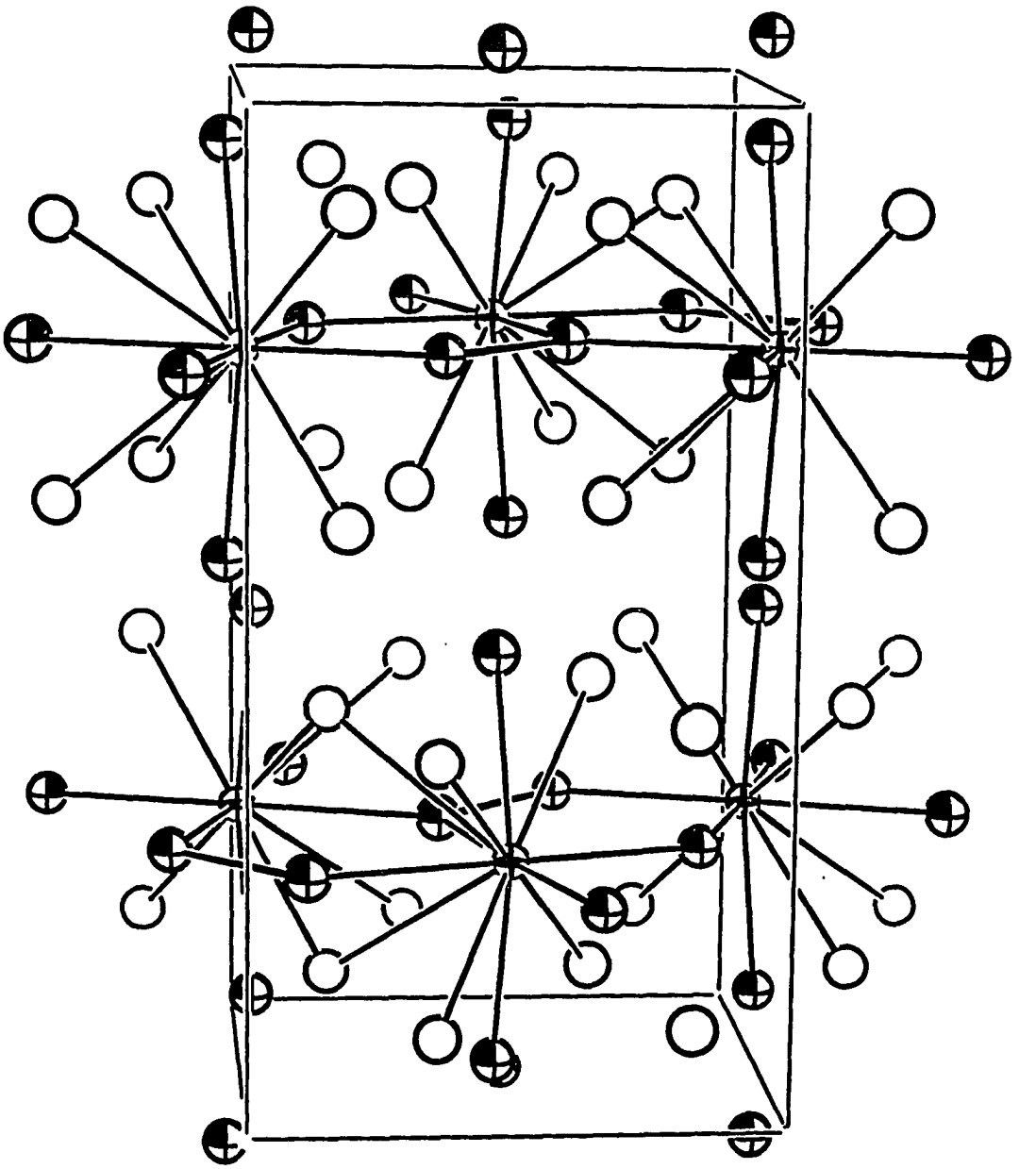

Figure 50. The unit cell of La_5Ge_4 (Sm_5Ge_4-type) drawn with La_9Ge_6 units forming layers along the a-c plane. Open and crossed-hatched circles: La, octant shaded circles: Ge

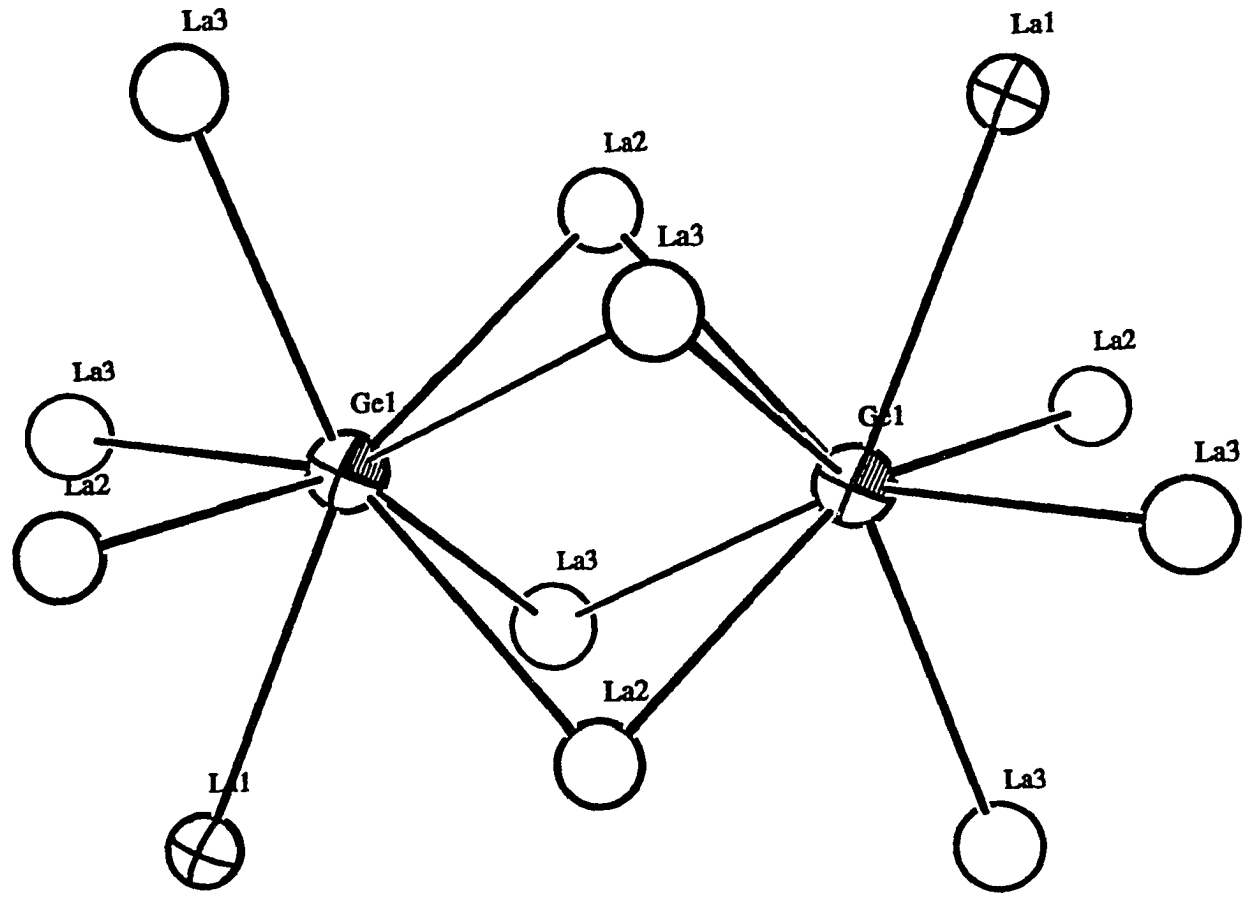

Figure 52. The coordination around two neighboring "apical" Ge(1) atoms in La_5Ge_4. The Ge(1) atoms and its La environment represent the connectivity of La_9Ge_6 units along the b-axis. Open and crossed-hatched circles: La, octant shaded circles: Ge

electronic effects (electron counts) preclude any significant bonding interaction between the "dangling" Ge(1) atoms.

However, the distances between the layers caused by the possible shifting of neighboring layers with respect to each other, as well as the greater tilting of the Ge(1) atoms toward or away from another Ge(1) atom, may result in the close approach of the Ge(1) atoms. This may enable us to tune the electronic count on the Ge(1)-Ge(1) "dimer". The close approach of the "dangling" tetrelide atoms in a Sm_5Ge_4-type structure is in fact observed in La_5Ge_3Ga (to be discussed in the next section) isotypic with the Gd_5Si_4-type.

Applying the electron counting scheme on the two La_5Ge_3Si phases results in Zintl formulations

Sm_5Ge_4-type:

$$[\ 5(La^{3+}) - 2(T^{4-}) - 1(T_2^{6-}) = 1 \text{ electron/formula unit}],$$

Zr_5Si_4-type:

$$[5(La^{3+}) - 2(T_2^{6-}) = 3 \text{ electrons/formula unit}].$$

The results are surprising in that both phases do not satisfy the requirements of a Zintl phase. However, lanthanum-rich silicides have been observed to deviate from the Zintl rules. The existence of La_5Si_3 and La_5Si_4 in the Cr_5B_3-type and Zr_5Si_4-type structures, respectively are examples having more Si_2 dimers than what their electron counts predict. Hence, the simple electronic scheme as applied to polar intermetallics seems to fail in La_5Ge_3Si. The failure could be attributed to strong mixing of the lanthanum orbitals with the tetrelide states that leads to large band widths. This would lower the low lying La-bands and raise the higher lying tetrelide bands and result in the overlap between the

tetrelide-derived and the metal-derived bands. The introduction of a smaller Si atom also enhances the orbital mixing between La states. Hence, this predicts that the compounds La_5Si_3, La_5Si_4, α-, and β-La_5Ge_3Si are metallic. Another possible explanation would be the fractional character of the tetrelide-tetrelide bonds.

Since it is known that the silicide La_5Si_4[263] also exists in the Zr_5Si_4-type, it is possible that β-La_5Ge_3Si is part of a homogeneity range existing in $La_5Si_{4-x}Ge_x$. This is supported by the subsequent synthesis, using arc-melting, of isostructural compounds $La_5Ge_{2.5}Si_{1.5}$ and $La_5Ge_{2.0}Si_{2.0}$. However, the limits of the homogeneity range were not determined and the range the Sm_5Ge_4-type compounds of $La_5Ge_{4-x}Si_x$ exist over remains an open question.

However, annealed reactions of $La_5Ge_2Si_2$ and $La_5Ge_{2.5}Si_{1.5}$ did not result in any observed transformation of the Zr_5Si_4-type into a Sm_5Ge_4-type phase, contrary to what is observed in La_5Ge_3Si. These observations suggest that the phase relationship between the Sm_5Ge_4-type (α-La_5Ge_3Si) and β-La_5Ge_3Si-type compounds are affected by stoichiometry and temperature. Furthermore, the structural relationships and the phase behavior of La_5Ge_3Si indicate that the transformation from the α-phase to the β-phase is best described as first order.

La_5Ge_3Sn and La_5Ge_3Pb

The results in the $La_5Ge_3Si_x$ experiments provided the incentive to synthesize Sn and Pb analogs of La_5Ge_3Si. The results from these synthetic experiments indicate the existence of La_5Ge_3Sn and La_5Ge_3Pb in the Sm_5Ge_4 structure (see Table 37). The compounds were obtained from high temperature reactions of the elements in sealed tantalum containers heated in the high-temperature furnace. Since the high-temperature

furnace did not provide an adequate route to high-temperature phases, and arc-melting routes were inadequate in giving clean reactions for Sn and Pb, quenching reactions were done using reactions in sealed tantalum containers inside an evacuated silica jacket. The reactions were heated in tubular resistance furnaces to 1050°C for two weeks, and the reactions were quenched by dropping the jacketed containers into cold water. Powder diffraction patterns of the quenched reactions did not indicate any β-La_5Ge_3Si-like products. Instead, the diffraction patterns of all the reactions, slow cooled and quenched, indicated a Sm_5Ge_4-type product. Attempts to quench the reactions from higher temperatures were then attempted by using an induction furnace. The reactions in sealed tantalum containers were heated to 1500°C and quenched by liquid N_2 off-gas that was sucked into the evacuated reaction chamber. The results were still identical to that of previous reactions -- there were no tetragonal phases observed. As a final attempt to synthesize a high-temperature phase in both La_5Ge_3Sn and La_5Ge_3Pb, pre-reacted La_5Ge_3Z compounds were arc melted. The powder diffraction patterns of the arc melted reactions revealed again only Sm_5Ge_4-type phases. The absence of a β-La_5Ge_3Si-type phase in the Sn and Pb analogs could be ascribed to the larger sizes of Sn and Pb compared to Si that result in larger interatomic distances between the tetrelides and La, and also between tetrelide atoms. This makes the tetrahedral packing found in β-La_5Ge_3Si unfavorable. An additional factor is the fact that La_5Sn_4[264] and La_5Pb_4[265] both exist in the Sm_5Ge_4 structures and the compounds La_5Ge_3Sn and La_5Ge_3Pb could be part of a solubility range between the various 5-4 phases. The solubility ranges of La_5Ge_4 with La_5Sn_4 and La_5Pb_4 with the Sm_5Ge_4 structure were not determined, but it could be hypothesized to be relatively wider than that existing in La_5Ge_4 and La_5Si_4.

La_5Ge_3Z (Z = Group 13 Elements)

The results of the experiments involving silicon led us to investigate the reactions of La_5Ge_3 with group 13 elements. Simple electron counting rules predict that if a group 13 element were to be substituted into the germanium sites of the La_5Ge_4 structure, it would lead to the Zintl phases La_5Ge_3Ga, La_5Ge_3In or La_5Ge_3Al with a Sm_5Ge_4 structure.

Reactions involving the elements La and Ge with Ga, In or Al in the desired stoichiometry were loaded in welded tantalum containers and heated in a high temperature furnace. The temperature profile was identical to that used in other La_5Ge_3Z compounds. Slow cooling of the reactions was required to obtain single crystals. Guinier powder diffraction patterns of the products in reactions involving Ga and In with the stoichiometry La_5Ge_3Z were similar. Both patterns indexed to an orthorhombic cell of the Sm_5Ge_4-type; a = 7.9099(8)A, b = 15.6558(26)A, and c = 8.2523(8)A. However, the relative intensities of some lines clearly differed from the calculated powder pattern of a Sm_5Ge_4-type model, particularly the relative intensities of the reflections [132] and [231]. This is illustrated in Figure 53. Furthermore, the b/a and b/c ratios of the compounds were larger than that of the corresponding La_5Ge_4 and other known Sm_5Ge_4-type compounds.

La_5Ge_3Ga

Structure determination Hoping to better understand the structure, single crystals of La_5Ge_3Ga were isolated and investigated using a AFC6R Rigaku diffractometer and the TEXSAN crystallographic software. Similar crystals obtained and selected from reactions containing La_5Ge_3In were found to be unsatisfactory.

Four-fold redundant data sets (h, ±k, ±l) up to $2\theta_{max} = 55°$ were collected after an orthorhombic cell was observed, based on the indexing of 25 reflections obtained by SEARCH. Axial photos confirmed the presence of mirror planes perpendicular to the each axes resulting in the Laue symmetry mmm. As no decay corrections were necessary, the data were initially corrected only for absorption (based on three ψ-scans), Lorentz and polarization effects. Following data averaging in the corresponding Laue class, inspection of the reflection data and axial photos indicated reflection conditions corresponding to the space groups Pnma and $Pn2_1a$. The former proved to be correct during refinement. The data were then transformed to the standard setting and refinement proceeded in the usual manner. Other important crystal data are listed in Table 41.

Since the lattice parameters were similar to those found for Sm_5Ge_4 and the possible space groups were the same, a first attempt was made to fit the observed structure factors using the atomic parameters of Sm_5Ge_4. However, initial isotropic refinements using the Sm_5Ge_4 structure as a starting model resulted in unsatisfactory residuals of R = 20%; R_w = 24% even when occupancies were refined. It was evident that the refinement was not going to converge to an acceptable value of R, and direct methods (SHELXS) were employed to provide a better starting model. Since x-ray methods cannot effectively distinguish Ge from Ga, the corresponding peaks were all assigned to Ge. The rough model from direct methods was refined toward completion by using standard full-matrix calculations and Fourier syntheses. The absorption effects were further improved by the application of DIFABS before anisotropic refinement was carried out. The final anisotropic residuals gave R = 3.3%; R_w = 3.6%. The structure solution showed well-behaved thermal parameters and satisfactory esd's. The

Table 41. Data collection and refinement parameters for La_5Ge_3Ga

space group	Pnma
Z	4
crystal dimension	0.08 x 0.08 x 0.12 mm
diffractometer	Rigaku AFC6R
2θ max	55°
collected indices	h, ±k, ±l
reflections:	
measured	5036
observed (>$3\sigma_I$)	3594
independent	981
R_{ave}	13.4% (all data)
no. of parameters refined	50
R (refinement)	3.3%
R_w (refinement)	3.6%
largest parameter shift	0.00
absorption coefficient	316.0 (cm^{-1}, Mo Kα)
secondary extinction coeff.	$5.3(3) \times 10^{-8}$
largest residual peaks	1.7 e^-/A^3
cell parameters (Guinier):	
a = 7.910(1) A	
b = 15.294(2) A	
c = 8.252(1) A	
volume = 1021.9(5)A^3	

Table 42. Refined parameters for La_5Ge_3Ga

atom	x	y	z	Occupancy
La(1)	-0.1504(1)	0.25	-0.0163(1)	1.0
La(2)	0.18325(7)	0.37871(4)	0.17699(7)	1.0
La(3)	0.02506(7)	0.40420(4)	-0.31652(7)	1.0
Ge(1)	0.1501(1)	0.54055(7)	-0.0291(1)	0.992(3)
Ge(2)	0.2388(1)	0.25	-0.1243(1)	0.998(3)
Ge(3)	-0.0224(1)	0.25	0.3969(1)	0.976(4)

U values

Atom	U11	U22	U33	U12	U13	U23
La(1)	0.0205(4)	0.0138(4)	0.0169(4)	0.0	-0.0012(3)	0.0
La(2)	0.0147(3)	0.0099(3)	0.0112(3)	-0.0000(2)	-0.0014(2)	0.0004(2)
La(3)	0.0157(3)	0.0148(3)	0.0130(3)	-0.0031(2)	0.0021(2)	0.0020(2)
Ge(1)	0.0185(6)	0.0119(6)	0.0125(6)	-0.0017(4)	-0.0011(4)	0.0021(4)
Ge(2)	0.0186(6)	0.0136(6)	0.0137(6)	0.0	0.0010(4)	0.0
Ge(3)	0.0138(8)	0.0122(8)	0.0163(8)	0.0	0.0032(6)	0.0

Table 44. Atomic position parameters of different M_5X_4 structures

	La_5Ge_3Ga	Sm_5Ge_4	Gd_5Si_4
M(1)	La(1)	Sm	Gd
x	0.3499(1)	0.2880(8)	0.3560(1)
y	0.25	0.25	0.25
z	0.0163(1)	0.0024(8)	0.0113(1)
M(2)	La(2)	Sm	Gd
x	0.31675(7)	0.3795(5)	0.3164(1)
y	0.62129(4)	0.6157(3)	0.6223(0)
z	0.17699(7)	0.1612(5)	0.1795(1)
M(3)	La(3)	Sm	Gd
x	0.02506(7)	0.0253(5)	0.0289(1)
y	0.40320(4)	0.3996(3)	0.4028(1)
z	0.18348(7)	0.1781(5)	0.1827(1)
X(1)	Ge(2)	Ge	Si
x	0.2388(1)	0.176(1)	0.241(1)
y	0.25	0.25	0.25
z	0.3757(1)	0.367(1)	0.375(1)
X(2)	Ge(3)	Ge	Si
x	0.4776	0.413(1)	0.479(1)
y	0.25	0.25	0.25
z	0.6031	0.612(1)	0.599(1)
X(3)	Ge(1)	Ge	Si
x	0.1501	0.221(1)	0.1435(6)
y	0.54055	0.5449(6)	0.5395(3)
z	0.4709	0.469(1)	0.4716(7)
b/a	1.934	1.928 (1.919):La_5Ge_4	1.970
b/c	1.853	1.906 (1.894):La_5Ge_4	1.903

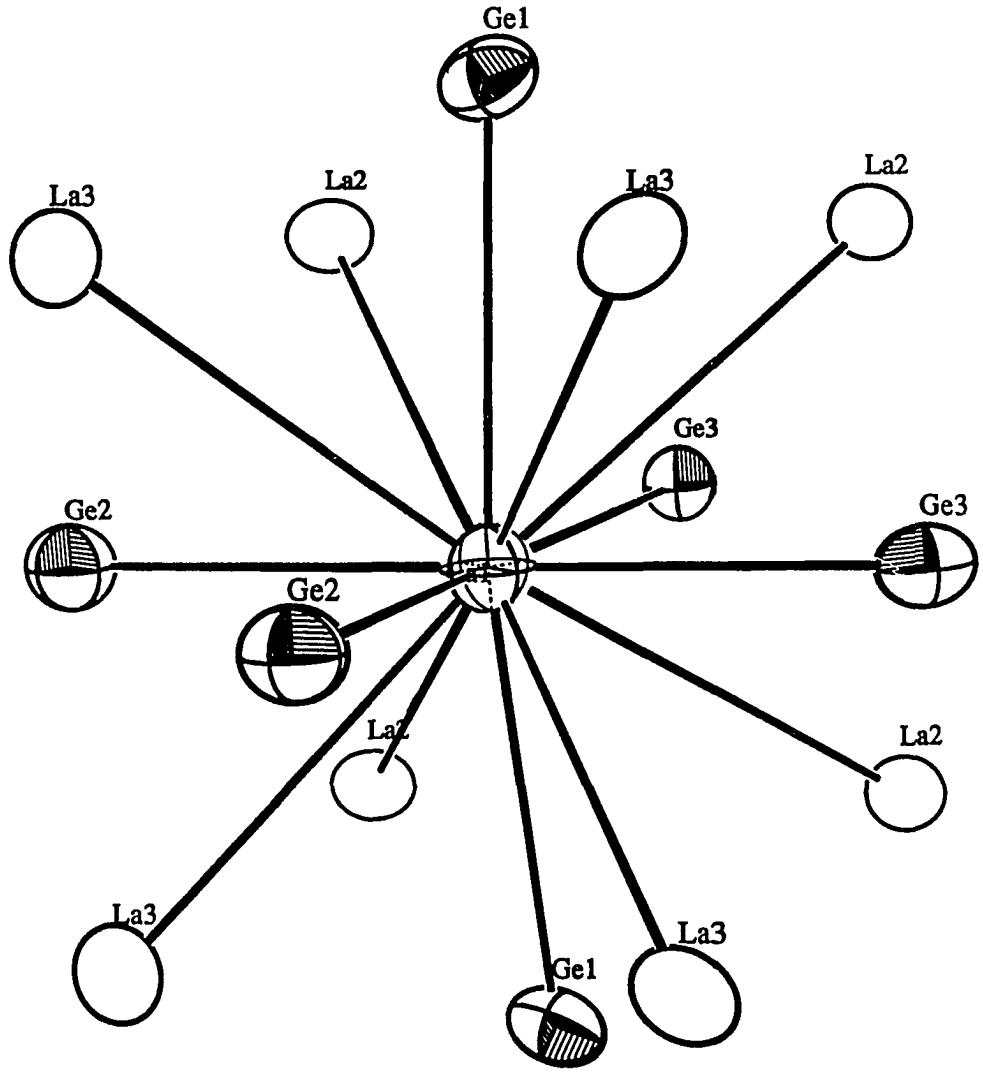

Figure 54. A La_9T_6 (T = Ge, Ga) structural unit in La_5Ge_3Ga (Gd_5Si_4-type). Open and crossed-hatched circles: La, octant shaded circles: Ge = (Ge, Ga)

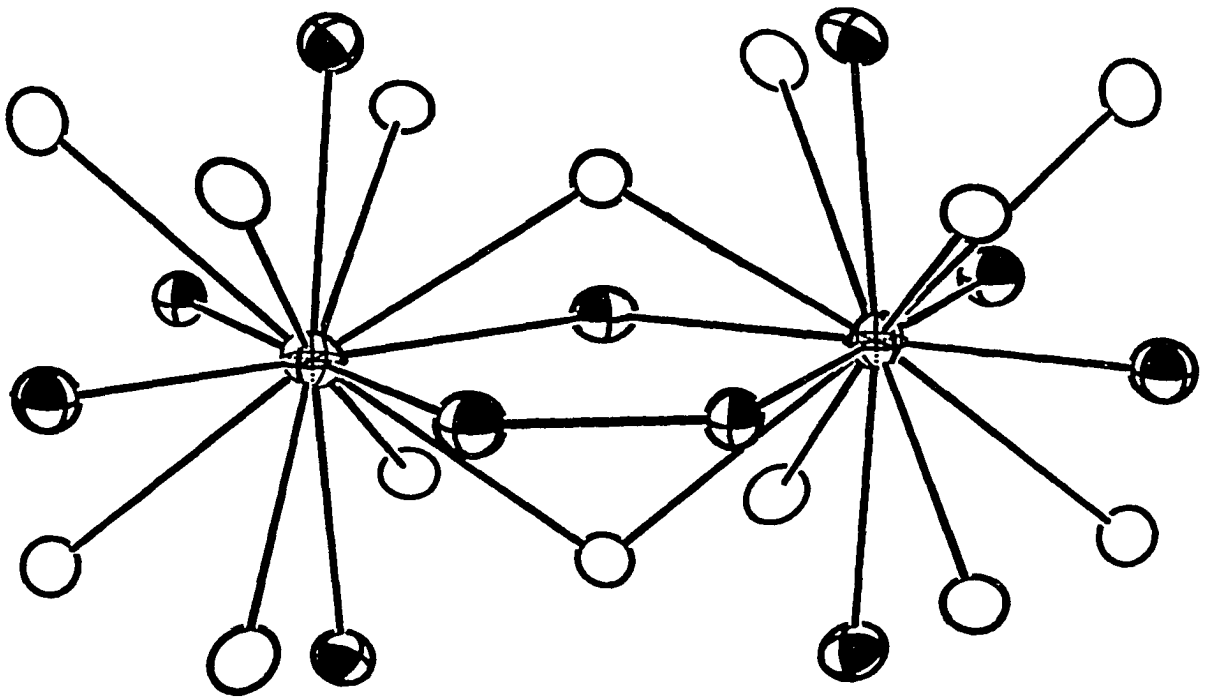

Figure 55. Connectivity of two La_9T_6 units in La_5Ge_3Ga along the a-c plane. This is similar to that found in β-La_5Ge_3Si and La_5Ge_4. Open and crossed-hatched circles: La, shaded octant circles: Ge = (Ge, Ga)

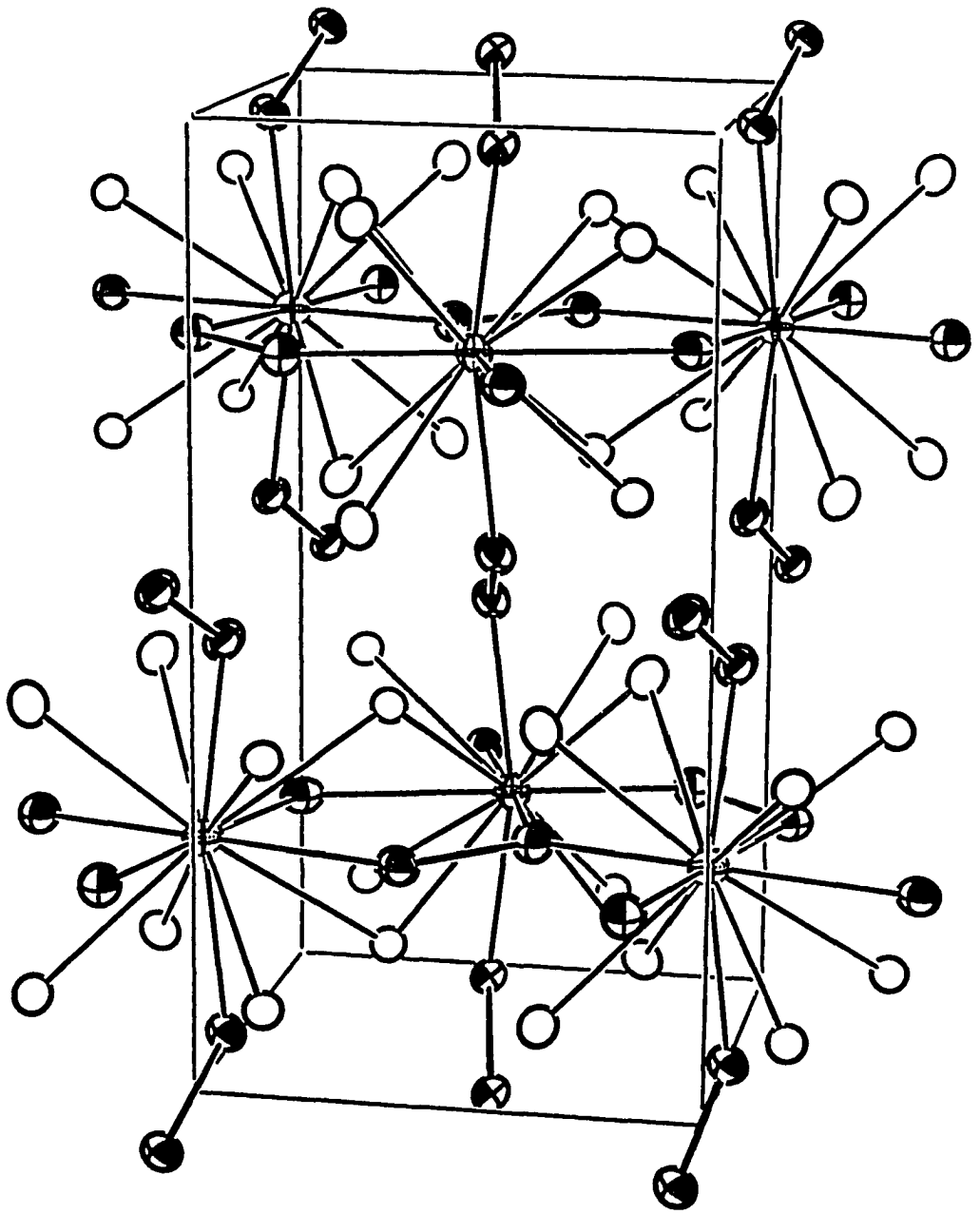

Figure 56. ORTEP drawing of the unit cell of La_5Ge_3Ga. Open and crossed-hatched circles: La, shaded octant circles: Ge = (Ge, Ga). Ellipsoids are drawn at 90% probability

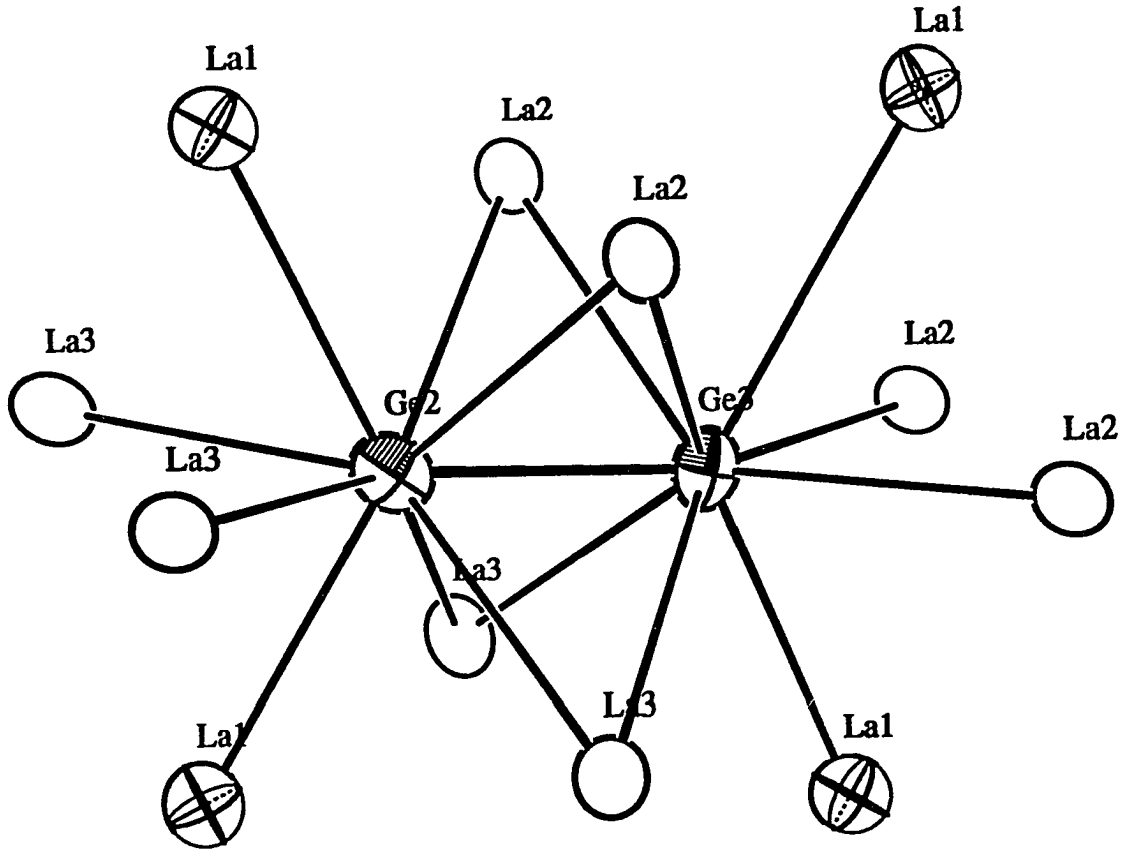

Figure 57. A Ge(2)-Ge(3) dimer and its La coordination. The dimer lies on the a-c plane. Open and crossed-hatched circles: La, shaded octant circles: Ge

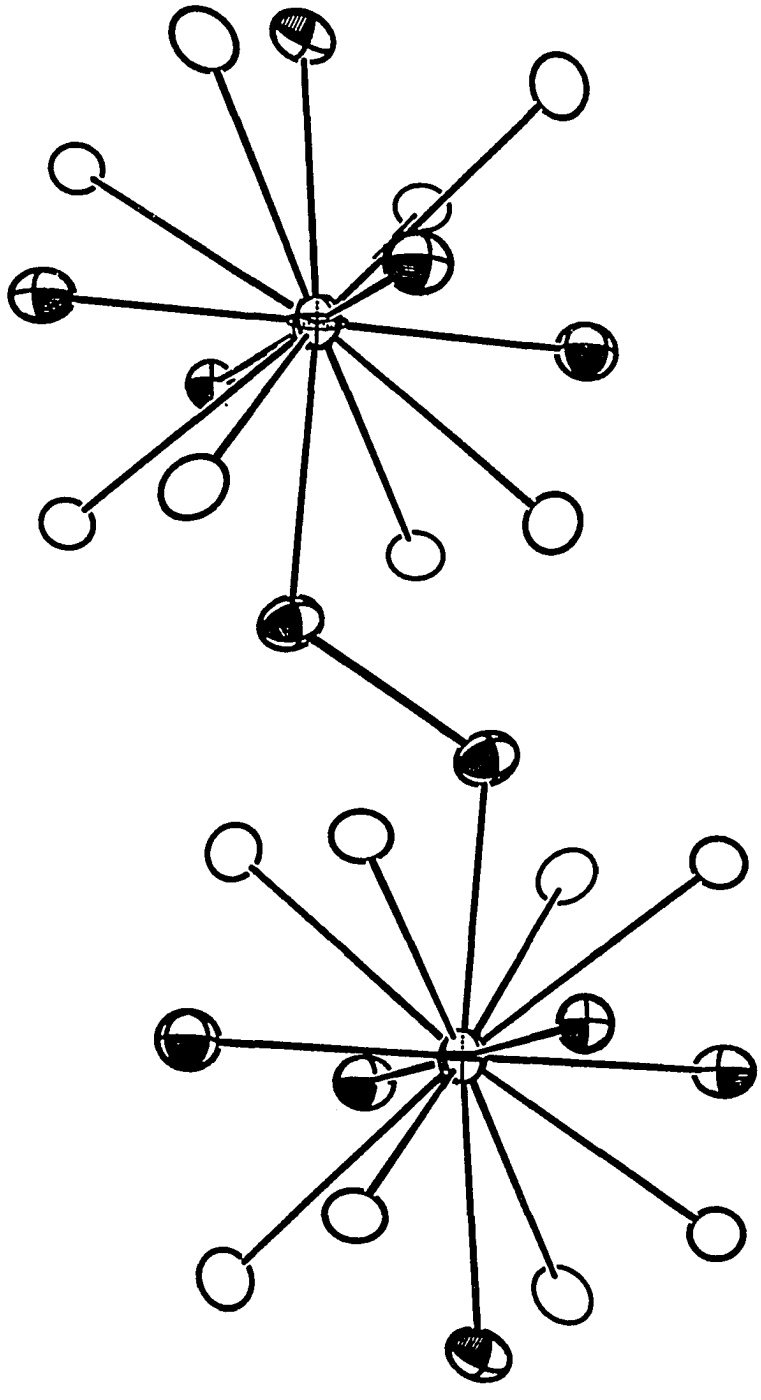

Figure 58. Connectivity of two La_9T_6 units along the b-axis in La_5Ge_3Ga. Note the close approach of the "dangling" Ge(1) atoms

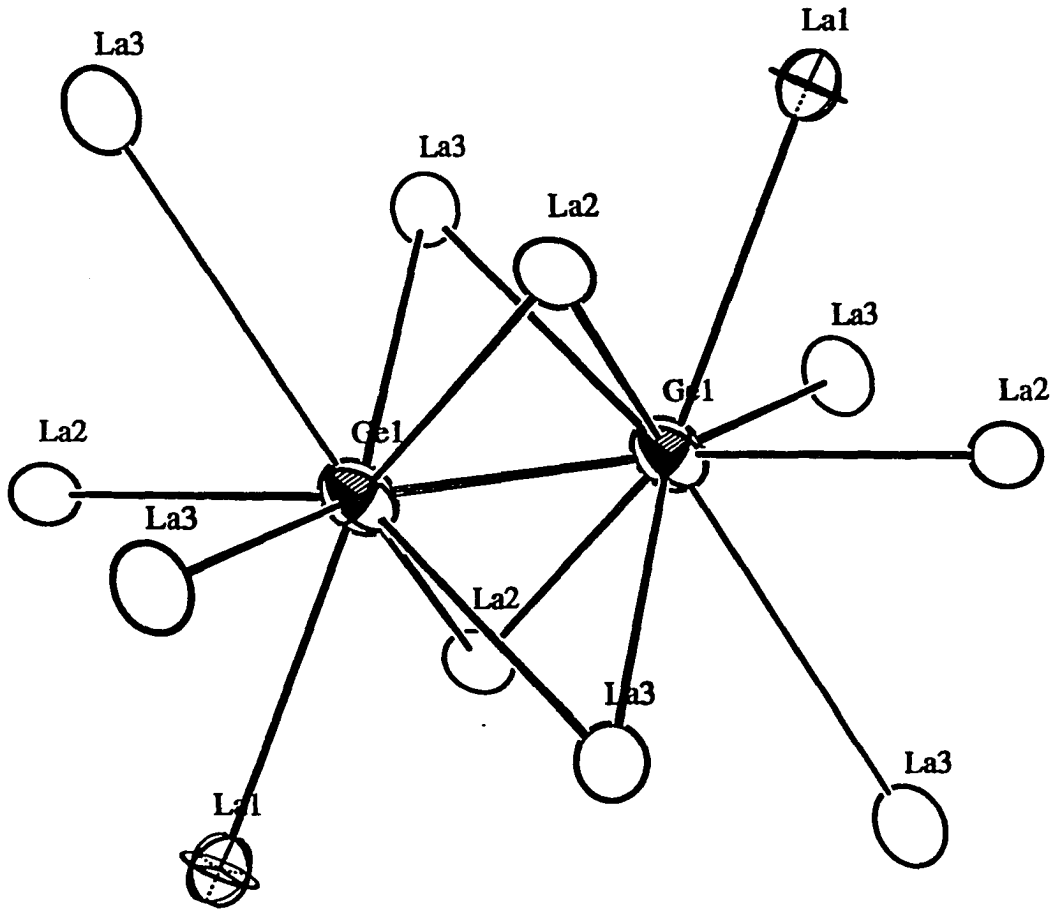

Figure 59. A Ge(1)-Ge(1) dimer and its La coordination. The dimer is formed from the close approach of the "dangling" Ge atoms. Open and crossed-hatched circles: La, shaded octant circles: Ge

some of the electrons if the (Ge,Ga) dimer bonds were fractional. An interesting electron counting experiment would be to decrease the number of electrons contributed by the metal, i.e., substitution (doping) of La by an alkaline earth metal. This could possibly raise some of the metal states above the valence bands and possibly lead to a Zintl phase.

The apparent failure of a simple Zintl picture on the La_5T_4 compounds led us to search for its Zintl-prototype. Our search led us to the Eu_5As_4 structure type.[216] The structure of Eu_5As_4, in the space group Cmca, can be described as a more symmetric variant of the Sm_5Ge_4 and Gd_5Si_4 (Pnma) structure types. The structure, as shown in Figure 60, reveals As_2 dimers and isolated As atoms. In Eu_5As_4 the same M_9T_6 units are connected and arranged in the same manner as that found in Sm_5Ge_4 and Gd_5Si_4. However, the Eu_9As_6 units are more symmetric. The As atoms form an angularly regular octahedron. All angles formed by the As atoms at the vertices and the central Eu atom are 90°. The regular octahedral shape of the $EuAs_6$ fragment results in the absence of any bonding interactions between the "dangling" As atoms (d>4.0A). Hence, the structure satisfies the electron count for a Zintl phase if Eu were divalent.

$$[10e^-(Eu^{2+}) - (\text{isolated})\ 2As^{3-} - (\text{dimer})\ As_2^{4-}] = 0.$$

Yet, there have been no reports of other compounds being isostructural with Eu_5As_4. As illustrated in Figure 61, the calculated powder pattern of La_5Ge_4 with the Eu_5As_4 structure, however, is similar to its powder patterns with the parameters of Sm_5Ge_4 and Gd_5Si_4 structure types. The fact that most of previously reported Sm_5Ge_4-type compounds were established by Debye-Scherer methods may indicate the possibility that some are actually of the Eu_5As_4-type.

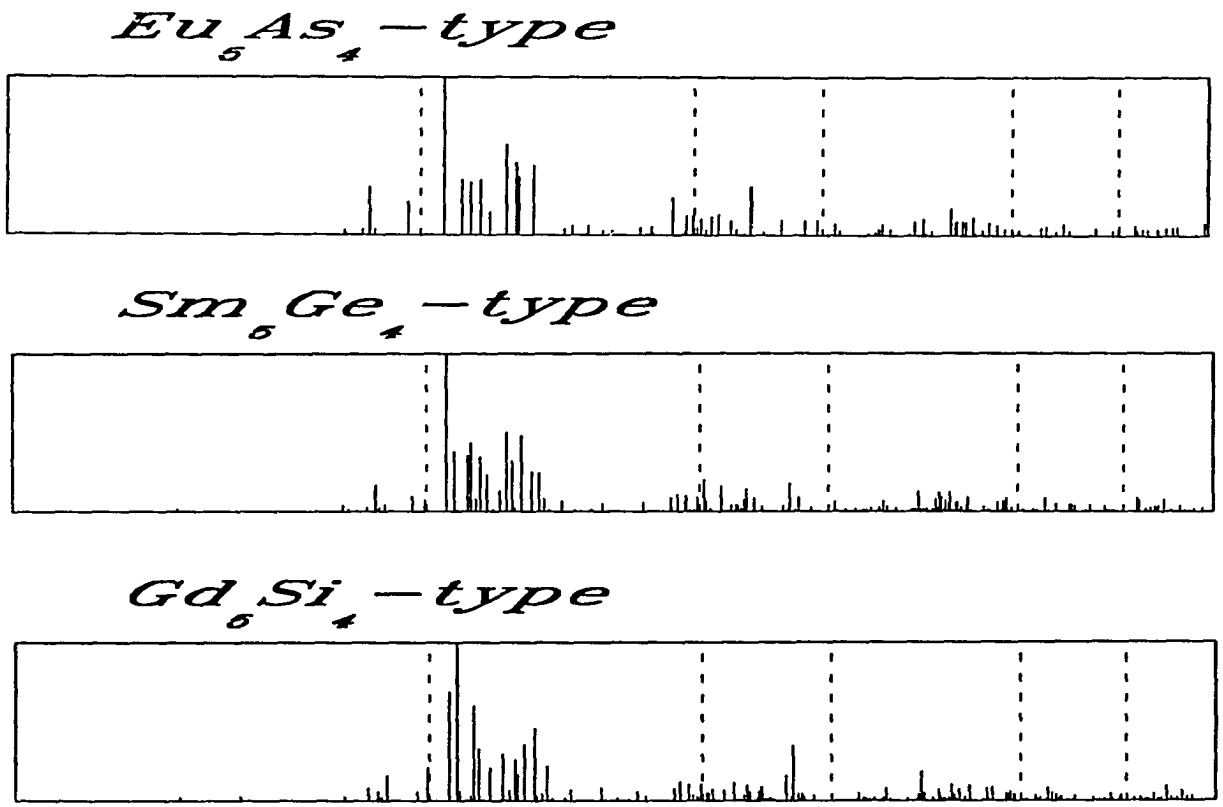

Figure 61. Calculated Guinier powder diffraction patterns of La_5Ge_4 having the Eu_5As_4 (top), Sm_5Ge_4 (middle), and Gd_5Si_4 (bottom) structure types. The tetragonal cell is derived by averaging the short axes of the orthorhombic cell. Dashed lines indicate the silicon reference lines

The different 5-4 type structures discussed all have the common unit M_9X_6. In a formal sense, we can also associate this building unit with an analogous anti-type, a filled-M_6X_8Z unit found in many metal cluster compounds. The differences between the different 5-4 tetrelide compounds lie on how the M_9X_6 units are interconnected and arranged in space. Dimers may assemble or disassemble themselves based on how the units are linked with one another.

The structural preference between the Zr_5Si_4-type structure and the Sm_5Ge_4-type related structures maybe dominated by the size factors that affect the packing of the M_9T_6 units. Electronic effects in the Zr_5Si_4-types are of minor significance because a Sm_5Ge_4-type arrangement also allows for the dimerization of all the tetrelides. However, the effective tetrahedral packing of the 9-6 units in Zr_5Si_4 leads to a smaller coordination spheres around the T_2 dimers. This is clearly favored by smaller tetrelides.

The Sm_5Ge_4-type arrangement evidently allows more structural variety. Depending on the tendency to form dimers, the Sm_5Ge_4 structure probably accommodates a wider range of electron counts. It has been suggested that in understanding rare-earth metal compounds with main group metalloids in terms of the Zintl concept, one has to include the electronic effects of the 4f-orbitals.[266] This occurs particularly in cases where there are more homoatomic bonds between main-group metalloids than the Zintl counting rule would predict. However, more synthetic and physical studies on ternary and binary rare-earth-metal compounds have to be undertaken to validate the idea. Thus, the preferences between the various Sm_5Ge_4-type arragements is probably governed by electronic factors that are yet to be completely understood.

La_5Ge_3Al and La_5Ge_3In

Reactions of La_5Ge_3 with Al resulted in products with complicated powder diffraction patterns. Although a Mn_5Si_3-type phase could be detected, its exact stoichiometry could not be determined. Another phase which could be assigned with $LaAl_2Ge_2$[267] (anti-La_2O_3-type) was also observed. Electron counts for the compound show it has one electron more than its structure would suggest. The possibility of interstitial stabilization or phase width determination were not pursued. The presence of other powder diffraction lines that could not be indexed to known La-Al-Ge ternaries characterized most reactions. Our interest on the La-Al-Ge system was based on the relationships of LaAlGe to the $ThSi_2$ and LaPtSi structures. This is in relation to our investigations on $LaGe_{2-x}$.[204]

The synthetic products for the indium analog La_5Ge_3In were in most cases identical to the Ga reactions. The compound La_5Ge_3In was indexed and found to be isostructural with La_5Ge_3Ga. Although the exact In-In distances corresponding to the Ge(1) dimers could not be determined. Nevertheless, the difference of the relative intensities of the [132] and [231] lines aided in differentiating the (2-dimer) La_5Ge_3Ga structure from the (single-dimer) Sm_5Ge_4- and Eu_5As_4-types. Efforts to grow single crystals of La_5Ge_3In by prolonged heating and slow cooling failed. Further investigations on the ternary system of lanthanum, indium and germanium resulted in the syntheses of two new metal-rich compounds La_3In_4Ge and La_3InGe.[268] These new and interesting compounds exhibit novel In-In substructures that include significant In-In interactions, represented by interconnected tetrahedral In_4 clusters in La_3In_4Ge, and In_2 dimers in La_3InGe.

TERNARY RUTHENIUM DERIVATIVES

The propensity of Ru to form metal bonded networks with rare-earth metals directed us to separately discuss novel ruthenium compounds obtained from our exploratory investigations on rare-earth-ruthenium-tetrelides. Our investigations on the ternary La-Ru-Ge system in a narrow stoichiometric region near $La_5(Ge,Ru)_3$ was surprisingly prolific. Moreover, work in this laboratory on ruthenium-centered rare-earth-metal iodide clusters have yielded an assortment of novel metal-metal chains.[269]

As previously presented, a variety of intermetallics have been prepared that involve Ru as interstitials namely, La_5Ge_3Ru, and $La_{15}Ge_9Ru$. The syntheses of these compounds indicated Ru behaves in a similar manner to 3d transition metals. However, the similarity ends with the subsequent syntheses of $La_4Ge_{2.5}Ru_{1.1}$,[270] which can be considered a partially filled La_4Ge_3, as well as the preparation of the new compounds, La_5RuGe_2 and Nd_5RuGe_2 with a novel chain structure.

Published work on ternary compounds involving rare-earth metals, ruthenium and the tetrelides have been meager, in spite of the numerous publications on molecular ruthenium coordination compounds that exhibit metal-metal bonding. Literature search of known La-Ru-Ge intermetallic phases revealed only 3 known ternary compounds[255], namely $LaRu_2Ge_2$, $LaRuGe_3$, and $La_2Ru_3Ge_5$. Phases richer in their metal components have yet to be reported. A similar situation exists with other rare-earth metals.

The new rare-earth metal ruthenium germanide compounds were synthesized at high temperatures (>1250°C) from the elements (cold pressed La shavings, Ge ingots and

Ru powder) inside welded Ta containers. Heating was done with the aid of the high-temperature furnace equipped with a programmable ramp and soak controller.

The temperature profile most successful in synthesizing the ruthenium compounds involved heating from room temperature to 1150°C in two days, and after equilibration the temperature is slowly raised to 1300°C in one day and kept at that temperature for another 3 days. The temperature is slowly decreased to 1100°C in four days and annealed for another 4-7 days. Afterward the reaction is finally slow cooled to 350°C in three days. These steps produced single phase products with well faceted crystals many of which proved single.

Nd_5RuGe_2 and La_5RuGe_2

Previous investigations in the area of syntheses and characterization of transition metal (T)-centered reduced rare-earth metal iodides have led to the discovery of families of compounds rich in structural variety. Many of these novel "alloy-clusters", particularly those containing Ru and rare-earths, show interesting metal-metal bonding in clusters between the Ru interstitial and the rare-earth metal atoms.

Parallel to these ideas, attempts were made to synthesize structurally-related rare-earth metal ruthenium-rich germanides. It was hoped that interesting rare-earth metal-ruthenium clusters in a matrix of germanium atoms would be synthesized. Furthermore, research on metal-rich rare-earth-metal ruthenium germanides have been sparse and any outcome would be interesting. Results of these speculative ideas resulted in the synthesis of Nd_5RuGe_2 and its lanthanum analog, La_5RuGe_2. The structures of these compounds can be related to the Yb_5Sb_3 and Rh_5Ge_3 structure types. Taking into account the short

adequate crystal. Single crystal structure determination of the compound proceeded using an Enraf-Nonius CAD4 diffractometer and the SDP software.

An orthorhombic cell with a = 12.098(3); b = 8.877(2); c = 7.900(2) A was determined by indexing 25 reflections obtained by the program SEARCH. Axial photos confirmed its mmm symmetry represented by three mutually perpendicular mirror planes. Accurate cell parameters were later calculated by least squares fit of the experimental powder diffraction pattern to the theoretical powder pattern based on the refined crystal structure. Two octants of data were collected up to 2θ of 60.0°. Four ψ-scans were measured and used in the empirical absorption correction. Other important crystal data are listed in Table 45.

Additional reflection conditions 0kl; k+l = 2n, hk0; h+k = 2n, h00; h = 2n, 0k0; k = 2n, and 00l; l = 2n were observed after the intensities of the reflections were carefully examined. These conditions led to Pnma as the possible space group. As no decay corrections were necessary (net intensity change 0.2%), the two sets of redundant data were averaged for Laue class mmm, R_{ave} = 7.4%, after an empirical absorption correction was applied. Then SHELXS direct methods were employed to provide initial models for least squares refinements. The rough model was refined toward completion by using standard least-squares, full-matrix calculations and difference Fourier maps. Isotropic refinement resulted in residuals of R = 5.4%; R_w = 7.1%. Additional absorption corrections using DIFABS was applied before beginning anisotropic refinements. Anisotropic refinement, with ideal occupancies, proceeded smoothly to final residuals of R = 3.1; R_w = 3.6%. At the final stage of the structure determination, the occupancies of both Ru and Ge sites were studied by varying their multiplicities and thermal parameters

simultaneously. This resulted in 99.0(3)% occupied Ru positions and 100.3(4)% occupied Ge sites, indicating insignificant mixing of Ru and Ge at both sites. These two positions were then fixed at 100% occupancies in the final refinement corresponding to the formula Nd_5RuGe_2. A final Fourier difference map revealed the largest residual peak of 2.3 e^-/A^3 near Nd(3) (~0.3A). The positional and thermal parameters are listed in Table 46, and the important distances and angles calculated with lattice constants from powder diffraction data are reported in Table 47.

The refined formula was later confirmed by the subsequent high temperature synthesis of the compound in very high yield with stoichiometric amounts of the elements. However, studies to determine the presence of a homogeneity range in the compound were not pursued.

Attempts were made to synthesize the lanthanum analog. The compound La_5RuGe_2 was obtained from the high-temperature reactions of the elements in stoichiometric proportions. Its resulting powder diffraction pattern was completely indexed with the Nd_5RuGe_2 structure resulting in unit cell dimensions, a = 12.204(3)A; b = 8.978(1)A; and c = 8.103(1)A.

Structure description The structure of Nd_5RuGe_2, based on a comparison of unit cell axial ratios and atomic positional parameters, can be derived from the orthorhombic Yb_5Sb_3 structure.[275] The structure was previously described as a column structure of [Yb_6Sb] trigonal prisms forming hexagonal channels occupied by [Yb_2Sb_2] rhomboid "ribbons".[274] Likewise, its structural relationship with the Mn_5Si_3 and Y_5Bi_3 structures has been discussed by Wang.[276] A literature search revealed that other reported structure types, U_3S_5,[277] Ca_5Sb_3,[278] and Ca_5Bi_3[279] can likewise be considered

Table 46. Refined parameters for Nd_5RuGe_2

atom	x	y	z	Occupancy
Nd(1)	0.21470(8)	0.25	0.83681(8)	1.0
Nd(2)	0.07216(7)	0.46967(7)	0.18455(6)	1.0
Nd(3)	0.99859(7)	0.25	0.53286(8)	1.0
Nd(4)	0.79599(8)	0.25	0.14172(8)	1.0
Ru	0.4843(1)	0.25	0.5728(1)	0.990(3)
Ge	0.1709(1)	0.5047(1)	0.3969(1)	1.003(4)

U values

Atom	B11	B22	B33	B12	B13	B23
Nd(1)	0.55(3)	0.86(3)	0.79(2)	0.0	-0.08(2)	0.0
Nd(2)	0.78(3)	1.08(2)	0.81(1)	0.03(2)	-0.10(2)	0.03(1)
Nd(3)	0.44(3)	0.96(3)	0.85(2)	0.0	0.03(2)	0.0
Nd(4)	0.46(4)	0.97(4)	0.77(2)	0.0	-0.05(2)	0.0
Ru	0.73(5)	0.99(4)	1.23(3)	0.0	0.19(3)	0.0
Ge	0.34(5)	0.70(4)	0.91(3)	0.01(5)	-0.06(3)	0.06(3)

Table 47. Important interatomic distances and angles in Nd_5RuGe_2

atom	atom	distance	atom	atom	distance
Nd(1)	Nd(2)	3.785(1) (2x)	Nd(2)	Nd(4)	3.887(1) (2x)
Nd(1)	Nd(2)	3.780(1) (2x)	Nd(2)	Nd(4)	3.604(1) (2x)
Nd(1)	Nd(3)	3.550(1) (2x)	Nd(2)	Ru	3.011(1) (2x)
Nd(1)	Nd(3)	3.585(1) (2x)	Nd(2)	Ru	2.7274(8) (2x)
Nd(1)	Nd(4)	3.905(1) (2x)	Nd(2)	Ge	3.268(1)
Nd(1)	Ru	3.872(1) (2x)	Nd(2)	Ge	3.251(1)
Nd(1)	Ru	2.877(1) (2x)	Nd(3)	Nd(4)	3.947(1) (2x)
Nd(1)	Ge	3.150(1) (2x)	Nd(3)	Nd(4)	3.849(1) (2x)
Nd(1)	Ge	3.159(1) (2x)	Nd(3)	Ru	3.121(1) (2x)
Nd(2)	Nd(2)	3.4411(7)	Nd(3)	Ge	3.087(2) (2x)
Nd(2)	Nd(3)	3.4881(8) (2x)	Nd(3)	Ge	3.094(2) (2x)
Nd(2)	Nd(3)	3.4509(7) (2x)	Nd(4)	Ru	2.843(1) (2x)
			Nd(4)	Ge	3.191(1)

Distances are in Angstroms. Estimated standard deviations in the least significant figure are given in parentheses

Interatomic angles,

atom	atom	atom	angle(°)	atom	atom	atom	angle(°)
Nd(1)	Ru	Nd(1)	133.03(3)	Nd(2)	Ru	Nd(2)	153.88(4)
Nd(1)	Ru	Nd(2)	131.39(4)	Nd(2)	Ru	Nd(4)	83.17(4)
Nd(1)	Ru	Nd(2)	67.33(4)	Nd(2)	Ru	Nd(4)	89.53(5)
Nd(1)	Ru	Nd(4)	157.78(5)	Nd(1)	Ru	Nd(2)	79.96(4)
Nd(2)	Ru	Nd(2)	80.73(4)	Nd(1)	Ru	Nd(2)	99.34(5)
Nd(2)	Ru	Nd(2)	73.50(3)	Ru	Nd(2)	Ru	106.50(3)

Angles are in degrees. Estimated standard deviations in the least significant figure are given in parentheses

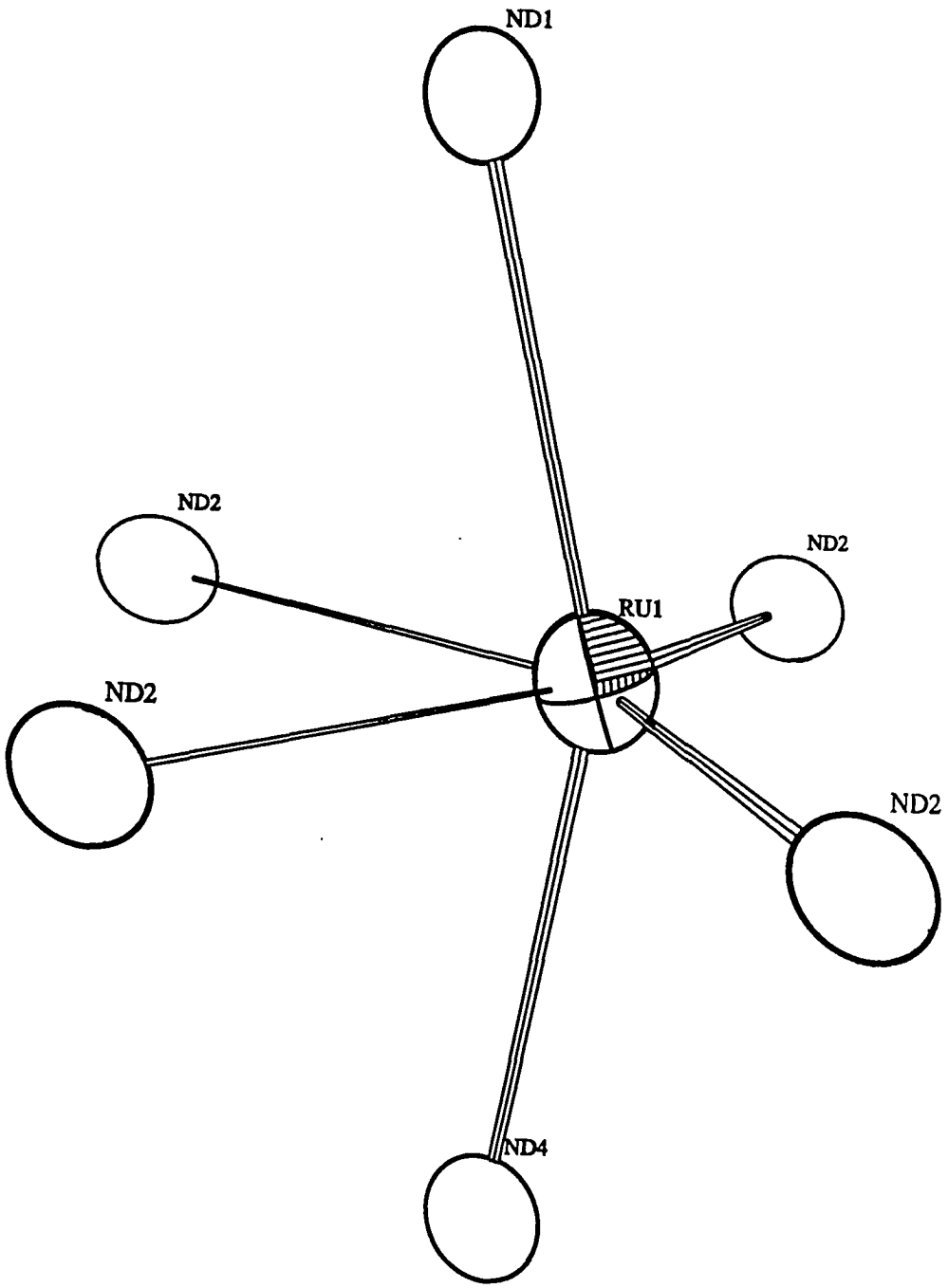

Figure 62. The Nd coordination around Ru in Nd_5RuGe_2. Thermal ellipsoids are drawn at 90% probability. Open circles: Nd, octant shaded circles: Ru

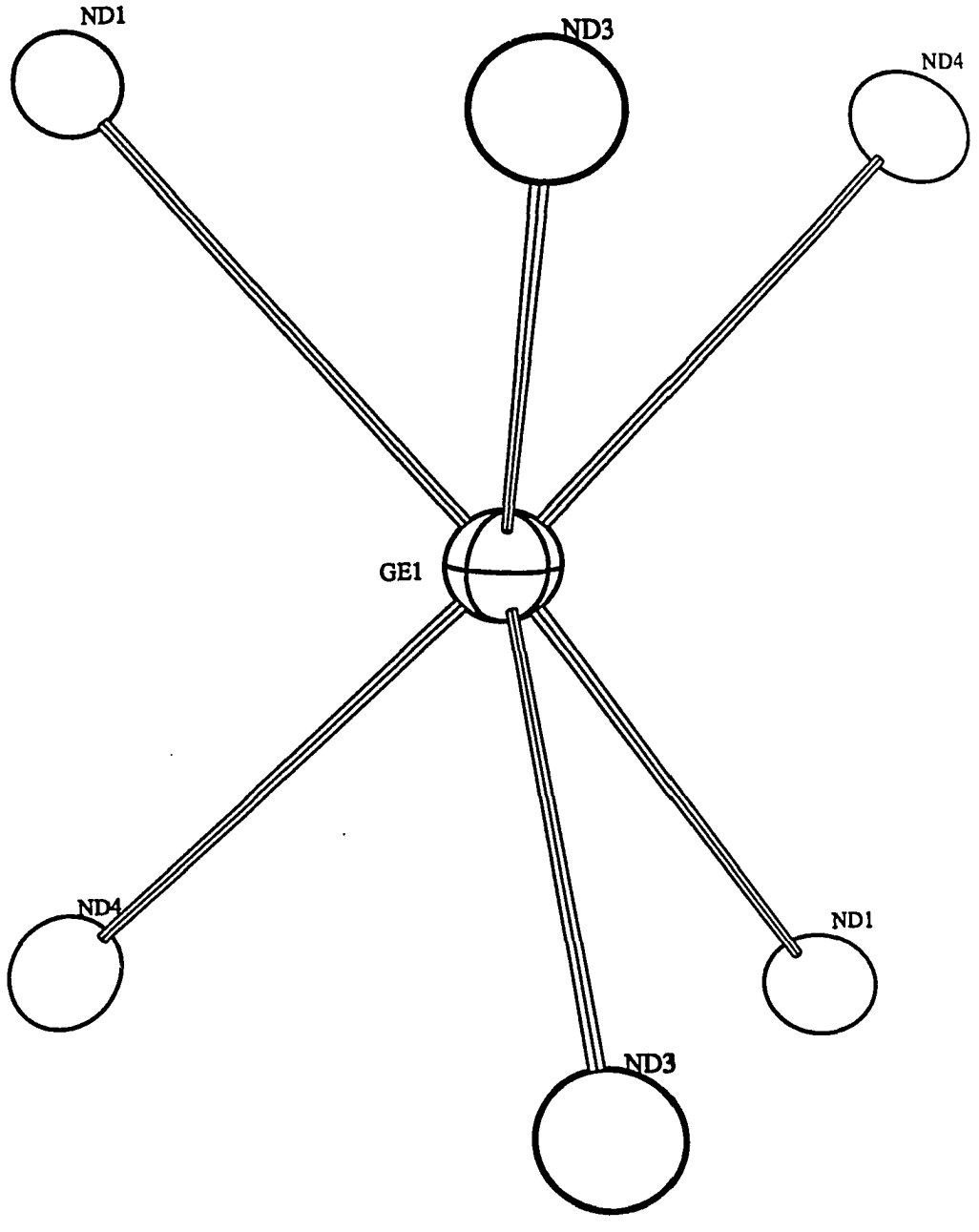

Figure 63 The trigonal prismatic coordination around Ge in Nd_5RuGe_2. Thermal ellipsoids are drawn at 90% probability. Open circles: Nd, crossed-hatched circles: Ge

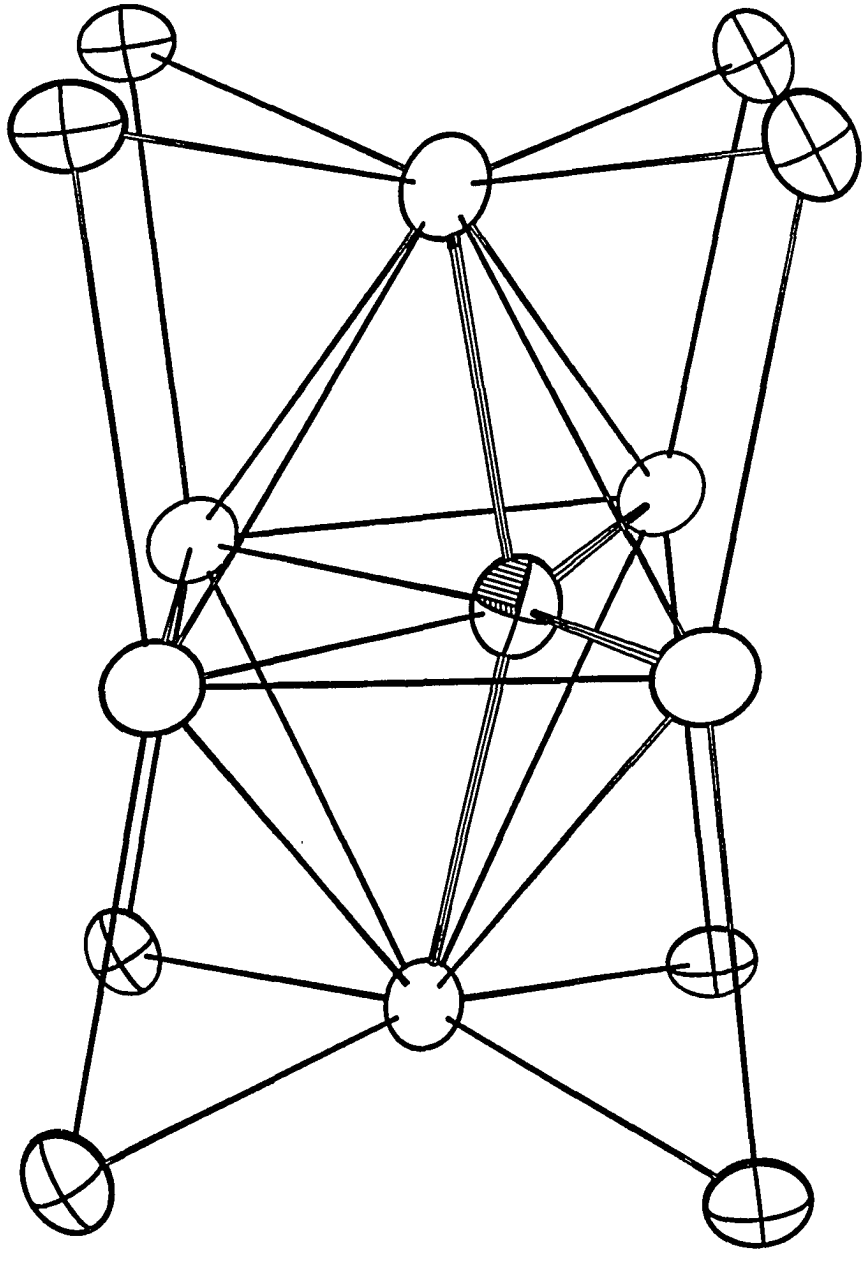

Figure 64. A $RuNd_6Ge_8$ unit in Nd_5RuGe_2. Note the displacement of Ru from the center of the Nd_6 octahedron resulting in four long and two short Nd-Ru distances. Open circles: Nd, crossed-hatched circles: Ge, octant shaded circle: Ru. Thermal ellipsoids are drawn at 90% probability

are connected to form trans-edge sharing metal chains within the hexagonal channels of germanium. The germanium atoms act as axial edge-bridging ligands between neighboring octahedra and sheath the chains of Nd_6Ru distorted octahedra. This structural chain unit results in a stoichiometry Nd_4RuGe_4. The Nd_4RuGe_4 metal chains are similar to the ruthenium centered rare-earth-metal iodide cluster chains present in Pr_4I_5Z.[280] However, the alternate displacements of neighboring Ru atoms from the octahedral center leads to a zigzag chain arrangements of the ruthenium atoms within the Nd_4RuGe_4 chains along [010] not present in the reduced iodides. The formal Nd_4RuGe_4 chain is shown in Figure 65. Its differences with the chains in Pr_4I_5Ru lie in the location of the Ru atoms in the octahedral unit of the metal chains, the absence of terminal ligands, and the interconnectivity of the chains.

The Nd_4RuGe_4 chains are connected to other chains through the sharing of the edge-bridging germanium atoms (see Figures 65 and 66). Each germanium atom is shared by two Nd_4RuGe_4 chains acting as axial edge-bridging ligands to both chains. The two chains that share an edge-bridging germanium atom have their principal axes twisted in opposite directions from the principal axis (b-axis) of the unit cell (see Figure 66). The germanium atoms also formally bridge an equatorial edge of another Nd_4RuGe_4 chain but the Nd-Ge distance of the equatorial edge-bridging fragment is significantly larger (>3.7A) than the Nd-Ge distances (3.1 - 3.3 A) of the axial Ge bridges. Hence, a single chain is essentially $Nd_{4/2}Nd_2RuGe_{8/2} = Nd_4RuGe_4$ and the connectivity of the chains results in the formula $Nd_4RuGe_{4/2} = Nd_4RuGe_2$. The 3-D network of Nd_4RuGe_2 also results in nominal square prism channels along [010] formed by Nd(2)

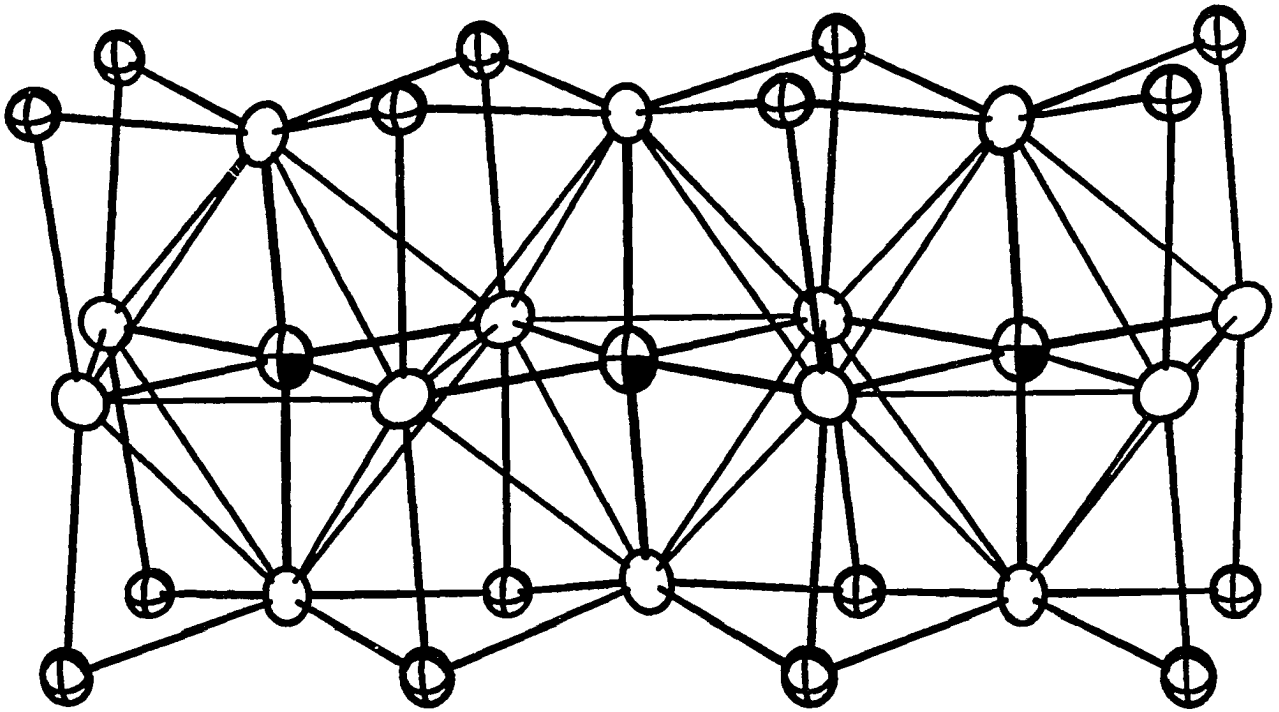

Figure 65. A formal Nd_4RuGe_4 chain; $[Nd_2(Nd_{4/2})Ru(Ge_{8/2})]$, in Nd_5RuGe_2. Open circles: Nd, crossed-hatched circles: Ge, octant shaded circles: Ru

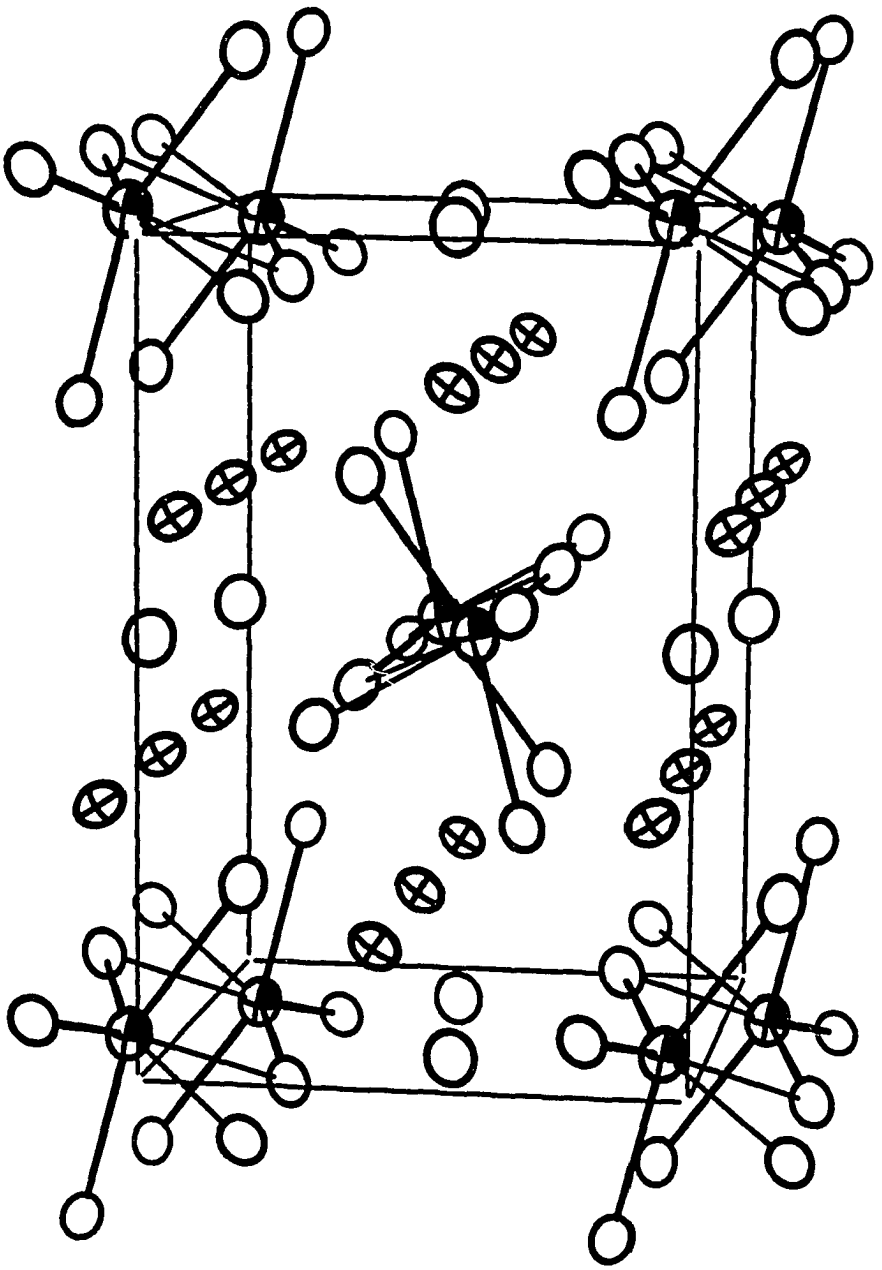

Figure 66. An ORTEP view along [010] of the Nd_5RuGe_2 unit cell. Note the connectivity of the Nd_4RuGe_4 chains via edge bridging Ge atoms. Open circles: Nd, crossed circles: Ge, octant shaded circles: Ru

and germanium atoms. These formally eight coordination sites are occupied by another Nd atom (Nd(3)). However, the distortions in the Nd_6Ru octahedra result in close approaches of two Nd(1) atoms and Ru (3.12A) as shown in Figure 67. However the shortest Nd(3)-Ru distance is 0.1A longer than any of the Nd-Ru distances in the distorted octahedron. It can be inferred that the close approach of the extra Nd(3 atoms may be related to the distortion observed in the Nd_6Ru octahedra.

A formal electron count on the condensed cluster chain $[Nd_4Ge_4Ru]^{3-}$ results in

$$[(4(Nd^{3+}) \times 3) - ((4/2)(Ge^{4-}) \times 4) + (8(Ru) \times 1) = 15e^- \text{ per Ru.}$$

This counting indicates that an isoelectronic relationship with Pr_4I_5Ru (15 e^- per Ru). It is tempting to suggest a structure bonding correlation between a very polar compound Pr_4I_5Ru and the intermetallic Nd_5RuGe_2. Since the similarity is so striking, the electronic factors that govern both structures must be, in a certain way, closely related. The d(Nd-Ru) found in Nd_5RuGe_2, 2.73 -3.01 A, is comparable to those calculated for trigonal prismatic environments around Ru in the intermetallics Nd_5Ru_2 (2.75 A) and Nd_3Ru (2.90 A).[281] This is similar to the trend found in Pr_4I_5Ru and in contrast to the differences commonly observed in the more oxidized cluster phases where host-Z distances differ from the corresponding distances in intermetallics by values in excess of 0.2 A. This trend can be used as a measure of the polarity of the bonding in reduced phases.

Magnetic data The magnetic susceptibility data corrected for core diamagnetism of Nd_5RuGe_2 and the isostructural La_5RuGe_2 are shown in Figures 68 and 69. The paramagnetic property illustrated in Nd_5RuGe_2 follows the Curie-Weiss law over the temperature range 55 - 298 K, with a Curie-Weiss constants $\theta = 45.02$ K;

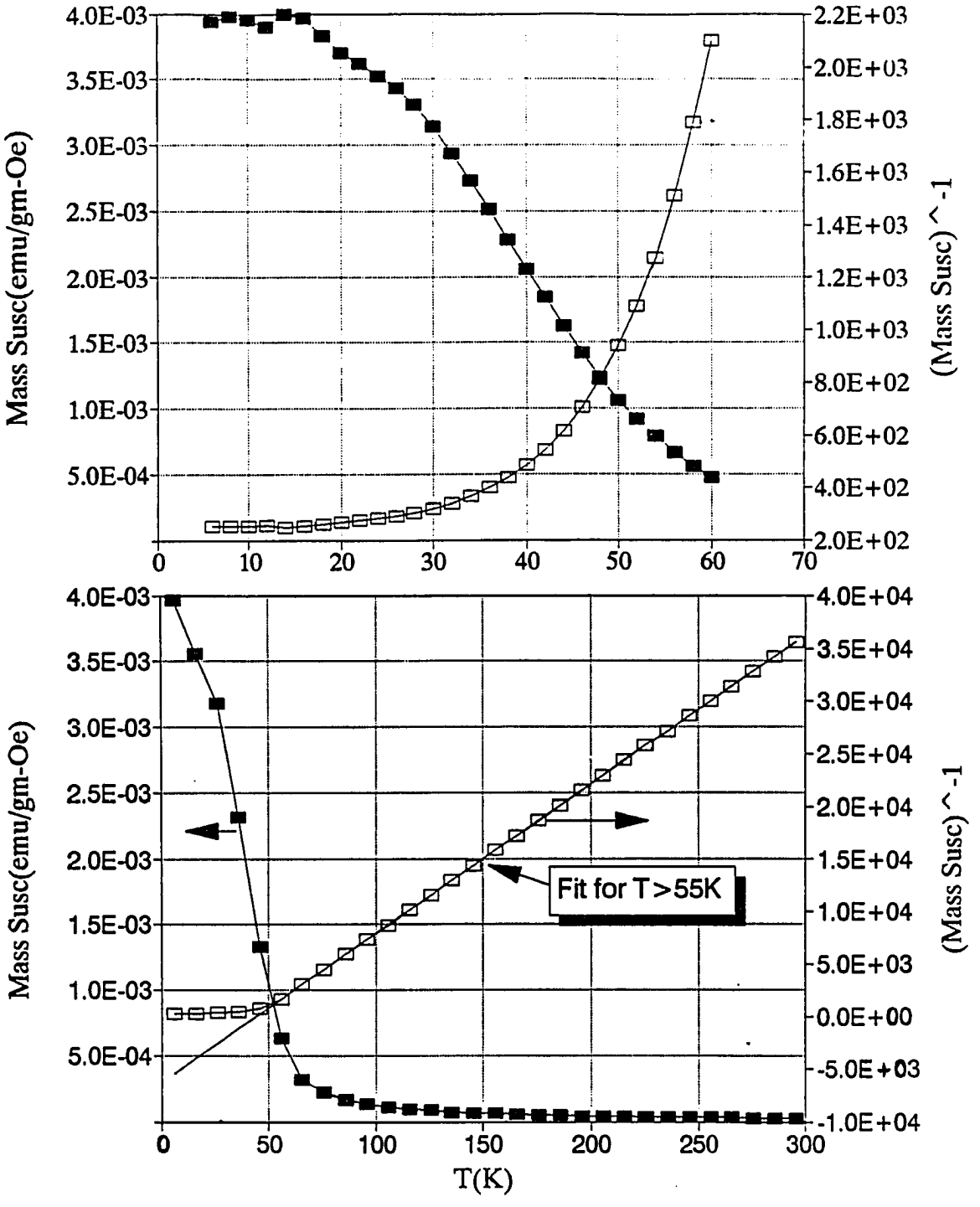

Figure 68. Mass susceptibility of Nd_5RuGe_2 as a function of temperature at 1 Tesla

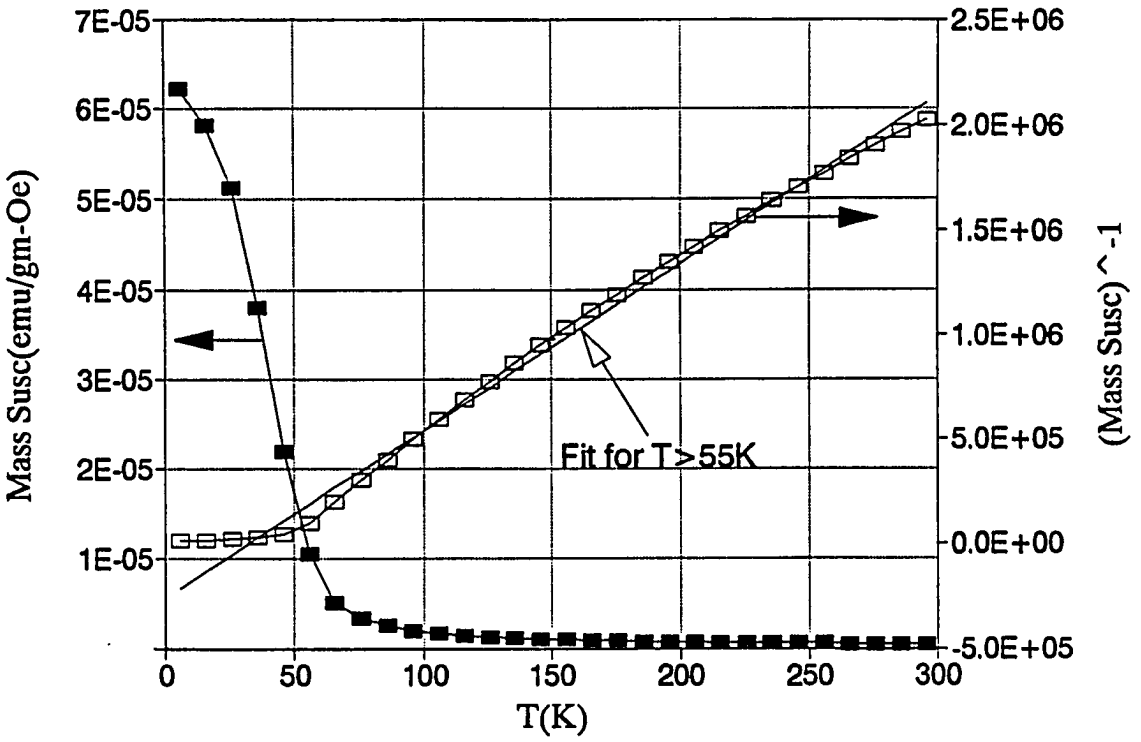

Figure 69. Mass susceptibility of La_5RuGe_2 as a function of temperature at 1 Tesla

C= 6.88 x 10^{-3}. The data yielded a magnetic moment, μ_{eff} = 7.30 $\mu_B$per formula unit. At temperatures lower than 55 K, the magnetic behavior deviates from a Curie-Weiss behavior and an antiferromagnetic character is observed. A similar paramagnetic-antiferromagnetic behavior is also observed in the lanthanum analog La_5RuGe_2. The calculated magnetic constants are: θ = 32.76 K; C = 9.611 x 10^{-5}; μ_{eff} = 0.85 μ_B per formula unit.

If we assume that the magnetic moment of La_5RuGe_2 was assigned to Ru (assume La^{3+} moment = 0.0), then the moment on each Nd atom in Nd_5RuGe_2 is averaged to ~1.29 μ_B/Nd atom. The result is an interesting contrast to the classical moment of 3.62 μ_B of the Nd^{3+} ion ($4f^3$).[282] Assuming a zero contribution of Ru in the total magnetic moment would still result in a weaker effective moment for Nd than the free ion moment. The lower effective moment on the Nd atoms in Nd_5RuGe_2 could be attributed to the coupling of the core moments via itinerant conduction electrons.[250] This is supported by the metallic character predicted by band structure calculations on La_5RuGe_2. Although the simple electron counting rules on result in an odd number of electrons for one formula unit, the moment on Ru (0.85μ_B) in La_5RuGe_2 can be compared with a spin-only value of 1.73μ_B/ (d^1) for 1 unpaired electron. The lower moment could be attributed to strong spin-orbit coupling and itinerant electron coupling of the magnetic moments of ruthenium.

The low temperature antiferromagnetic behavior is characterized by an almost unchanging but slightly decreasing susceptibility at temperatures below 15 K. This behavior is observed in both Nd_5RuGe_2 and La_5RuGe_2, hence, we could attribute the antiferromagnetic character to magnetic interactions between the Ru atoms within the

chain. The distances between nearest neighboring Ru atoms in the column structure is greater than 4.0A, which is considerably large for any strong direct magnetic coupling to occur. However, the antiferromagnetic coupling between Ru atoms could also be achieved via the conduction electrons.

Chemical bonding In order to qualitatively examine RE-Ru and RE-Ge bonding in Nd_5RuGe_2 and La_5RuGe_2, a three-dimensional extended Hückel calculation was carried out at 48 k-points for the actual structure of La_5RuGe_2. Lanthanum and germanium parameters were those used in the La_5Ge_3Z calculations. Ruthenium parameters were obtained from those used in the initial Pr_4I_5Ru calculations.[283] A summary of the results are presented in Table 48.

Figures 70 and 71 show the calculated DOS (densities of states) and COOP (crystal orbital overlap population) curves for La_5RuGe_2. Atomic contributions of ruthenium and germanium to the densities of states are projected out with the total DOS.

The total DOS curve can be divided into 4 parts, the Ge-derived s-band lie lowest in energy at -17.0 eV width a band width of about 1.0 eV. The Ru-derived d- and s-bands lie around -15.0 and -13.0 eV with band widths of about 0.5 and 0.7 eV, respectively. The Ge-derived p-bands lie with the La-derived bands above -12.0 eV and form the fourth part. Obviously, the calculations present an unreasonably large negative charge on Ru(-3.0) and that charge iteration calculations are necessary to obtain satisfactory charges. The possible effects of such calculations would be to raise the Ru d-levels closer to the Fermi level. This would essentially increase the orbital mixing of Ru- and La-derived states. However, the qualitative picture obtained from these calculations, wherein p-bands of Ge lie higher in energy and strongly mix with the La d-bands, would

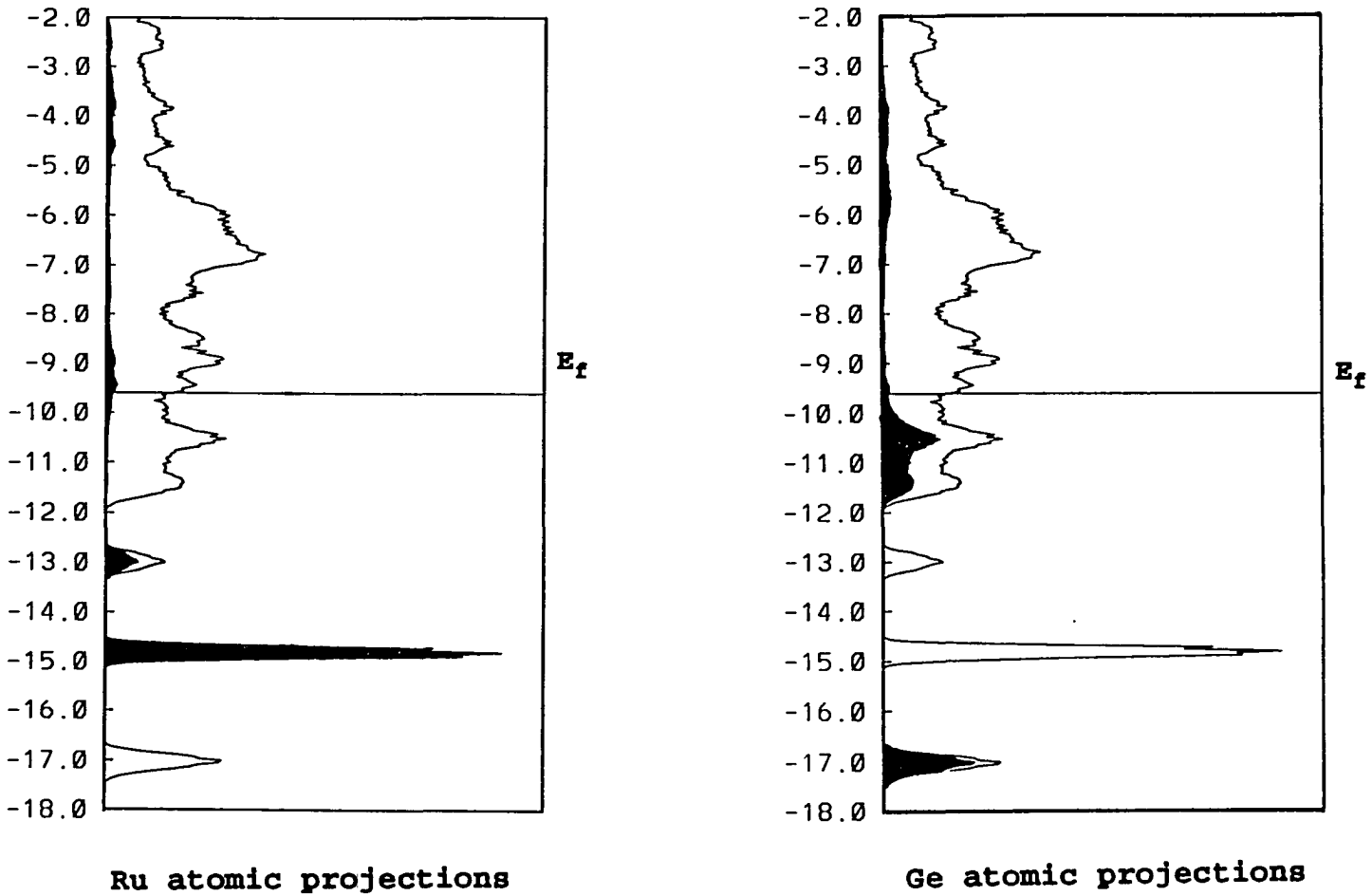

Figure 70. DOS curves for La_5RuGe_2. The shaded regions represent the atomic orbital projections as indicated in the labels. The Fermi level, E_f, is indicated by a solid line

not change and is consistent with previous charge iterated calculations on La_5Ge_3Z. The high density of states at the Fermi level, E_f, predicts the compound is metallic. Since neglect of the f-orbitals was applied, results of these calculations could be extended to the Nd analog.

The COOP curves show more interesting results. The COOP curve of the average La-Ge interactions show a maximum at ~-9.0 eV, close to E_f. Hence, like in La_5Ge_3 and La_5Ge_3Z, the La-Ge interactions are nearly maximized at E_f. The La-Ru interactions are also strongly bonding at E_f and extend to higher energies. The average La-La interactions also show bonding interactions at E_f up to ~-8.0 eV, but are significantly weaker than the La-Ge or La-Ru overlaps. The above results suggest that the bonding in the structure is dominated by strong La-Ge and La-Ru overlaps. It also suggests, based on overlap values, that the structure could accommodate a wide range of electron counts predicting the occurrence of isostructural analogs, RE_5ZGe_2, Z = Rh, Pd and Ag, that have higher electron counts. However, the major determining factor for the existence of these analogs would still be the stability of alternate phases.

A more important question of why the RE_4RuGe_2 chains distort in the off-center displacement of the Ru atom is very interesting. Yet our calculations did not attempt to derive the orbital interactions responsible for the off-center displacement of the Ru atoms relative to the isoelectronic Pr_4I_5Ru chains. One could just suggest that the germanium-derived orbitals in RE_4RuGe_2 have more direct structural effects on the chains than the iodines in Pr_4I_5Ru due to the less polar character of the heteroatomic bonds.

(a = 9.532(2)A, c = 9.974(3)A), for samples obtained after induction heating in tantalum containers that were different from previously reported values. Moreover, the purity of Demel's starting materials were better in terms of carbon (90 ppm), and oxygen (40 ppm) contents. It was also interesting to note that the reported cell parameters of La_5Pb_3C (a = 9.531(3), c = 6.997(2)) closely resembled those reported by Jeitschko and Parthé for La_5Pb_3.

The investigations on La_5Pb_3Z systems set out to establish reliable methods for the synthesis of ordered, single-phase samples of such compounds as well as to explore the scope of the interstitial chemistry. This led to broad explorations of powder-sintering, vapor phase transport and metal-flux methods for synthesis and to the identification of at least 15 examples of compound formation with heteroatomic Z.

La_5Pb_3

The seeming conflict between the structural reports of Jeitschko and Parthé, and that of Demel led us to re-investigate the binary La_5Pb_3. The question of whether this compound is an impurity-stabilized ternary compound or a real binary was addressed by a series of reactions leading to products near the ideal 5:3 stoichiometric ratio.

Samples of La_5Pb_x with x ranging from 2.5 to 3.3 in intervals of 0.1 contained in Ta tubing were slowly cooled from 1250°C or water-quenched from 1050°C. The Guinier powder patterns could be entirely accounted for with a hexagonal Mn_5Si_3-type structure and the proper La_5Pb_4 and La patterns on the lead-rich and lead-poor sides of the La_5Pb_3, respectively. Average values of the refined cell parameters are given in Table 49 along with our data for other relevant phases and literature values for La_5Pb_3.

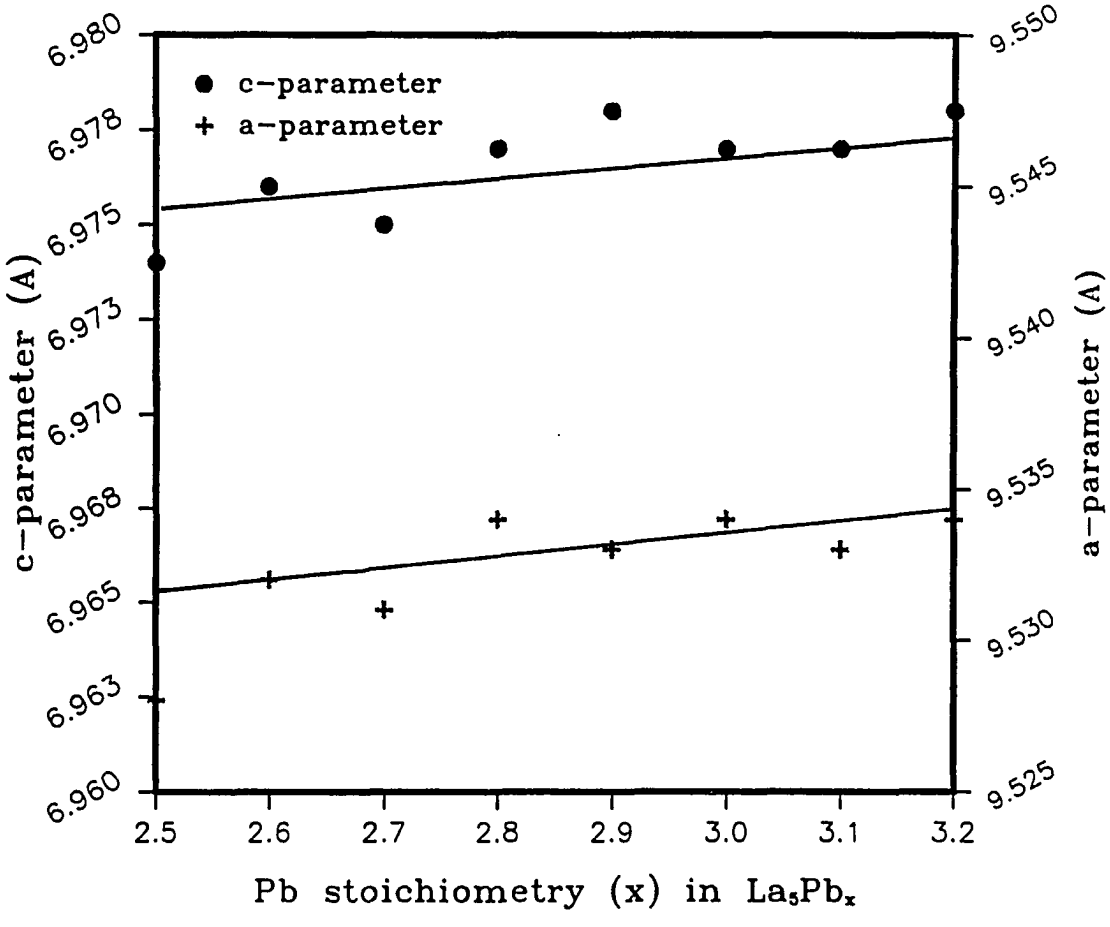

Figure 72. Variation of unit cell parameters **a** and **c** (A) of La_5Pb_x with Pb content (x)

Our refined parameters; a = 9.534(1) and c = 6.977(1), agree well with Demel's values for La_5Pb_3. Furthermore, as illustrated in Figure 72, there seems to be little indication of a significant amount of non-stoichiometry evidenced by the small deviations of the cell parameters.

Attempts to obtain samples quenched from high temperatures were made to test if these samples had cell parameters similar to those reported by Jeitschko and Parthé. Arc-melting was not successful due to the inherent air-sensitivity of the reactants and the products. Instead samples contained in welded Ta tubes were enclosed in silica jackets, held at 1050°C for 3 weeks in a tubular resistance furnace, and then quenched by dropping them into cold water. Samples of La_5Pb_x with x = 2.75, 3.0, and 3.25 again all gave only the Mn_5Si_3 for the La_5Pb_3 component and the appropriate La and La_5Pb_4 patterns on the Pb-poor and Pb-rich sides, respectively. Identical samples that were inductively heated to 1400°C and cooled by turning the power off also yielded a Mn_5Si_3-type phase. A rapid cooling technique wherein the off-gas from liquid nitrogen was sucked into the vacuum system gave the same results. The refined parameters of all quenched phases were in accord with the parameters of the unquenched samples. Although La_5Pb_3 indeed has the Mn_5Si_3 structure the dimensions of earlier reported Mn_5Si_3-type phases do not correspond to the binary La_5Pb_3.

Since La_5Pb_3C has been previously studied and the closely related La_5Ge_3 exhibits substantial interstitial chemistry, reactions were carried out to investigate the interstitial chemistry of La_5Pb_3.

La_5Pb_3Z Interstitial Compounds

Conditions for the successful syntheses of more than 15 new ternary La_5Pb_3Z phases, usually via powder-sintering and melting of the elements in tantalum containers, the lattice constants, and cell volumes for these new products together with the reference value for La_5Pb_3 are given in Table 50. The most important criterion for success in most of these reactions is the production of a sample that has the known structure and is single phase according to its Guinier powder diffraction pattern. Furthermore, visual inspection of single phase samples revealed that all the interstitial compounds were less air and moisture sensitive than La_5Pb_3. However, compared to La_5Ge_3Z phases the La_5Pb_3Z compounds were more air-sensitive. Changes in powder pattern intensities should also aid in product identification of interstitial compounds, however, these changes could also be mimicked by possible substitution products $La_5Pb_{3-x}Z_x$. Hence, changes in lattice dimensions are characteristic and useful. The small volume changes exhibited by the La_5Pb_3Z phases compared to the hosts's could be explained in terms of the large free volume of the interstitial sites in La_5Pb_3. Unsuccessful reactions usually resulted in multi-phase products containing La_5Pb_4 and other unknown phases, possibly binaries of La with Z. Details associated with obtaining a good sample of each La_5Pb_3Z phase together with a comparison with other filled-Mn_5Si_3-type rare-earth tetrelides follow.

Reactions were all run using the high temperature furnace as heating source. Mixtures of weighted reagents were cold-pressed into pellets within a glovebox, sealed in Ta containers, and heated to 1150° over two days. The samples were then melted at 1300°C, slowly cooled to 1150° over 7 four days, and then cooled to 300° over 4 more days.

Table 50. Summary of La_5Pb_3Z with Mn_5Si_3-type structure Z = ternary interstitial elements

composition	conditions	lattice parameters of Mn_5Si_3-type phase (A)	cell volume (A^3)	c/a ratio
La_5Pb_3	S	a = 9.534(1); c = 6.977(1)	549.2(2)	0.732
$La_5Pb_3B_x$	S	a = 9.537(1); c = 6.997(2)	551.1(3)	0.734
La_5Pb_3C	S	a = 9.535(1); c = 6.995(1)	550.8(2)	0.733
La_5Pb_3P	B	a = 9.545(1); c = 7.009(2)	553.0(3)	0.734
La_5Pb_3As	B	a = 9.553(1); c = 7.024(2)	555.1(3)	0.735
La_5Pb_3Sb	S	a = 9.558(1); c = 7.035(1)	556.6(2)	0.736
La_5Pb_3S	B	a = 9.547(1); c = 7.022(1)	554.0(2)	0.736
La_5Pb_3Se	B	a = 9.553(1); c = 7.035(1)	556.0(2)	0.736
La_5Pb_3Cl	B	a = 9.549(1); c = 7.020(2)	554.3(3)	0.735
La_5Pb_3Fe	S	a = 9.543(1); c = 7.008(2)	552.7(3)	0.734
La_5Pb_3Co	S	a = 9.542(1); c = 7.009(1)	552.7(2)	0.734
La_5Pb_3Cr	B	a = 9.547(1); c = 7.012(2)	553.5(3)	0.734
La_5Pb_3Mn	B	a = 9.543(1); c = 7.010(1)	552.9(2)	0.734
La_5Pb_3Ni	S	a = 9.545(1); c = 7.011(2)	553.2(3)	0.734
La_5Pb_3Cu	B	a = 9.550(1); c = 7.026(2)	554.9(3)	0.736
La_5Pb_3Zn	B	a = 9.551(1); c = 7.028(2)	555.2(3)	0.736
La_5Pb_3Ru	S	a = 9.558(1); c = 7.035(1)	556.6(2)	0.736
La_5Pb_3Ag	S	a = 9.560(1); c = 7.037(2)	557.0(3)	0.736

S: Sintering reactions at 1250-1350°C over a total of 10-14 days

B: Prereacted binaries are slowly heated to 1100-1250°C and annealed at 1000 C over 10 days

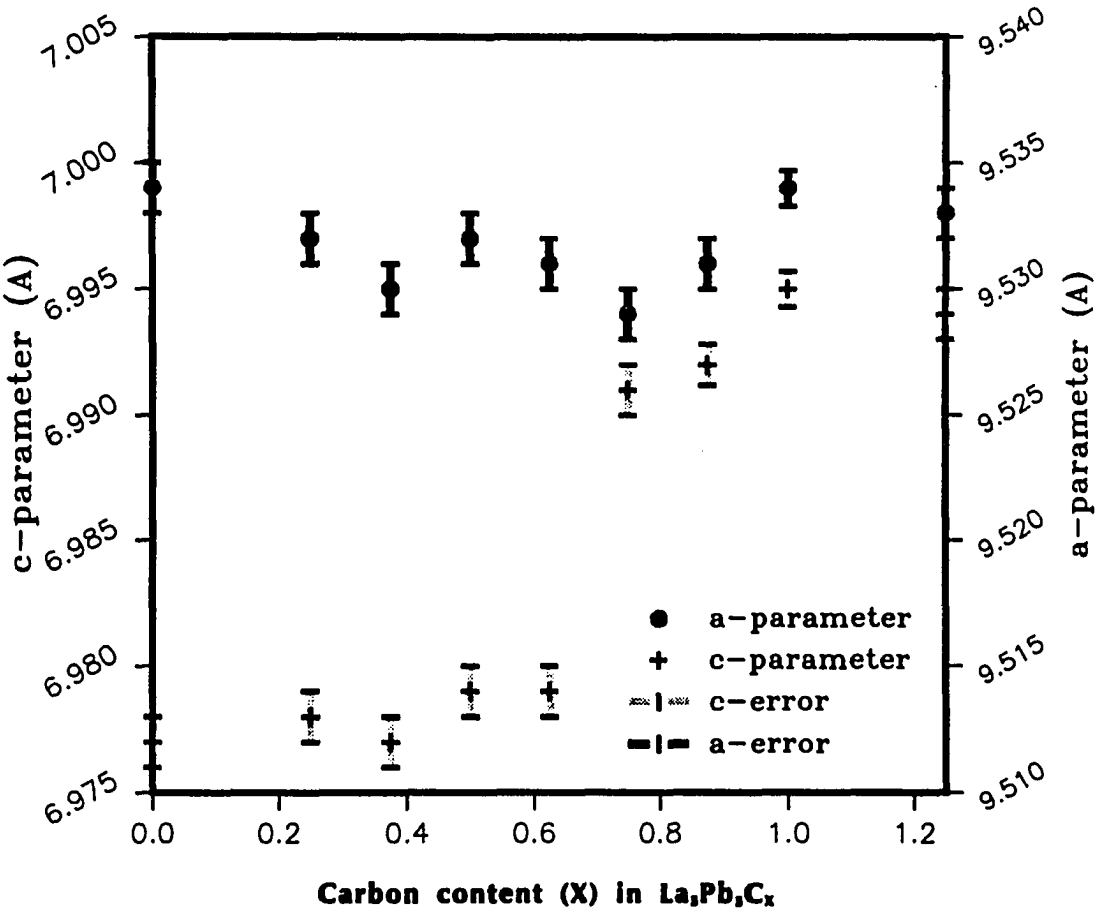

Figure 73. Variation of a and c unit cell cell parameters (A) in $La_5Pb_3C_x$ with carbon content(x)

welded Ta tubes. The reactions were slowly heated over two days to 1000°C. After 2 more days, the temperature was raised to 1200°C and kept at that temperature for another week. The last part of the heating stage was to slowly cool the reactions to 300°C before turning off the furnace. The reactions involving antimony proceeded with the elements as reagents and the usual temperature profile. Results were successful, based on single phase products and the accompanying increase in lattice parameters relative to the binary La_5Pb_3.

La_5Pb_3Z (Z = S and Se)

The procedure for the preparation of La_5Pb_3S and La_5Pb_3Se was similar to the group 15 syntheses with the binary LaS and LaSe as starting reagents. Inspection of the used tantalum containers did not show any noticeable interference from a tantalum sulfur(selenium) reaction. The single phase products were also marked by their large c lattice constants and c/a ratios. This was also observed in Zr_5Sb_3S and was attributed to the large repulsion between the seemingly negative S(Se) interstitials along the c-axis.[235]

La_5Pb_3Cl

The procedure for the preparation of La_5Pb_3Cl followed that of La_5Ge_3Cl. Stoichiometric amounts to the reagents were loaded into welded Ta tubes, slowly heated to 1000°C in two days, annealed at 1100°C for 10 days, then slowly cooled to room temperature over three days. The reaction is expressed by the equation

$$1/3\ LaCl_3 + 2/3\ La + La_4Pb_3 \text{ ---> } La_5Pb_3Cl.$$

The success of the reaction was distinguished by the large cell constants of the single phase product. Single crystals were obtained from the reactions but were not investigated.

La_5Pb_3Z (Z = Transition metals)

Iron The reactions involving iron were best made by lining the Ta containers with thin molybdenum sheets. This was done to ensure stoichiometric reaction of Fe with La_5Pb_3 at high temperatures. Previous work in the Zr-Sb and Zr-Sn systems have shown that iron diffuses into Ta containers upon powder sintering and annealing. Furthermore, the absence of a binary compound between La and Fe, as well as between Fe and Pb, effectively limited the use of binary phases as starting materials. Despite the difficulties, cold-pressed pellets of the elements were heated to 1000°C for four days. The temperature was slowly increased to 1350°C over 2 days and kept at that temperature for another 4 days. The temperature was slowly decreased to 1050°C over 20 hours and finally to room temperature over 12 hours. This procedure resulted in the successful synthesis of La_5Pb_3Fe. The compound was distinguished by the significant increase of the cell parameters and its dull appearance compared to La_5Pb_3. The compound was also found to be strongly attracted by a magnet. Subsequent magnetic susceptibility measurements revealed the compound was ferromagnetic (saturation moment = 1.8 μ_B) with a Curie temperature above room temperature. The possibility that the observed behaviors are due to metallic iron dispersed in the sample could not be completely discounted and further investigations into the nature of the Fe should be pursued. SEM and XPS experiments would help clarify this question.

Z = (Co, Cr, Mn, and Ni) The preparation of these ternary phases took in to account some of the problems encountered with the ternary iron compound. Furthermore, the higher volatilities of the Cr and Mn elements were also considered. Thus, whenever necessary, the interstitials were introduced as their binaries with lanthanum. Elemental

reagents also provided positive results but required higher annealing temperatures (>1200°C) and longer reaction times (14-21 days at 1250°C).

Copper The reactions of La_5Pb_3 and Cu gave good results. Their Guinier powder patterns were marked by clear and sharp lines that yielded refined lattice parameters larger than those of La_5Pb_3 and the other transition-metal interstitial compounds La_5Pb_3Z. Powder sintering of binaries La_4Pb_3 and LaCu provided a lower temperature route for the synthesis of the compound.

Zinc The synthesis of La_5Pb_3Zn was part of the our attempts to use zinc-fluxed reactions in the synthesis of La_5Pb_3Z compounds. Quantitative results could be obtained by the reaction of stoichiometric amounts of Zn and La_5Pb_3 at 1000°C. Guinier powder patterns were marked by diffuse lines corresponding to the Mn_5Si_3-type phase. No other lines were observed that indicated any superstructure.

Ruthenium A contrasting result in the difficulty of synthesizing La_5Pb_3Fe is the single phase sample of La_5Pb_3Ru obtained after powder sintering La_5Pb_3 with Ru. The compound is clearly characterized by large lattice parameters and a dull physical appearance of the compound in contrast to the metallic lustre of the binary La_5Pb_3. The compound was also found to be very hard and brittle.

Silver This compound was prepared from the elements at 1350°C. Attempts to prepare the compound at lower temperatures were unsuccessful. The product gave the largest cell of any La_5Pb_3Z phase so far obtained.

Other reactions Attempts to synthesize other transition-metal interstitial compounds La_5Pb_3Z (Z = V and Ti)proved to be unsuccessful. The reaction involving vanadium resulted in multi-phasic products that included V_3Pb (Cr_3Si-type). The

titanium reaction also yielded a multi-phasic product that included Ti_4Pb (Ni_3Sn-type). The other phases common to the two powder patterns were La and La_5Pb_3.

Crystal chemistry of Mn_5Si_3-type La_5Pb_3Z phases

The lattice dimensions, ratios, and volumes of the above phases show that these are characteristic and different from La_5Pb_3. This information coupled with the single-phase products obtained from all reactions is strong evidence for the indicated compounds. This conclusion is further supported by volume trends observed.[290]

Based on the structural parameters, some generalities and trends can be deduced from the cell data. The volume trends are illustrated in Figure 74 as a function of period and group. Noticeable are the relatively small but distinct expansions of the La_5Pb_3 unit cell. Phases containing 3d metals uniformly exhibit c/a ratios (0.734) comparable to the host's and have volume trends that follow the atomic volumes of the interstitials. The largest cells were found upon incorporation of Ru and Ag. Likewise, significant increases in volume and in c/a are detectable between group 15 and 16 elements.

Moreover, S, Se, and Cl are the ternaries that relatively exhibit the largest c/a ratios. This marked increase in cell volume and c probably reflects the coulombic repulsion between the somewhat negatively charged chalcogens and halogen along the chain of clusters.

The volume changes observed reflect not only the presence of free interstitial volume in La_5Pb_3 but also substantial differences in effective interstitial volumes. Comparisons of the standard volumes derived by Biltz[291] with these data show a significantly lower observed volume changes than what would be expected.

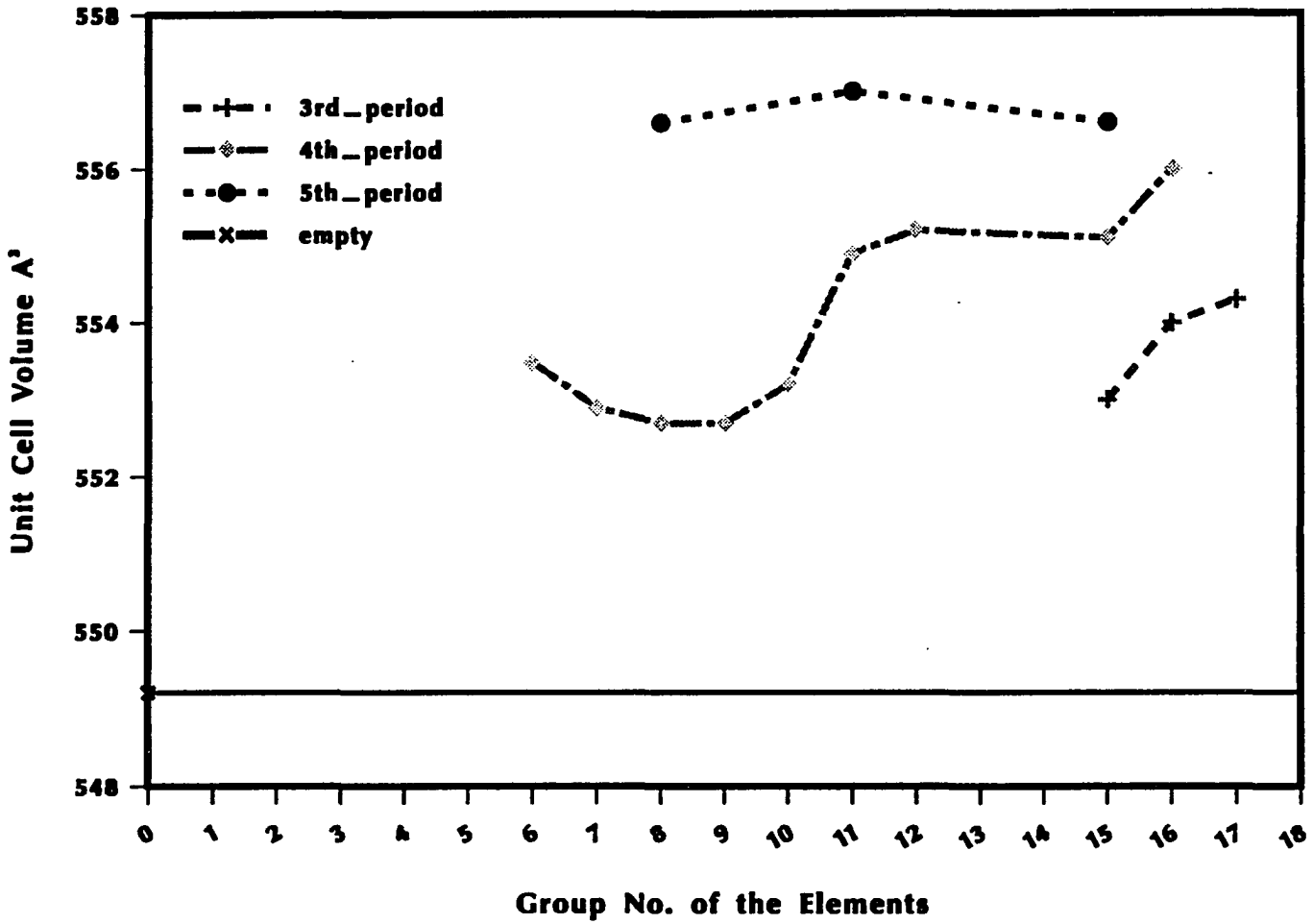

Figure 74. Variation of cell volume in La_5Pb_3Z interstitial compounds

La_5Pb_3Z (Z = Group 14 elements)

Powder sintering between La_5Pb_3 and the group 14 elements Si, Ge, and Sn gave essentially single-phase products which were completely indexed to the Sm_5Ge_4 structure type. Subsequent quenching and prolonged annealing experiments, using an induction furnace, on the La_5Pb_3Si compound did not yield any Zr_5Si_4-type phase. The failure to form a Zr_5Si_4-type product could be ascribed to the large size difference of Pb and Si. Hence it is possible that Si would prefer the "dangling" tetrelide site (refer to the discussion on La_5Ge_4 and related structures) in the Sm_5Ge_4 structure. Single crystal investigations are necessary to confirm this hypothesis.

La_5Pb_3Z (Z = O and N)

Syntheses The compound La_5Pb_3O was first synthesized as a minor phase in a reaction with nominal stoichiometry La_5Pb_3Mn. Although the major phase was a Mn_5Si_3-type phase, some crystals were isolated and later investigated. Chemical analysis by SEM on selected crystals revealed the absence of Mn. The crystals were later found to represent La_5Pb_3O with a structure that is isopointal with Cr_5B_3.[299] The compound was later synthesized in high yield by the powder sintering reactions:

$$La_4Pb_3 + 1/3\ La + 1/3\ La_2O_3 \text{ ---> } La_5Pb_3O \text{ and}$$

$$4.33\ La + 1/3\ La_2O_3 + 3\ Pb \text{ ---> } La_5Pb_3O.$$

These were done by cold-pressing the starting reagents into pellets. The pellets were then placed inside tantalum containers, sealed and heated in the high temperature furnace.

The effective heating conditions for the synthesis of pure La_5Pb_3O and the production of single crystals is as follows. The temperature is rapidly increased to 950° in about 4 hours, then kept at that temperature for 2 days. Afterwards the temperature is

slowly increased to 1250°C in two days. The temperature is kept at 1250°C for another day and slowly cooled to 1100°C in 4 days. The reaction is annealed at 1100°C for another 6 days and then cooled to room temperature in 12 hours. La_5Pb_3O could also be synthesized by arc-melting the desired proportions of La_4Pb_3 , La and a slight excess of La_2O_3. The as-cast button is then annealed for one week at 1000°C.

The synthesis of the nitrogen analog La_5Pb_3N was more straight forward via the reaction

$$La_4Pb_3 + LaN \text{ ---> } La_5Pb_3N.$$

The LaN was obtained in pure form from H.J. Meyer. The temperature profile necessary for the nitride reaction was less severe. Powders of the starting materials were pressed into pellets, placed in tantalum containers, sealed and then heated to 1050°C for 2 weeks. Heating was done using the high temperature furnace.

The compounds La_5Pb_3O and La_5Pb_3N are dull-black in color and very air and water sensitive. Their reaction with water results in the evolution of a gas.

Structure determination Crystal obtained from the reaction with a stoichiometry La_5Pb_3Mn were isolated and mounted into glass capillaries. The singularities of the crystals were checked by preliminary oscillation photos. A gem-like single crystal was investigated using an Enraf-Nonius CAD4 diffractometer.

A body-centered tetragonal cell was obtained from the refinement and indexing the 2θ values of 25 reflections using the programs SEARCH and INDEX. All reflections within 2 octants of the reciprocal sphere up to $2\theta_{max} = 55°$ were measured. The first 100 reflections were collected without the absence condition due to body centering. After careful examination of the initial reflections, the systematic absence was confirmed and

only reflections satisfying the condition h+k+l = 2n were subsequently measured. Empirical absorption corrections were applied on the data based on four ψ-scans. After data reduction (3σ) and averaging (R_{ave} = 4.6%) 272 independent reflections were available for least squares refinement of the La_5Pb_3O structure. The relatively high R of averaging attested to the inadequacy of the initial absorption correction. This was improved by the later application of DIFABS after the isotropic phase of the structure refinement (R_{ave} = 3.2%). Systematic absences based on careful inspection of the reflection data as well as axial photos taken on the crystal indicated that the Laue class was I4/mmm and that the possible space groups were I4cm, I-4c2 and I4/mcm. The last space group proved to be correct during refinement. Accurate cell constants were later obtained by least squares fit of the Guinier powder data using NBS silicon as internal standard. The observed powder diffraction patterns were carefully compared with a calculated powder pattern based on the refined structure to make sure that proper assignments of the diffraction lines were made.

Initial parameters for the full-matrix least squares refinement were obtained from a solution given by direct methods using SHELXS-76. The weighting scheme was according to the counting statistics, and the parameter accounting for isotropic secondary extinction was refined (3.2(3) x 10^{-7}) and applied to the calculated structure factors. Isotropic refinement of the La and Pb atoms indicated positional parameters very similar to the Cr_5B_3 structure. Following a difference Fourier calculation, an interstitial atom was located with an electron density of ~11.0 e^-/A^3. The interstitial atom was initially refined as half of Mn atom. Subsequent refinement resulted in residuals of R = 5.7% and R_w = 8.1%. Refinement with oxygen as the interstitial atom led to better residuals R =

Table 51. Data collection and refinement parameters for La_5Pb_3O

space group	I4/mcm
Z	4
crystal dimension	0.06 x 0.06 x 0.08 mm
diffractometer	Enraf-Nonius CAD4
2θ max	55°
collected indices	h, k, ±l
reflections:	
measured	1428
observed ($>3\sigma_I$)	1000
independent	272
R_{ave}	3.2% (observed data)
no. of parameters refined	16
R (refinement)	3.0%
R_w (refinement)	3.5%
largest parameter shift	0.01
absorption coefficient	795.6 (cm^{-1}, Mo Kα)
secondary extinction coefficient	$3.2(3) \times 10^{-7}$
largest residual peaks	3.0 e^-/A^3 at (0,0,0.02)
cell parameters (Guinier):	
a = 8.6895(2) A	
c = 14.540(1) A	
volume = 1097.9(1)A^3	

Table 52. Refined parameters for La_5Pb_3O

atom	x	y	z	Occupancy
La(1)	0.15232(7)	x + (1/2)	0.15039(7)	1.0
La(2)	0.0	0.0	0.01142(7)	0.493(2)
Pb(1)	0.0	0.0	0.25	1.0
Pb(2)	0.35558(7)	x + (1/2)	0.0	1.0
O	0.0	0.5	0.25	1.0

B values

Atom	B11	B22	B33	B12	B13	B23
La(1)	0.60(2)	B11	0.24(3)	-0.20(2)	0.05(2)	B13
La(2)	0.28(3)	B11	0.13(3)	0.0	0.0	0.0
Pb(1)	0.57(2)	B11	0.47(4)	0.0	0.0	0.0
Pb(2)	0.34(1)	B11	0.23(3)	0.04(2)	0.0	0.0
O	1.1(2)					

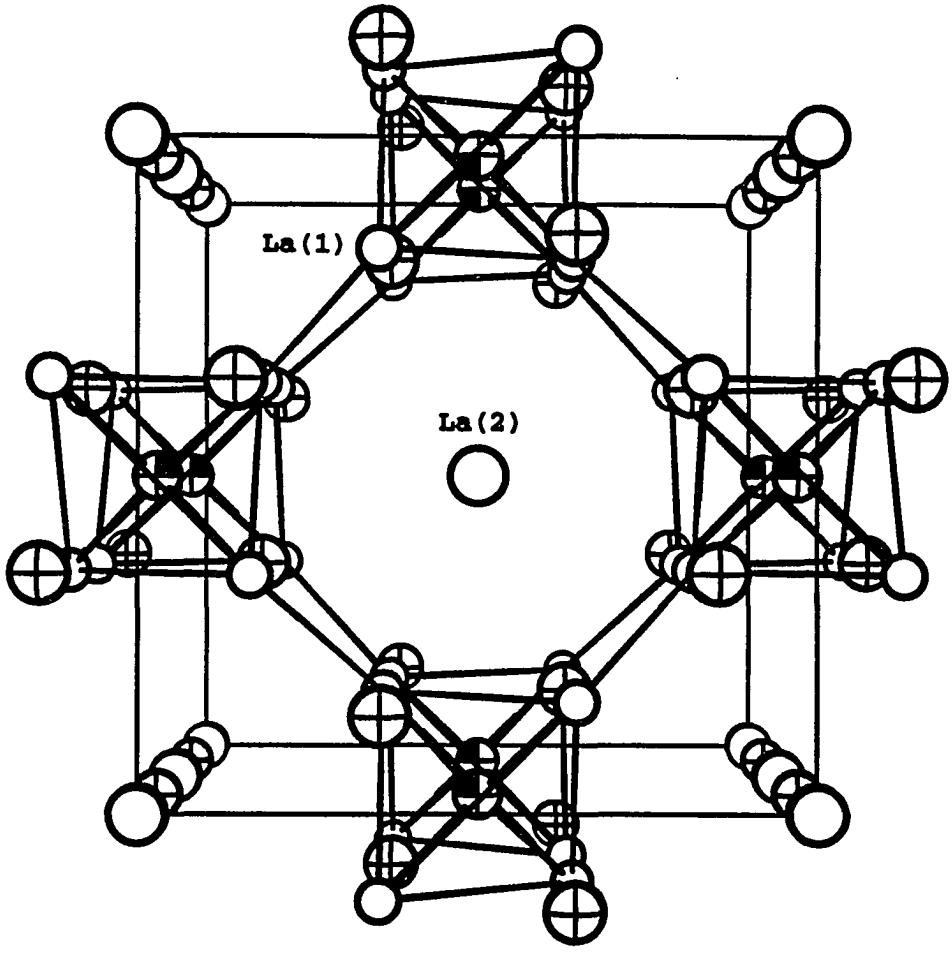

Figure 75. ORTEP drawing of the unit cell of La_5Pb_3O along [001]. Open circles: La, crossed-hatched circles: PB, octant shaded circles: O. Isotropic thermal ellipsoids are drawn at 90% probability

square antiprism channels wherein nominal linear chains of alternating La and Pb atoms extend parallel to the c-axis.

A nominal structural unit of one column of La_4Pb_2O is a La_4Pb_2 octahedron with the two Pb atoms at opposite apices (see Figure 76). Neighboring La_4Pb_2 octahedra do not share edges. Instead, they are rotated 90° with respect to each other and their closest edges form a tetrahedron. The pattern is repeated along the the c-axis to form a column of La_4Pb_2O, as shown in Figure 77. The centers of the tetrahedral interstices formed are occupied by oxygen atoms.

The La-O distances (2.37A) yield Pauling bond order[291] of 0.926. Surprisingly, applying bond-valence rules and parameters[292] that were derived for oxides also resulted in a reasonable bond order of 0.59 for La-O in La_5Pb_3O. This yields a bond order sum of 2.36 close to the known valence of 2 for oxides. Recently, Schleid and Lissner reported the synthesis and structure of $RE_{10}S_{14}O$ compounds containing nominal RE_4O "clusters".[293] The reported La-O distances of 2.45A in $La_{10}S_{14}O$, a valence compound, can be compared with La-O distances in La_5Pb_3O. The La-La distances in the La_4O tetrahedral "cluster" are 3.767(1)A and 3.744(1)A and this corresponds to a Pauling bond order of 0.24 and 0.28 respectively.

The La_4Pb_2O columns are interconnected to other columns along the a-b plane through the apical Pb atoms. These Pb atoms formally bridge the edges of the neighboring La_4Pb_2 octahedron, as shown in Figure 78. A lanthanum edge of an octahedron is bridged by one apical Pb atom of the next octahedra. What is observed again is a 90° rotation of the neighboring octahedron, but this time the rotation is along an axis perpendicular to the principal axis of the columns, c-axis.

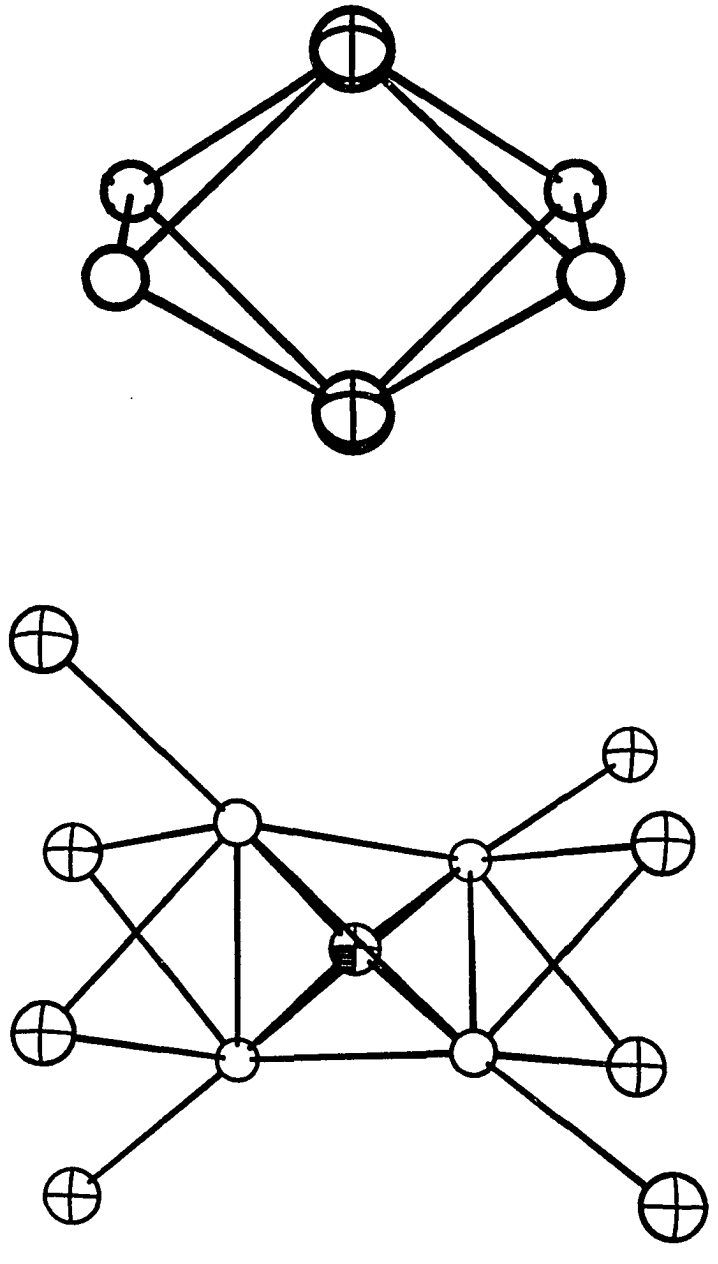

Figure 76. The structural unit La_4Pb_2(top) and the Pb coordination around the La_4O tetrahedron(bottom). Open circles: La, crossed-hatched circles: Pb, octant shaded circle O

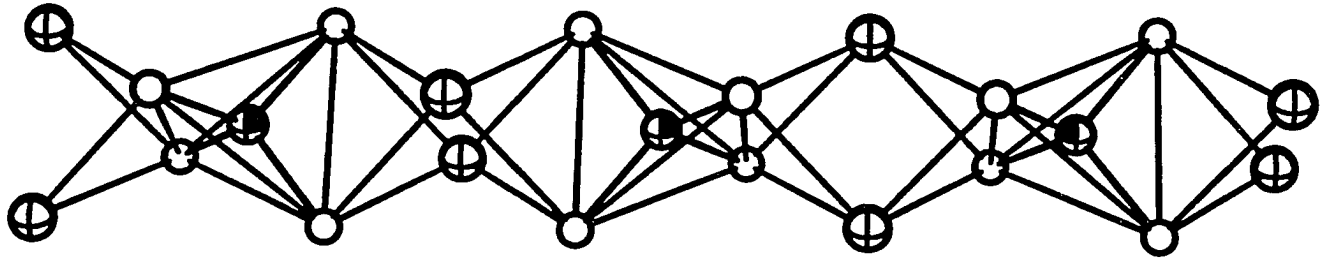

Figure 77. The connectivity of La_4Pb_2 octahedra along the c-axis resulting in the formation of La_4O tetrahedral "clusters". Open circles: La, crossed-hatched circles: Pb, octant shaded circles: O

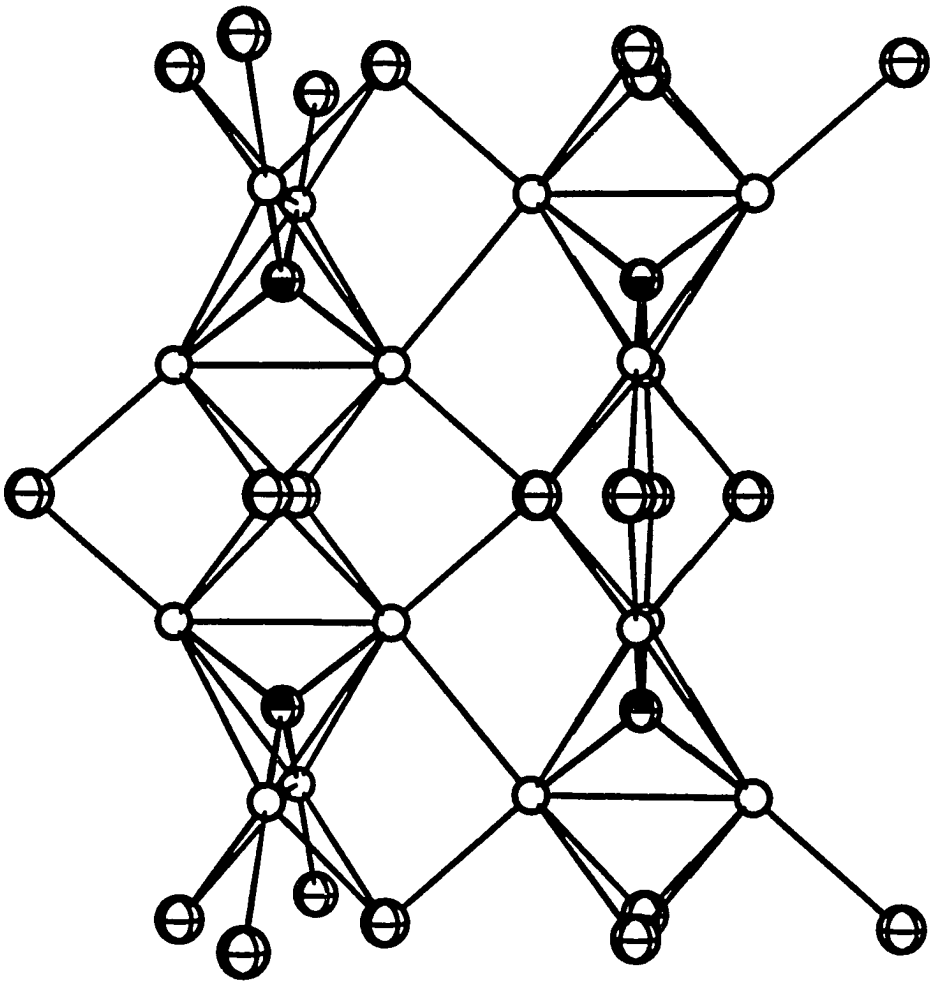

Figure 78. The connectivity of two La_4Pb_2 columns along the a-plane. Note the trigonal prism environment of La(1) atoms around Pb(2) atoms. Open circles: La, crossed-hatched circles: Pb, octantant shaded circles: O

From the above discussion, it is observed that the Pb atoms of the La_4Pb_2 octahedra have C.N. = 6, with 6 La atoms forming a distorted trigonal prism around the Pb atom. The shortest Pb-Pb distances (3.55A) are between the 2 apical Pb atoms of the La_4Pb_2 octahedron. This distance is slightly longer than what is found in $Ca_{5.67}Pb_3$ and in metallic Pb.[294] The Pb-Pb bond order, using Pauling bond order parameters, is 0.12. In La_5Pb_3O, the Pb-Pb distance could be considered non-bonding based on the electron count; there are more electrons than necessary to allow Pb-Pb bonds. The cell volumes of La_5Pb_3 -- (549.2 x 2)= 1098.4A^3, and La_5Pb_3O -- 1097.9A^3 show a volume contraction of La_5Pb_3O with respect to the binary La_5Pb_3 host. Hence, the Cr_5B_3-type structure is more closely-packed than the Mn_5Si_3-type phase, and the close Pb-Pb contacts may be attributed to matrix effects.

Other interesting features of the La_5Pb_3O structure are the linear chains of La(2) and Pb(1)that lie along the c-axis within the channels formed by the interconnected columns (see Figure 75). The lanthanum atoms in the linear chains, La(2) at (0, 0, 0), originally presented crystallographic problems in that it showed B_{33}/B_{11} = 8.0, giving a mean displacement about 0.4A along the c-direction. Thus, split positions, (0,0,z), for La(2) were introduced. The observed splitting corresponds to a ~0.33A displacement between La(2) atoms. This behavior of the nominal LaPb linear chains in La_5Pb_3O was also observed in the Nb chains in $NbTe_4$.[295] Both the La-Pb and Nb chains in their respective structures lie within square antiprism channels. The pathological behavior of the thermal parameters of Nb in in $NbTe_4$ was explained in terms of a modulated structure along the chain axis. The modulation is brought about by the formation of Nb pairs in an incommensurate manner. To investigate the possibility of a similar behavior

The electron counting scheme in La_5Pb_3O is interesting since we have a compound with one electron more than for a Zintl phase, i.e.

$$[(5 \times 3(La^{3+})) - (3 \times 4(Pb^{4-})) - 2(O^{2-})] = 1\ e^-/La_5Pb_3O$$

The observed structural anomaly of the La-Pb chains may be related to the presence of an "extra" electron. Band structure calculations could possibly aid in understanding the electronic effects of the "extra" electron on the structure. Magnetic and electronic property measurements on the compound would also greatly help in understanding the observed structural phenomena. Preliminary two probe measurements on selected chunks (~2-5 mm sizes) of La_5Pb_3O indicated a resistance of 0.02 ohms.

An interesting question is whether the observed disorder in La_5Pb_3O is also present in the La_5Pb_3N which is presumably a Zintl phase. If indeed the structural disorder is related to the excess electron then substituting nitrogen for oxygen could result in an ordered chain. Thus, it is necessary to investigate the crystal structure of La_5Pb_3N. However, despite many attempts single crystals of La_5Pb_3N could not be obtained.

The structural preference of La_5Pb_3O and La_5Pb_3N relative to that of La_5Pb_3 and other La_5Pb_3Z isostructural with Mn_5Si_3 is puzzling. It has been reported that compounds, particularly alkaline earth tetrelides, that have Cr_5B_3 structure type contain dimers of the main group atoms,[297] as illustrated in Ca_5Ge_3 (see Figure 79). Based on the structural investigations, and electron counting rules the compounds La_5Pb_3O and La_5Pb_3N do not contain Pb-Pb dimers. Why then are these compounds isostructural with Cr_5B_3? One can infer that the large octahedral interstices generated in the Mn_5Si_3-type arrangement of La and Pb are too large for oxygen and nitrogen interstitials. Moreover, oxygen and nitrogen atoms are more comfortable in the close-packed arrangement and

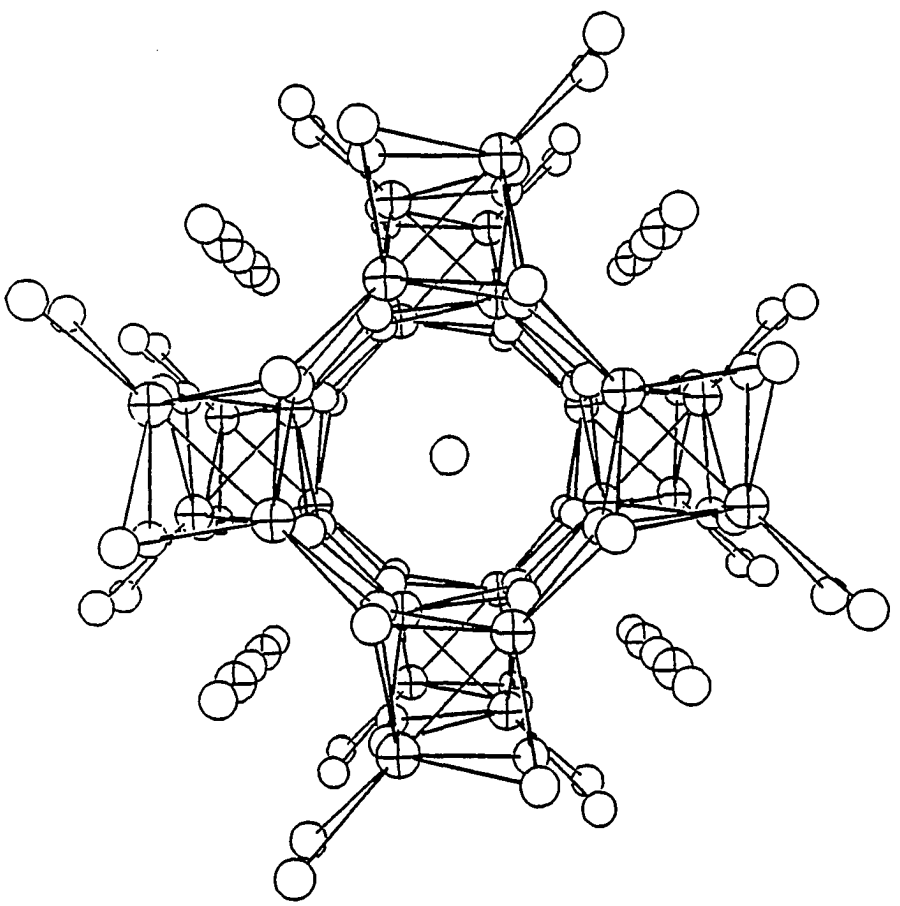

Figure 79. A [001] view of Ca_5Ge_3, a normal Cr_5B_3-type compound. Note the close approach of the Ge atoms resulting in a less symmetrical Ca_4Ge_2 octahedra as compared to La_5Pb_3O (see Figure 75). Open circles: Ca, cross-hatched circles: Ge

INTERSTITIAL STABILIZATION OF La_5Sn_3[301]

Introduction

Our attention was drawn to La_5Sn_3 by reports that this is dimorphic, exhibiting both the Mn_5Si_3- and W_5Si_3-type structures, in clear contrast to the analogous germanide and lead compounds that occur only in the former structure.The first two reports on La_5Sn_3 indicated that the Mn_5Si_3-type was obtained first by Palenzona and Merlo after melting a pressed pellet at 1200°-1500°C in tantalum[302] and then by Jeitschko and Parthé from arc-melting.[303] Both obtained comparable results for many heavier lanthanide stannides (other than for Eu, Yb), except that only the second investigation produced single phase Ce_5Sn_3. A later review by Iandelli and Palenzona[304] listed Mn_5Si_3-type phases for stannides of all of the lanthanides, although they gave somewhat different lattice constants for La_5Sn_3 without information on the synthesis conditions. This single-structure picture was altered when Franceschi[305] reported a low-temperature R_5Sn_3 phase with the tetragonal W_5Si_3 structure was obtained for R = La, Ce, and Pr. This resulted from slow cooling of the molten alloy in Mo containers or after annealing at 400°C. Alloys for the three elements also yielded products with the Mn_5Si_3 structure on (undefined) rapid cooling and with lattice constants found to be in excellent agreement with those in the literature. Reversibility of the supposed transition was not demonstrated. The only subsequent information has been the note by Borzone et al.[306] that both forms of La_5Sn_3 had been observed, but no synthetic details were provided only lattice constants. In all cases, the W_5Si_3 form exhibited the smaller molar volume.

Results

La_5Sn_3

To establish the true nature of the dimorphism, samples of La_5Sn_x with x ranging from 2.6 to 3.4 in 0.1 intervals contained in Ta tubes were slowly cooled from 1350°. The Guinier powder patterns of all samples could be entirely accounted for with a tetragonal W_5Si_3-type structure (I4/mcm) and the appropriate La_3Sn and La_5Sn_4 patterns on the tin-poor and tin-rich sides of La_5Sn_3, respectively. Refined lattice parameters for this phase in the annealed samples are shown in Figure 80. There seems to be very little indication of a significant nonstoichiometry. Average values of the parameters are given in Table 54 along with the data for other relevant phases and literature results for La_5Sn_3.

A convenient description of a W_5Si_3-type structure[307] starts with Si-filled square antiprisms of W that share square faces to generate infinite chains $[W_{8/2}(Si)]^1$. The other Si atoms form another set of confacial square antiprism surrounding the W square antiprism columns. The arrangement is illustrated in Figure 81 in a projection down the short c axis. This is analogous to the trigonal antiprism columns of Mn and Si in Mn_5Si_3. The square antiprisms are not regular, in the sense that their top and bottom faces are rotated with respect to each other by ~35° instead of 45°. The structure also contains parallel, linear chains of W (d = c/2) that lie within shared $[WSi_{4/2}]^1$ tetrahedra centered on the side faces of the cell. The two chains are not as independent as the description implies, however; the same Si atoms envelope both chains, those in the tetrahedra also bridge pairs of edges of of the W antiprisms.

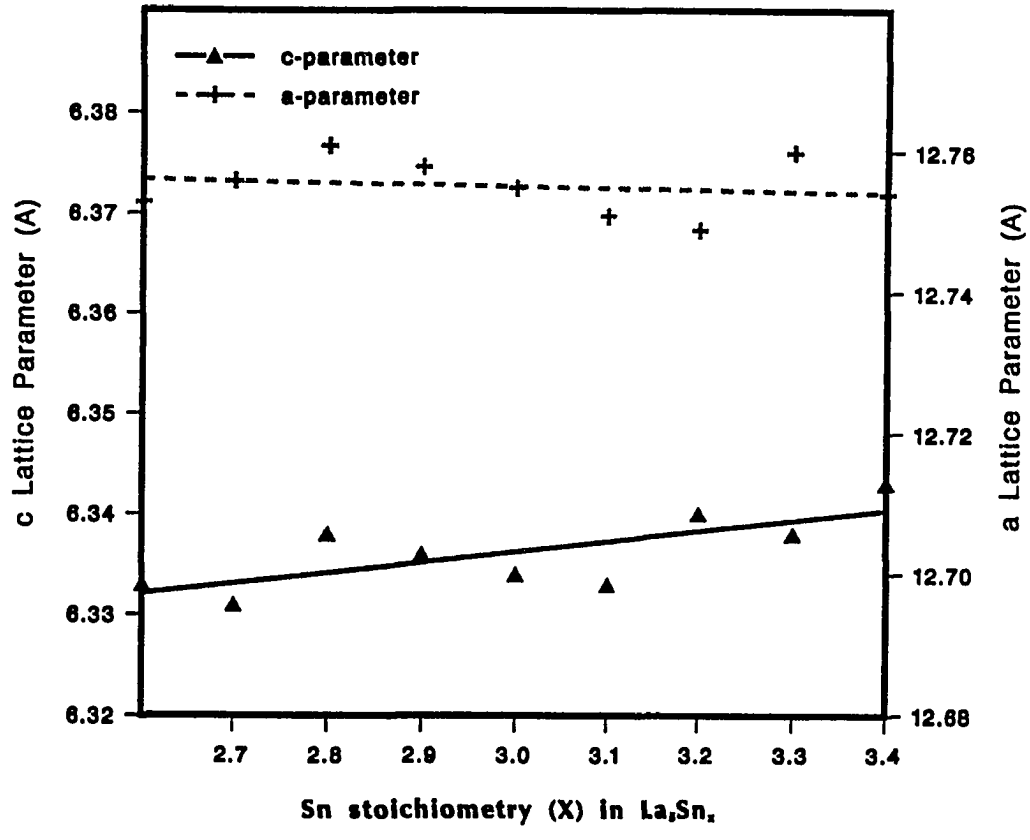

Figure 80. Variation of the lattice parameters (A) of La_5Sn_x (W_5Si_3-type, I4/mcm) as a function of x: a, +; c, Δ (standard deviations are as follows: a, (2-8) x 10^{-3}; c, (2-5) x 10^{-3} A)

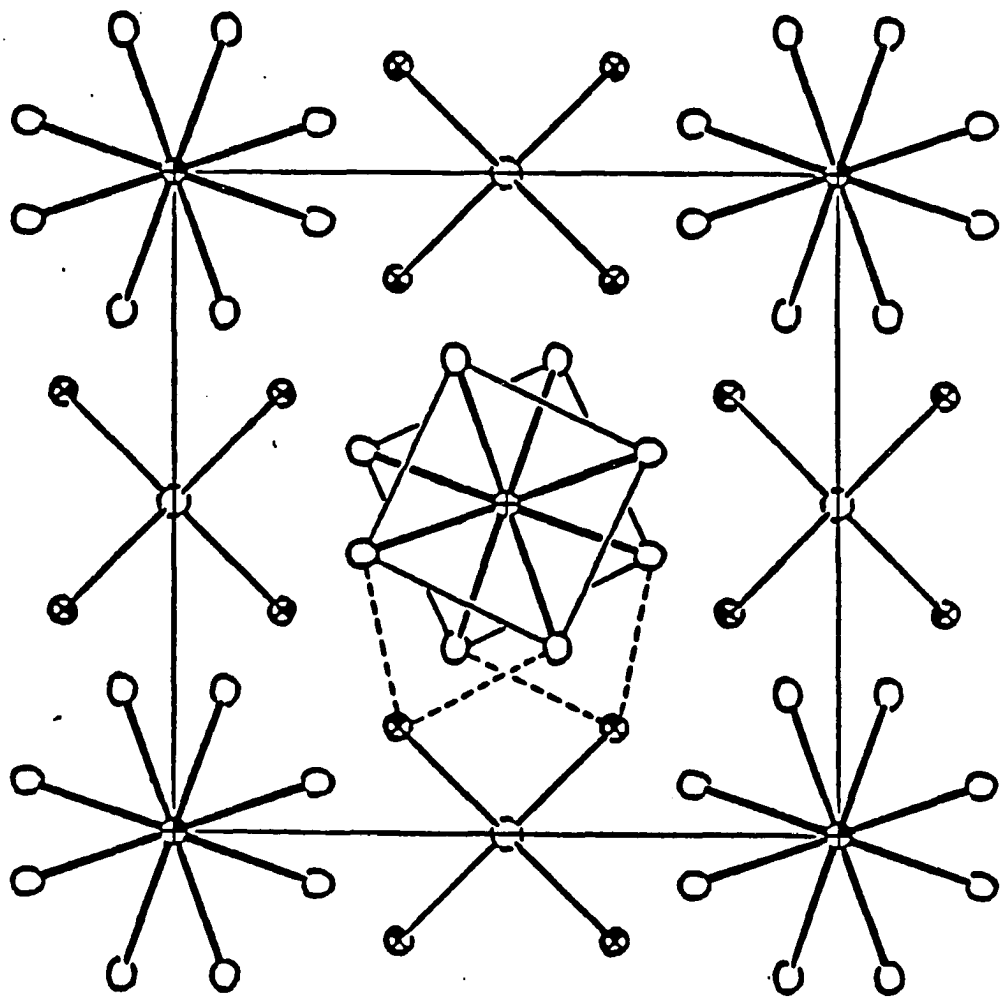

Figure 81. A projection of the tetragonal structure of W_5Si_3 down the c-axis. Note two types of chains; Si-centered square antiprism chains of W, and W-centered edge-sharing tetrahedral chains. Dashed lines illustrate the commonality of silicon to both chains. Open circles: W, octant shaded circles: Si

Franceschi reported that rapid cooling was necessary to get the Mn_5Si_3-type phase. Hence, similar SiO_2-jacketed samples were held for 2 weeks at 1050°C in a resistance furnace, and the contents quenched by dropping the container into water. Samples of La_5Sn_x with x = 2.75, 2.9, 3.0, 3.1, and 3.25 again all gave only the W_5Si_3 structure for the La_5Sn_3 component. Moreover, similar samples of La_5Sn_3 that were induction heated to 1400°C and cooled by turning the power off were always W_5Si_3-type, even when liquid N_2 was sucked into the vacuum system to hasten cooling. Thus, the earlier observations of the Mn_5Si_3 structure are not correctly attributed to either a quenchable from, as proposed, or because of a compositional difference between this and the W_5Si_3-type structure.

Mn_5Si_3-type structure of La_5Sn_3

Since we found a significant interstitial (Z) chemistry for the closely related La_5Ge_3Z and La_5Pb_3Z systems, reactions were carried out as before but with a variety of third elements, carbon and oxygen particularly. The oxide could be readily obtained by arc melting La, Sn, and La_2O_3 followed by annealing, whereas $La_5Sn_3C_x$ samples were obtained by powder sintering of the elements. In these cases, the expected Mn_5Si_3-type structure was always found. Lattice dimensions determined for $La_5Sn_3C_x$, x = 0.5, 0.75, 1.0, 2.0, and for $La_5Sn_3O_x$, x = 0.3, 0.10, are included in Table 54. It is in fact sufficient to obtain Mn_5Si_3-type samples to simply melt W_5Si_3-type La_5Sn_3 or a mixture of the elements in an arc furnace. The lattice dimensions of these products are close to those of $La_5Sn_3O_{0.3}$. Most importantly, no Mn_5Si_3-type product would revert to the W_5Si_3 form when annealed at 1000-1050°C for 3-7 days, so the two structures for nominal La_5Sn_3 are not related by a phase transition.

been seen in centered cluster halides[308,309] and could certainly occur here. There is not much reason to doubt that La_5Sn_3N will exist.

In contrast to the binary R_5T_3 germanides and plumbides, the stannides appear to be consistently Mn_5Si_3-type from neodymium on without (and presumably with) suitable impurities. The factors that make only the W_5Si_3 form more stable for the larger La_5Sn_3 and Pr_5Sn_3 are probably rather subtle.

Initial attempts to prepare transition metal interstitial analogs of La_5Sn_3Z have been promising. Single crystal investigations on crystals obtained from nominal reactions La_5Sn_3Zn indicate a tetragonal cell with lattice parameters which resemble a Cr_5B_3-type structure.[310] Reactions involving Fe, Mn and Co obtained from high-temperature reactions have resulted in Mn_5Si_3-type products. These products exhibit larger unit cell volumes than that of La_5Sn_3O. Careful inspection of their Guinier powder patterns do not show the extra lines attributed to a $La_{15}Ge_9Fe$-type structure. Similar results have been reported by Reiger and Parthe'[311] in the Ce_5T_3 and Yb_5T_3 (T = Sn, and Pb) systems. They reported the preparation of Cu- and Ag-stabilized Mn_5Si_3-type phases having the nominal stoichiometry R_5Sn_3Z and R_5Pb_3Z (Z = Ag, and Cu).

conclusive about its exact stoichiometry, especially in distinguishing between $Nb_{10}Ge_7$ (half-filled) and $Nb_{15}Ge_{10}$ (1/3-filled). The possibility of light elements stabilizing the structure was not addressed but arbitrarily discounted. Furthermore, the reported space group of this compound (P-3m1) was different from that found for Ca_5Pb_3 and $La_{15}Ge_9Fe$. It is also puzzling how a compound which has only half of the interstitial holes occupied could form a superstructure that is triple that of the parent Nb_5Ge_3 structure, but this was not explained.

The compound Ca_5Pb_3 was the first reported example of a $\sqrt{3} \times \sqrt{3}$ superstructure related to Mn_5Si_3. The Ca_5Pb_3 structure refinement was unsatisfactory because it was entirely based on film work. No anisotropic refinements were done, and thermal parameters were arbitrarily assigned from tables. No other single crystal investigations on Ca_5Pb_3 have been reported since the first work by Helleis et al. The more recent work by Bruzzone and Merlo[316] dealt with equilibration experiments and improved the data on Ca-Pb compounds particularly on the existence of Ca_3Pb which was established by Helleis et.al. We can presume that Ca_3Pb is actually Ca_3PbO[317] as manifested by a large volume contraction (30%) and supported by valence consideration. However their work did not address the structural problems pertaining to Ca_5Pb_3.

In addition to the challenging structural problem, Ca_5Pb_3 also presented a more interesting question about its chemical bonding. The Zintl concept predicts that binary compounds between alkaline-earth metals and tetrelides having the 5:3 ratio will form structures with equal proportions of dimers and isolated atoms of the main-group

In the spirit of the Zintl-Klemm concept, if indeed Ca_5Pb_3 is a true binary, it can be inferred that addition of divalent cations as interstitials might help stabilize the structure and fulfill its valence requirements. Results from powder and single crystal refinements seem to support this idea. A new class of compounds stabilized by cationic transition metals, Ca_5Pb_3Z, was discovered.

This chapter will discuss the final results of the reinvestigation of the Ca_5Pb_3 structure and the subsequent syntheses and structure of the novel interstitial compounds having the formula Ca_5Pb_3Z. The results of theoretical calculations on $Ca_{17}Pb_9$ using the tight-binding scheme based on extended-Hückel theory will also be presented and discussed.

Experimental Section

Materials The calcium metal chunks were obtained from Ames Lab as triply distilled elemental metal. It was stored and handled only in a Helium atmosphere glovebox. Lead metal sheet obtained from a commercial source (Aesar) was quoted to be 99.999% pure. Manganese powder (99.99%), iron chips (99.95%), ruthenium powder (99.999%), nickel sheets (99.99%), copper chips (99.999%), chromium powder (99.99%), vanadium powder (99.999%), magnesium strips, cobalt wire (99.99%), silver powder (99.98%), zinc pellets (99.999%), and cadmium strips (99.999%) were introduced as third elements. (Sources in Chapter 1, Table 1)

Reactions To ensure that the total content of each reaction was known and that minimum contamination occurred during the handling of the reagents, all manipulations and accurate weighting were done in a helium atmosphere glovebox (Dri-Lab). Welded reaction containers made from tantalum tubes appear to be satisfactory as was

demonstrated by the absence of any visible attack and the ductility of the tubes before and after the heat treatments. Mixtures of the weighed reagents were loaded and sealed into 3/8" tantalum containers and heated in a high-temperature vacuum furnace or in a resistance furnace (inside a silica jacket) to 950-1050°C over three days. The samples were then melted at 1300°C and slowly cooled to 1000°C over five more days. For some quenching reactions, the welded Ta containers were sealed in evacuated and well baked SiO_2 jackets, heated in a resistance furnace and afterwards dropped into cold water. For other quenching reactions, the welded Ta containers were heated in an induction furnace and quenched by back-filling the reaction chamber with the off-gas from liquid nitrogen.

The reaction products were characterized with the aid of Guinier X-ray powder diffraction using NBS silicon as an internal standard. The stoichiometries of selected binary products were confirmed by atomic absorption spectrometry. Samples for atomic absorption analysis were prepared by dissolving crystals in 1.5M HNO_3 at 40°C. Electron microscopic analysis was also attempted on some of the binary products to confirm equilibration results. However, the severe air sensitivity of the binary compounds of Ca and Pb made the SEM results less reliable.

Magnetic susceptibility measurements were done taking into account the air sensitivity and weak magnetic signals of the binary compound.

The syntheses of the ternary interstitial compounds required longer heat treatments to ensure the reactions reached equilibrium, i.e., the reaction tubes were heated at 1300°C for an additional four days. To confirm the stoichiometry of the interstitial compounds, electron microscopic analysis were done on the Fe, Co, Cu, and Mn analogs. This was

made possible by the seemingly lower air-sensitivity of the ternary interstitial compounds compared with the binary Ca-Pb compounds.

Results

$Ca_{5.67}Pb_3$

Synthesis The most recent Ca-Pb phase diagram[317] indicated that Ca_5Pb_3 forms by peritectic reactions at 1127°C from the liquidus and Ca_2Pb. The phase diagram also reveals that CaPb forms from a peritectic reaction of Ca_5Pb_3 with the liquidus below 968°C. The compound Ca_5Pb_3 also lies between two eutectics, at 40 at% and 90 at% Ca at 630° and 700°C, respectively, which makes it possible to grow single crystals from the melts at temperatures below 1127°C and above 968°C where the intermediate CaPb disappears. Single crystals were obtained from slowly cooled samples using the high-temperature high-vacuum furnace from 1100°C. To achieve equilibrium composition, Ca-rich products also need prolonged annealing at high temperatures above 750°C. Otherwise, a thermal arrest near 670°C is observed[324] which corresponds to the melting point of $CaPb_3$.

Structure determination A rod-like single crystal (0.03 x 0.03 x 0.15 mm) of Ca_5Pb_3 obtained from a reaction with a 5:3 loaded stoichiometry was isolated and investigated using the AFC6R-Rigaku diffractometer. The cell parameters were refined from 2θ values of 25 reflections ($10<2\theta<22°$) using programs SEARCH and INDEX. The lattice parameters were later recalculated by least squares fit of the Guinier powder data using (NBS) silicon as an internal standard. To make sure that proper assignments of the lines were done, the observed powder patterns were carefully compared with a

calculated powder pattern for the refined structure of $Ca_{5.67}Pb_3$. Reflections within two octants of the reciprocal sphere up to $2\theta_{max} = 68°$ were measured in the ω-2θ scan mode. Three standard reflections (3,-6,0); (4,-5,-1) and (5,-4,-1) were measured with an average intensity variation of -4.2% for a total exposure time of 72 hours. Initial empirical absorption corrections were applied based on 3 psi scans. Data averaging in the Laue group 6/mmm resulted in 394 independent reflections (R_I=12.2%, including unobserved reflections) for the structure refinement of $Ca_{5.67}Pb_3$.

Precession photographs were taken on the Ca_5Pb_3 crystal to confirm the $\sqrt{3}$ x $\sqrt{3}$ expansion and to look for any possible ordering along the **c**-axis. The hexagonal block shape of the single crystal made it relatively easy to align for precession film work. Zero layer photographs confirmed the $\sqrt{3}$ x $\sqrt{3}$ expansion along the **a**-**b** plane and gave a lattice parameter of **a** = 16.16 A. Cone photographs also confirmed the **c**-axis parameter, **c** = 6.91 A, obtained from the single crystal diffractometer. Longer film exposures (48-50 hours) produced no visible diffraction spots corresponding to any superstructure along **c** or any further ordering along the **a**-**b** plane. Laue photographs showed the existence of a six-fold axis of rotation along the **c**-axis and two mirror planes perpendicular to the **a**-**b** plane and bisecting the angles formed by the **a** and **b** axes. Higher level photographs also indicated a systematic absence corresponding to the conditions for the space groups $P6_3/mmc$(194), P62c(190) and $P6_3mc$(186), hhl: $l \neq 2n$, and 00l: $l \neq 2n$. The last space group, $P6_3mc$, proved to be the correct one during the refinement.

The structure was refined in the space group $P6_3mc$ using the initial atomic parameters reported by Helleis et al. for the Ca_5Pb_3. The weighting scheme was according to the counting statistics, and the parameter accounting for isotropic secondary

Table 55. Data collection and refinement parameters for $Ca_{17}Pb_9$

Space group	$P6_3mc$
Z	2
Crystal dimension(mm)	0.03 x 0.03 x 0.15
Diffractometer	Rigaku AFC6R
2θ max	68°
no. of octants	2(h,k,±l)
Reflections:	
measured	4208
observed($>3\sigma_I$)	1451
independent	394
R_I (averaging)	12.2%(all reflections)
no. of parameters refined	36
R (refinement)	3.2%
R_w(refinement)	4.0%
G.O.F. 1.14	
Largest parameter shift	0.00
Absorption coefficient	659 cm^{-1} (Mo Kα)
Secondary extinction coeff	8.29(3) x 10^{-7}
Transmission range	0.236 - 0.995
Largest residual peaks	+2.18, -1.90 e/A^3
Cell Parameters (Guinier):	
a = 16.1618(2)A	
c = 6.9831(6)A	
V = 1579.6(1)	

Table 57. Important interatomic bond distances and angles in $Ca_{17}Pb_9$

atom1	atom2	distance (A)	atom1	atom2	distance (A)
Ca(1)	Pb(1)	3.3764(7)	Ca(1)	Pb(1)	3.6105(7)
Ca(1)	Pb(2)	3.3517(4)	Ca(1)	Pb(2)	3.4108(5)
Ca(1)	Pb(3)	3.2306(5)	Ca(1)	Pb(3)	3.3615(6)
Ca(1)	Ca(1)	3.501(1)	Ca(5)	Ca(5)	3.5015(5)
Pb(1)	Pb(2)	3.5080(1)	Ca(2)	Ca(6)	3.130(4)
Ca(4)	Ca(5)	3.096(3)	Ca(4)	Ca(5)	3.128(4)
Ca(2)	Pb(1)	3.164(2)	Ca(2)	Pb(3)	3.157(1)
Ca(2)	Pb(2)	3.461(1)	Ca(2)	Ca(1)	3.725(4)
Ca(2)	Pb(2)	3.907(2)	Ca(2)	Ca(1)	3.922(4)
Ca(2)	Ca(3)	4.086(3)	Ca(2)	Ca(2)	4.457(3)
Ca(3)	Pb(3)	3.192(1)	Ca(3)	Ca(6)	3.303(3)
Ca(3)	Pb(3)	3.3537(6)	Ca(3)	Pb(2)	3.3608(6)
Ca(3)	Ca(1)	3.572(3)	Ca(3)	Ca(1)	4.054(2)
Ca(3)	Pb(3)	4.094(2)	Ca(4)	Pb(1)	3.2283(7)
Ca(4)	Pb(2)	3.2442(4)	Ca(4)	Ca(1)	4.055(4)
Ca(4)	Ca(4)	4.281(2)	Ca(4)	Ca(1)	4.125(4)
Ca(4)	Ca(4)	4.271(2)			

Distances are in Angstroms. Estimated standard deviations in the least significant figure are given in parentheses

Interatomic angle,

atom1	atom2	atom3	angle
Ca(1)	Ca(1)	Ca(1)	174.6(2)° [164.36° in $La_{15}Ge_9Fe$]

Table 58. Chemical analyses[a] of Ca_5Pb_3Z phases

loaded stoich.	at% Ca	at% Pb	at% Z	calc. formula	remarks
$Ca_{17}Pb_9$	65.2(1)	34.8(1)		$Ca_{5.62(1)}Pb_3$	A.A.(x'tals)
$Ca_{17}Pb_9$	65.3(1)	34.7(1)		$Ca_{5.65(1)}Pb_3$	X-ray single x'tal
$Ca_{17}Pb_9$	65.0(1)	35.0(1)		$Ca_{5.6(1)}Pb_3$	SEM
Ca_5Pb_3	64.9(2)	35.1(2)		$Ca_{5.54(8)}Pb_3$	A.A.(isolated x'tals)
Ca_5Pb_3Fe	56.4(1)	32.73(4)	10.8(1)	$Ca_5Pb_{2.9}Fe_{.96}$	SEM
Ca_5Pb_3Mn	55.2(1)	34.25(5)	10.5(1)	$Ca_5Pb_{3.1}Mn_{.95}$	SEM
Ca_5Pb_3Mn	55.26(4)	33.56(1)	10.73(6)	$Ca_5Pb_{3.04}Mn_{.97}$	X-ray single x'tal
Ca_5Pb_3Cu	55.5(1)	32.22(5)	12.2(1)	$Ca_5Pb_{2.9}Cu_{1.1}$	SEM
Ca_5Pb_3Co	55.9(1)	33.56(5)	10.5(1)	$Ca_5Pb_{3.0}Co_{.93}$	SEM

[a] the Pb composition was determined by difference

misassignments and lower resolution (Debye-Scherer) in their powder data. This is not surprising because the calculated powder diffraction patterns of $Ca_{5.67}Pb_3$ and its Mn_5Si_3-type subcell, as shown in Figure 82, are very similar. These differ mainly in three weak lines that could easily mislead the indexing of their powder diffraction peaks. The other lines which do not match in the calculated powder patterns are very weak and could not be observed in the experimental powder data.

Structure description The structure of $Ca_{5.67}Pb_3$, as shown in Figure 83, can be described as the "hole" version of the $La_{15}Ge_9Fe$ structure. Both structures show the $\sqrt{3}$ x $\sqrt{3}$ expansion of the Mn_5Si_3 parent structure and have the same empty "host" interatomic connectivity. They also have two types of columns of trigonal antiprisms in a ratio of 2:1. In $La_{15}Ge_9Fe$, the octahedral interstitial holes are one-third filled in an ordered manner, wherein one type of chain is half-filled and the other is empty. In $Ca_{5.67}Pb_3$, the interstitial sites are two-thirds filled, that is, one chain is half-filled and the other is completely filled. The differences between the two structures lie in that the columns which are empty in $La_{15}Ge_9Z$ are fully filled in $Ca_{5.67}Pb_3$. Moreover, the interstitials in the half-filled columns lead to contractions of metal-interstitial distances in $La_{15}Ge_9Z$, whereas, the opposite effect is observed in $Ca_{5.67}Pb_3$.

The interatomic in-plane and interplanar distances between the Ca atoms in the filled confacial antiprisms are 4.27 and 4.28A long, respectively. The half-filled confacial chains exhibit a wider range of interatomic distances; 4.17 and 4.21A for in-plane distances and 4.08A (short) and 4.43A (long) for the interplanar distances. These distances are large compared to the Pauling single bond distance of 3.48 A[325] and the

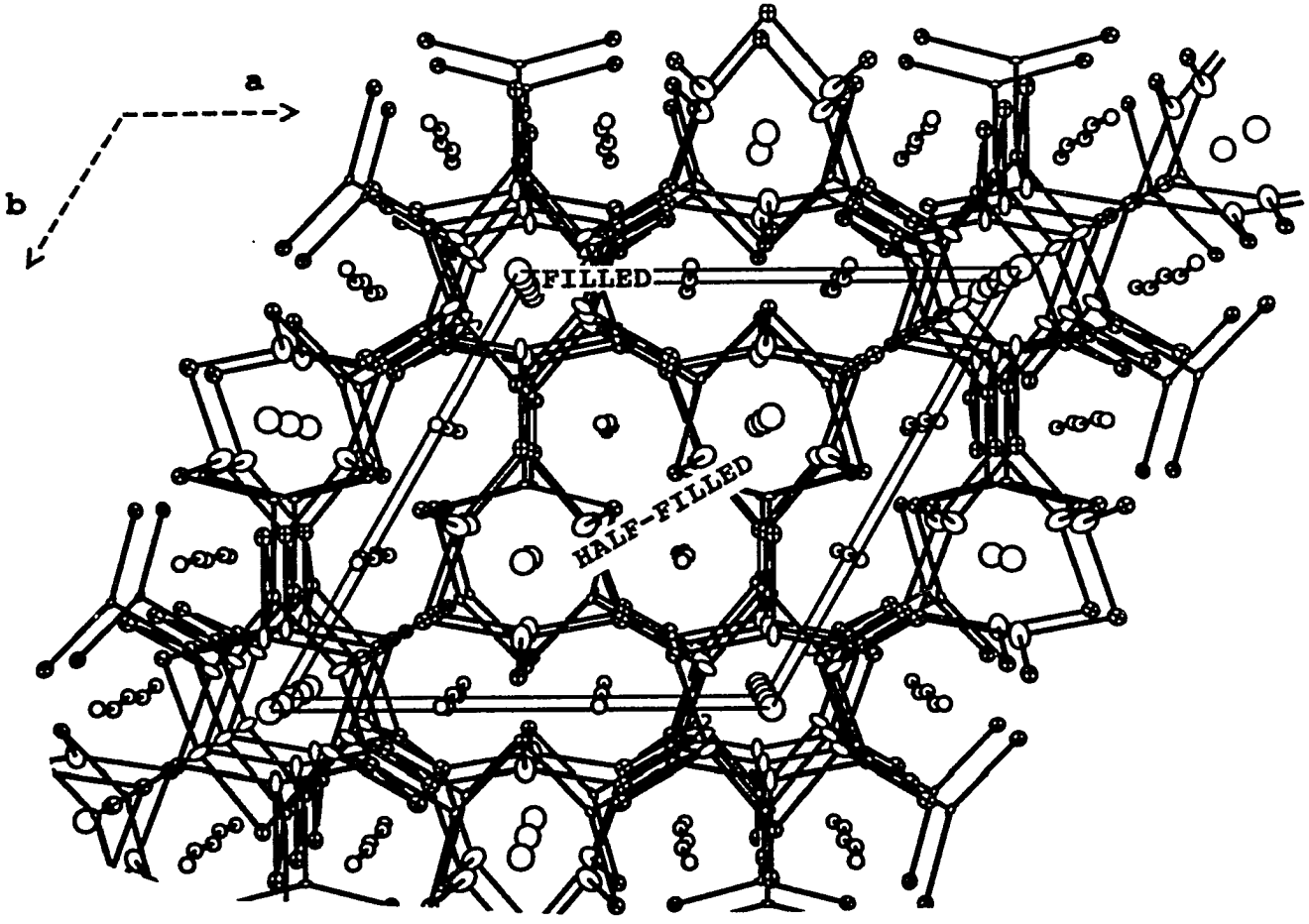

Figure 83. An ORTEP drawing of a [001] view of a section of the $Ca_{5.67}Pb_3$ structure. Ca, Pb atoms are represented by open and crossed-hatched circles, respectively. The two types of filled antiprisms are indicated. The "Pb-Pb" bonds interconnect the different types of columns which differ by the filling of their interstitial sites. Ca(2)-Pb and Ca(1)-Ca(1) contacts are drawn for clarity. The isotropic thermal ellipsoids are sketched

shortest Ca-Ca distance in the metal, 3.90 A.[326] This is not observed in the metallic $La_{15}Ge_9Z$ compounds, where the La-La distances in the confacial antiprisms are shorter or comparable to that in the metal. It is also surprising that some of the observed nearest neighbor distance between calcium atoms of the antiprisms and the calcium atoms in the nominal linear chain is even shorter, Ca(1)-Ca(3) d = 3.57A, than the distances between calciums within an antiprism chain. This behavior has not been observed in any other Mn_5Si_3-type and related compounds that have been investigated. The nearest neighbor Ca-Ca distances between those defining the trigonal antiprisms and the interstitial Ca are very short, ranging from 3.15 to 3.16 A as compared to the Pauling single bond distance of 3.48 A. This is surprising in that electron counts indicate that there are no electrons left for Ca-Ca bonding and that no Ca clusters have ever been reported in the solid state. In a review[327] on metal-metal bonds, Simon asserts that short metal-metal distances alone do not constitute a valid chemical bond and that metal-metal distances in metal-rich compounds are largely affected by metal-nonmetal interactions. The availability of electrons for bonding, i.e. the valence requirement, is more important in determining whether a metal-metal bond exists in a compound. Hence, the short distances between Ca atoms only reflects the smaller size of the Ca^{2+} ion compared to the uncharged atom.

An ionic picture using Shannon's ionic radius of 1.14A (CN=6) for Ca would satisfy the non-bonding distance requirements in $Ca_{5.67}Pb_3$. The presence of interstitials in alternating holes in the columns of trigonal antiprisms produce a Peierls-like distortion of the columns. An expansion of the filled trigonal antiprism and contractions around the empty interstitial site is observed, the opposite to that in $La_{15}Ge_9Fe$. In the structure, each half-filled metal confacial chain has 6 nearest neighboring confacial chains, 3 half-

filled chains and 3 filled chains. Neighboring half-filled antiprism columns are shifted by z+1/2 with respect to the filled sites (see Figure 84). There are no close Pb-Pb contacts between the Pb atoms making up the confacial trigonal antiprisms surrounding the neighboring half-filled metal columns. However, Figure 85 shows the closest Pb-Pb distances, 3.51A, are found between the Pb(1) and Pb(2) which make up the Pb antiprisms surrounding the filled chains and part of the half-filled chains respectively. Other nearest neighboring Pb-Pb distances are found to be more than 4.0 A.

The other important structural features of $Ca_{5.67}Pb_3$ are the nearby linear chains of calcium atoms running parallel with the columns of metal antiprisms. The observed Ca-Ca distances in these linear chains (3.5 A) correspond to single bonds based on the Pauling radius, 3.48A. A slight ($\Delta = 5°$) buckling distortion of the Ca(1) chains from linearity is also observed. This angular distortion is coupled to a distortion of the confacial trigonal antiprisms because of the ordered occupancy of the interstitial sites by Ca and effects of the non-planarity of the Pb atoms. Figure 86 illustrates the coordination (d<3.7A) around the Ca linear chains, 6 Pb atoms and one Ca(3). We can observe that the close approach of Pb(1) and Pb(2) opens up the the space across the dimer, allowing Ca(3) to move into the void, hence matrix effects cause the close approach of Ca(3) and Ca(1) (d=3.57A).

The observed Ca-Pb nearest neighbor distances (3.16-3.38 A) are comparable to known Ca-Pb distances in Ca_2Pb and CaPb. The relatively large distance between Pb(1) and Ca(1) in the linear chain can also be attributed to the distortion caused by the pairing of Pb(1) and Pb(2) (see Figure 85). The unique Ca-Pb framework can be described as a distorted analog of the Mn-Si framework in the Mn_5Si_3 type. The distortion is seen in the

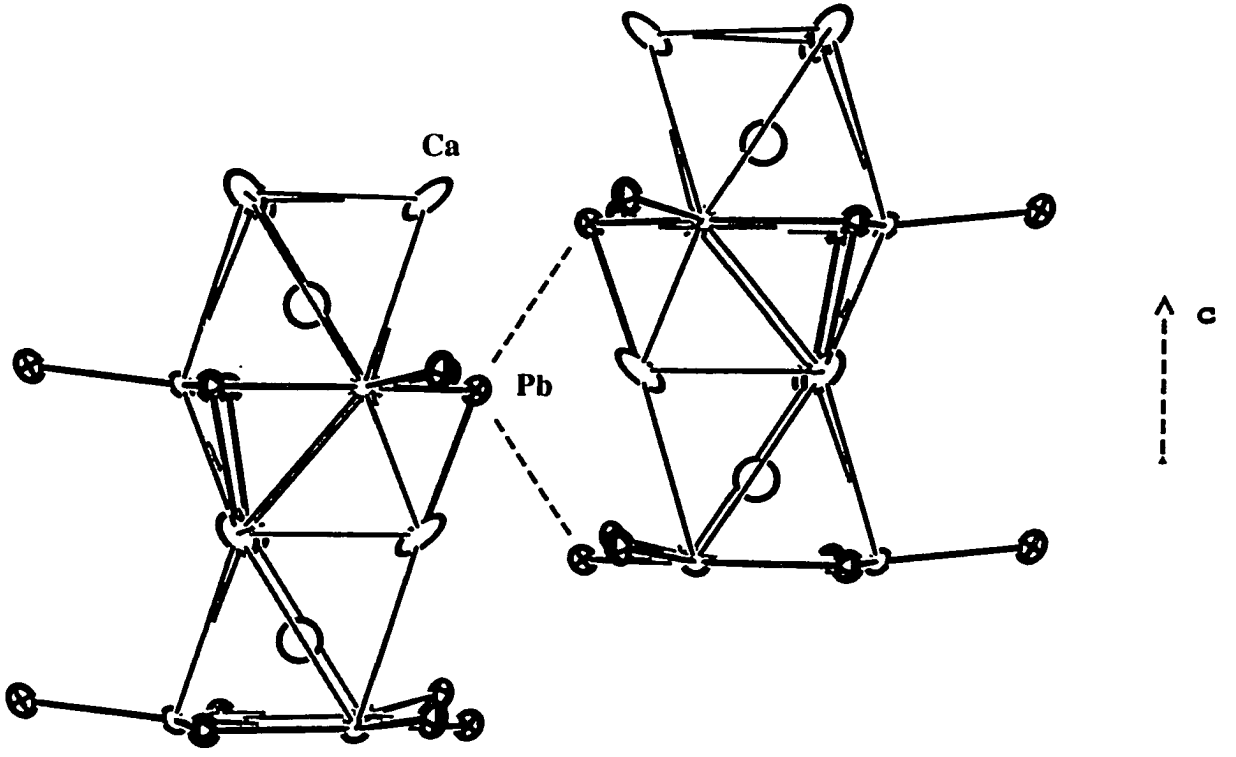

Figure 84. An ORTEP drawing of the [110] view of a pair of neighboring half-filled-trigonal antiprism columns in $Ca_{5.67}Pb_3$. Note their relative displacement (1/2+z) with respect to the filled interstitial sites. Pb atoms (crossed-hatched) are shown with the Ca atoms (open circles). There are no short Pb-Pb contacts between the Pb atoms of the same type of columns. The thermal ellipsoids are sketched at 90% probability

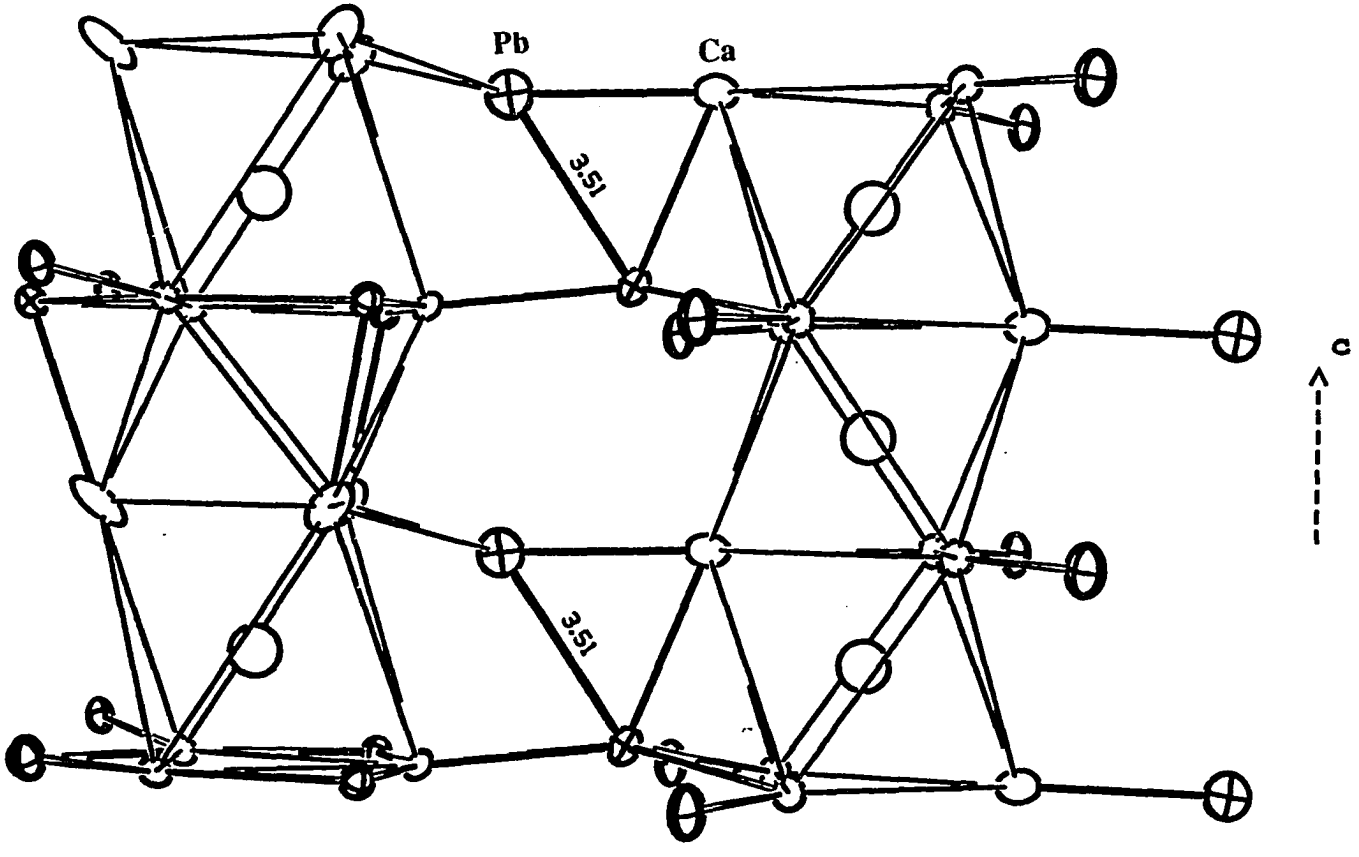

Figure 85. An ORTEP drawing of the [110] view of neighboring filled-trigonal and half-filled antiprism columns in $Ca_{5.67}Pb_3$. The non-planarity of the Pb atoms (crossed-hatched) with the Ca atoms (open circles) lead to a distorted picture of the chains. Pb(1)-Pb(2) bonds (3.51A) connect the two columns. Ca-Ca lines are drawn to outline the antiprisms. The thermal ellipsoids are sketched at 90% probability

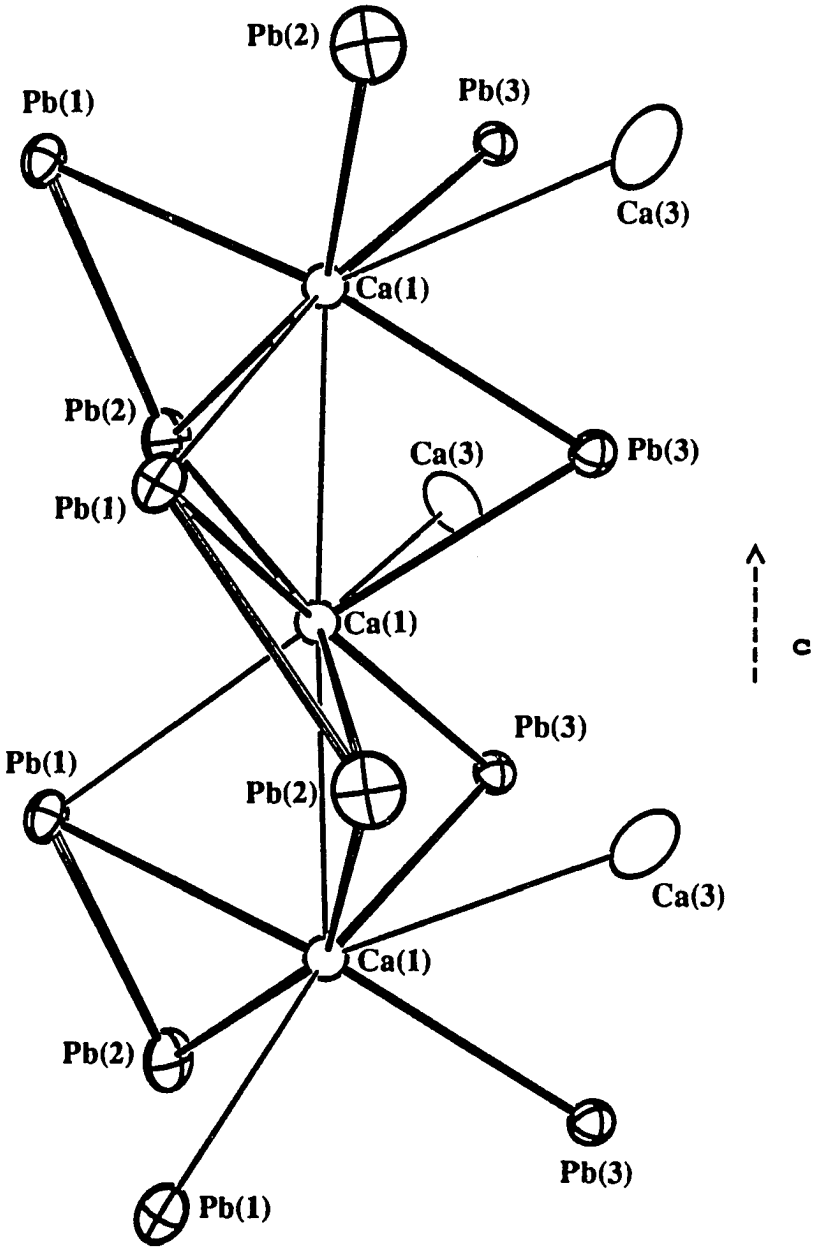

Figure 86. The nearest neighbors (d<3.7A) of Ca(1) linear chain atoms. Note the distortion of the Pb arrangement due to the close approach of Pb(1) and Pb(2) atoms results in two Ca(1)-Pb(1),Pb(2) and Pb(3) distances and a short Ca(1)-Ca(3)

shifting of the Pb atoms (Pb(1) and Pb(2)) from the trigonal plane of Ca atoms thereby causing half of the bridging Pb atoms of a half-filled trigonal antiprism column to approach the Pb atoms of the nearest neighboring fully-filled antiprism columns. This non-planarity of the Pb atoms with respect to the Ca triangles is not observed in the $La_{15}Ge_9Z$ compounds where the Ge atoms are coplanar with the La triangles. This was not imposed by the symmetry of the space group $P6_3mc$. This difference is manifested by the different axial **c/a** ratios $Ca_{5.67}Pb_3 = 0.42$; $La_{15}Ge_9Z = 0.47$ and by an inspection of the shape of the anisotropic parameters of Pb(1) and Pb(2) (see Figures 84 and 85). The closest Pb-Pb distance in $Ca_{5.67}Pb_3$ is 3.51 A, comparable to the nearest neighbor distance in Pb metal of 3.48 A. A bond order calculation based on the Pauling equation yields 0.20. Since refined stoichiometry and the structure description shows that the compound is still "electron-poor", this leads us to infer that some Pb-Pb bonding must be present to account for the necessary electrons needed to fill up the valence bands of Pb.

Chemical bonding and electronic structure There are 6 close Pb(1)-Pb(2) contacts/unit cell in the $Ca_{5.67}Pb_3$ structure. In a limiting case, if these were all single Pb-Pb bonds, then the electron counting for the hypothetical distorted Ca_5Pb_3 would satisfy the Zintl concept since 12 Pb^{3-} and 6 Pb^{4-} atoms would require 36+24=60 electrons from the 30 Ca atoms in the cell. However, the observed Pb-Pb distances are relatively longer and suggest a weaker than single bond. Some known Pb-Pb bonding distances in the solid state are shorter than 3.5 A. However, interactions between Pb atoms at larger distances (>3.8A) have been used to rationalize the structural preference of PbO.[328] This variation would suggest that the formation and the extent of Pb-Pb bonding in $Ca_{5.67}Pb_3$ maybe a tuning variable in the compound's electronic structure.

The electrons donated by the interstitial calciums fill up the necessary bonding states created by the close approach of the Pb(1) and Pb(2) atoms. The electronic factor for the actual $Ca_{5.67}Pb_3$ structure requires only 2 dimers per 18 Pb atoms in a unit cell, hence it is not puzzling why the Pb-Pb bonds are long and weak. A similar case may exist in $Ca_{16}Sb_{11}$ and its analogs.[329]

The formation of partial Pb-Pb bonds may explain the structural puzzle observed in the compound. The matrix effect induced by the off-planar approach of Pb atoms leads to shorter Ca(antiprism)-Ca(interstitial) distances in antiprism chains that have fully filled interstitial sites compared with those in half-filled chains, since all Pb atoms that bridge the calciums in the filled-antiprism chains are "bonded" to a bridging Pb atom of a neigboring half-filled chain. In the half-filled chains only half, three, of the bridging Pb atoms interact with the Pb atoms of a neighboring chain (see Figures 83 and 85).

Magnetic susceptibility measurements on $Ca_{5.67}Pb_3$ indicate that the compound is diamagnetic after corrections for core diamagnetism; Pb^{2+} = -32.0 x 10^{-6} emu/mole, Ca^{2+} = -10.4 x 10^{-6} emu/mole (see Figure 87). This suggests that there are no localized unpaired electrons in the compound and that the electronic structure is characterized by filled bands or a very low DOS at the Fermi level. A possibility of weak temperature independent paramagnetism cannot be completely ruled out because of the weak diamagnetic signal obtained from the measurements and possible inaccurate diamagnetic correction for the filled valence bands near the fermi level derived from Pb 6s and 6p orbitals. The severe air sensitivity of the compound did not allow us to do any accurate 4-probe electrical conductivity measurements. Simple 2-probe measurements on a clean block sample (~1.0 x 1.0 x 0.5 cm) of $Ca_{5.67}Pb_3$ using a commercial ohmmeter inside the

helium atmosphere glovebox indicated a resistance of 0.10 ohms which was constant regardless of point of contact. However, electrical resistivity measurements using the electrodeless Q-method[330] over the range of 77-295°K provided a quantitative temperature dependence of the electrical resistivity, -0.21% per degree; E_g = 0.05 eV; ρ = 350 $\mu\Omega$-cm, characteristic of a semimetal or a narrow-gap semiconductor. The above results led us to search for compounds with similar "problems".

The compound Li_2Sb[331] presents a similar problem; isolated Sb and Sb_2 dumbbells occur in a ratio 1:1. Applying the Zintl concept would formally lead to Sb^{-3} and Sb_2^{-4} anions. However, there are only six Li atoms which cannot provide the necessary seven electrons. It was proposed[332] that the large Sb-Sb distances between the "isolated" Sb atoms represented half-bonds that compensate for the lacking electron. Hence all Sb atoms gain one net single bond and the Zintl-Klemm concept applies accordingly.

An analogy between Li_2Sb and $Ca_{5.67}Pb_3$ can be made. The closest Pb-Pb distances (3.55 A) found in $Ca_{5.67}Pb_3$ can be considered as sufficient bonding distance, especially in dumbbell-like (X^--X^-) dimers where bond lengthening is accounted for by the electrostatic repulsion between equally charged atoms. As stated earlier, the electronic requirements do not need a full Pb-Pb single bond, and if the closest Pb-Pb contacts were considered bonds with n=1/3, then the Pb matrix gains one single bond per unit cell and $Ca_{5.67}Pb_3$ may be considered a Zintl phase. This is formally expressed as $(Ca^{2+})_{17}[Pb^{3-}\text{-}Pb^{3-}][Pb^{4-}]_7$.

Extended-Hückel calculations The above results led us to investigate the electronic band structure of $Ca_{5.67}Pb_3$ and extract the various electronic factors which govern the structural and physical behavior of the compound. Extended-Hückel band

structure calculations were done on an ideal Ca_5Pb_3 having a Mn_5Si_3 structure and on the actual $Ca_{5.67}Pb_3$ structure. This enabled us to trace the orbital interactions responsible for the observed superstructure. Details of the calculations is presented in Table 60 and in Appendix A.

Results of the calculations on the ideal Ca_5Pb_3 structure show that its calculated DOS (Density of States), shown in Figure 88, is characterized by seemingly well separated Pb bands, (Pb)6s-bands at ~ -18 to -15.5 eV, the (Pb)6p-bands at around -11 to -6 eV, and the Ca metal bands, at -3.5 eV and higher. These bands have relatively large bandwidths (dispersions) and atomic projections of the DOS reveal strong Ca-Pb mixing. The DOS also reveals a relatively high density of states at the calculated fermi levels of Ca_5Pb_3 and $Ca_{5.67}Pb_3$. The large Ca-Pb mixing is also illustrated by the COOP (Crystal Orbital Overlap Population) of Ca-Pb bonds (see Figure 89). The maximum summed overlap between Ca and Pb atoms, assuming a rigid band picture, are calculated to be around -6.6 eV which corresponds to the Fermi energy for the electron count of $Ca_{5.67}Pb_3$. The COOP of Pb-Pb (Figure 89) interactions show the bonding and anti-bonding interactions between Pb atoms correspond to Pb(1) and Pb(2) interactions in the actual structure. The COOP curve also indicates that the Pb-Pb interactions are strongly anti-bonding around the Fermi level. It is surprising that even in an ideal Mn_5Si_3-type structure with Pb-Pb distances greater than 4 A, the Pb orbital interactions are significant enough to cause a splitting of the Pb 6p-orbitals in to its x-y and z components.

A close inspection of the orbital projections of the DOS (Figure 88) show that the Pb p-bands can be characterized as two types, those that lie on the a-b plane P$\parallel$(p_x and p_y) and those perpendicular to the a-b plane P$\perp$(p_z). The P$\perp$ orbitals which lie at higher

Table 60. Summary of extended-Hückel calculations[a] on $Ca_{5.67}Pb_3$

system	Fermi level (eV)	E_{tot}/Pb atom (eV)	Pb-Pb overlap population
Ca_5Pb_3 ($P6_3/mcm$)	-6.90	-81.31	-0.006
$Ca_{5.67}Pb_3$ ($P6_3/mcm$)	-6.60	-82.42	-0.064
Ca_5Pb_3 ($P6_3mc$)	-7.16	-80.28	+0.233
$Ca_{5.67}Pb_3$ ($P6_3mc$)	-6.86	-81.64	+0.226

[a] An Extended Hückel crystal orbital method was used with the parameters given in the Appendix. The κ-space integrations were performed with a 40 and 60 κ-point sets for the actual ($P6_3mc$) and ideal ($P6_3/mcm$) structures respectively

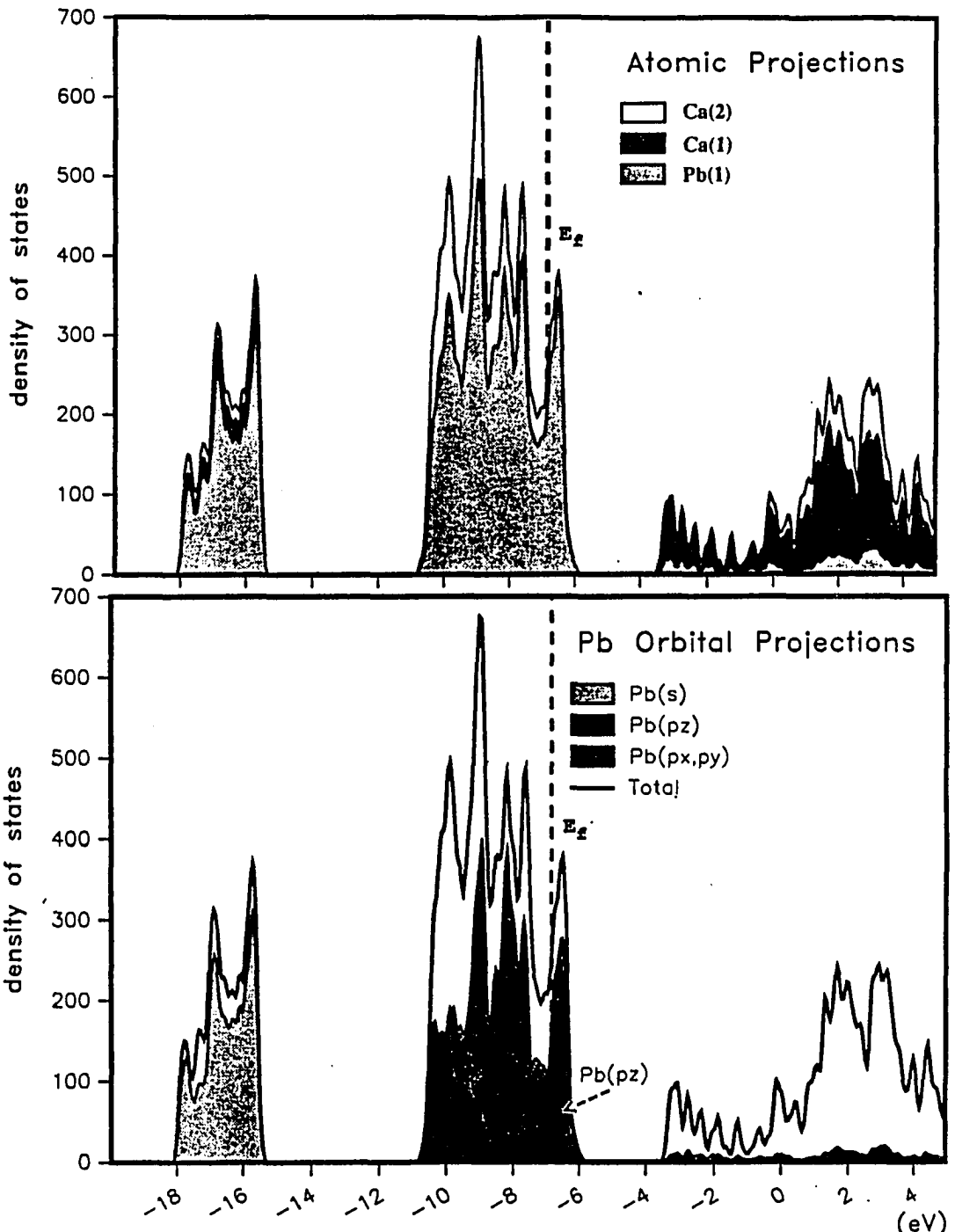

Figure 88. Calculated Density of States of Ca_5Pb_3 (Mn_5Si_3-type), N(E) vs energy(eV) and its different atomic (top) and Pb orbital (bottom) projections. The Fermi level, E_f, for $Ca_{5.67}Pb_3$ is indicated by a dashed line

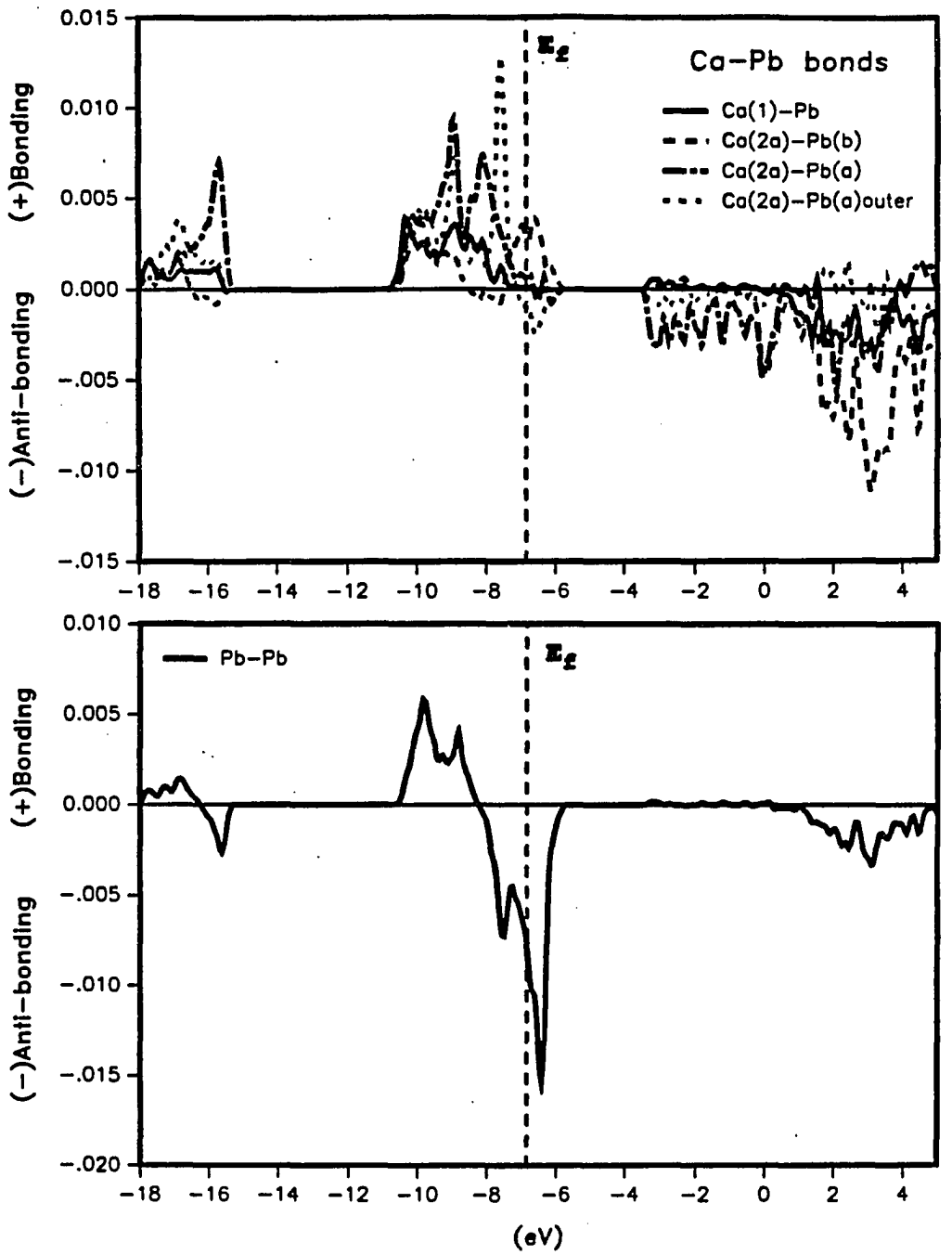

Figure 89. The Crystal Orbital Overlap Population (COOP) of (a)Ca-Pb and (b)Pb-Pb interactions in Ca_5Pb_3 with the Mn_5Si_3 structure. The Fermi level, E_f, for $Ca_{5.67}Pb_3$ is indicated by a dashed line

energies represent the bands that cross the Fermi energies corresponding to the empty and two-thirds filled compounds. These higher lying P$\perp$ bands represent the antibonding interactions between Pb atoms which largely influence the chemical bonding of $Ca_{5.67}Pb_3$. An orbital analyses of the Pb(p_z) bands will help us understand the effects of these bands on the electronic structure of $Ca_{5.67}Pb_3$.

The interactions between Pb p_z-orbitals in the ideal $Ca_{5.67}Pb_3$ can be assigned to 6 bands which include two single representations and two pairs of doubly degenerate bands represented in Figure 90. At the Γ point (center of the Brillouin zone) the first three bands are stabilized by the bonding interactions between the Pb atoms of neighboring antiprism chains. The interaction between neighboring unit cells represented by the low lying p_z states (e_g and a_{1g}) is illustrated by the large bandwidths observed, which range from about -10 to -6.0 eV. The other 3 p_z bands (e_u and a_{2u}) lie slightly higher in energy between -9 to -6 eV. As the bands move out from the center of the Brillioun zone their overlap population characteristics change and lead to interesting results.

The band structure of the ideal Ca_5Pb_3 structure along the symmetry lines Γ-**K**, Γ-**M** and Γ-**A** are shown in Figure 91. At the Γ point there are three low lying P$\perp$ bands corresponding to the a_{1g} representation at -10.13 eV and a pair of degenerate e_g bands at -9.33 eV. These bands illustrate Pb-Pb σ-type bonding interactions along the z-axis between non-coplanar Pb atoms; hence they lie at lower energies. The a_{1g} band is further stabilized by π-type interactions between coplanar Pb atoms. The other P$\perp$ bands , a pair of degenerate e_u and the a_{2u}, have higher energies and lie close to the Fermi level at -7.77 and -5.9 eV respectively. The e_u and a_{2u} bands show σ-type antibonding between non-coplanar Pb atoms. The π-type interactions between coplanar Pb atoms found in a_{2u} is

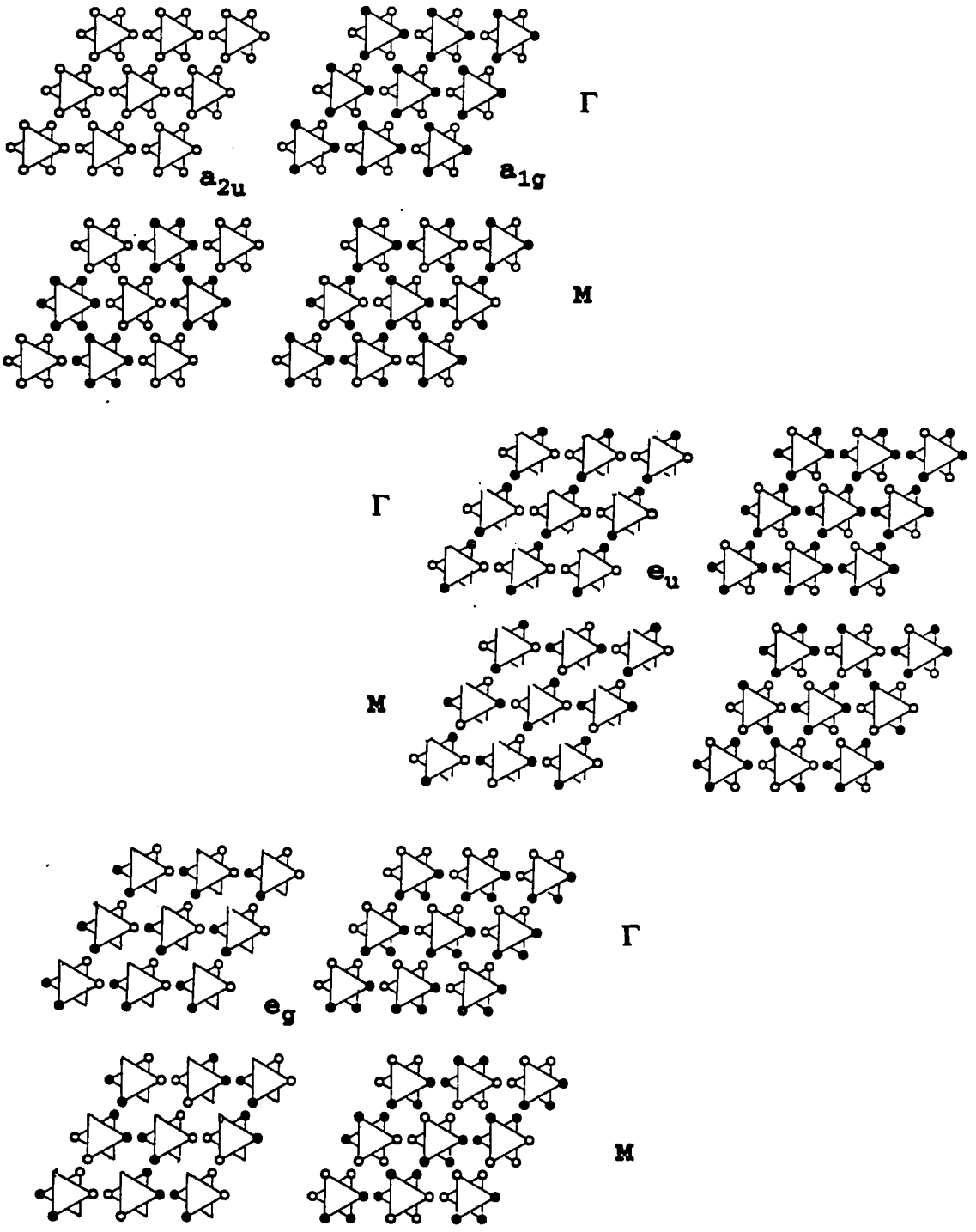

Figure 90. Orbital representations of the Pb(p_z) a_{2u} and a_{1g} (top), e_u (middle) and e_g (bottom) bands at Γ and M point

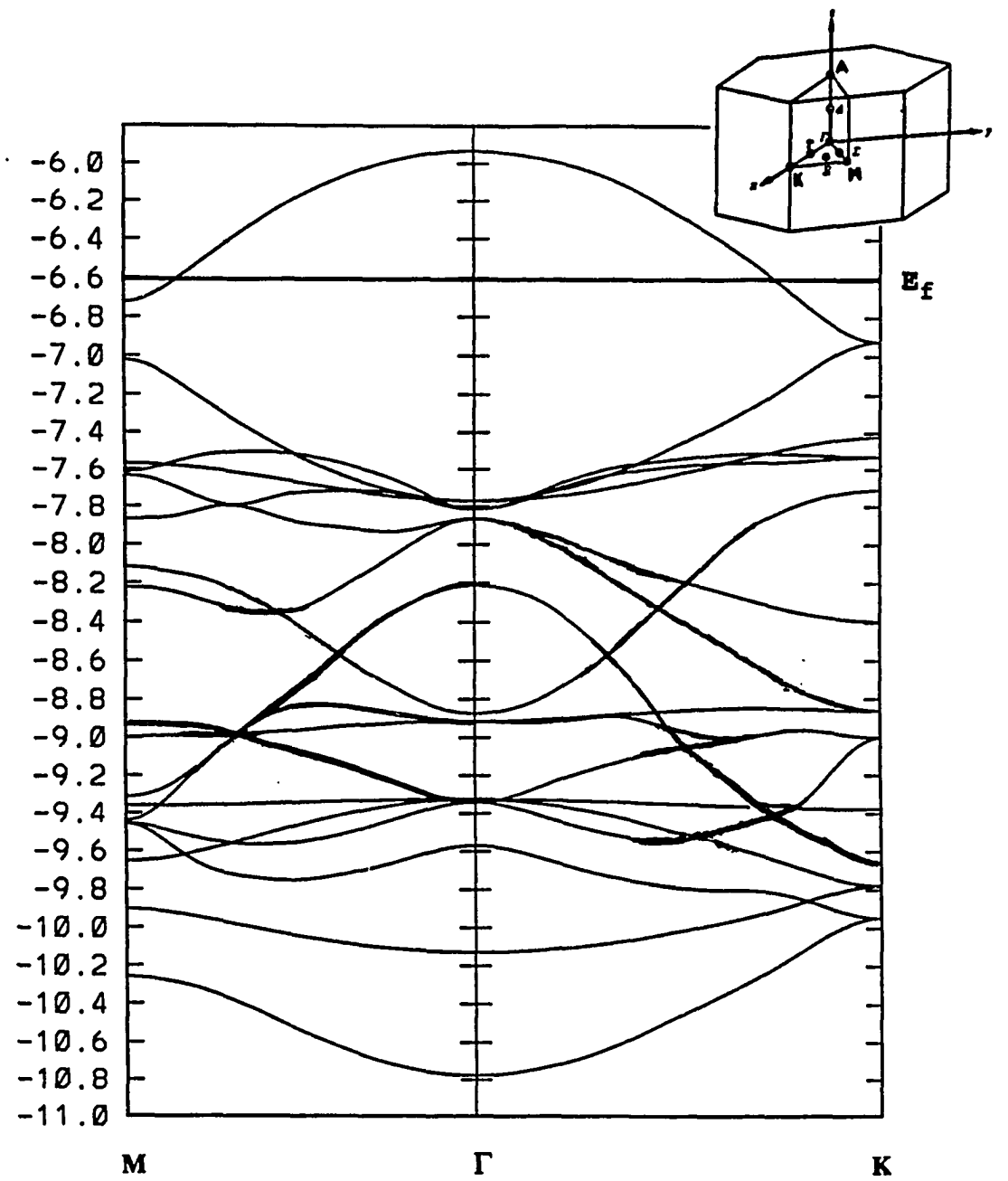

Figure 91. Energy band structure of ideal $Ca_{5.67}Pb_3$. The insert shows the notation of the Brillouin zone. E_f indicates the Fermi level for $Ca_{5.67}Pb_3$.

dispersions (bandwidths) of the P⊥ bands are seen along this symmetry line owing to the strongest interactions along the trigonal antiprism chains. These dispersions are represented by the (Pb)p_z orbitals interactions along the z-axis and partly aided by the allowed mixing of p_z with other p_x and p_y orbitals. The largest dispersion (~2 eV) exhibited by the a_{2u} band, which crosses the fermi level, shows antibonding and strong bonding interactions at Γ and **A**, respectively. Consequently, the strong interactions along **z** implicitly suggest that this may have an effect on the observed distortions in the real structure wherein a loss of symmetry operations, especially the inversion center and mirror plane perpendicular to **z**, would lift many of the observed degeneracies and allow orbital mixing of the e bands as well as the splitting of the a_{2u} band.

Along symmetry line T (Γ to **K**), the orbital representations become complex because of Bloch's theorem.[333] Difficulty arises from the the application of a phase factor associated to every translation. In the hexagonal system, the phase factor is exp(iϕ) and exp(-iϕ), where ϕ = (2π/3) for one in-plane lattice vector translation, if they are chosen at 60° with respect to each other. However, the behavior of the bands can still be appreciated by tracing the energies of the symmetry related orbitals. A close inspection of the P⊥ bands along this line shows a pair of degenerate e_g bands very close to the fermi level. Furthermore, the behavior of the a_{2u} band along this symmetry line is similar to that found along the Δ line, i.e. it falls in energy at **K** due to the significant bonding (at **K**) and antibonding (at Γ) interactions between non-coplanar Pb atoms resulting from the effect of the phase factor. The A_{2u} band also crosses the Fermi level along T. Theoretically, a distortion leading to band-folding would result in the splitting the A_{2u} band into bonding and anti-bonding combinations and effectively remove the degeneracy

of E_g at **K**. The **K** point also defines the $\sqrt{3}$ x $\sqrt{3}$ superstructure vector κ^* (1/3,1/3,0). This vector can be described using the lattice vectors of the Mn_5Si_3-type sub-cell, i.e. (**a'=a+2b**; **b'=a-b**; **c'=c**), where the primed vectors represent those of the superstructure. Consequently, application of band folding distortion on a two-thirds filled band results in the observed $\sqrt{3}$ x $\sqrt{3}$ superstructure.

The results of our calculations on the real structure confirm the validity of the orbital analyses discussed previously. The band structure of $Ca_{17}Pb_9$ (see Figure 92) show a small indirect band gap of about 0.2 eV. The experimental bandgap was found to be .15 eV smaller and could be atttributed to the inaccurate extended-Hückel parameters used for calcium (s and p orbital exponents and H_{ii} values) in our calculations; hence the calculated bandgap was overestimated. Although the Pb bands are found to be less dispersed (smaller band-widths) than the bands of the ideal structure, the largest dispersion were still exhibited along the Γ-**A** line signifying the large interactions along z still remains. The DOS and COOP curves (Figures 93 and 94) show the effective splitting of the Pb($6p_z$) bands around -7.0 eV into bonding (below E_f) and antibonding states (above E_f). These are results of the band-folding effects generated by the superstructure and the allowed orbital mixing caused by the lowering of symmetry.

The COOP also shows that the Ca-Pb bonding states are maximized near the E_f and further filling of the Pb states above E_f leads to the occupation of strongly antibonding Pb-Pb and then Ca-Pb states and destabilization of the electronic structure.

The stability of the $Ca_{17}Pb_9$ structure can be derived from the partial filling of antibonding Pb-p_z states in the Mn_5Si_3 structure which is stabilized by a $\sqrt{3}$ x $\sqrt{3}$ superstructure resulting in the effective splitting of the partially-filled antibonding states

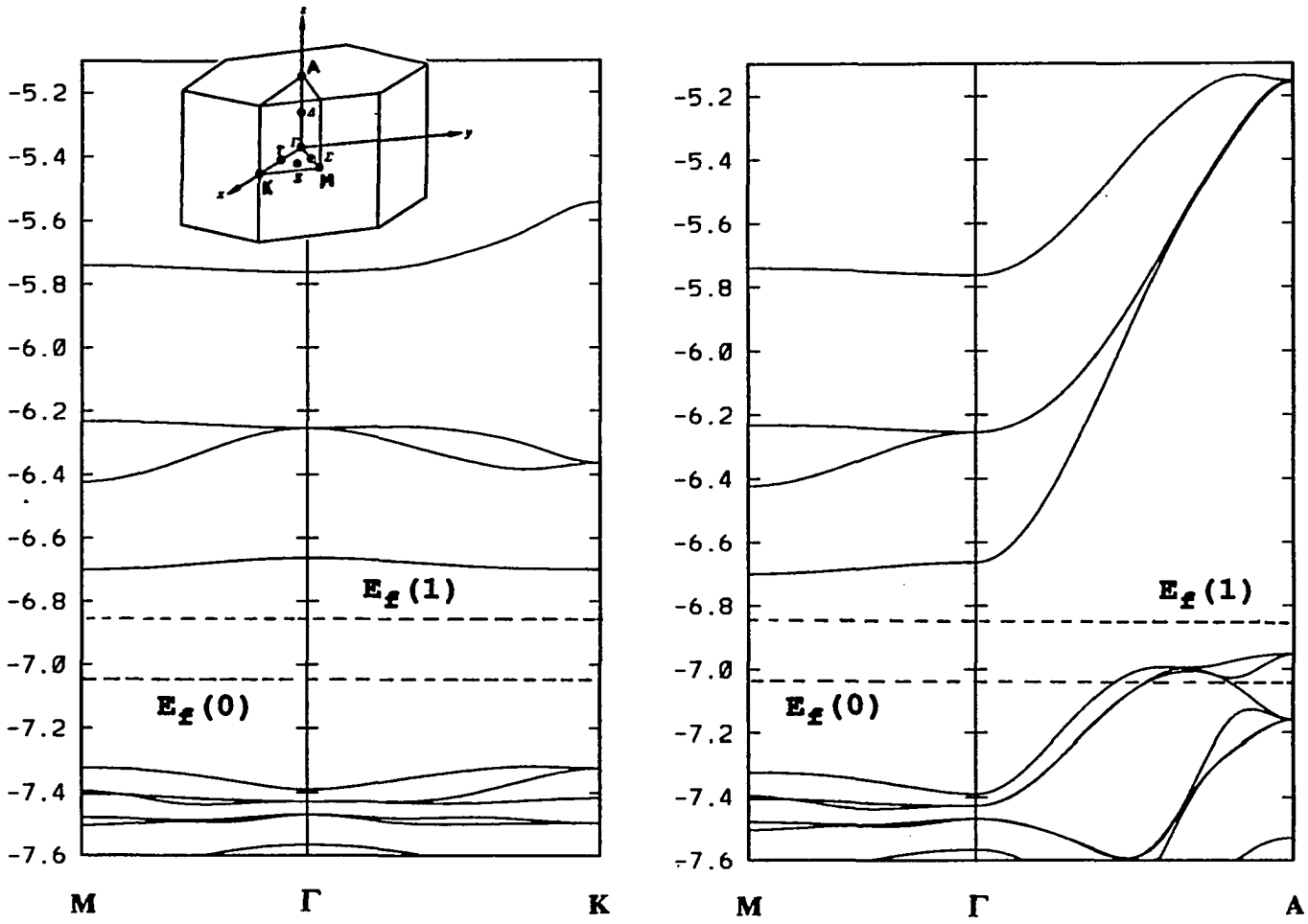

Figure 92. Energy band structure of $Ca_{5.67}Pb_3$ based on the refined structure. The inset shows the notation of the Brillouin zone. $E_f(0)$ and $E_f(1)$ indicate the Fermi levels for electron counts corresponding to the empty and two-thirds filled Ca_5Pb_3, respectively

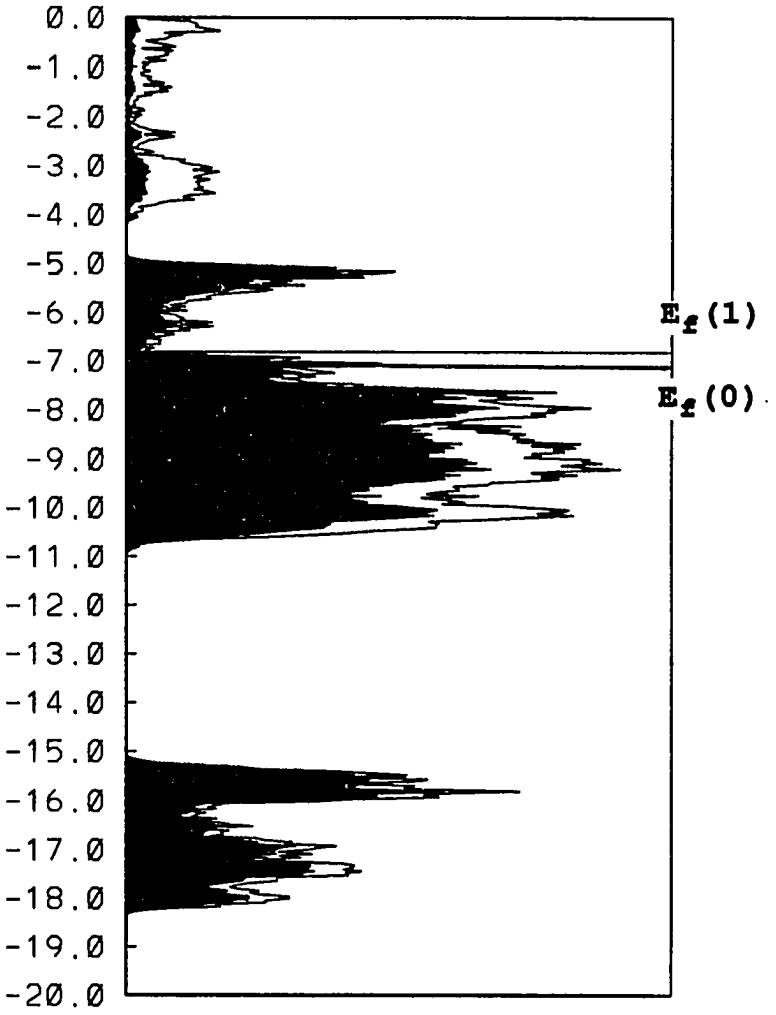

Figure 93. Density of States (DOS) and its Pb atomic projection of $Ca_{5.67}Pb_3$ based on the actual structure. $E_f(0)$ and $E_f(1)$ indicate the Fermi levels for Ca_5Pb_3 and $Ca_{5.67}Pb_3$

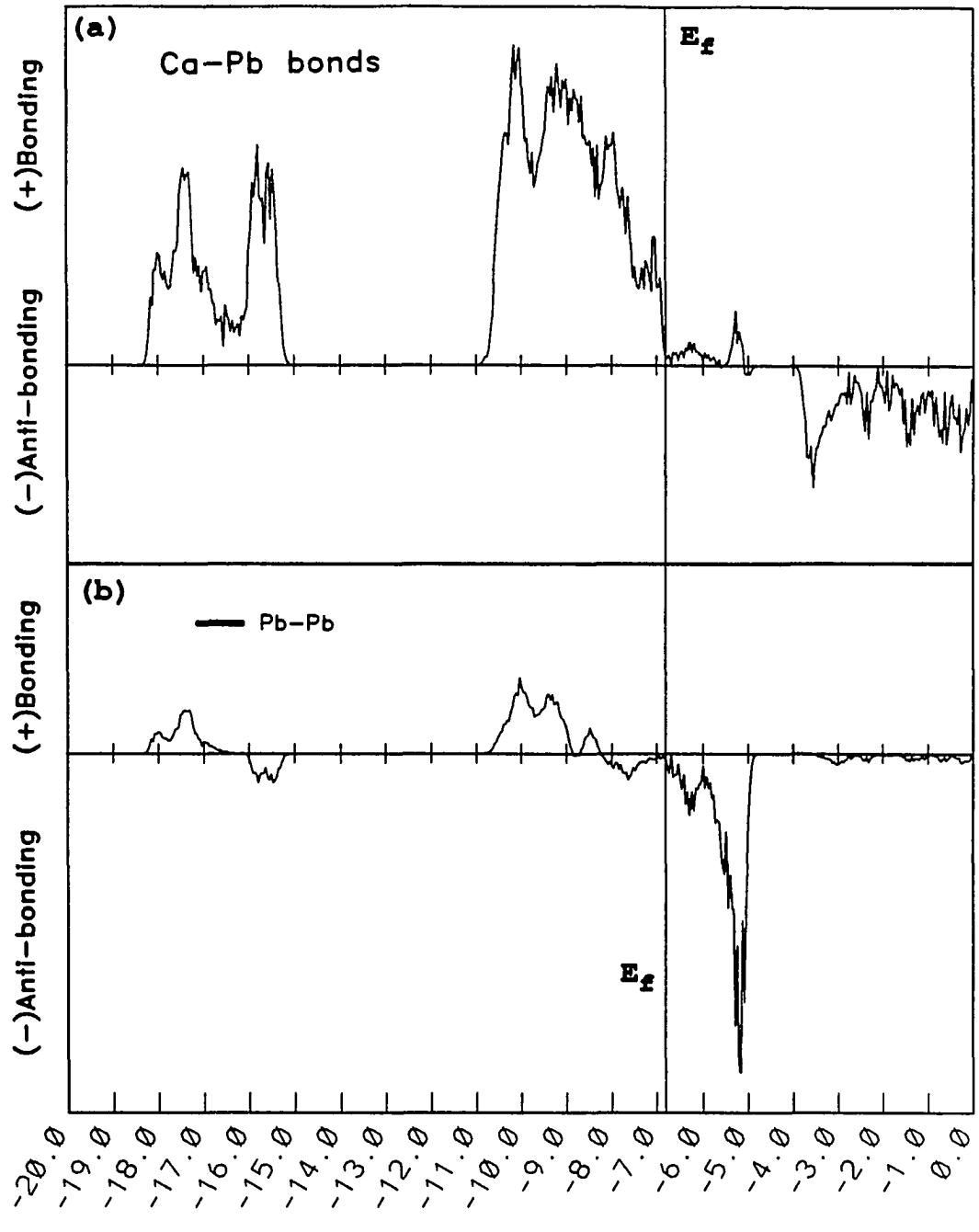

Figure 94. Crystal Orbital Overlap Populations (COOP) of (a) averaged Ca-Pb and (b) Pb(1)-Pb(2) interactions in $Ca_{5.67}Pb_3(P6_3mc)$. The solid line indicates the Fermi level(E_f) at -6.86 eV

and rationalized in terms of symmetry breaking steps that result in the stabilization of its electronic structure.

Summary The filled antiprisms of Ca surrounded by Pb atoms in $Ca_{5.67}Pb_3$ can then be considered as "pieces of Ca metal" without electrons in a Pb matrix[336] and this represents an interesting and novel type of homonuclear Pb-Pb bonding in alkaline-earth-metal lead systems. Phase width determination experiments (see Table 58 and 59), subsequent chemical analysis and subsequent magnetic and electrical measurements support the idea that the compound is more Ca-rich than Ca_5Pb_3 and that some localized Pb-Pb bonding exists to account for the "electron deficiency".

A more interesting question is the observation that if indeed Pb-Pb dimers exist, then why does Ca_5Pb_3 exist in a Mn_5Si_3 related structure and not in a Cr_5B_3 type which is the common structure type for "electron-poor" 5-3 combinations having dimers? Calcium-(Ge, Si) and Ba,Sr - (Si,Sn,Pb) analogs exist in the Cr_5B_3 type.[320]

A geometric radius-ratio rationale[337] - that a large (r_{anion}/r_{cation}) atomic radius ratio destabilizes the Cr_5B_3 with respect to the Mn_5Si_3 in "electron-poor" systems - might explain why Ca_5Pb_3 does not exist in a Cr_5B_3 structure type. The (metallic) radius[338] ratio of 0.88 in Ca/Pb is too large compared to other alkaline-earth-metal tetrelides with a Cr_5B_3 structure which range from 0.57 in Ba_5Si_3 to 0.79 in Sr_5Pb_3. Unlike the Cr_5B_3-structure, the Mn_5Si_3-type structure is known to accommodate a wider range and larger values of atomic radius-ratios. These observations coupled with the electronic requirements (electronegativity differences and valence requirements) of 5:3 alkaline-earth tetrelides may help explain the existence of $Ca_{5.67}Pb_3$ in a structure related to the Mn_5Si_3 type.

One interesting observation in the alkaline-earth-metal tetrelide systems is the reported absence of a 5:3 combination between Ca and Sn.[339] The compound closest to the 5:3 ratio is reported to have the formula $Ca_{31}Sn_{20}$. The $Ca_{31}Sn_{20}$ structure[340] was described as an intergrowth of two known metallic structures, W_5Si_3-type[341] and Y_3Rh_2-type.[342] As shown in Figure 95, the presence of square antiprism arrangements of the calcium atoms, typical of the W_5Si_3 structure type, and the linear arrangement of the tin atoms running along the center of the square antiprisms characterize the main features of the structure. In addition, other tin atom similarly form distorted square antiprisms around the calcium square antiprisms and dimers similar to those found in Ca_5Ge_3 and similar Cr_5B_3-type compounds. The "twisting" distortion of the Sn square antiprism also lead to the formation of Sn dimers.

The existence of $Ca_{31}Sn_{20}$ ($Ca_5Sn_{3.225}$) initially presents a problem. However, a closer look at the $Ca_{31}Sn_{20}$ structure, particularly at close Sn-Sn distances (<3.2 A) in the Sn substructure, reveal isolated Sn atoms, Sn dimers and a unique linear pentamer Sn_5 in a ratio of 5 : 5 : 1. The 5-membered linear oligomer was derived from the distortion of the linear chain inside the column of calcium square antiprisms producing Sn_5 + isolated Sn. The electron counting suggests a Zintl formalism of 31 $Ca^{(+2)}$ - [5 $Sn^{(-4)}$ + 5 $Sn_2^{(-6)}$ + 1 $Sn_5^{(-12)}$] = 62e^- (from Ca) - [20 + 30 + 12]e^- (for Sn). Hence $Ca_{31}Sn_{20}$ can then be considered a Zintl phase.

The atomic radius ratio (r_a/r_c = 0.82) and electronic requirements may make Cr_5B_3-type and Mn_5Si_3-type structures unfavorable in the binary Ca-Sn system. It would then be interesting to attempt to induce the formation of Ca_5Sn_3 in either of the two structure types (Mn_5Si_3 and Cr_5B_3) by adding a stabilizing interstitial component as was observed

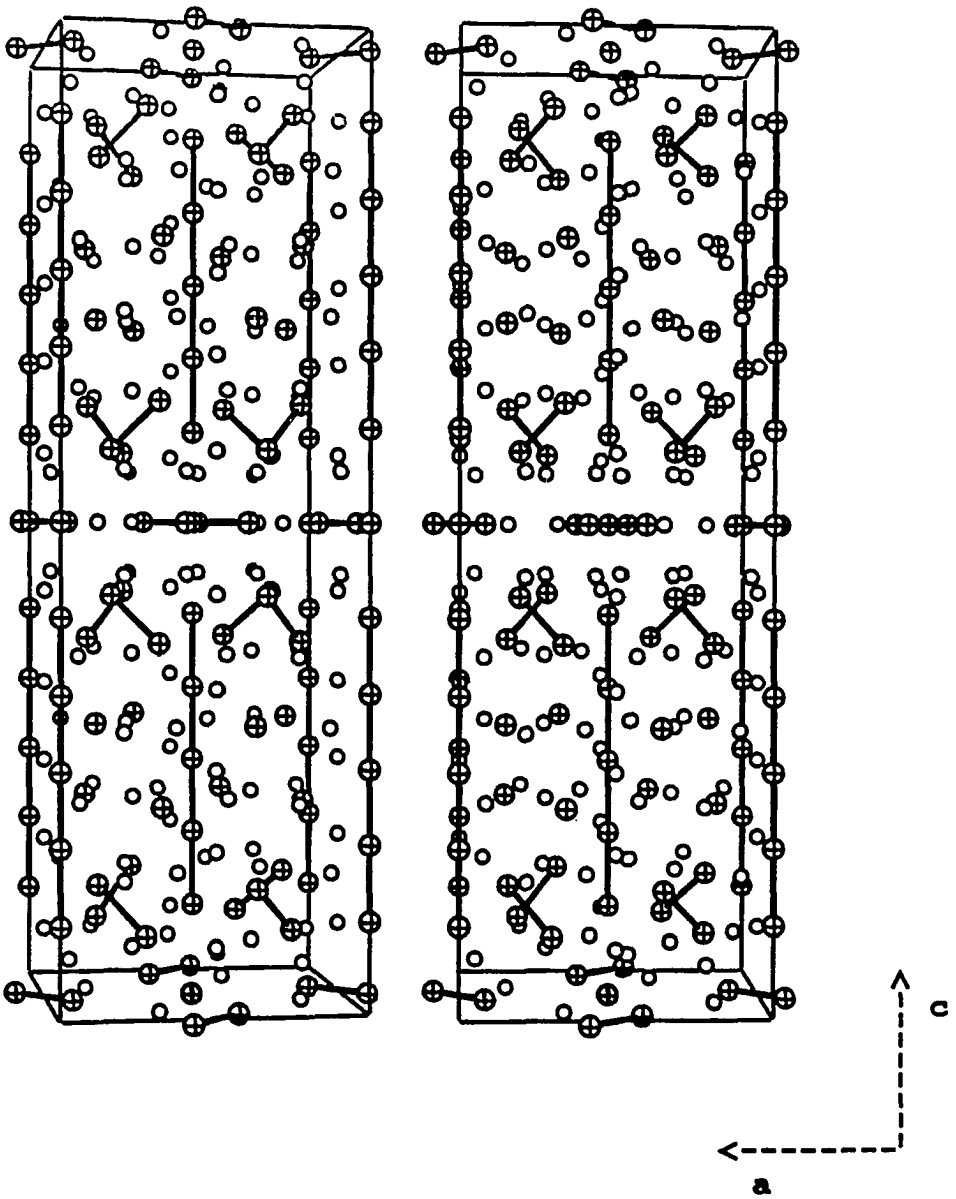

Figure 95. A stereoscopic [100] view of the $Ca_{31}Sn_{20}$ structure. Ca and Sn atoms are represented by open and cossed hatched circles, respectively. The short bonding Sn-Sn distances are emphasized. Note the presence of isolated Sn atoms, Sn_2 dimers and linear Sn_5 oligomers

in La_5Pb_3O and La_5Sn_3C. Initial work on ternary Ca-Sn-Z systems has led to the syntheses of Ca_5Sn_3Zn and its Cd analog with the Mn_5Si_3-type.[343] These encouraging results seem to suggest that the presence of divalent interstitials aid in satisfying the electronic requirements and help overcome the geometric barrier in the formation of a Ca_5Sn_3Z compound with the Mn_5Si_3 structure.

Interstitial Compounds of Ca_5Pb_3

Inspired by the results in the structural investigation on the binary $Ca_{5.67}Pb_3$ and the observation that the compound was still "electron-deficient", attempts were made to synthesize compounds having divalent cations as interstitials. Guided by the Zintl concept, these attempts produced a series of Ca_5Pb_3Z compounds where Z=divalent transition metals. It provided an entry to a new class of cationic-interstitial compounds. A number of the different transition metals proved to successful as interstitials, namely: V, Cr, Mn, Fe, Co, Ni, Cu, Zn, Cd, Ru, and Ag. Attempts to synthesize Ca_5Pb_3Z interstitial compounds with other divalent cations like magnesium and strontium, as well as with the common interstitial carbon, were unsuccessful. In the successful reactions (see Table 61), the weak extra lines corresponding to the $Ca_{5.67}Pb_3$ superstructure were absent in their powder patterns. The powder data could be indexed with the Mn_5Si_3 structure type and were characterized by a slight lattice expansion of the ternary interstitial compounds relative to the calculated subcell of $Ca_{5.67}Pb_3$.

The discovery of these new class of compounds also provides a system wherein our results from the investigations on the rare-earth metal tetrelides interstitial lattices could be compared and contrasted.

Table 61. Formation of Ca_5Pb_3Z phases (Z = transition metals)

loaded composition	conditions (anneal for 10 days) (slow cool = 5 days)	products (single phase)	lattice parameters (A) volume (A^3)
5 : 3 : 1; V	1300° slow cooled	Ca_5Pb_3V ($P6_3/mcm$)	a= 9.3585(2); c= 7.011(1) V= 531.8(1)
5 : 3 : 1; Cr	1300° slow cooled	Ca_5Pb_3Cr ($P6_3/mcm$)	a= 9.3591(2); c= 7.015(1) V= 532.1(1)
5 : 3 : 1; Fe	1300° slow cooled	Ca_5Pb_3Fe ($P6_3/mcm$)	a= 9.3554(5); c= 7.009(1) V= 531.3(1)
5 : 3 : 1; Co	1300° slow cooled	Ca_5Pb_3Co ($P6_3/mcm$)	a= 9.3547(3); c= 7.006(1) V= 530.9(1)
5 : 3 : 1; Ni	1300° slow cooled	Ca_5Pb_3Ni ($P6_3/mcm$)	a= 9.3547(4); c= 7.0073(7) V= 531.05(4)
5 : 3 : 1; Mn	1300° slow cooled	Ca_5Pb_3Mn ($P6_3/mcm$)	a= 9.3580(3); c= 7.009(1) V= 531.6(1)
5 : 3 : 1; Cu	CaCu + Ca + Pb 850° slow cooled	Ca_5Pb_3Cu (P-3c1)	a= 9.4130(3); c= 7.052(1) V= 541.0(3)
5 : 3 : 1; Zn	$CaZn_2$ + Ca + Pb 850° slow cooled	Ca_5Pb_3Zn ($P6_3/mcm$)	a= 9.3626(2); c= 6.992(1) V= 530.8(1)
5 : 3 : 1; Cd	CaCd + Ca + Pb 850° slow cooled	Ca_5Pb_3Cd ($P6_3/mcm$)	a= 9.3705(1); c= 7.012(1) V= 533.2(1)
5 : 3 : 1; Ag	850° slow cooled	Ca_5Pb_3Ag (P-3c1)	a= 9.4317(2); c= 7.055(1) V= 542.7(1)
5 : 3 : 1; Ru	1300° slow cooled	Ca_5Pb_3Ru ($P6_3/mcm$)	a= 9.3650(1); c= 7.028(1) V= 533.8(1)

Ca_5Pb_3Mn

Structure determination A rod-like single crystal(0.05 x 0.05 x 0.20 mm) of Ca_5Pb_3Mn obtained from a high temperature stoichiometric reaction was isolated and studied using a Rigaku AFC6R diffractometer. The cell parameters were refined from 2θ values of 25 reflections ($10°<2\theta<22°$) using the programs SEARCH and INDEX. The lattice parameters were later recalculated by least squares fit of the Guinier powder data using NBS silicon as an internal standard. To make sure that assignments of the lines were proper, the observed powder data were carefully compared with a calculated powder pattern from the refined structure of Ca_5Pb_3Mn.

Reflections within 2 octants of the reciprocal lattice up to $2\theta_{max} = 70.2°$ were measured in the ω-2θ scan , and a $I>3\sigma_I$ restriction was imposed to determine observed reflections. Decay corrections were deemed unnecessary based on the small intensity variations measured on three standard reflections over the total exposure time. Empirical absorption corrections were applied based on 3 psi scans. Data averaging in the Laue group 6/mmm resulted in 221 independent reflections with (R_I=6.1%) for the structure refinement of Ca_5Pb_3Mn.

Precession photos taken on the Ca_5Pb_3Mn crystal confirmed the absence of a $\sqrt{3}$ x $\sqrt{3}$ expansion or any other superstructure. The hexagonal shape of the crystal made it relatively easy to align. Cone and Laue photographs confirmed the presence of a six-fold axis. Higher level photos also indicated a systematic absence corresponding to the conditions for the space groups $P6_3/mcm$, P6c2 and $P6_3cm$, as was confirmed by a careful examination of the single crystal data. The space group $P6_3/mcm$ proved to be the correct one during refinement.

The structure was refined and the initial parameters were obtained from a Mn_5Si_3 model obtained from a structure determination of La_5Ge_3. The weighting scheme was according to the counting statistics, and the parameter accounting for isotropic secondary extinction was refined ($6.62(2) \times 10^{-7}$). Structure refinements with isotropic parameters resulted in R=4.2% and R_w=5.4%. Refinement with anisotropic thermal parameters without DIFABS[344] led to satisfactory refinement values, R=4.0 R_w=4.4%, but the thermal parameters of all atoms were elongated along c-axis which was the short axis. Application of DIFABS produced a significant improvement in the thermal parameters and better esd's. It must be noted that DIFABS was successful only if the correct(data collection) orientation matrix was included in the calculations. If the improved lattice parameters were used, an incorrect absorption sphere results in inadequate absorption corrections. Final least squares refinement included varying the occupancy of the atoms. There were no significant deviations from ideal stoichiometry; keeping Pb(1)=1.0 yields 0.97(2), 1.00(2), 0.96(2), for Ca(1), Ca(2), and Mn respectively. A final difference Fourier calculation showed the largest residual peak, 2.06 e^-/A^3, was within 1A of Pb(1) (neg=2.32 e/A). The summary of the crystal data, atomic parameters and important bond distances and angles are given in Tables 62 and 63.

Structure description The Ca_5Pb_3Mn structure was found to be isostructural with the ideal filled-Mn_5Si_3 structure type, also known as Ti_5Ga_4-type. The structure consists of confacial Mn-centered Ca(2) trigonal antiprism chains surrounded by a larger confacial trigonal antiprism of Pb(1) (see Figure 96). Unlike other Mn_5Si_3-type compounds which show relatively short interatomic contacts between antiprism atoms, the distances between Ca(2) antiprism atoms in Ca_5Pb_3Mn are relatively large (4.29A).

Table 62. Data collection and refinement parameters for Ca_5Pb_3Mn

Space group	$P6_3/mcm$
Z	2
Crystal dimension(mm)	0.05 x 0.05 x 0.20
Diffractometer	Rigaku AFC6R
2θ max	70.2°
no. of octants	4(±h,k,±l)
Reflections:	
measured	4909
observed(>3σ_I)	1666
independent	221
R_I (averaging)	6.1% (all reflections)
no. of parameters refined	14
R (refinement)	3.7%
R_w(refinement)	3.9%
G.O.F. 1.15	
Largest parameter shift	0.00
Absorption coefficient	757 cm^{-1} (Mo Kα)
Secondary extinction coeff	6.62(3) x 10^{-7}
Transmission range	0.311 - 1.00
Largest residual peaks	+2.06, -2.32 e/A
Cell Parameters (Guinier):	
a = 9.3580(3)A	
c = 7.009(1)A	
V = 531.6(1)	

Table 63. Refined parameters for Ca_5Pb_3Mn

atom	x	y	z	B(eq)	Occupancy
Pb(1)	0.6117(1)	0	1/4	2.98(6)	1.00
Ca(1)	1/3	2/3	0	1.4(2)	0.97(2)
Ca(2)	0.2649(4)	0	1/4	2.4(3)	1.00(2)
Mn	0	0	0	3.5(3)	0.96(2)

U values,

atom	U11	U22	U33	U12	U13	U23
Pb(1)	0.0304(4)	0.054(5)	0.076(1)	0.003	0	0
Ca(1)	0.024(2)	0.024	0.040(3)	0.012	0	0
Ca(2)	0.031(2)	0.052(2)	0.075(4)	0.002	0	0
Mn	0.047(2)					

Important interatomic distances,(A)

atom	atom	distance	atom	atom	distance
Pb(1)	Ca(1)	3.3854(3) (6x)	Ca(2)	Ca(2)	4.292(1) (4x)
Pb(1)	Ca(2)	3.246(2)	Ca(2)	Ca(2)	4.294(1) (2x)
Pb(1)	Ca(2)	3.690(2) (2x)	Ca(2)	Mn	3.036(3) (6x)
Pb(1)	Ca(2)	3.216(1) (2x)	Mn	Mn	3.5045(5) (2x)
Ca(1)	Ca(1)	3.5045(5) (2x)	Pb(1)	Pb(1)	4.0809(1) (2x)
Ca(1)	Ca(2)	3.900(2) (6x)			

Distances are in Angstroms. Estimated standard deviations in the least significant figure are given in parentheses

Hence the volume of interstitial site is comparatively larger. The average Ca-Ca distances found in the antiprism columns of Ca_5Pb_3Mn are also longer than the corresponding distances found in binary $Ca_{5.67}Pb_3$.

The high symmetry of the structure makes the Ca-Pb distances more uniform than those of the binary compound. The short Pb-Pb contacts found in the binary are absent in the ternary interstitial compound.

The channels formed by the trigonal antiprism arrangement of Pb atoms are occupied by linear chains of Ca(1) atoms which have the shortest Ca-Ca contacts (3.5045(5)A) found in the structure. However, this distance is longer than those of the buckled chains in binary $Ca_{5.67}Pb_3$. The nearest neighbor environment around each Ca(1) atom is made up of Pb atoms, forming a six coordination sphere which is intermediate between a regular trigonal antiprism and a trigonal prism. This is typical of Mn_5Si_3-type compounds.

Each Mn interstitial atom is surrounded by a regular antiprism of Ca(2) atoms. The Ca(2)-Mn distance of 3.04 A can be compared with the Pauling single bond radii sum of 2.92 A, but electron counting suggests that there are no electrons available for Ca(2)-Mn bonds. There are also no known Ca-Mn binary or ternary compounds with which we can correctly compare the observed Ca-Mn distance.

The Mn-Mn interstitial distances in the Ca(2) antiprism columns are, by symmetry, identical to the distance between Ca(1) chains (3.505 A) and these are well larger than the Pauling single bond[326] of 2.35 A and the interatomic distance of 2.54 A in elemental manganese. The size of the interstitial Mn atom seems to fit the interstitial site quite well. A calculation of the interstitial site volume in Ca_5Pb_3Mn, based on the Ca(2)

the filling-up of the valence bands of the larger Pb atoms may overcome the electrostatic barrier imposed by the smaller cations. On the other hand, the short Ca-Mn distance may allow for some mixing of the Ca-Mn orbitals and the Pb valence bands. This leads to a complicated electronic structure relating to the prediction of physical properties.

Ca_5Pb_3Fe

Synthesis and structure The iron compound was synthesized in the same manner as the Mn compound and it was surprising that, like Mn, iron does not form any binary compound with Ca. Chemical analysis using SEM confirmed the stoichiometry to be very close to Ca_5Pb_3Fe. Single crystal structure analysis (same as in Ca_5Pb_3Mn) was done on a hexagonal crystal, and this was found to be isostructural with Ca_5Pb_3Mn. A summary of our single crystal investigation on Ca_5Pb_3Fe is presented in Tables 64 and 65. The structural details of the iron interstitial compound were found to be identical to its manganese analog.

Physical properties The compound Ca_5Pb_3Fe was found to be strongly attracted to a magnet indicating that it was ferromagnetic at room temperature. Subsequent measurement of its magnetic susceptibility using a SQUID magnetometer showed that it was ferromagnetic with a moment of $6.3(1)\mu_B$/Fe atom. This relatively large moment compared to the ferromagnetic moment of $1.92(3)\mu_B$/Fe in the isostructural compound La_5Ge_3Fe indicates that the character of Fe in Ca_5Pb_3Fe approaches that of cationic Fe(II)($^5T_2 = 6.7\mu_B$). The compound was still ferromagnetic above 200°C, the temperature limit of the magnetometer, and the Curie temperature was not determined. Magnetic experiments (M vs H) on the Ca_5Pb_3Fe compound showed, within experimental uncertainty of ±2 Oe, that there is no hysteresis and zero coercivity

Table 65. Refined parameters for Ca_5Pb_3Fe

atom	x	y	z	B(eq)	Occupancy
Pb(1)	0.6108(1)	0	1/4	2.58(5)	1.0
Ca(1)	1/3	2/3	0	1.6(1)	0.99(2)
Ca(2)	0.2640(4)	0	1/4	2.6(2)	1.00(2)
Fe	0	0	0	3.7(2)	0.98(2)

U values,

atom	U11	U22	U33	U12	U13	U23
Pb(1)	0.0401(3)	0.044(5)	0.066(1)	0.003	0	0
Ca(1)	0.026(2)	0.026	0.045(3)	0.012	0	0
Ca(2)	0.041(2)	0.046(2)	0.072(4)	0.002	0	0
Mn	0.049(2)					

Important interatomic distances, (A)

atom	atom	distance	atom	atom	distance
Pb(1)	Ca(1)	3.3854(3)	Ca(1)	Ca(2)	3.900(2)
Pb(1)	Ca(2)	3.246(2)	Ca(1)	Ca(2)	3.900(2)
Pb(1)	Ca(2)	3.690(2)	Ca(1)	Ca(2)	3.900(2)
Pb(1)	Ca(2)	3.216(1)	Ca(2)	Fe	3.036(3)
Pb(1)	Ca(2)	3.216(1)	Ca(2)	Fe	3.036(3)
Pb(1)	Ca(2)	3.690(2)	Fe	Fe	3.5045(5)
Ca(1)	Ca(1)	3.5045(5)			

Distances are in Angstroms. Estimated standard deviations in the least significant figure are given in parentheses

and remanence. This is characteristic of "very soft" ferromagnets[348] (see Figure 97). The compound La_5Ge_3Fe behaves similarly. However, the behavior of metallic La_5Ge_3Fe could be explained in terms of an itinerant ferromagnetic model,[349,350] which generally explains the magnetic properties of metallic compounds and alloys. A similar magnetic behavior was also observed in a metallic ferromagnet derivative of C_{60}, $C_{60}TDAE_{0.86}$.[351] and was attributed to superparamagnetism. However, if the interstitials in the compounds Ca_5Pb_3Z are indeed cationic then they should behave as semiconductors and local models of magnetism are more applicable in explaining the ferromagnetism of Ca_5Pb_3Fe.[352] This is supported by the large magnetic moment exhibited by Ca_5Pb_3Fe which is comparable to ferromagnetic Fe^{II}. It is interesting to note that soft ferromagnets are used as transformer cores and in motors and generators owing to their high permeability and low coersive field to reduce energy loss.[353]

The ferromagnetic character omay be attributed to the weak interactions between Fe (d_{Fe-Fe}=3.5045(6)A) interstitial atoms along the trigonal antiprism chains of calcium atoms. The structure of Ca_5Pb_3Fe with "linear chains" of Fe running along the z-axis suggests that its magnetic property may also be anisotropic.

It is quite intriguing to note that theoretical calculations on idealized $FeCa_{18}$ clusters were done by McHenry et.al.[354] to study the formation of local moments on iron in alkali and calcium metal hosts. Using spin-polarized, self-consistent, scattered-wave cluster calculations, they suggested that a local magnetic moment on iron in a calcium and electron-rich environment is unstable due to significant presence and mixing of the Ca d-states with the Fe d-states. Therefore, a simple charge transfer picture from Ca-s and Fe-s states to Fe-d states is invalid. They also suggest that this s-d and d-d

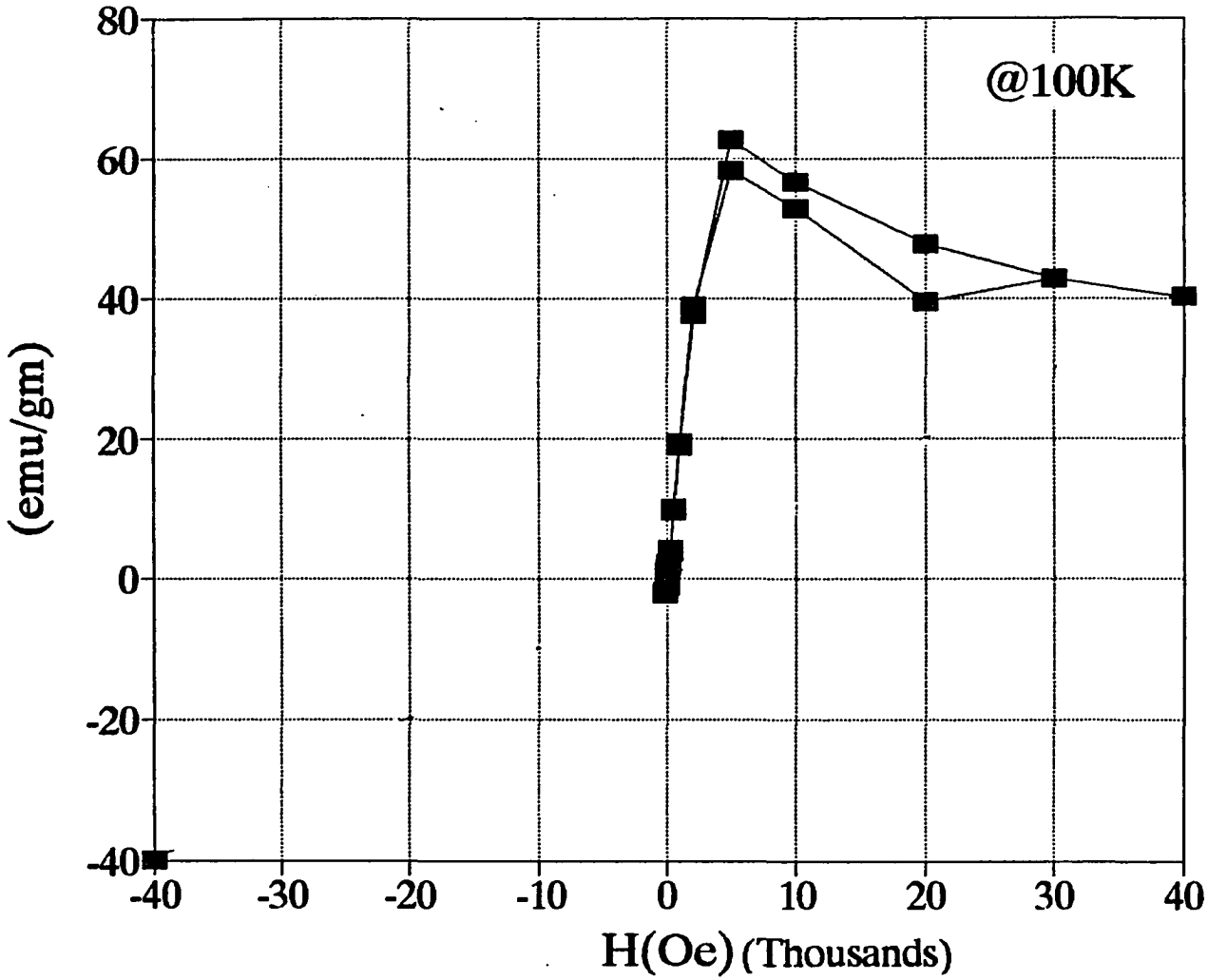

Figure 97. The M vs H (hysteresis) curve for Ca_5Pb_3Fe at T=100K. The curve is characteristic of very soft ferromagnetism

had trigonal symmetry compared to the hexagonal Ca_5Pb_3Mn. This was not immediately clear from the powder data but precession photographs on a single crystal and data averaging indicate and confirm that the symmetry is indeed trigonal. There are no superstructures similar to the $La_{15}Ge_9Z$ type, and the lattice parameters are similar to a Mn_5Si_3-type cell.

The Ca_5Pb_3Cu refinement results are shown in Tables 66 and 67. Its structure is topologically identical to Mn_5Si_3 (see Figure 98). The difference lies on the orientation of the linear chains with respect to one another and to the trigonal antiprism columns. Its lower trigonal symmetry is manifested by the "slipping" of the Ca(1) linear chains past the Ca(2) antiprism chains in an ordered manner; hence Ca(1) atoms are not co-planar with the interstitial Cu atoms. The close packing arrangement within the a-b plane of the interstitial and Ca(1) atoms is puckered, as shown in Figure 99, wherein each nearest neighbor calcium atom is alternately displaced by about 0.15A above and below the layer formed by the interstitials. The local environment of the copper atoms with respect to the Ca(1) atoms is like a "squashed" antiprism. The last structural feature can be attributed to the possible matrix effects of the Pb atoms and copper interstitials on the calcium linear chains. The relatively large expansion of the c-axis parameter in Ca_5Pb_3Cu compared with other 3d-transition metal Ca_5Pb_3Z interstitial compounds leads to larger channels formed by the Pb atoms and occupied by Ca(1) atoms. The isolated Ca(1)linear chain by itself remains equidistant as those found in ideal Mn_5Si_3-type. However, the coordination around each Ca(1) atom is distorted due to the displacement of the Ca(1) atoms from the center of the twisted-trigonal antiprism formed by its Pb nearest neighbors (see Figure 100). This means that the metal linear chains and the confacial

Table 66. Data collection and refinement parameters for Ca_5Pb_3Cu

Space group	P-3c1
Z	2
Crystal dimension(mm)	0.05 x 0.05 x 0.15
Diffractometer	Rigaku AFC6R
2θ max	50.0°
no. of octants	4(±h,k,±l)
Reflections:	
measured	1996
observed($>3\sigma_I$)	1044
independent	152
R_I (averaging)	11.1% (all reflections)
no. of parameters refined	14
R (refinement)	3.0%
R_w(refinement)	4.3%
G.O.F.	1.08
Largest parameter shift	0.01
Absorption coefficient	550 cm^{-1} (Mo Kα)
Secondary extinction coeff	1.28(2) x 10^{-6}
Transmission range	0.640 - 1.00
Largest residual peaks	+3.32, -3.19 e/A
	(<1A from Pb(1))
Cell Parameters (Guinier):	
a = 9.4130(3)A	
c = 7.052(1)A	
V = 540.97(3)A^3	

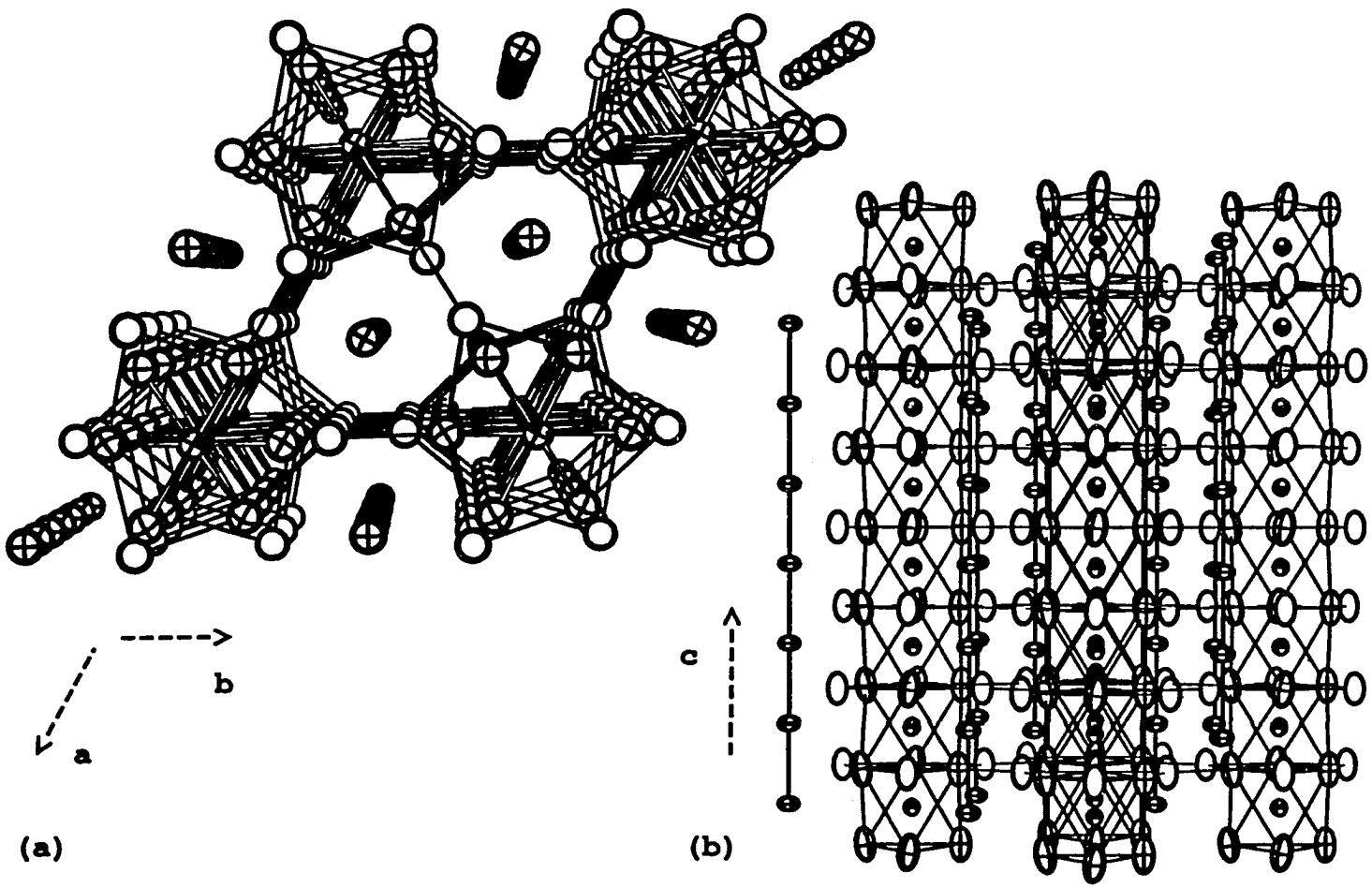

Figure 98. ORTEP drawings of two views, (a)[001] and (b)[110], of the Ca_5Pb_3Cu structure. This structure is very similar to Mn_5Si_3. Ca and Pb atoms are represented by cross-hatched and open circles, respectively. Cu atoms at (0,0,0) are shown as crossed-hatched circles with octant shading. The thermal ellipsoids are drawn at 90% probability

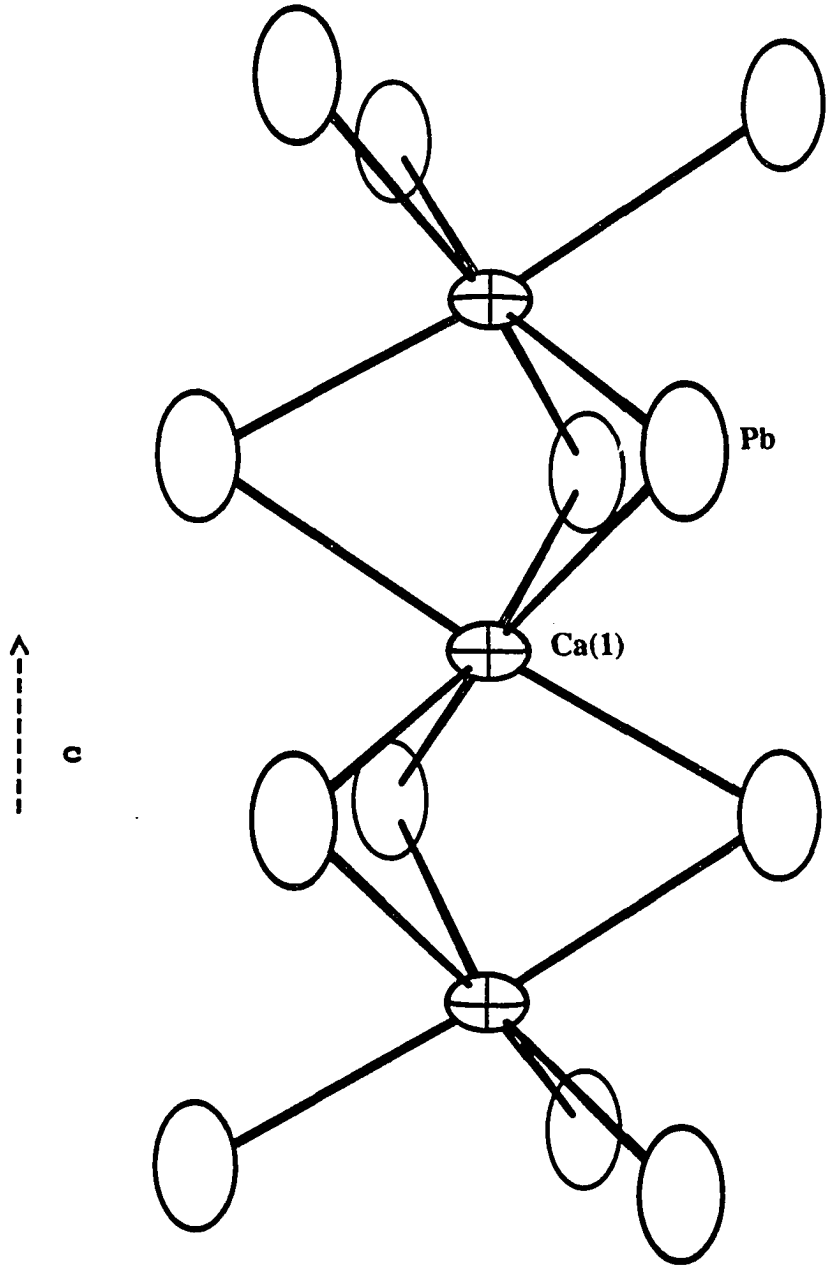

Figure 100. Twisted antiprism environment of Pb atoms around the off-center Ca(1) linear chain atoms in Ca_5Pb_3Cu

antiprism columns in Mn_5Si_3-structure are independent in Ca_5Pb_3Cu, due to the large channel formed by Pb atoms. This allows for the displacement of each Ca(1) chain relative to its nearest Ca(1) linear chain neighbors. This suggests that the linear Ca(1) chains' overall structure is dominated by geometric effects, and electronic factors do not seem to be dominant. Madelung calculations[355,356] on an ideal $Ca_5Pb_3Z^{II}$, and its Ca_5Pb_3Cu variant in an ionic picture slightly favor the distortion found in Ca_5Pb_3Cu over an ideal Mn_5Si_3 structure (see Table 68). This can be traced to the repulsive interactions between the divalent interstitials and the co-planar Ca(1) ions, which is relieved by a puckering distortion.

The Ca(2) environment arround the Cu atoms also show a marked deviation from those observed in Ca_5Pb_3Mn and Ca_5Pb_3Fe. The Ca(2)-Ca(2) distances in the antiprisms are larger; 4.31A (in plane) and 4.32A (interplanar). However, the interplanar distances in the Cu compound are longer than those in-plane. This is in contrast with those in the Mn and Fe compounds which show the opposite trend. This can be portrayed as a anisotropic elongation of the antiprisms, wherein the axial is larger than the equatorial elongation.

An ionic picture also suggests that the the magnetic property of the Cu interstitial compound should reflect the divalent character(d^9) of the interstitial atom. However, magnetic susceptibility measurements show that the compound is diamagnetic after corrections. This maybe attributed to possible Cu-Cu interactions along the interstitial channel. The observed Cu-Cu distance, $d_{Cu\text{-}Cu}$ = 3.525(3)A, allows for some Cu-Cu interactions to occur.

Table 68. Summary of Madelung calculations[a] on Ca_5Pb_3Cu

structure model Ca_5Pb_3Cu	total ionic energy per formula unit (eV)	Displacemment of Ca(1) chains along **c** (fractional coord.)
($P6_3/mcm$)	-300.16	0.00
(P-3c1)	-300.26	0.02*
(P-3c1)	-300.54	0.04
(P-3c1)	-301.01	0.06
(P-3c1	-301.61	0.08

atom position (type)	ionic energy (eV) at each atom site
Pb site	-105.69
Ca(1) linear chain	-40.26
Ca(2) antiprism	-23.55
Z^{II}(interstitial)	+3.69

[a] Madelung calculations were made based on the Ewald method

* actual displacement of Ca(1) is 0.021 from (1/3,2/3,0)

Ca_5Pb_3Ag

The silver compound was made as a null test on the idea that divalent cations may stabilize the Ca_5Pb_3 compound. Surprisingly, the synthesis of the compound was successful using the same low temperature route as that used in the synthesis of Ca_5Pb_3Cu but in a one step reaction of the elements. This compound showed the largest expansion of the lattice parameters compared to other analogous ternary interstitial compounds (see Figure 101). A close analysis of the powder diffraction data and the lattice parameter ratios indicate that the compound is not of the Mn_5Si_3 type but was of lower symmetry and isostructural with Ca_5Pb_3Cu (see Figure 102). A similar geometric argument used in the Cu analog, that large Ag atoms lead to larger matrix effects on the co-planar calcium atoms, could also be applied to the observed structure of Ca_5Pb_3Ag. Unlike Ca_5Pb_3Cu, however, magnetic susceptibility measurements on Ca_5Pb_3Ag showed weak temperature-independent paramagnetism typical of Pauli paramagnets. This observation indicated that the compound is metallic, suggesting a more complicated picture of the electronic structure of these compounds than the simple idea that was proposed earlier. Silver being a monovalent metal lends doubts on the validity of a purely cationic picture.

Other Ca_5Pb_3Z interstitial compounds

The Co,Ni,Ru,Cr and V analogs were synthesized using the high temperature route identical to the syntheses of the Mn and Fe analogs (see Table 61). It must be noted that the reactions must be subjected to the 1300°C treatment for their completion. If the treatment is not followed, the interstitials seem to be unreacted especially if the interstitials are not introduced in powder form. The initial melting of the Ca_5Pb_3 seems

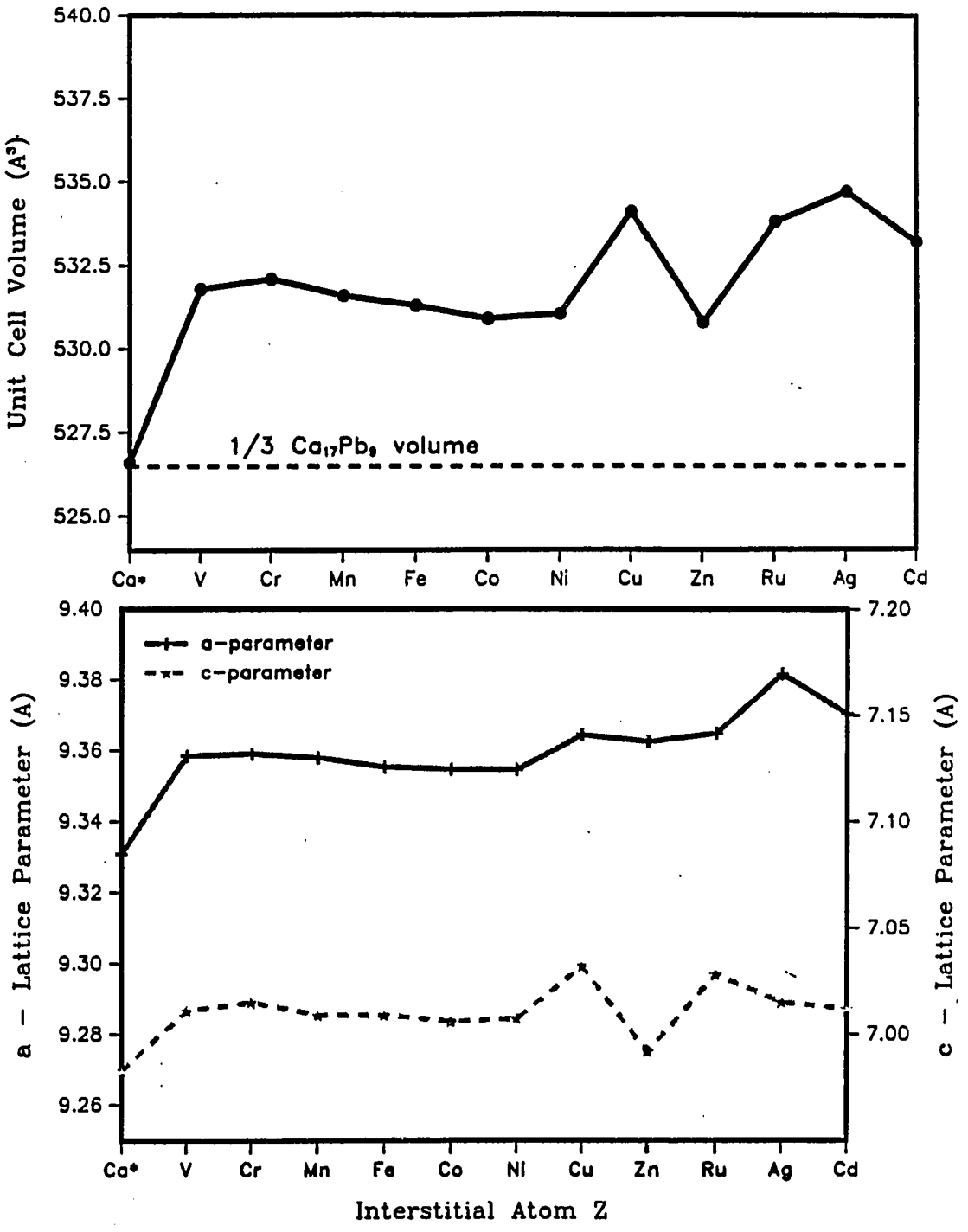

Figure 101. Graphical representations of the variation of unit cell volume (top), and lattice parameters (bottom) of Ca_5Pb_3Z phases, with increasing atomic number of Z. The ideal Mn_5Si_3 subcell of $Ca_{5.67}Pb_3$ is used as reference

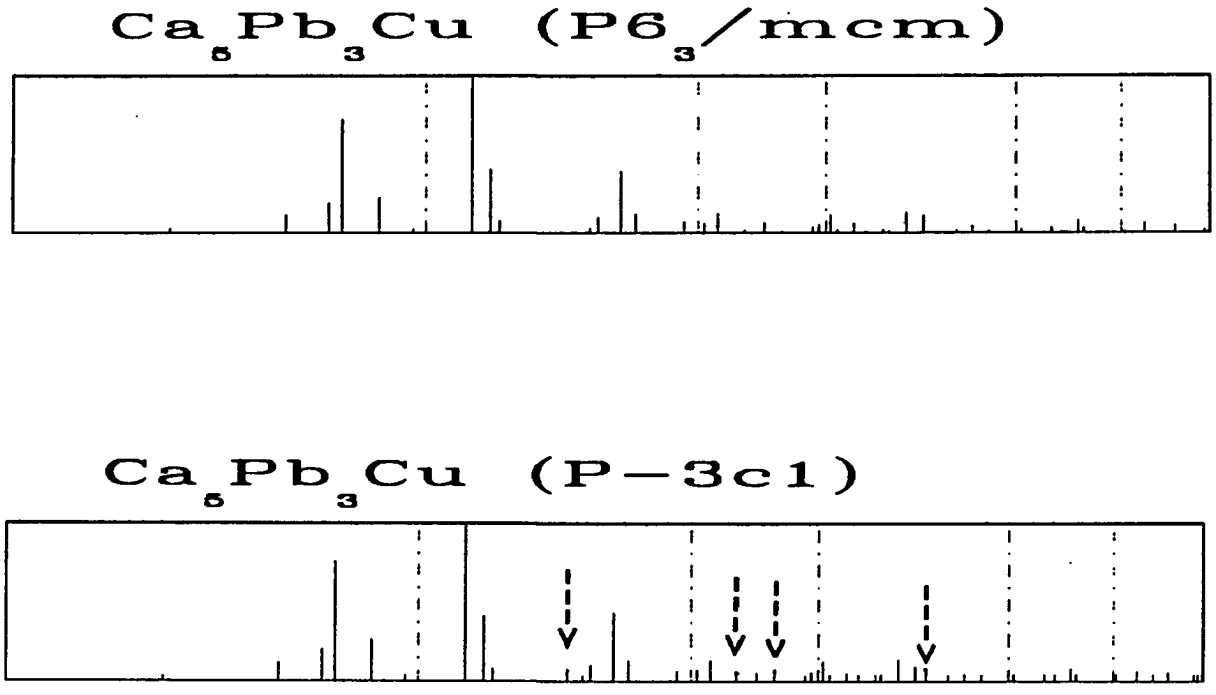

Figure 102. The calculated Guinier powder diffraction patterns of Ca_5Pb_3Cu having (a)filled-Mn_5Si_3 structure ($P6_3/mcm$) and (b)low symmetry Ca_5Pb_3Cu (P-3c1). The difference of the patterns sre indicated by arrows. The dashed lines represent the silicon reference lines

to be necessary in bringing the reaction into equilibrium. Of the above elements, only nickel is known to form binary compounds with calcium, and there are no published binary phase diagrams of Cr, V and Ru with Ca.

The Zn, Cd analogs were synthesized according to the same procedures used in making the Cu and Ag analogs, prereacted $CaZn_2$ and CaCd were used as intermediates, respectively. It was quite easy to make these compounds at temperatures of 1000°C or lower. The analogs were found to produce sharp and well defined peaks in their powder data, and they all index well in the Mn_5Si_3 structure type.

Plots of the lattice parameters and volumes of the different interstitial compounds are compared with the binary compound $Ca_{5.67}Pb_3$ in Figure 101. The graphs show a general volume expansion compared with the calculated subcell of the binary compound. The trend of the lattice volumes follow that of the atomic sizes of the interstitials except for the Cu and Ag interstitial compounds which have a different structure.

Attempts to synthesize $Ca_5Pb_3X_n$ with fractional interstitial occupancy were pursued and yielded surprising results. Powder diffraction analysis and single crystal precession photographs of products obtained from reactions with iron, $Ca_5Pb_3Fe_n$; n=0.5, indicated that a doubling of the c-axis was present compared to a model Mn_5Si_3 structure.[357] This is quite surprising based on the assumption that two electrons transfer from the interstitial stabilizes the Mn_5Si_3-type structure in Ca_5Pb_3Z. However, based on the $Ca_{5.67}Pb_3$ problem, it is not improbable that some Pb-Pb bonding may exist and that the Fe ordering coupled with Pb-Pb interactions may provide a rationale to the observed structure. This suggests that the electronic structures of these compounds are more complicated than what has been inferred, and much of the uncertainty maybe due to the

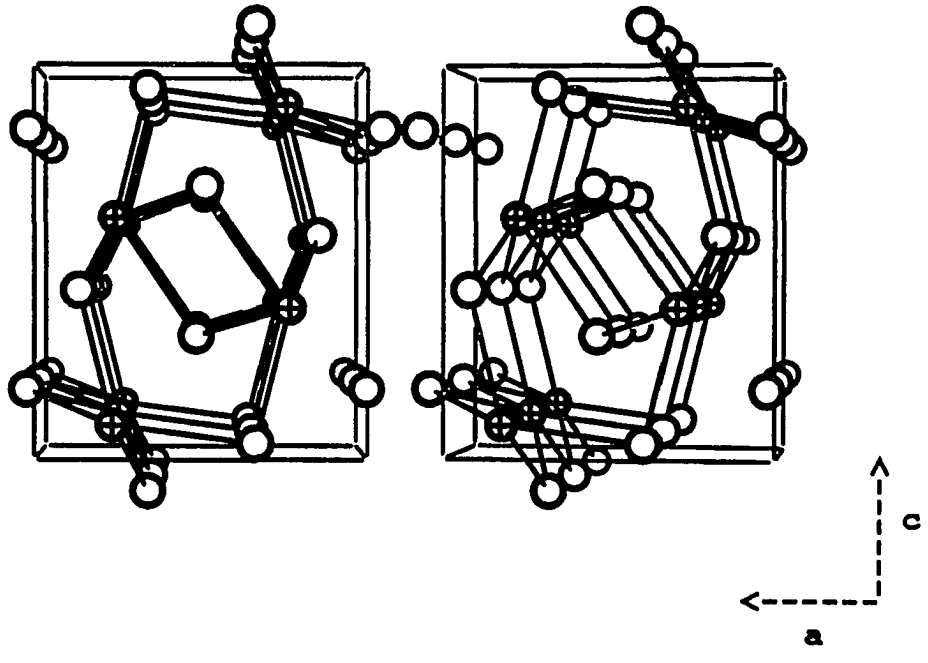

Figure 103. A stereoscopic view of the unit cell of Ca_2Pb(after Eckerlin et al.)[362] with the Co_2Si structure type. The structure is viewed along the b-axis with Ca and Pb atoms represented by open and cross-hatched circles

Table 69. Formation of Ca_5Pb_3Z phases (Z = alkaline-earth metal)

Loaded Compositions	Conditions	Products	Lattice Parameters (A)
-Mg Reactions-			
5 : 3 : 1	1100° slow cooled	Ca_5MgPb_3 (Co_2Si-type)	a= 8.0146(3); b= 4.923(1) c= 9.314(1)
5 : 3 : 1	1050° quenched	Ca_5MgPb (Co_2Si-type)	a= 8.014(1); b= 4.924(1) c= 9.315(1)
3 : 3 : 3	1100° slow cooled	$CaMgPb$ (Co_2Si-type)	a= 7.904(1); b= 4.772(1) c= 8.880(1)
Ca_2Pb	1100° slow cooled	Ca_2Pb (Co_2Si-type)	a= 8.0720(4); b= 5.100(1) c= 9.647(1)
5 : 3 : 1; C	1300° slow cooled	CaPb + unknown phase(s)	
5 : 3 : 1; Sr	1300° slow cooled	Ca_5SrPb (Co_2Si-type)	

This is shown by comparing the lattice parameters of the isotypic compounds Ca_2Pb, CaMgPb and synthesized $Ca_{2-x}Mg_xPb$ phases. The observed lattice parameters for the orthorhombic (Pnma) Ca_2Pb[361] are **a**=8.0720(4)A; **b**=5.100(1)A; **c**=9.647(1)A. The observed lattice parameters of Ca_5MgPb_3 are **a**=8.0146(3)A; **b**=4.923(1)A; **c**=9.314(1)A. CaMgPb[362] is also reported to have the Co_2Si structure with **a** = 7.90(2)A; **b** = 4.77(2)A; **c** = 8.88(2)A. Interpolation of the lattice parameters of Ca_2Pb and CaMgPb give theoretical lattice parameters **a** = 8.0148A; **b** = 4.99A; **c** = 9.391A for Ca_5MgPb_3 which are in good agreement with the observed lattice parameters. The deviations of the calculated from the observed parameters are 0.067A and 0.077A for **b** and **c**, respectively. Thus, it may mean that Ca_2Pb and CaMgPb form a solid solution over the entire range $Ca_{6-x}Mg_xPb_3$;$0<x\leq3$ which is the reason why the filled-Mn_5Si_3 structure does not occur for Ca_5Pb_3Mg. The negative results of the Mg experiments can also be attributed to geometric requirements that Mg is not large enough to provide the necessary size ratio in the formation of a Mn_5Si_3-type structure as was the case in La_5Pb_3O and La_5Pb_3N.

SUMMARY AND SUGGESTIONS FOR FUTURE WORK

The exploratory investigations on the rare-earth metal and alkaline-earth metal tetrelides have resulted in the broad interstitial chemistry of La_5Ge_3, La_5Pb_3, Ca_5Pb_3, and possibly La_5Sn_3. During the course of this work different classes of compounds having structures related to the Mn_5Si_3-type were discovered. Furthermore, incorporation of different interstitial atoms or substitution of the tetrelide have resulted in structures related to other 5:3-types, namely, Cr_5B_3 and Yb_5Sb_3. The existence of binary La_5Sn_3 only in the W_5Si_3 structure yet adds another dimension to the structural interrelationships of these tetrelides.

The structural preferences of the different 5:3 tetrelides may be associated with geometric and electronic factors. The geometric factor can be classified through comparison of average cell volumes of the different 5:3 structure classes normalized to equal number of formula units. Many binary 5:3 tetrelides that are reported to be dimorphic (or even trimorphic, e.g. Nb_5Ge_3) with the W_5Si_3, Mn_5Si_3 and/or the Cr_5B_3 structure types have the W_5Si_3-type phases with the smallest and the Mn_5Si_3-type phases with the largest cell volumes.[363] Although, the possibility of interstitial stabilization in the reported Mn_5Si_3-type phases cannot be discounted the presence of free volume connected with the octahedral interstitial site can explain the relatively larger cell volumes of Mn_5Si_3-type phases. Pearson[364] as well as Hyde and Andersson[365] have described the W_5Si_3 structure as "tetrahedrally close-packed", typical of metallic structures that seem to follow the Frank-Kasper rules. The high coordination of the the constituent atoms result in efficient packing, shorter metal-metal distances and lower cell

and Ti_3P structure types. An interesting host would be one that has different types of interstitial sites, tetrahedral, octahedral and even trigonal prismatic voids, of sufficient sizes. The Mn_3Al_{10} structure type the parent structure of the so-called Kappa-phases,[366] and Th_7Fe_3-type phases[367] are two examples. Study of interstitial site preferences would be worthwhile. Included in the study of site preferences is the interstitial ordering in a host structure parallel in scope to that in $La_{15}Ge_9Z$.

The novel interstitial chemistry of Ca_5Pb_3 implies the possibility of synthesizing filled-Mn_5Si_3 type phases with cationic interstitials. Initial results on a possible interstitial chemistry in Ca_5Sn_3 is encouraging. Extension of the work to heavier alkaline-earth metal tetrelides is recommended owing to their larger interstitial cavities which may lead to a wider variety of interstitials. Another appealing "electron-poor" host would be Ca_5Ga_3 (Cr_5B_3-type).[368]

To a certain degree, the application of the Zintl concept was successful. However, a degree of overlap between the metal states and tetrelide states in the electronic structure of the compounds seems to be a major factor in the successful syntheses of Zintl phases. This was particularly true with La_5Ge_4 and related phases La_5Ge_3Si(Sn, Pb) and La_5Ge_3Ga(In). Investigations on polar and semipolar intermetallics that lie on either side of the Zintl boundary would aid us understand the bonding relationships between "metallic" and polar structures. Hence, exploratory syntheses of binary and ternary compounds involving the group 12 and 13 elements with alkaline-earth and rare-earth metals is strongly recommended. Initial results in our investigation on the lanthanum-indium-germanium system have yielded two novel compounds La_3In_4Ge and

La_3InGe.[369] The compound La_3In_4Ge contains In_4 tetrahedral fragments interconnected via vertices to form a two dimensional network of In_4 clusters. La_3InGe contains In_2 dimers which seem to contradict the Zintl rule. However, the presence of short La-La contacts may provide a rationale for the observed structural behavior.

The syntheses of La_5RuGe_2 and Nd_5RuGe_2 implies an interesting bonding relationship between intermetallics and the more polar condensed metal clusters found in the reduced rare-earth metal halide Pr_4I_5Ru. This was inferred from the similarity of their structures and identical electron counts per Ru atom. Further work in interrelating intermetallic structures and their bonding with the condensed metal frameworks of the polar reduced metal halides/chalcogenides should be pursued. Investigations in this area may be just as exciting.

In conclusion, the varied results of this investigation attests to the effective use of electron-counting schemes in directing exploratory syntheses of polar and semipolar intermetallics.

21. Westgren, A.; Phragmen, G. Arkiv. Mat. Astron. Fysik. **1926** 19B, 1.

22. Mott, N.F.; Jones, H. Theory of the Properties of Metals and Alloys; Clarendon Press: Oxford,1936.

23. Heine, V. In Phase Stability in Metals and Alloys; Rudman, P.S., Stringer, J.S., and Jafee, R.I., Eds.; McGraw-Hill: New York,1966, p 135.

24. Pettifor, D.G. In Physical Metallurgy; Cahn, R.W., and Haasen, P., Eds.; Elsevier: Amsterdam,1983, 3rd edn.,Chapter 3.

25. Massalski, T.B.; Mizutani, V. Prog. Mater. Sci. **1978** 22, 151.

26. Hume-Rothery, W.; Mabbott, G.W.; Channel-Evans, K.M. Phil. Trans. Royal Soc. Lond. **1934** A233,1.

27. Hume-Rothery, W.; Smallman, R.E.; Haworth, C.W. Structure of Metals and Alloys; Institute of Metals: London, 1969.

28. Darken, L.S.; Gurry, R.W. Physical Chemistry of Metals; McGraw-Hill: New York, 1953, pp 74-92.

29. Gschneidner, K.A. In Theory of Alloy Phase Formation; Bennet, L.H., Ed.; Conference Proceedings; Metallurgical Society of AIME: New Orleans,1979, pp 1-39.

30. Alonso, J.A.; March, N.H. Electrons in Metals and Alloys; Academic Press: London, 1989, pp 265-285.

31. Biltz, W. Angew.Chem. **1935** 48, 729.

32. Laves, F.; Witte, H. Metallwirtschaft **1935** 14, 645.

33. Laves, F. Naturwissenschaften **1939** 27, 65.

34. Laves, F. In Intermetallic Compounds; Westbrook, J.H., Ed.; John Wiley and Sons: New York, 1967, p 129.

35. Frank, F.C.; Kasper, J.S. Acta Crystallogr. **1958** 11, 184.

36. Frank, F.C.; Kasper, J.S. Acta Crystallogr. **1959** 12, 483.

37. Laves, F. In Phase Stability in Metals and Alloys; Rudman, P.S., Stringer, J.; Jaffee, R.I., Eds.; McGraw-Hill: New York, 1967, pp 85-99.

38. Berry, R.L.; Raynor, G.V. Acta Crystallogr. **1953** 6, 178.

39. Shoemaker, C.B.; Shoemaker, D.P. In Developments in the Structure of Alloy Phases; Giessen, B.C., Ed.; Plenum: London, 1969, p 107 and references therein.

40. Sinha, A.K. Prog. Mater. Sci. **1972** 15, 79.

41. Johannes, R.L.; Haydock, R.; Heine, V. Phys. Rev. Lett. **1976** 36, 372.

42. Machlin, E.S.; Loh, B. Phys. Rev. Lett. **1981** 47, 1087.

43. Simon, A. Angew. Chem. **1983** 95, 94.

44. Ohba, T.; Kitano, Y.; Komura, Y. Acta Crystallogr. **1984** C40, 1.

45. Hafner, J. J. Phys. **1976** F6, 1243.

46. Hafner, J. Phys. Rev. B **1980** 21, 406.

47. Hafner, J. From Hamiltonians to Phase Diagrams; Solid State Sciences, Vol.70; Springer-Verlag: Berlin,1987, Chapter 8 and references therein.

48. Pauling, L. The Nature of the Chemical Bond; Cornell University: Ithaca, 1960, Chapter 3.

49. Watson, R.E.; Bennet, L.H. Phys. Rev. B **1978** 18, 6439.

50. Laves, F. In Intermetallic Compounds; Westbrook,J.H.,Ed.; John Wiley and Sons: New York, 1967, pp 129-143.

51. Pearson, W.B. The Crystal Chemistry and Physics of Metals and Alloys; Wiley-Interscience: New York, 1972, Chapter 5.

52. Zintl, E.; Dullenkopf, W. Z. Phys. Chem. **1932** B16, 195.

53. Zintl, E.; Neumayr, S. Z. Phys. Chem. **1933** B20, 272.

54. Zintl, E.; Schneider, A. Z. Electrochem. **1934** 40, 588.

55. Zintl, E.; Schneider, A. Z. Electrochem. **1934** 40, 107.

56. Zintl, E.; Harder, A. Z. Phys. Chem. **1936** B34, 238.

57. Zintl, E. Angew. Chem. **1939** 52, 1.

58. Laves, F. Naturwissenschaften **1941** 29, 244.

59. Joannis, A. Compt. rend. **1891** 113, 795.

60. Joannis, A. Compt. rend. **1892** 114, 585.

61. Zintl, E. Naturwissenschaften **1929** 17, 782.

62. Zintl, E.; Goubeau, J.; Dullenkopf, W. Z. Phys. Chem. **1931** A154, 1.

63. Zintl, E.; Harder, A. Z. Phys. Chem. **1931** A154, 47.

64. Zintl, E.; Dullenkopf, W. Z. Phys. Chem. **1932** B16, 183.

65. Marsh, R., and Shoemaker, D. Acta Crystallogr. **1953** 6, 197.

66. Kummer, D.; Diehl, L. Angew. Chem. Int. Ed. Engl. **1970** 9, 895.

67. Corbett, J.D.; Adolphson, D.; Merryman, D.; Edwards, P.; Armatis, F. J. Am. Chem. Soc. **1975** 97, 6267.

68. Corbett, J.D. Chem. Rev. **1985** 85, 383 and references therein.

69. Corbett, J.D. Nova Acta Leopoldina **1985** 59, Nr. 264, 183.

70. Hume-Rothery, W. In Phase Stability in Metals and Alloys; Rudman, P.S., Stringer, J., Jaffee, R.I., Eds.; McGraw-Hill: New York, 1967, pp 3-23.

71. Parthé, E. Z. Krist. **1961** 115, 52.

72. Girgis, K. In Physical Metallurgy; Cahn, R.W., and Haasen, P., Eds.; North-Holland: Amsterdam, 1983, Vol.1, Chapter 5, pp 220-269.

73. Pettifor, D.G. J. Phys. C **1986** 19, 285.

74. Pettifor, D.G. In Alloy Phase Stability; Stocks, G.M., and Gonis, A., Eds.; Kluwer Academics: Dordrecht,Netherlands, 1989, pp 329-350.

75. Villars, P.; Mathis, K.; Hulliger, F. In The Structures of Binary Compounds; de Boer, F.R., and Pettifor, D.G., Eds.; North Holland: Amsterdam, 1989, Chapter 1, and references therein.

76. Engel, N. Powder Met. Bull. **1954** 7, 8.

77. Brewer, L. In Electronic Structure and Alloy Chemistry of the Transition Elements; Beck, P.A., Ed.; John Wiley and Sons: New York, 1963, pp. 221-235.

78. Brewer, L. In High-Strength Materials; Zackay, V.F., Ed.; John-Wiley and Sons: New York, 1965, pp. 12-103.

79. Miedema, A.R.; de Chatel, P.F. In Theory of Alloy Phase Formation; Bennett, L.H., Ed.; Metallurgical Society of AIME: New York, 1980, pp 344-389 and references therein.

80. Seitz, F. Modern Theory of Solids; McGraw-Hill: New York, 1940, pp 345-384.

81. Chelikowsky, J.R.; Phillips, J.C. Phys. Rev. **1978** B17, 2453.

82. Cottrell, A. Introduction to the Modern Theory of Metals; Institute of Metals: London, 1988, pp 129-131.

83. Zintl, E.; Brauer, G. Z. Phys. Chem. **1933** B20, 245.

84. Zintl, E.; Kaiser, H. Z. Anorg. Chem. **1933** 211, 113.

85. Zintl, E.; Harder, A. Z. Phys. Chem. **1932** B16, 206.

86. Brauer, G.; Zintl, E. Z. Phys. Chem. **1937** B37, 323.

87. Zintl, E.; Harder, A.; Dauth, B. Z. Electrochem. **1934** 40, 588.

88. Klemm, W. Proc. Chem. Soc. London **1958** ,329.

89. Busmann, E. Z. Anorg. Allg. Chem. **1961** 313, 90.

90. Klemm, W.; Busmann, E. Z. Anorg. Allg. Chem. **1963** 319,297.

91. Kubaschewski, O.; Villa, H. Z. Electrochem. **1949** 53, 32.

92. Klemm, W. Z. Electrochem. **1945** 51, 14.

93. Mooser, E.; Pearson, W.B. Phys. Rev. **1956** 101,1608.

94. Mooser, E.; Pearson, W.B. Acta Crystallogr. **1959** 12,1015.

95. Mooser, E.; Pearson, W.B. In Progress in Semiconductors; Gibson, Kröger and Burgess,Eds; Wiley and Sons: New York,1960,Vol.5,103.

96. Pearson, W.B. Acta Crystallogr. **1964** 17, 1.

97. Klemm, W.; Westlinning, H. Z. Electrochem. **1943** 49, 198.

98. Grube, G. Z. Electrochem. **1950** 54, 99.

99. Klemm, W.; Fricke, H. Z. Anorg. Chem. **1955** 282,162.

100. Suhrmann, R.; Kangro, C. Naturwissenschaften **1953** 40, 137.

101. Grube, G.; Schneider, A. Z. Anorg. Chem. **1956** 286,118.

102. Grube, G.; Vosskühler, H.; Vogt, H. Z. Electrochem. **1932** 38,869.

103. Bennett, L.H. In Developments in the Structural Chemistry of Alloy Phases; Giessen, B.C., Ed.; Plenum Press: New York, 1969, pp 41-44.

104. Pearson, W.B. In Developments in the Structural Chemistry of Alloy Phases; Giessen, B.C., Ed.; Plenum Press: New York, 1969, pp 45-48.

105. Zintl, E.; Neumayr, S. Z. Electrochem. **1933** 39, 86.

106. Schäfer, H.; Eisenmann, B.; Müller, W. Angew. Chem. Int. Ed. Engl. **1973** 12, 694.

107. Schäfer, H.; Eisenmann, B. Rev. Inorg. Chem. **1981** 3, 29.

108. Schäfer, H. Ann. Rev. Mater. Sci. **1985** 15, 1.

109. von Schnering, H.G. Angew. Chem. Int. Ed. Engl. **1981** 20, 33.

110. Schuster, H.U. Nova Acta Leopoldina **1985** 59, Nr. 264, 199.

111. Bronger, W. Angew. Chem. Int. Ed. Engl. **1981** 20, 52.

112. Jeitschko, W.; Reehuis, M. J. Phys. Chem. Solids **1987** 48, 667 and references cited therein.

113. Böttcher, P. Angew. Chem. **1988** 100, 781.

114. Kauzlarich, S. Comments Inorg. Chem. **1990** 10, 75.

115. Hoffmann, R. Solids and Surfaces - A Chemist's View of Bonding in Extended Structures; VCH: New York, 1988 and references therein.

135. Sleight, A.W. Proceedings of the Robert A. Welch Foundation Conference on Chemical Research **1988** XXXII, Chapter 6, p 123.

136. Anderson, P.W. Proceedings of the Robert A. Welch Foundation Conference on Chemical Research **1988** XXXII, Chapter 1, p 1.

137. Rudnick, J.; Stern, E.A. Phys. Rev. **1973** B7, 5062.

138. Villars, P.; Calvert, L.D. Pearson's Handbook of Crystallographic Data for Intermetallic Phases; American Society for Metals: Metals Park, OH, 1985; 3 vols.

139. Garcia, E.; Corbett, J.D. Inorg. Chem. **1988** 27, 2353.

140. Garcia, E. Ph.D. Dissertation, Iowa State University, 1986.

141. Kwon, Y.U. Ph.D. Dissertation, Iowa State University, 1991.

142. Rossteutscher, W.; Schubert Z. Metallkunde **1965** 56, 813.

143. Rieger, W.; Novotny H.; Benesovsky, F. Monats. Chem. **1964** 95, 1413.

144. Parthe', E.; Rieger, W. J. Dental Res. **1968** 47, 829.

145. Novotny, H.; Benesovsky In Phase Stability in Metals and Alloys; Rudman, P.S.; Stringer, J.; Jaffee, R.I., eds., McGraw-Hill: New York, 1966, pp.319-336.

146. Hyde, B.G.; Andersson, S. Inorganic Crystal Structures; John Wiley and Sons: New York, 1989, pp. 356-371.

147. Chevrel, R.; Sergent, M.; Prigent, J. J. Solid State Chem. **1971** 3, 515.

148. Matthias, B.T.; Marezio, M.; Corenzwit, E.; Cooper, A.S.; Barz, H.E. Science **1972** 175, 1465.

149. Schubert, K. Kristallstrukturen zweikomponentiger Phasen; Springer-Verlag: Berlin, Germany, 1964, pp. 305-307.

150. Novotny, H.; Parthé, E.; Kieffer, R.; Benesovsky, F. Monatsh. Chem. **1954** 85, 255.

151. Novotny, H.; Lux, B.; Kudielka, H. Monatsh. Chem. **1956** 87, 447.

152. Kieffer, R.; Benesovsky, F.; Lux, B. Planseeber. Pulvermetallurgie **1956** 4, 30.

170. Henry, N.F.M.; Lipson, H.; Wooster, W.A. The Interpretation of X-Ray Diffraction Photographs; Macmillan, London, 1960.

171. Jacobson, R. CHES.CAT Program; USDOE, Ames Laboratory.

172. Texsan: Single Crystal Structure Analysis Software, Version 5.0; Molecular Structure Corporation: The Woodlands, TX, **1989**.

173. SDP User's Guide; Enraf-Nonius, Delft, Holland, and B.A. Frenz and Associates, Inc., College Station, TX, **1988**.

174. Walker, N.; Stuart, D. Acta Crystallogr. **1983** A19, 158.

175. North, A.C.T.; Phillips, D.C.; Mathews, F.S. Acta Crystallogr. **1968** A24, 351.

176. Sheldrick, G. SHELXS-76 programs for Structural Determination, Universität Göttingen, Germany, 1976.

177. Busing, W.R.; Martin, K.O.; Levy, H.A. ORFFE, A FORTRAN Crystallographic Function and Error Program; Report ORNL-TM-306, Oak Ridge National Laboratory: Oak Ridge, TN, **1964**.

178. Filliben, J.J. DATAPLOT; Center for Applied Mathematics, National Engineering Laboratory, NBS, Washington,D.C. 1984.

179. Wolfe, L.G. MS Thesis, ISU, 1990.

180. Shinar, J.; Dehner, B.; Beaudry, B.J.; Peterson, D.T. Phys. Rev. B **1988** 37, 2066.

181. Albright, T.A.; Burdett, J.K.; Whangbo, M.-H. Orbital Interactions in Chemistry; Wiley-Interscience: New York, 1985, Chap. 20.

182. Whangbo, M.-H.; Hoffmann, R.; Woodward, R.B. Proc. Royal Soc. **1979** A366, 23.

183. Burdett, J. Nature **1979** 279, 121.

184. Kertesz, M., Georgetown University, personal communication, 1989.

185. Kirk-Othmer Encylopedia of Chemical Technology, 3rd ed., 1980, pp.791-802.

186. Samsonov, G.; Bondarev, V. Germanides; Consultants Bureau: New York, 1969.

207. Tharp, A.G.; Smith, G.S.; Johnson, Q. Acta Crystallogr. **1966** 20, 583.

208. Rud, B.M.; Lynchak, K.A.; Pademo Yu.B. Sov. Powder Metall. Met. Ceram. **1968** 72, 216.

209. Smith, G.S.; Johnson, Q.; Tharp, A.G. Acta Crystallogr. **1967** 22, 269.

210. Kwon, Y.U. PhD. Thesis, ISU 1991.

211. Havinga, E.E. J. Less-Common Metals **1972** 27, 169.

212. Frank, F.C.; Kasper, J.S. Acta Crystallogr. **1959** 12, 483.

213. Zachariasen, W.H. Acta Crystallogr. **1949** 2, 94.

214. Iglesias, J.E.; Steinfink, H. J. Less-Common Met. **1972** 26, 45.

215. Pfeifer, H.-U.; Schubert, K. Z. Metallkunde **1966** 57, 884.

216. Wang, Y.; Calvert, L.D.; Gabe, E.J.; Taylor, J.B. Acta Crystallogr. **1978** B34, 1962.

217. Hohnke, D.; Parthé, E. Acta Crystallogr. **1966** 21, 435.

218. Meisel, K. Z. Anorg. Chem. **1939** 240,300.

219. Kripyakevich, P.I. Soviet Phys. Crystallogr. **1963** 7, 556.

220. Heim, H.; Bärnighausen, H. Acta Crystallogr. **1978** B34, 2084.

221. Hyde, B.G.; Andersson, S. Inorganic Crystal Structures, Wiley and Sons: New York, N.Y. 1989, pp. 333.

222. Baenziger, N.C.; Rundle, R.E.; Snow, A.I; Wilson, A.S. Acta Crystallogr. **1950** 3, 34.

223. Atoji, M.; Lipscomb, W.N. Acta Crystallogr. **1954** 7, 597.

224. Green, J.L.; Arnold, G.P.; Leary, J.A.; Nereson, N.G. J. Nuclear Materials **1970** 34, 281.

225. Helms, A.; Klemm, W. Z. Anorg. Allg. Chem. **1939** 242, 201.

226. Dwight, A.E. Acta Crystallogr. **1977** B33, 1579.

248. Hyde, B.G.; Andersson, S. In Inorganic Crystal Structures, John Wiley and Sons, New York, N.Y., 1989, p.335.

249. Guloy, A.; Corbett, J.D. unpublished report, 1990.

250. Herring, C. J. Appl. Phys. **1960** 31, 3S-11S.

251. Wagner, C.D.; Riggs, W.M.; Davis, L.E.; Moulder, J.F.; Muilenberg, G.E. Handbook of X-Ray Photoelectron Spectroscopy; Perkin-Elmer Corp.: Eden Prairie, MN, 1979.

252. Varma, C.M.; Wilson, A.J. Phys. Rev B **1980** 22, 3805.

253. Andersen, O.K. In The Electronic Structure of Complex Systems, Phariseau, P.; Temmerman, W.M. (ed.), Plenum Press, New York, 1984.

254. Andersen, O.K. In Highlights of Condensed Matter Physics, Bassani, F.; Fumi, F.; Tossi, M.P. (eds), North-Holland, New York, 1985.

255. Gschneidner, K.A. In Rare Earth Alloys; Van Nostrand: Princeton, 1961, pp 187-188.

256. Villars, P.; Calvert, L.D. Pearson's Handbook of Crystallographic Data for Intermetallic Phases, ASM International: Materials Park, Ohio, 1991, Vols. 1-4.

257. Hughbanks, T.; Corbett, J.D. Inorg. Chem. **1988** 27, 2022.

258. Wagner, C.D.; Riggs, W.M.; Davis, L.E.; Moulder, J.F.; Muilenberg, G.E. Handbook of X-ray Photoelectron Spectroscopy; Perkin-Elmer Corporation, Physical Electronics Division: Eden Prairie, Minnesota, 1979.

259. Pfeifer, H.U.; Schubert, K. Z. Metallkunde **1966** 57, 884.

260. Pearson, W.B. The Crystal Chemistry and Physics of Metals and Alloys; Wiley-Interscience: New York, 1972, pp. 772.

261. Pauling, L.; Pauling, P. Acta Crystallogr. **1956** 9, 127.

262. Karpinskii, O.G.; Evseev, B.A. Inorg. Mater. **1968** 4, 1094.

263. Smith, G.S.; Tharp, A.G; Johnson, Q. Acta Crystallogr. **1967** 22, 940.

264. Borzone, G.; Borsese, A.; Ferro, R. Z. Anorg. Allg. Chem. **1983** 501, 199.

265. Merlo, F.; Fornasini, M.L. Atti Accad. Naz. Lincei., Cl. Sci. Fis. Mat. Nat., Rend. **1971** 50, 186.

266. Miller, G. private communication, 1991.

267. Murav'eva, A.A; Zarechnyuk, O.S. Inorg. Mater. **1970** 6, 933.

268. Guloy, A.M. Quarterly Report, December 1991.

269. Payne, M.; Corbett, J.D. unpublished work.

270. Guloy, A.M.; Corbett, J.D. unpublished work.

271. Payne, M.W.; Dorhout, P.K.; Corbett, J.D. Inorg. Chem. **1991** 30, 1467.

272. Kauzlarich, S.M.; Payne, M.W.: Corbett, J.D. Inorg.Chem. **1990** 29, 3777.

273. Palenzona, A. J. Less-Common Met. **1979** 29, 27.

274. Sharifrazi, P.; Mohanty, R.C.; Raman, A. Z. Metallkunde **1984** 75, 801.

275. Brunton, G.D.; Steinfink, H. Inorg. Chem. **1971** 10, 2301.

276. Wang, Y.; Gabe, E.J.; Calvert, L.D.; Taylor, J.B. Acta Crystallogr. **1976** B32, 1440.

277. Potel, M; Brochu, R.; Padiou, J.; Grandjean, D. C. R. Acad. Sci. Paris, Ser. C **1972** 275, 1419.

278. Martinez-Ripoll, M.; Brauer, G.; Acta Crystallogr. **1974** B30, 1083.

279. Martinez-Ripoll, M.; Haase, A.; Brauer, G. Acta Crystallogr. **1974** B32, 2004.

280. Payne, M.W.; Dorhout, P.K.; Corbett, J.D. Inorg. Chem. **1991** 30, 1467.

281. Palenzona, A. J. Less-Common Met. **1979** 66, 27.

282. Morrish, A.H. The Physical Principles of Magnetism; John Wiley and Sons: New York, 1965, pp. 55-75.

283. Dorhout, P.K. private communications, 1991.

284. Jeitschko, W.; Parthé, E. Acta Crystallogr. **1965** 19, 275.

303. Jeitschko, W.; Parthé, E. Acta Crystallogr. **1967** 22, 551.

304. Iandelli, A.; Palenzona, A. In Handbook on Physics and Chemistry of Rare Earths; Gschneidner, K.A., Jr., Eyring, L., Eds.; North-Holland Publishing: Amsterdam, 1979; Vol.2, p.1.

305. Franceschi, E. J. Less-Common Met. **1979** 66, 175.

306. Borzone, G.; Borsese, A.; Ferro, R. Z. Anorg. Allg. Chem. **1983** 501, 199.

307. Aronsson, B. Acta Chem. Scand. **1955** 9, 1107.

308. Smith, J.D.; Corbett, J.D. J. Am. Chem. Soc. **1985** 107, 5704.

309. Hwu, S.-J.; Corbett, J.D. J. Solid State Chem. **1986** 64, 331.

310. Guloy, A.M.; Rzeznik, M.; Corbett, J.D. unpublished work.

311. Reiger, W.; Parthé, E. Monats. Chem. **1968** 99, 291.

312. Taylor, J.B.; Calvert, L.D.; Utsunomiya, T.; Wang, Y.; Despault, J.G. J. Less-Common Met. **1978** 57, 39.

313. Helleis, O.; Kandler, H.; Leicht, E.; Quiring, W.; Wolfel, E. Z. Anorg. Allg. Chem. **1963** 320, 86.

314. Arita, M.; Nissen, H.-U. J. Solid State Chem. **1990** 84, 386.

315. Wang, Y.; Calvert, L.D.; Gabe, E.J.; Taylor, J.B. Acta Crystallogr. **1978** B34, 2281.

316. Bruzzone, G.; Merlo, F. J. Less-Common Met. **1976** 48, 103.

317. Widera, A.; Schäfer, H. Mat. Res. Bull. **1980** 15, 1805.

318. Bruzzone, G.; Franceschi, E.; Merlo, F. J. Less-Common Met. **1978** 60, 59.

319. Eisenmann, B.; Schäfer, H. Z. Naturforsch. **1974** 29b, 460.

320. Schäfer, H.; Eisenmann, B.; Müller, W. Angew. Chem. Int. Ed. **1973** 12, 694.

321. Bruzzone, G.; Merlo, F. J. Less-Common Met. **1976** 48, 103.

322. Zintl, E.; Harder, A. Z. Phys. Chem. **1936** B34, 238.

342. Moreau, J.-M.; Paccard, D.; Parthé, E. Acta Crystallogr. **1976** 32B, 1767.

343. Guloy, A.M.; Ganguli, A.K.; Corbett, J.D. unpublished work.

344. Walker, N.; Stuart,D. Acta Crystallogr. **1983** A39,158.

345. Brown, I.D. Acta Crystallogr. **1988** B44, 545.

346. Shannon, R.D. Acta Crystallogr. **1976** A32, 751.

347. Carlin, R.L. Magnetochemistry; Springer-Verlag, berlin, Germany, 1986, pp. 10-12.

348. Newnham, R.E. Structure-Property Relations; Springer-Verlag: New York, 1975.

349. Moriya, T. Spin Fluctuations in Itinerant Electron Magnetism; Springer-Verlag, Berlin, Germany, 1985.

350. Berkowitz, A.E.; Kneller, E. Magnetism and Metallurgy; Academic Press, New York, 1969.

351. Allemand, P.M.; Khemani, K.C.; Koch, A.; Wudl, F.; Holczer, K.; Donovan, S.; Grüner, G.; Thompson, J.D. Science **1991** 253, 301.

352. Boudreaux, E.A.; Mulay, L.N. Theory and Applications of Molecular Paramagnetism; Wiley and Sons, New York, 1976.

353. Cullity, B.D. Introduction to Magnetic Materials; Addison-Wesley, Reading, Massachusetts, 1972, pp.491.

354. McHenry, M.E.; MacLaren, J.M.; Vvedensky, D.D.; Eberhart, M.E.; Prueitt, M.L. Phys. Rev. **1989** B40, 10111.

355. McLaman, T.J.; Miller, G. A program to calculate Madelung energies was used in the calculations.

356. Metzger, R.M. J. Chem. Phys. **1972** 57, 1870.

357. Guloy, A.; Corbett, J.D. unpublished work.

358. Geller, S. Acta Crystallogr. **1955** 8, 83.

359. Vegard, L. Z. Phys. **1922** 5, 17.

360. Pearson, W.B. The Crystal Chemistry and Physics of Metals and Alloys; Wiley-Interscience, New York, 1972, pp.174-179.

361. Eckerlin, P.; Leicht, E.; Wölfel, E. Z. Anorg. Allg. Chem. **1961** 307, 145.

362. Eisenmann, B.; Schäfer, H.; Weiss, A. Z. Anorg. Allg. Chem. **1972** 396, 241.

363. Villars, P.; Calvert, L.D. Pearson's Handbook of Crystallographic Data for Intermetallic Phases; ASM International: Materials Park, OH, 1991, Vols. 1-4.

364. Pearson, W.B. The Crystal Chemistry and Physics of Metals and Alloys; Wiley-Interscience: New York, 1972, p. 731.

365. Hyde, B.G.; Andersson, S. Inorganic Crystal Structures; Wiley-Interscience: New York, 1989, pp. 355-365.

366. Harsta, A; Rundqvist, S. J. Solid State Chem. **1987** 70, 210.

367. Matthias, B.T.; Compton, V.B.; Corenzwit, E. J. Phys. Chem. Solids **1961** 19, 130.

368. Bruzzone, G.; Franceschi, E.; Merlo, F.; J. Less-Common Met. **1978** 60, 59.

369. Guloy, A.; Corbett, J.D. unpublished work, 1991.

APPENDIX A. ORBITAL PARAMETERS USED IN EXTENDED-HÜCKEL BAND STRUCTURE CALCULATIONS

APPENDIX B. DIAMAGNETIC CORRECTIONS USED IN MAGNETIC SUSCEPTIBILITY MEASUREMENTS